Build with nature

Biomechanical properties and performance of self-growing connections in interconnected trees

Wang, X.

DOI
10.4233/uuid:8557da44-3a73-4c6b-a32a-0e9dd3c1ae73

Publication date
2024

Document Version
Final published version

Citation (APA)
Wang, X. (2024). *Build with nature: Biomechanical properties and performance of self-growing connections in interconnected trees*. [Dissertation (TU Delft), Delft University of Technology]. https://doi.org/10.4233/uuid:8557da44-3a73-4c6b-a32a-0e9dd3c1ae73


Build with Nature


Biomechanical properties and performance of self-growing connections in interconnected trees

Xiuli Wang

Build with Nature
Biomechanical Properties and Performance of Self-growing Connections in Interconnected Trees

Build with Nature
Biomechanical Properties and Performance of Self-growing Connections in Interconnected Trees

Dissertation

for the purpose of obtaining the degree of doctor
at Delft University of Technology
by the authority of the Rector Magnificus prof. dr. ir. T.H.J.J. van der Hagen,
chair of the Board for Doctorates
to be defended publicly on
Wednesday 10 April 2024 at 10:00 o'clock

by

Xiuli WANG

Master of Engineering in Architectural and Civil Engineering,
Tongji University, China,
born in Shandong, China.

This dissertation has been approved by the promotors.

Composition of the doctoral committee:

Rector Magnificus,	chairperson
Prof. dr. ir. J. W. G. van de Kuilen	Delft University of Technology, promotor
Prof. ir. N. A. de Vries	Delft University of Technology, promotor
Independent members:	
Prof. dr. H. M. Jonkers	Delft University of Technology
Dr. J. W. Byng	Delft University of Technology
Dr. A. Stokes	National Research Institute for Agriculture, Food and the Environment (INRAE), France
Dr. E. Verkasalo	Natural Resources Institute Finland (LUKE), Finland
Prof. dr. ir. A. V. Metrikine	Delft University of Technology, reserve member
Other member:	
Drs. W. F. Gard	Delft University of Technology

Keywords: Vertical greenery, self-growing connection, interconnected tree system, biomechanical property, self-growing structure, living tree structure

Printed by: Ipskamp Printing, the Netherlands

Cover: Designed by Xiuli Wang

ISBN 978-94-6384-561-8

An electronic version of this dissertation is available at
http://repository.tudelft.nl/.

To my family

Contents

Summary

Urban areas face a variety of ecological challenges in their development, including the urban heat island effect, loss of biodiversity, and urban flooding. To improve urban ecology, strategic use of vegetation, particularly trees, is essential. As the amount of land available in cities decreases, the combination of buildings with vertically planted trees has become a popular way to increase urban greenery. However, this presents new challenges, such as the mechanical stability of trees and their sustainable maintenance.

To address the challenge of tree mechanics, this research introduces a pioneering natural fixation technique from a structural engineering viewpoint. In this natural fixation, the trees are connected by *self-growing connections* and form in pairs as *the interconnected tree system*, or living structures. The fusion of a self-growing connection is based on the adaptive growth mechanism of trees, which is also referred to as 'inosculation' or 'thigmomorphogenesis' in arboriculture. In recent years, in the field of architecture and botany, there has been a gradual attention to the implementation of self-growing connections. However, the understanding of the living structures requires cross-disciplinary studies, and to the best of the author's knowledge, there is little directly relevant literature; and most discussions focus on qualitative analysis. To this end, the focus of this dissertation is on the quantitative examination of the fundamental characteristics and mechanical properties of self-growing connections and interconnected tree systems.

The main research question in this dissertation is '*what are the biomechanical characteristics of self-growing connections and the interconnected tree system?*' To answer this question, two tree species, *Ficus benjamina* L. and *Tilia cordata* Mill., were studied. *Ficus benjamina* was studied as a reference species to gain a fundamental understanding of these natural connections. The research of *Tilia cordata* was carried out to investigate the mechanical performance of interconnected tree systems. This work covered four levels of investigation, including material, connection, tree system, and growth monitoring. In addition, the mechanical properties of living structures were compared in different stages of growth.

The self-growing connection was characterized both at the macroscopic and microscopic levels. On the macroscopic scale, the self-growing connection was studied from three main aspects, namely the density distribution, geometric variation, and fiber structures. The results showed that the density of the intersected region was higher than that of the stem region in the same cross section within the self-growing connection. In the same cross-sectional view, the measured area of the intersected region was found to be larger than that of the stem region, indicating a greater allocation of material in the intersected region. Regarding fiber structures, the self-growing connection was primarily characterized by three groups of fibers, namely merged fibers, deviated fibers, and normal fibers. The group of merged fiber bundles combined two stems and played an important role in the structural integrity and mechanical strength of a self-growing connection.

At the microscopic level, the investigations were performed on the cellular and tissue scales. It explained and supported the macroscopic observations. The results indicated that on the edge of the interconnected region, especially at the small cross angle, the material was primarily composed of bark tissue. Notably, merged fibers were observed in the outer layer of the intersected region. In contrast, the inner section of the intersected region showed a lower concentration of continuous merged fibers. It consisted mainly of parenchyma tissues. Additionally, within the intersected region, the presence of tension wood with G-layers was identified. Furthermore, crystals within cells were found in the intersected area.

Following that, four-point spatial tensile tests were performed to investigate the tensile properties of self-growing connections. To characterize their fusion condition, two parameters (fusion degree and interface curvature) were proposed. During the tensile tests, it was observed that the connection gradually cracked from approximately 0.8 times its ultimate load. The propagation of cracks was primarily affected by the geometry of the interface and the content of the merged fibers. The failure occurred at the interface when the fusion degree reached around 15%, however, when the fusion degree exceeded this threshold, the failure cracks extended across the stems, forming a 'Y' shape. Additionally, statistical analyses of geometric parameters with mechanical properties were performed. Tensile strength exhibited negative correlations with cone ratio and interface curvature, whereas it had positive correlations with average diameter and fusion degree. The interface curvature was found to have a mediate correlation with the tensile strength. The average diameter and projected area were found to have better correlations with stiffness and load-carrying capacity compared to other parameters. In comparison to fusion degree, the interface curvature can better predict the tensile strength of a self-growing connection. An artificial neural network model was also utilized to establish a statistical model to predict the tensile strength of a self-growing connection. The results gave a good prediction, accounting for the variations of six input parameters.

After analyses of self-growing connections, this research focused on investigating the biomechanical characteristics of interconnected tree systems, including cross interconnected trees, parallel interconnected trees, and single standing trees. Investigations were carried out repeatedly before and after a two-year growth period. Experimental pulling tests were conducted under various loading scenarios, classified as in-plane and out-of-plane loading with respect to the trees connecting plane. Finite element models were used to complement the experimental measurements and provide additional information on the reactions of the interconnected tree system. The results revealed that the rigidity of all the interconnected systems increased as a result of tree growth. Regarding the cross interconnected tree system, an evident bracing effect was observed in the in-plane loading scenario. This was reflected in fewer deformations and lower stress levels compared to the out-of-plane scenario loaded on the same tree. However, the in-plane loading capacity was strongly influenced by the strength of the supporting tree. Regarding the parallel interconnected trees, they exhibited an increase in basal stiffness compared to single standing trees, as a result of the formation of a self-growing connection in the lower region, but may exhibit certain asymmetric behavior.

Finally, the growth of self-growing connections was investigated using the microdrilling technique. The method was first applied to self-growing connections fused by *Ficus* *benjamina* to explain the resistance distribution pattern in facilitation with anatomical characteristics and density changes. Subsequently, the approach was utilized to deduce internal features from self-growing connections fused by *Tilia cordata.* Regarding self-growing connections fused by *Ficus benjamina*, no significant statistical relationship was observed between resistance and density due to the limited range of density. In the intersected region of the self-growing connection, a drop-down effect was identified in the resistance profile. This effect corresponded to the findings of microscopic observations of the location of the included bark. Regarding the self-growing living connection fused by *Tilia cordata*, the resistance profile can provide information about the location of internal discontinuities (i.e., bark tissues). However, further conclusions require validation through anatomical studies (e.g., correspondence between resistance profile and locations of growth rings, orientations of fibers, as well as locations of knots).

Self-growing structures have three key benefits over traditional structures: entirely natural, developing geometry and material properties, as well as the potential to be adaptive and self-optimizing. Through quantitative studies, the purpose of this research is to provide insights and knowledge support for the structural design of living structures for future cities.

Samenvatting

Stedelijke gebieden worden bij hun ontwikkeling geconfronteerd met verschillende ecologische uitdagingen, waaronder het hitte-eilandeffect, verlies van biodiversiteit en overstromingen in de stad. Om de stedelijke ecologie te verbeteren is strategisch gebruik van vegetatie, met name bomen, essentieel. Nu de hoeveelheid beschikbare grond in steden afneemt, is de combinatie van gebouwen met verticaal geplante bomen een populaire manier geworden om het stedelijk groen te vergroten. Dit brengt echter nieuwe uitdagingen met zich mee, zoals de mechanische stabiliteit van bomen en hun duurzame onderhoud.

Om de uitdaging van boommechanica aan te gaan, introduceert dit onderzoek een baanbrekende natuurlijke fixatietechniek vanuit het oogpunt van constructietechniek. In deze natuurlijke fixatie worden de bomen verbonden door zelfgroeiende verbindingen en vormen ze paarsgewijs een samenhangend boomsysteem of levende structuren. De samensmelting van een zelfgroeiende verbinding is gebaseerd op het adaptieve groeimechanisme van bomen, dat in de boomkwekerij ook wel 'inosculatie' of 'thigmomorphogenesis' wordt genoemd. De laatste jaren is er op het gebied van architectuur en plantkunde een geleidelijke aandacht voor de implementatie van zelfgroeiende verbindingen. Het begrijpen van de levende structuren vereist echter interdisciplinaire studies, en voor zover de auteurs weten is er weinig direct relevante literatuur; en de meeste discussies richten zich op kwalitatieve analyse. Er is nog steeds een gebrek aan inzicht in de structurele prestaties van levende structuren. Daarom ligt de focus van dit proefschrift op het onderzoeken van de fundamentele kenmerken en mechanische eigenschappen van zelfgroeiende verbindingen en onderling verbonden boomsystemen.

De belangrijkste onderzoeksvraag in dit proefschrift is 'Wat zijn de biomechanische eigenschappen van zelfgroeiende verbindingen en het onderling verbonden boomsysteem? Om deze vraag te beantwoorden zijn twee boomsoorten, *Ficus benjamina* L. en *Tilia cordata* Mill. bestudeerd. *Ficus benjamina* werd bestudeerd als referentiesoort om een fundamenteel begrip te krijgen van deze natuurlijke verbindingen. Het onderzoek van *Tilia cordata* werd uitgevoerd om de mechanische prestaties van onderling verbonden boomsystemen te onderzoeken. Dit werk omvatte vier onderzoeksniveaus, waaronder materiaal, verbinding, boomsysteem en groeimonitoring. Bovendien werden de mechanische eigenschappen van levende structuren in verschillende groeistadia vergeleken.

De zelfgroeiende verbinding werd zowel op macroscopisch als op microscopisch niveau gekarakteriseerd. Op macroscopische schaal werd de zelfgroeiende verbinding bestudeerd vanuit drie hoofdaspecten, namelijk de dichtheidsverdeling, geometrische variatie en vezelstructuren. De resultaten toonden aan dat de dichtheid van het doorsneden gebied hoger was dan die van het stamgebied in dezelfde dwarsdoorsnede binnen de zelfgroeiende verbinding. In hetzelfde dwarsdoorsnedebeeld bleek het gemeten oppervlak van het doorsneden gebied groter te zijn dan dat van het stengelgebied, wat duidt op een grotere allocatie van materiaal in dit gebied. Wat betreft de vezelstructuren werd de zelfgroeiende verbinding voornamelijk gekenmerkt door drie groepen vezels, namelijk samengevoegde

vezels, afwijkende vezels en normale vezels. De groep van samengevoegde vezelbundels combineerde twee stengels en speelde een belangrijke rol in de structurele integriteit en mechanische sterkte van een zelfgroeiende verbinding.

Op microscopisch niveau werden de onderzoeken uitgevoerd op cel- en weefselschaal. Dit verklaarde en ondersteunde de macroscopische waarnemingen. De resultaten gaven aan dat aan de rand van het verbonden gebied, vooral bij de kleine dwarsdoorsnede, het materiaal voornamelijk bestond uit schorsweefsel. Met name in de buitenste laag van het doorsneden gebied werden samengevoegde vezels waargenomen. De binnenste sectie van het doorsneden gebied vertoonde daarentegen een lagere concentratie van continue samengevoegde vezels. Het bestond voornamelijk uit parenchymweefsel. Bovendien werd in het doorsneden gebied de aanwezigheid van spankap met G-lagen vastgesteld. Verder werden in het doorsneden gebied kristallen binnen cellen gevonden.

Vervolgens werden ruimtelijke trekproeven met vier punten uitgevoerd om de trekeigenschappen van zelfgroeiende verbindingen te onderzoeken. Om hun fusieconditie te karakteriseren werden twee parameters (fusiegraad en interfacekromming) voorgesteld. Tijdens de trekproeven werd waargenomen dat de verbinding geleidelijk scheurde vanaf ongeveer 0,8 keer de uiterste belasting. De voortplanting van scheuren werd voornamelijk beïnvloed door de geometrie van de interface en de inhoud van de samengevoegde vezels. De breuk trad op bij de interface wanneer de versmeltingsgraad ongeveer 15% bereikte, maar wanneer de versmeltingsgraad deze drempel overschreed, breidden de breukscheuren zich uit over de stengels en vormden een Y-vorm. Bovendien werden statistische analyses van geometrische parameters met mechanische eigenschappen uitgevoerd. Treksterkte vertoonde negatieve correlaties met kegelverhouding en interfacekromming, terwijl het positieve correlaties had met gemiddelde diameter en versmeltingsgraad. De interfacekromming bleek een mediërende correlatie te hebben met de treksterkte. De gemiddelde diameter en het geprojecteerde oppervlak bleken een betere correlatie te hebben met stijfheid en belastbaarheid dan andere parameters. In vergelijking met de fusiegraad kan de interfacekromming de treksterkte van een zelfgroeiende verbinding beter voorspellen. Een kunstmatig neuraal netwerkmodel werd ook gebruikt om een statistisch model op te stellen om de treksterkte van een zelfgroeiende verbinding te voorspellen. De resultaten gaven een goede voorspelling, rekening houdend met de variaties van zes inputparameters.

Na analyses van zelfgroeiende verbindingen richtte dit onderzoek zich op het onderzoeken van de biomechanische eigenschappen van onderling verbonden boomsystemen, waaronder kruislings verbonden bomen, parallel verbonden bomen en alleenstaande bomen. Onderzoeken werden herhaaldelijk uitgevoerd voor en na een groeiperiode van twee jaar. Er werden experimentele trekproeven uitgevoerd onder verschillende belastingsscenario's, geclassificeerd als in- en uit-vlak belasting ten opzichte van het verbindingsvlak van de bomen. Er werden eindige-elementenmodellen gebruikt om de experimentele metingen aan te vullen en aanvullende informatie te geven over de reacties van het onderling verbonden boomsysteem. De resultaten toonden aan dat de stijfheid van alle onderling verbonden systemen toenam als gevolg van de boomgroei. Bij het kruislings verbonden boomsysteem werd een duidelijk verstevigend effect waargenomen in het scenario met inplane belasting. Dit kwam tot uiting in minder vervormingen en lagere spanningsniveaus in vergelijking met het out-of-plane scenario dat op dezelfde boom werd belast. De inplane belastbaarheid werd echter sterk beïnvloed door de sterkte van de ondersteunende boom. De parallel met elkaar verbonden bomen vertoonden een toename in basale stijfheid in vergelijking met alleenstaande bomen, als gevolg van de vorming van een zelfgroeiende verbinding in de onderste regio, maar kunnen een bepaald asymmetrisch gedrag vertonen.

Tot slot werd de groei van zelfgroeiende verbindingen onderzocht met behulp van de microboortechniek. De methode werd eerst toegepast op zelfgroeiende verbindingen die versmolten zijn door *Ficus benjamina* om het weerstandsdistributiepatroon in facilitatie met anatomische kenmerken en dichtheidsveranderingen te verklaren. Vervolgens werd de benadering gebruikt om interne kenmerken af te leiden van zelfgroeiende verbindingen die zijn samengesmolten door *Tilia cordata*. Met betrekking tot zelfgroeiende verbindingen die vergroeid zijn met *Ficus benjamina* werd geen significant statistisch verband waargenomen tussen weerstand en dichtheid vanwege de beperkte gegevensintervallen voor dichtheid. In het doorsneden gebied van de zelfgroeiende verbinding werd een dalend effect geïdentificeerd in het weerstandsprofiel. Dit effect kwam overeen met de bevindingen van microscopische observaties van de locatie van de opgenomen schors. Met betrekking tot de zelfgroeiende levende verbinding die is samengesmolten door *Tilia cordata* kan het weerstandsprofiel informatie geven over de locatie van interne discontinuïteiten (d.w.z. schorsweefsels). Verdere conclusies moeten echter worden gevalideerd door anatomische studies.

Zelfgroeiende structuren hebben drie belangrijke voordelen ten opzichte van traditionele structuren: ze zijn volledig natuurlijk, ontwikkelen geometrie en materiaaleigenschappen en kunnen adaptief en zelfoptimaliserend zijn. Het doel van dit onderzoek is om door middel van kwantitatieve studies inzichten en kennisondersteuning te bieden voor het structurele ontwerp van levende structuren voor toekomstige steden.

1

Introduction

1

1.1 Background

Human society depends on the benefits provided by nature such as food, materials, clean water, clean air, climate regulation, flood prevention, pollination, and recreation. However, many of these benefits, often referred to as ecosystem services, are used if their supply is almost unlimited and treated as free commodities whose true value is not fully appreciated.

This gradually leads to urban development that neglects the natural process of a system and its subsequent consequences to nature. With the progression of global urbanization, 55% of the world's population lives in cities, and this is expected to reach 68% by 2050 [1]. Although cities offer many benefits and opportunities to people, they face many serious problems, such as the urban heat island effect, air pollution, and reduced biodiversity. To have a smart, sustainable, and inclusive development, it is necessary to address the concern of providing proper value to ecosystem services. As detailed in the United Nations goals [2], global initiatives such as sustainable cities and communities (goal 11) have been made and progressed with global collaboration. European Union has launched the Sustainable Commission, European Green Deal, and has invested in green infrastructure to address challenges in urban environments [3–6]. The effective vegetation and tree management strategy in cities acts as the most important means to ensure the natural environment and ecosystem services in this initiative.

Generally, the author observed that the development of the spatial relationship between landscape design (especially trees) and the design of buildings can conceptually be divided into three stages, as illustrated in Figure 1.1. When cities are less urbanized, the distribution of the land between trees and buildings is relatively equal and distributed in the horizontal space, as in Figure 1.1 a. However, as the number of high-rise buildings increases, vegetation and trees make room for the development of buildings, as sketched in Figure 1.1 b. The tree planting space has gradually evolved from the horizontal area to the vertical space. This process is coupled with the development of high-rise buildings in cities. Example cases are green roofs and vertical forests. The detailed description can be found in Chapter 2. With the need for greater integration of trees into development goals, the imaginary future city has the potential to evolve as an eco-city with a full integration of trees and buildings, where trees may have structural, decorative, and environmental functions. In the end, it becomes living tree structures, as in Figure 1.1 c. The reason for embedding living tree structures in cities is due to the fact that it can not only fulfill multiple functions as single trees, such as cooling the environment and storing carbon, but can also provide structural values (e.g., green facade, vegetation shelter) in the future.

The future vision in Figure 1.1 c is the ambition of this project. To realize the vision of the eco-city, the study of the living tree structure is conducted in the doctorate research.

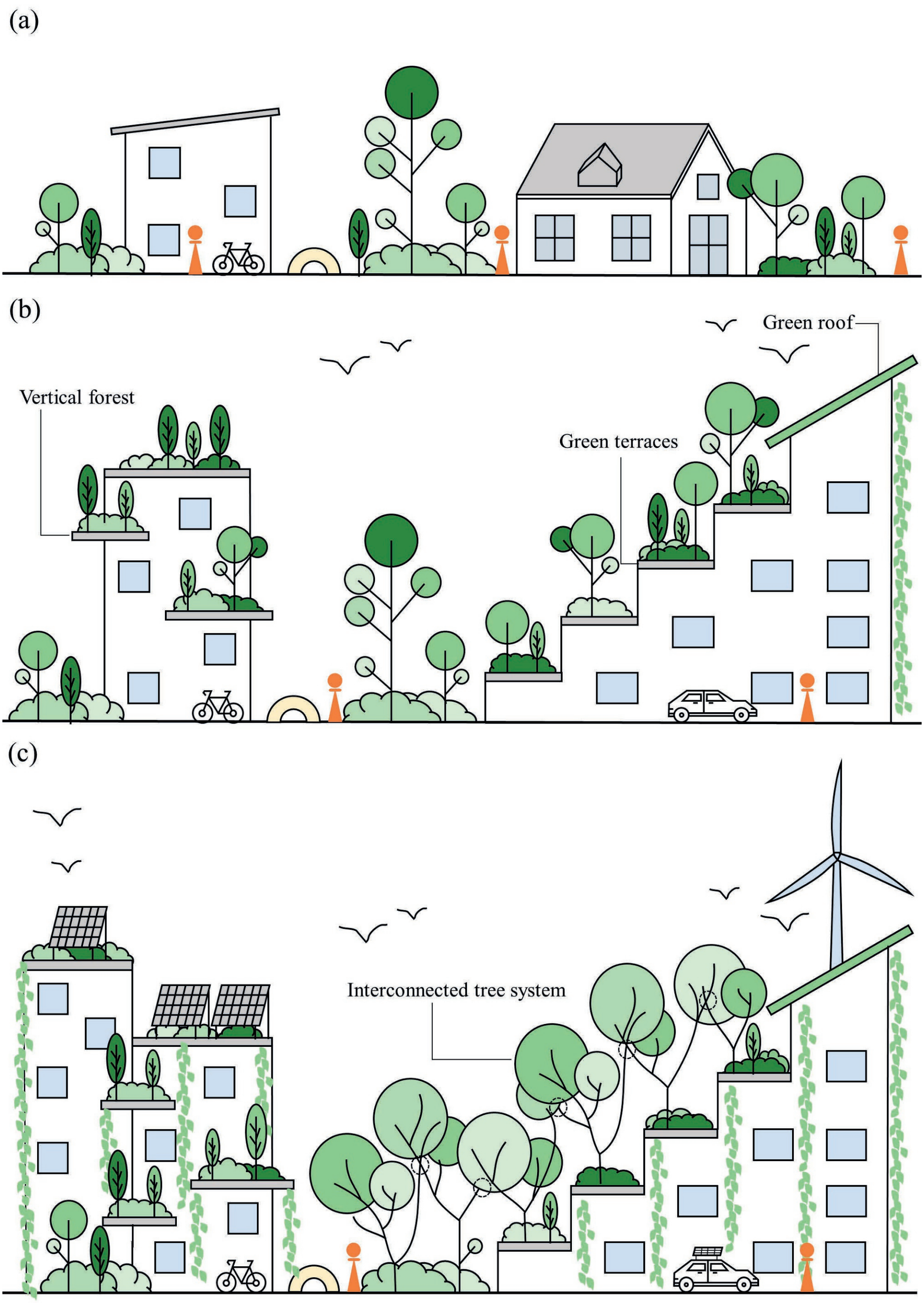

Figure 1.1: Evolution of urban greenery from horizontal design to future spatial outlook. (a) 2D green infrastructure planning; (b) 3D spatial development with vertical forests, green roof, and green terraces etc.; (c) imaginary future eco-city with living tree structures.

1.2 Challenges and opportunities

A better future requires visions and imaginations. However, it must also be realistic and supported by rigorous scientific evidence. The recent development has offered the potential to implement a future-oriented living tree structure in an urban environment. It is supported by the progress of more and more vertical forest constructions and the possibility of utilizing living tree connections, referred to as self-growing connections in this research.

1.2.1 Self-growing connection

The *self-growing connection* in this research is defined as the connection between living trees that are fused and grown by the trees themselves from the natural phenomenon, which is also termed inosculation or natural graft [7–9]. This type of connection is connected and developing in a pure natural process and may have the potential for future structural capacity. Figure 1.2 gives some examples of the natural connection and living structures fused by self-growing connections. The technique to fuse a self-growing connection varies, but the principle is to fuse the cambium, from which a bundle of fibers is developed connecting both tree members. In the scope of this research, as in Figures 1.2 a and b, the fused technique used is simple and prevents damage to the original trees. To be specific, two trees were tied by an elastic rope, by which they are subjected to compression and gradually fused over the course of growth. In trees, pressure applied to the bark and cambium was found to induce the development of proliferating undifferentiated cells into an organized xylem [10]. The bark of the trees was not cut or damaged at the fused interface at the time they were tied. The original trees used to form a connection have grown for several years; in the examples, they are of five years age. The discussion of the fusion technique is explained in Section 3.4.1. When the connection is created, the connected trees form a structural system that acts as a basic element for the further construction of a complex living structure. The potential application of the living structure can be in the production of decorative structures, such as fences and facades, or in the production of furniture, such as chairs in Figure 1.2 c, and it can also be built in the long term to form a civil structure, such as the example bridge in Figure 1.2 d.

1.2.2 Urban vertical greenery

Vertical urban greenery has developed rapidly in recent years, as it offers the possibility of expanding the spatial space of vegetation [11], in the mean time, through planning greenery, it provides benefits (e.g., mitigation of the urban heat island effect [12]) and drawbacks (e.g., safety concerns on falling trees or fire [13]) to the urban environment. However, from the perspective of engineers and biologists, attention is paid to trees and structures. Trees in vertical space usually grow on a restricted substrate that restricts the development of the root system. For example, trees grow on a balcony as in Figure 1.3 a and on the roof as in Figure 1.3 d. In these circumstances, tree growth is subject to a greater degree of complexity in loading due to human activities, such as the higher wind speed in vertical space than in ground level.

To ensure the stability of the elevated tree, some techniques have been applied from both engineering and botanical approaches. As shown in Figure 1.3, the first row of pictures gives the example of Bosco Verticale [14, 15], where trees are engineered to be fixed within

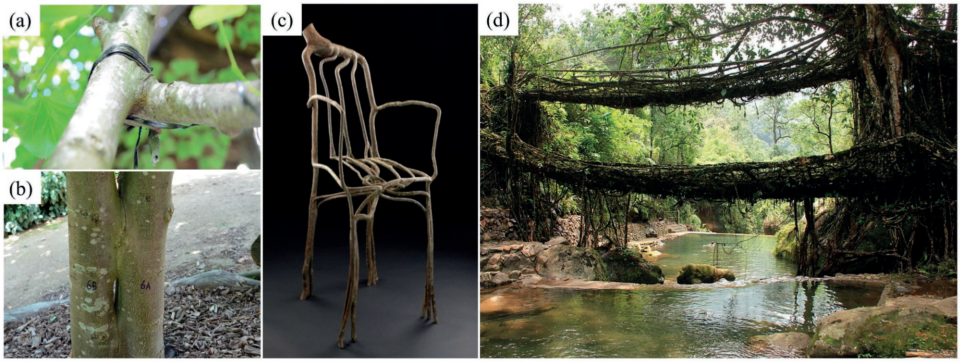

Figure 1.2: Self-growing connections and living tree structures. The cross (a) and parallel (b) self-growing connection at the TU Delft Hortus Botanicus; (c) a chair naturally grown from willow trees, photo credits Full Grown; (d) living root bridge in India, photo by Arshiya Urveeja Bose.

a steel cage on the balcony and, in the mean time, their stem is secured by a cable and connected to the main structure of the building (in Figure 1.3 b, indicated by yellow dots). The example in the second row of Figure 1.3 shows the case in Depot van Boijmans, where the trees are connected at the base, forming a multi-stem system so that the center of gravity is lowered compared to single standing trees (in Figure 1.3 c, indicated by yellow dots). Meanwhile, the root balls of this group of trees are belted and fixed to the structure of the building for stability concerns. The risk of an unstable tree occurs when the equilibrium between wind loads and tree resistance fails, as shown in Figure 1.3 f.

The challenges of this vertical greenery design can be analyzed from different points of view depending on the object studied. From the perspective of a tree, the surrounding wind environment is complex and uncertain. In addition, the speed and pressure of the wind increase exponentially with the height of the building. The resistance moment and shear of the tree itself are influenced by the size and morphology of the tree, as well as the strength of the wood of the stem and root systems [16]. The limited growth medium may restrict the development of self-adaptation to the environment if the nutritional level of the medium is assumed to be sufficient. It is not clear whether the combination of engineering fixation and adaptive growth can withstand severe external wind disturbance. Furthermore, from the perspective of the building structure, additional tree loads, such as growing biomass and saturated soil with storm water, pose threats to the safety of building use. However, despite the challenges mentioned above, the vertical greenery method provides great opportunities to extend urban greenery spatial planning. In this work, the author focuses on the approach to 'engineer' trees in a natural way, utilizing the self-growing connection acting as a fixation method to provide stability for trees in a vertical space.

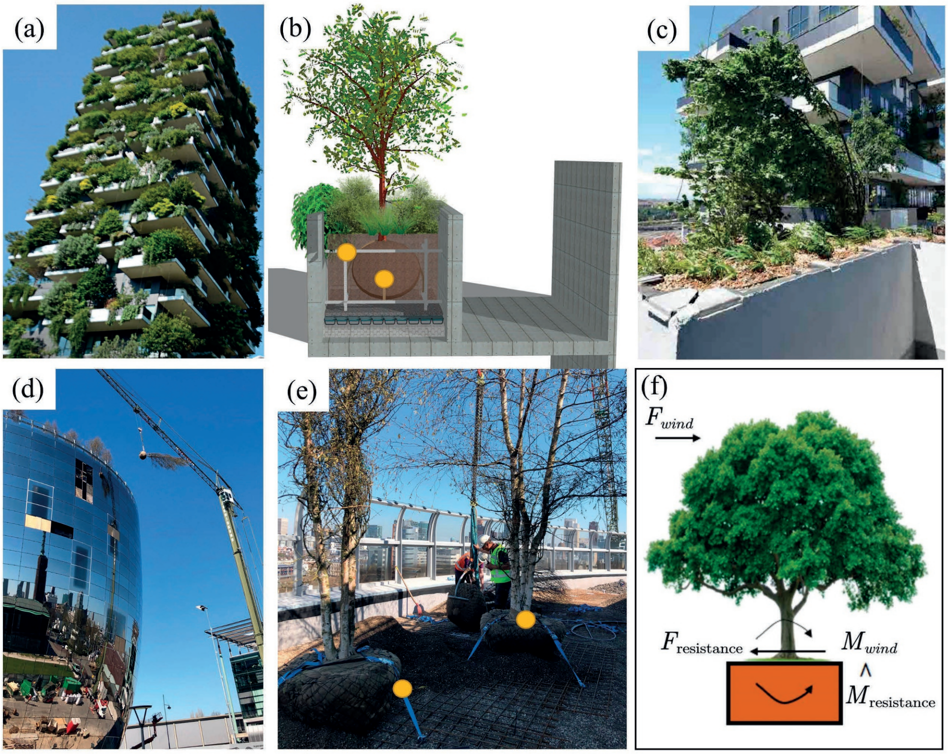

Figure 1.3: Examples of vertical greenery, techniques to fix trees, tree performance under wind and its equilibrium. (a) Picture of the Bosco Verticale located in Milan, Italy; (b) the engineering fixation approach of a balcony tree in Bosco Verticale; techniques used are the steel cage and belts for the root ball; (c) wind reaction of a balcony tree, from [14]; (d) transportation of roof trees to building Depot van Boijmans located in Rotterdam, the Netherlands; (e) the engineering fixation approach of roof trees in Depot van Boijmans; techniques are belts locking root ball and cultivated multi-stem trees; (f) the mechanism of wind resistance of a containerized tree. Photo (d) and (e) by Arjen Ketting.

1.2.3 Nature-based solution: Trees interconnected by self-growing connections

In this doctoral work, *an interconnected tree system* is proposed as a basic element for the design of living tree structures. As shown in Figure 1.4, the tree system is connected naturally by the self-growing connection. Therefore, the two connected trees form a plane shaped like 'X' in plane *yz*.

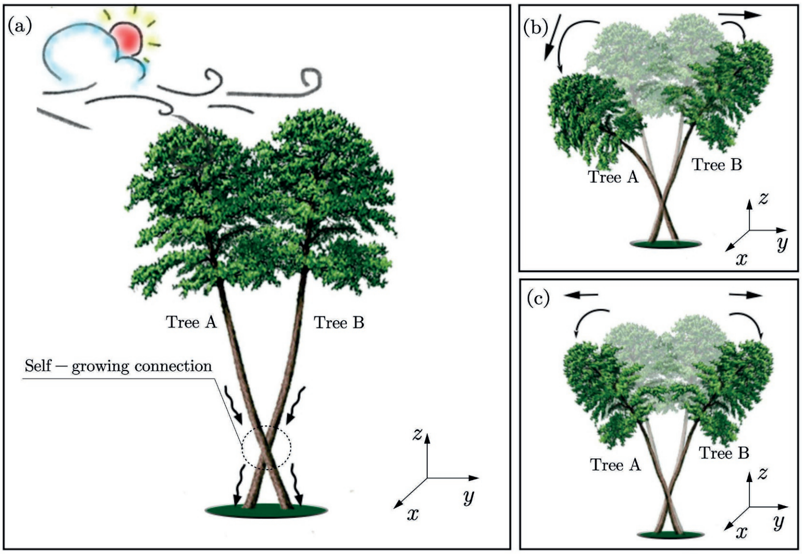

Figure 1.4: Schematic representation of an interconnected tree system and its reaction to load. (a) Interconnected trees forming a connecting plane which is the plane *yz*. (b) indicates the loading case of out-of-plane (plane *yz*) loading; whereas (c) represents the in-plane (plane *yz*) loading.

As illustrated in Figure 1.4, when external loads are exerted on the system, such as the wind load, the tree system resists the load and dissipates the energy deforming and transferring from the canopy through the self-growing connection to the root system. The advantage of the system is that it acts as a load-sharing system through the connection to better absorb and transfer loads together. Meanwhile, it provides the possibility to form and manage the shape of the system according to the idea of a designer. For example, one of the connected trees can be planted higher than the other, then extend the space in the vertical direction, as shown in Figure 1.1 c. In addition, the angle and location of the connection can be manipulated and designed in terms of loading conditions.

In Figure 1.4, the load transfer path can be further grouped into in-plane *yz* and out-of-plane *yz* cases as in Figures 1.4 b and c. However, following the fusion technology described in Section 1.2.1, the trees are hardly connected and fused into a perfect plane; in other words, the center lines of the two stems hardly cross in the same plane, and the centers of the biomass are also difficult to concentrate in the same plane. This is because at the time they start to create a connection, the trees have grown for a certain period. The later fusion growth is added on the basis of the original growth. As a result, the formed connection presents a certain eccentricity due to the difference in growth. Furthermore, the connecting interface is subject to bending, shear, and tension forces, which results in the rolling shear and tensile perpendicular stresses present at the interface. Regarding wood material, the rolling shear strength and the tensile perpendicular strength are much lower than the tensile strength in the fiber direction [17, 18]. This makes the connection the vulnerable region within the system.

To this end, the loading capacity of the tree system is governed by the splitting of the connecting interface. Regarding the self-growing connection, this research focuses on understanding the tensile loading out of the plane zy in Figure 1.4 b. Regarding the interconnected tree system, this work investigates and compares the performance of both out-of-plane 1.4 b and in-plane 1.4 c. Moreover, the mechanical properties of the self-growing connection are influenced by its growth stage and fusion quality. Therefore, to understand the performance of the living tree system under a certain loading condition, knowledge of the biological and mechanical properties of the self-growing connection and the living tree system is required.

1.3 Research scope and structures

Studies on interconnected trees can be performed on various topics in different fields according to the angle of study of the question of interest. For example, architects and landscape designers, the questions concerned include how to select appropriate plant species and optimize the design of the structure of living trees to better contribute to the urban environment [19]. Botanists and biologists are mostly concerned with the mechanism of the fusion process of the self-growing connection [20, 21]. For civil engineers, the greatest attention would be paid to the building and structure and to study the induced impacts of plant growth [22]. Additionally, strategic maintenance measures are also necessary for the long-term and sustainable development of these living tree structures.

In this work, the objects studied include the self-growing connection and the interconnected tree system. The focus is on their biomechanical properties. Thus, according to the limits of resources and the finite trajectory of Ph.D., the scope of the research is described as follows.

- **Tree species**. Due to limited resources (e.g., availability of test samples), the investigated tree species selected are *Ficus benjamina* L. (weeping fig) and *Tilia cordata* Mill. (small-leaved lime). Other tree species, such as willow and cherry, also show the potential to connect and fuse into a connection; they are beyond the scope of current research.

- **Study aspects**. The research aspects involve the mechanical performance of the self-growing connection and the connected tree system and the relevant biological features that may affect their mechanics.

- **Growth analogy**. The biological studies in the thesis focus mainly on the investigation of the self-growing connections fused by *Ficus benjamina.* It is assumed that the growth principles discovered can be generalized and analogous to some extent in connections fused by other species, e.g., *Tilia cordata*. However, further validations are not considered in the content.

- **Fusion technique**. The fusion technique implemented in the investigation is the same approach as described in Section 1.2.1 in the examples of Figures 1.2 a and b, so it can achieve comparable results.

- **Time dimension**. From the moment the stems are compressed together to form a connection, the fusion of a self-growing connection starts. However, the connection experiences several stages during the process [23]. Generally speaking, the soft tissues in the bark first attached and gradually formed a continuous cambium layer for growth as a connection. Then, from the cambium layer, stiff tissues, i.e., fiber bundles, are produced to add strength to the interface. This research focuses on the stage after fiber production. The mechanism of progress of fusion is not the focus of this study, but it will be investigated from the literature.

1.3.1 Research questions

In the context of urban vertical greenery, with a focus on the self-growing connections and interconnected tree systems, the main research question can be formulated as follows.

What are the biomechanical properties (i.e., biological characteristics and mechanical properties) of self-growing connections and the interconnected tree system?

Based on the differences among the perspectives studied, this main question is divided into several subquestions (RQ) of three aspects: self-growing connection, interconnected tree system, and growth monitoring. These subquestions are listed below.

On the level of the self-growing connection:

- RQ1. When two stems fuse into a connection, what are the fusion-induced characteristics in density, geometry, and fiber structures?

- RQ2. What are the fusion-induced changes in material compositions at the cellular and tissue levels?

- RQ3. How do self-growing connections perform under out-of-plane tensile loading?

- RQ4. How do growth-related parameters influence the mechanical performance of a self-growing connection?

On the level of an interconnected tree system:

- RQ5. How does the connected tree system perform under loads in and out of the connecting plane?

- RQ6. What is the effect of growth on the mechanical performance of the interconnected tree system?

From the growth monitoring perspective:

- RQ7. What internal features can be evaluated from the technique of micro-drilling resistance?

1

The relation between the main research question and the subquestions can be seen in Figure 1.5. In order to realize the construction of a self-growing structure, the study starts from the self-growing connection (RQ1 - 4) and extends to the interconnected tree system (RQ5 - 6). As the self-growing structure continues to grow, it is essential to keep track of its growth. Therefore, the study of the technique to monitor growth is performed both on the connection and on the interconnected tree system (RQ7).

In the study of the self-growing connection, the characterization of its biological properties and growth characteristics is performed at the macroscopic (RQ1) and microscopic (RQ2) levels. The study of the connection's mechanical properties (RQ3) and the relations with growth characteristics (RQ4) focuses on the study of tensile out-of-plane behavior. In the study of interconnected tree systems, with a focus on parallel and cross connected tree systems, the research investigates mechanical performance in and out of the plane (RQ5) and examines the growth effects (RQ6). By synthesizing the findings and studying the biomechanical properties from the connection level to the system level, the main research question can be answered. A more detailed chapter structure can be found in Section 1.3.2.

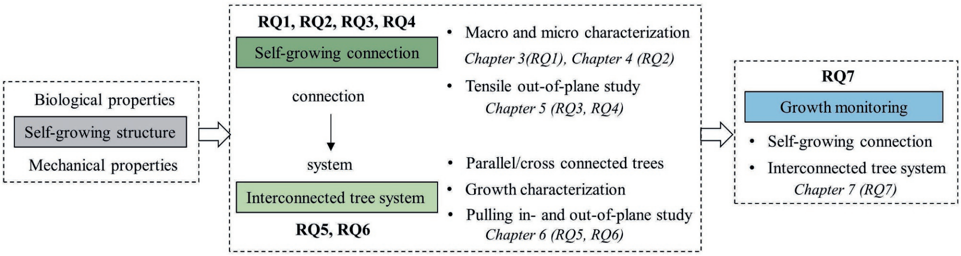

Figure 1.5: Relations between research questions (RQ) according to the studied objects and aspects.

1.3.2 Dissertation outline

The structure organization of the doctoral thesis is presented in Figure 1.6, which gives an overview of the main content of each section. This dissertation consists of eight chapters that aim to cover the most fundamental aspects of living tree structures. After the introductory chapter, a literature review on the current progress in vertical urban greenery is performed to provide the basis for the following chapters. With studies on self-growing connections, the characterization of growth features is performed at different scales, from cell to tissue and to entire connection. The study on the level of self-growing connection is considered as macroscopic scale, while the study on the wood material at the cellular and tissue level is considered as microscopic scale. After understanding the self-growing connection, the following studies are performed on the interconnected tree system. The focus is on its mechanical performance and its growth effects on the system level. In reality, destructive studies on existing living structures are not feasible; thus, a micro-drilling technique is implemented to inspect the internal features of the living structures without severe damage. The last chapter summarizes the main conclusions and future research are also recommended.

- Chapter 1 envisions the development of the future urban greenery. It introduces challenges and opportunities to implement self-growing connected tree systems in the urban ecosystem. This chapter maps out the structure of the dissertation and outlines the questions studied.
- Chapter 2 provides background information on the current progress in the development of building integrated greenery. The state of the art indicates the future trend for a sustainable, nature-based city.
- Chapter 3 characterizes the self-growing connection from aspects of density, geometry, fiber structure, and its influence from moisture content. It aims to answer the first sub-question (RQ1).
- Chapter 4 further investigates the self-growing connection at the cellular and tissue level. Observation focuses on the changes and differences in material compositions in the fused region and the stem region within a connection. This chapter answers the RQ2 sub-question.
- The biomechanical properties of self-growing connections are studied in Chapter 5. First, it quantifies the identified features that influence the mechanical performance of a connection. Then, the experimental work is carried out to understand the mechanical performance of the connections under tension. This chapter answers the research questions of RQ3 and RQ4.
- In addition to studies on the species of *Ficus benjamina*, the research is extended to investigate the species of *Tilia cordata* which forms an interconnected tree system, which is covered in Chapter 6. This chapter performs in-plane and out-of-plane loading scenarios on the cross- and parallel connected tree systems at two growth stages. The purpose of this chapter is to understand the growth effects and biomechanical behavior of a tree system. It answers the RQ5 and RQ6 sub-questions.
- Chapter 7 explores the possibilities of micro-drilling resistance. The aim is to interpret the internal features of a self-growing connection by the resistance profile. Thus, it further evaluates the fusion condition of the self-growing connection. It answers the last sub-question RQ7.
- Chapter 8 summarizes the main conclusions and provides recommendations for future research.

This dissertation has three highlights in terms of research methodology, as illustrated in Figure 1.7. It covers two species. Chapters 3, 4, 5 and 7 studied *Ficus benjamina*. Chapters 6 and 7 studied *Tilia cordata*. The growth development of the self-growing connection is quantified in Chapter 5; and the growth of the interconnected tree system is studied in Chapter 6. The entire study covers different scales, from the cellular and tissue scale in Chapter 4, to the scale of a connection in Chapter 3 and 5, and further studies on the braided tree structure in Chapter 3 and the interconnected tree system in Chapter 6 and 7. The aim is to establish a systematic methodology for studies on self-growing connections and interconnected systems, and thus to deepen the understanding of the utilization of living tree structures.

1

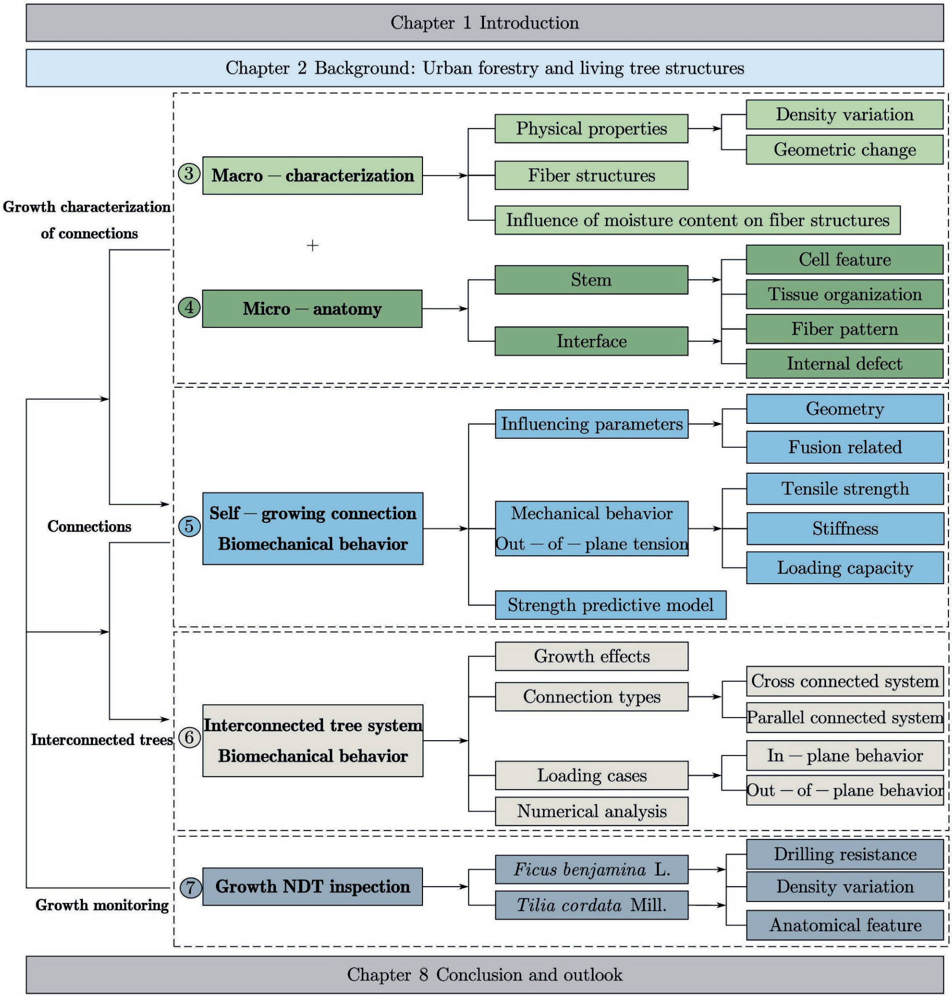

Figure 1.6: Outline and main content of the research.

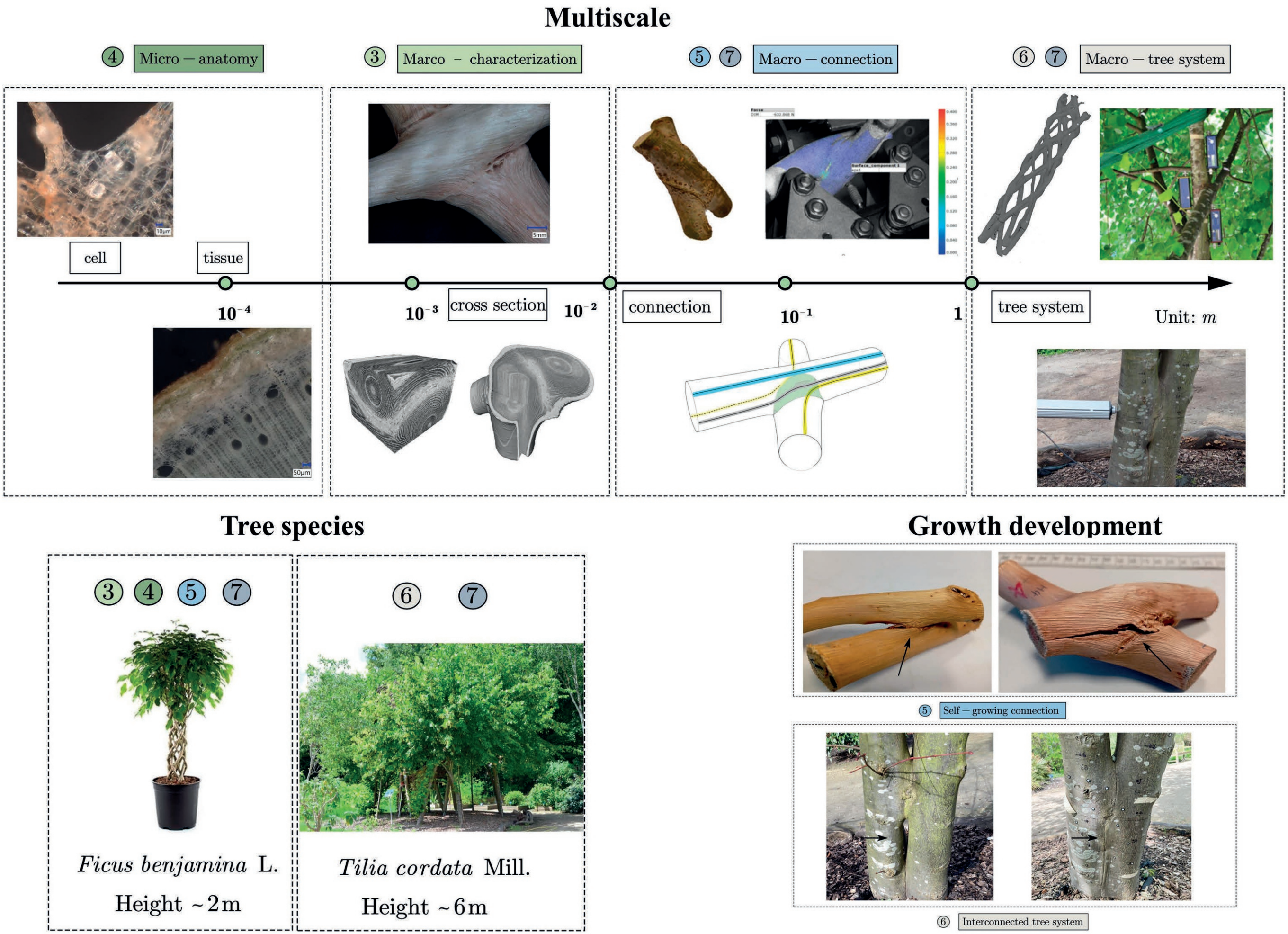

Figure 1.7: Illustration of the studied aspects: Multi-scale investigations from the cell level to the tree structure, two studied tree species *Ficus* and *Tilia*, and different growth stages in *Ficus* and *Tilia* connections.

1

References

[1] Eurostat. Energy statistics - an overview, 2022. URL https://ec.europa.eu/eurostat/statistics-explained/. Last visited 2023-05-20.

[2] United Nations General Assembly. Transforming our world: The 2030 agenda for sustainable development. Goal 11: Make cities inclusive, safe, resilient and sustainable, 2015.

[3] European Union. Forgoing a climate-resilient europe - the new EU strategy on adaption to climate change, 2020. URL https://eur-lex.europa.eu/legal-content/EN/TXT/?uri=COM:2021:82:FIN. Last visited 2023-05-20.

[4] European Union. EU biodiversity strategy for 2030. bringing nature back into our lives., 2020. URL https://environment.ec.europa.eu/strategy/biodiversity-strategy-2030{_}en. Last visited 2023-05-20.

[5] European Union. Green infrastructure (GI) - enhancing europe's natural capital, 2020. URL https://eur-lex.europa.eu/legal-content/EN/TXT/?uri=celex%3A52013DC0249. Last visited 2023-05-20.

[6] European Commission. The european green deal, 2019.

[7] T. Vallas and L. Courard. Using nature in architecture: Building a living house with mycelium and trees. *Frontiers of Architectural Research*, 6(3):318–328, 2017.

[8] F. Ludwig, H. Schwertfreger, and O. Storz. Living systems: Designing growth in baubotanik. *Architectural Design*, 82(2):82–87, 2012.

[9] F. Ludwig. Baubotanik: Designing with living material. In *Materiality and Architecture*, pages 182–191. Routledge, 2016.

[10] C. L. Brown and K. Sax. The influence of pressure on the differentiation of secondary tissues. *American Journal of Botany*, 49:683, 1962.

[11] X. Wang, W. Gard, H. Borska, B. Ursem, and J. W. G. Van De Kuilen. Vertical greenery systems: From plants to trees with self-growing interconnections. *European Journal of Wood and Wood Products*, 78:1031–1043, 2020.

[12] A. B. Besir and E. Cuce. Green roofs and facades: A comprehensive review. *Renewable and Sustainable Energy Reviews*, 82:915–939, 2018.

[13] A. Cheshmehzangi, C. Butters, L. Xie, and A. Dawodu. Green infrastructures for urban sustainability: Issues, implications, and solutions for underdeveloped areas. *Urban Forestry and Urban Greening*, 59:127028, 2021.

[14] E. Giacomello. Case study: Bosco Verticale, Milan: A new urban forest rises in Milan. *CTBUH journal*, (1):12–18, 2015.

[15] S. Boeri. Il Bosco Verticale. *ASPENIA*, 81:77–84, 2018.

[16] B. Gardiner, H. Peltola, and S. Kellomäki. Comparison of two models for predicting the critical wind speeds required to damage coniferous trees. *Ecological Modelling*, 129:1–23, 2000.

[17] J. W. G. Van de Kuilen, W. Gard, G. Ravenshorst, V. Antonelli, and A. Kovryga. Shear strength values for soft-and hardwoods. In *CIB-W18 Proceedings*, 2017. Pages 49–70.

[18] T. Ehrhart and R. Brandner. Rolling shear: Test configurations and properties of some european soft-and hardwood species. *Engineering structures*, 172:554–572, 2018.

[19] C. Bartesaghi Koc, P. Osmond, and A. Peters. Towards a comprehensive green infrastructure typology: A systematic review of approaches, methods and typologies. *Urban ecosystems*, 20:15–35, 2017.

[20] O. Hamant, M. G. Heisler, H. Jönsson, P. Krupinski, M. Uyttewaal, P. Bokov, F. Corson, P. Sahlin, A. Boudaoud, E. M. Meyerowitz, Y. Couder, and J. Traas. Developmental patterning by mechanical signals in *Arabidopsis*. *Science*, 322:1650–1655, 2008.

[21] F. W. Telewski. Mechanosensing and plant growth regulators elicited during the thigmomorphogenetic response. *Frontiers in Forests and Global Change*, 3:147, 2021.

[22] Q. Wang, Y. Cheng, A. Garg, and Z. Zhu. Characteristics of local wind pressure distribution and global aerodynamic forces on a vertical forest. *Ecological Engineering*, 138:61–70, 2019.

[23] A. N. Rao. Developmental anatomy of natural root grafts in *Ficus globosa*. *Australian Journal of Botany*, 14(3):269–276, 1966.

2

Progress in the building integrated vertical greenery

This chapter examines recent progress in the integration of trees with buildings. It aims to provide background information for the future implementation of living structures as a nature-based solution to improve urban environments. Therefore, the study begins with the classification and definition of the building integrated greenery. It can be organized into horizontal greenery and vertical greenery systems. Within the vertical greenery system, it can be divided into a green facade, a green wall, green terraces, and a vertical forest. The vertical greenery system provides the opportunity to extend the planting of greenery in the vertical space.

The design of the integration of trees with buildings requires both quantitative and qualitative understanding. The qualitative evaluation of the greenery with the building is discussed from both the benefits and drawbacks. However, planting trees without strategic approaches can have a negative effect on the urban environment. Therefore, this chapter explores the cooling mechanism of trees and the characteristics that help to regulate the microclimate in urban environments. Based on the information studied, this chapter provides decision-making considerations for the implementation, from planning to installation.

This chapter is partly based on *Vertical greenery systems: from plants to trees with self-growing connections.* [1].

2.1 Introduction

The Sustainable Development Goal 11 of the United Nations [2] promotes making cities inclusive, safe, resilient, and sustainable. On the urban scale, the European Union (EU) has encouraged investments in green and blue infrastructure, as well as systematic integration of ecosystems and nature-based solutions into urban design [3]. Green infrastructure (GI) is defined in the EU's green strategy as 'a strategically planned network of natural and semi-natural areas with other environmental characteristics designed and managed to deliver a wide range of ecosystem services'. Green infrastructure is also incorporated into the most recent EU biodiversity strategy and the EU environmental strategy on spatial planning and land use change [4, 5]. The use and management of woody plants in and around cities is central to this discussion. It requires the exchange of experiences from multiple disciplines to achieve successful implementation. In densely populated cities, the concept of integrating nature into high-rise buildings represents an innovative and sustainable opportunity for the spatial plantation of vegetation to improve the aesthetics of the city and enhances people's well-being. The relevant trend in building design involves vertical forests and green roofs. The integration of woody plants, i.e., trees, with buildings is the focus of this study.

Despite the fact that the EU Commission has provided a broad definition, practical implementation guidance is lacking. Various stakeholders, including policymakers, scholars, and the general public, frequently interpret it differently. Terminology is used differently in different contexts. This has resulted in a wide range of and frequently contradictory research agendas, priorities, and outputs, as well as a vast range of literature, as reviewed in [1, 6–10]. Thus, before investigating, a clear classification and definitions are required for broad communication.

Implementing GI is necessary because it serves numerous functions for the human community. This green solution to implement green infrastructure has multiple ecological [11, 12], social [13, 14], and economic [15] benefits that help the performance of buildings and the surrounding urban environment. However, trade-offs during the implementation process must also be addressed. In general, some of these factors, such as social impacts and economic rewards, are difficult to quantify. As a result, many practitioners believe that further application is questionable. This indicates that it requires a clear identification and comparison between the benefits and drawbacks of all aspects during the decision-making process.

In this chapter, the objective is to provide background information for the implementation of living structures as a nature-based solution to improve urban environments. Due to the ambiguity of the concept of green infrastructure, the research begins with the classification and definitions of green infrastructure. The second section identifies and discusses the benefits and drawbacks of this integrated green infrastructure on buildings. One of the most important impacts of trees, the cooling effect, is further explained in detail to measure and quantify the influencing factors. In the end, this chapter attempts to provide the design considerations for the implementation of building an integrated GI system.

2.2 Building integrated green infrastructure

Greenery can be inserted into buildings in many forms, including horizontal and vertical, exterior and interior spaces [16, 17]. In this study, integrated green infrastructures with buildings are organized into two main categories, namely horizontal greenery and vertical greenery systems. For horizontal greenery, it includes green roofs and elevated forests. For vertical greenery systems, they include a green façade, a green wall, green terraces, and vertical forests, as shown in Figure 2.1 a.

2.2.1 Horizontal greenery

Green roofs are one of the first forms of green infrastructure [18]. Their structural details can be seen in Figure 2.1 b. Green roofs can be explained as roofs with a vegetated surface and substrate. It can be classified into extensive and intensive green roofs, depending on the depths of the substrate, the dimension of the roof, and the intensity of use. It can provide ecosystem services in urban areas, including improved storm water management, better regulation of building temperatures [19, 20], increased sound insulation [21], reduced effects of urban heat islands [22], and increased habitat for urban wildlife [23]. Its relatively lightweight nature allows it to be used on many roofs without the need for structural strengthening. It has seen a surge in installations around the world. Another form of horizontal greenery is the elevated forest. This class of greenery refers to trees that grow in sheltered horizontal spaces, forming a kind of forest in the sky. While horizontal spaces provide accommodation for plants, vertical spaces offer different possibilities. In addition to the development of horizontal surfaces, vertical spaces provide opportunities for the integration of vegetation with buildings.

2.2.2 Vertical greenery

Vertical greenery systems can be defined as structures that spread vegetation that may or may not be attached to a building façade or to an interior wall [25]. It is also called vertical garden, green wall, vertical green, and sky-rise greenery [26–28]. There are four main components in vertical greenery systems: plants, planting media such as substrates and containers, support systems that can hold plants and irrigation systems (for details, see Figure 2.1 c).

According to the strategies in development for vertical greenery systems, they can be categorized as green façade, green wall, green terraces, and vertical forest [29–31]. However, there are some differences between the definitions in various fields. For a more common understanding, within this vertical forest engineering study, the characteristics and definitions of various types of vertical greenery systems have been formulated according to application and location, as can be seen in Figure 2.1 a and Table 2.1.

- The green façade refers to vegetation rooted on the ground, which makes use of either the wall itself for climbing (traditional direct systems) or independent supporting systems, such as trellis, wires, cables or meshes (double-skin indirect system) affix to walls [32].

- A green wall has been made using geotextile, pots, panels, boxes or modular nets where precultivated vegetation has been planted and subsequently suspended and

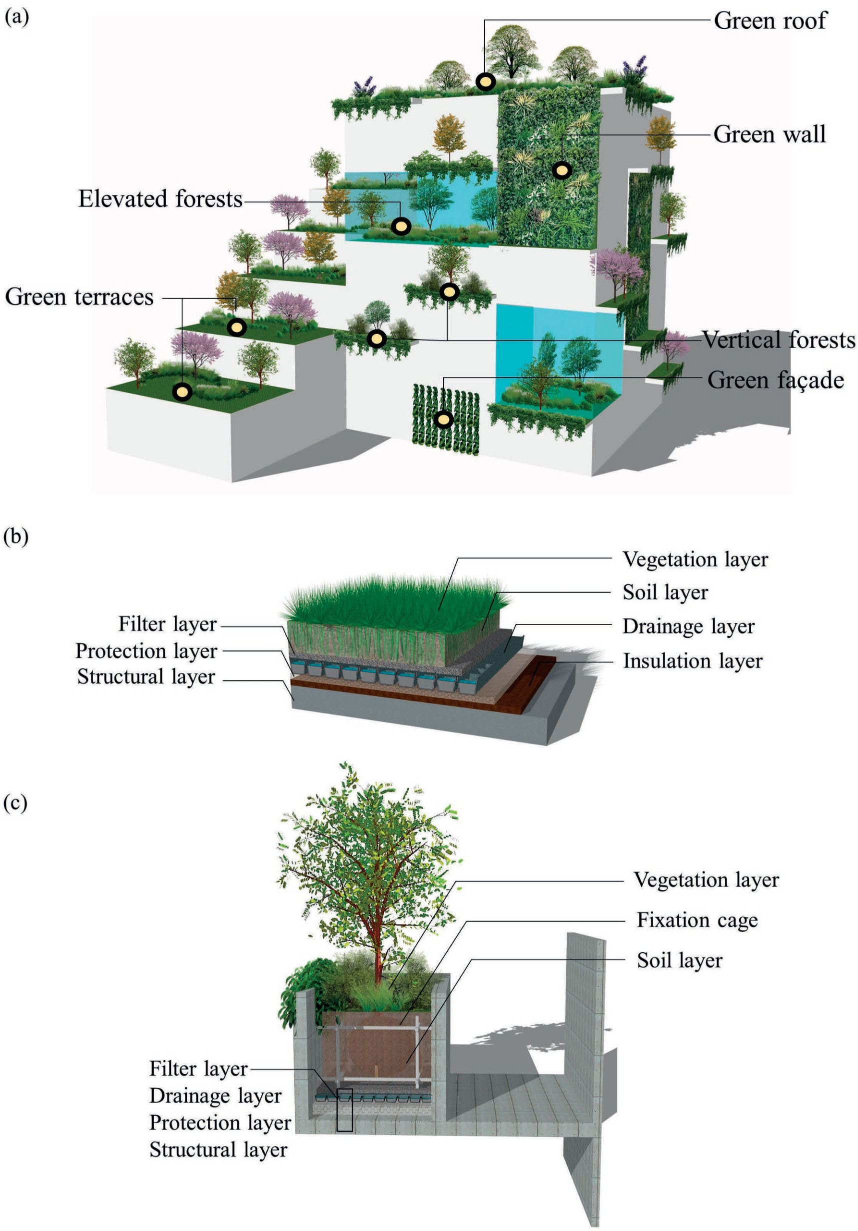

Figure 2.1: Overview of forms of vertical greenery, structural compositions of green roof and the vertical planted tree. (a) Overview of classifications of the building integrated greenery; (b) structure layers of the green roof; the author sketched according to the description in [18]. (c) The engineering technique of the balcony tree in vertical forests; the author sketched according to personal communication with designers [24].

Table 2.1: Typologies, plant types and features of building integrated greenery

Typologies	Plants	Characteristics
Green façade	Climbing plants	Plants rooted on the ground and climbing on the façades of the building by themselves or through the support of other structures
Green wall	Modular plants or plants with hanging-down branches	Supporting structures such as steel nets, modular rails and planter boxes that should be built on façades for hanging and placing plants
Green terraces	Short, medium and tall plants	Growing in the planting media which is located on horizontal terraces at different levels continuously along the façade
Elevated forest	Trees	Trees growing in the sheltered horizontal (open) spaces
Vertical forest	Trees	Groups of trees growing on cantilevering balconies

fixed to a building structure [17]. Green walls require more complex constructions and imply higher installation and maintenance costs compared to green façades [18].

- Green terraces are defined as plants that continuously grow on horizontal terraces along the façade, which are built at different heights and levels.
- The vertical forest uses cantilevered balconies around the building envelope, acting as an accommodation for trees to grow, where the group of trees is formed into vertical forests.

The vertical forest is a relatively new field for architects, botanists, and structural engineers. It requires deeper studies with respect to plant and tree species, nutrition, and growth conditions (e.g. root system development in a confined soil space, sunlight, prevailing winds, nearby façades), as well as engineering aspects with regard to horizontal loads (wind, earthquakes), tree stability. An important aspect is also how these parameters develop over the course of time.

2.3 Benefits and drawbacks

There is a substantial body of evidence from research and practice that green infrastructure benefits people and society. However, if the implementation is done incorrectly, it will have negative consequences. In this section, the advantages and disadvantages of building integrated greenery will be discussed from three perspectives: social, economic, and environmental aspects.

2.3.1 Social aspect

A 2011 WHO report [33] concludes that air and noise pollution have a negative impact on human health. Noise can be reduced by using trees as a natural barrier. The interaction of green infrastructure design and air pollutants can have an impact on personal exposure and thus human health. Trees can act as a filter for pollutants by depositing them on their leaves, thus reducing the amount of pollution in the air [34, 35]. However, when trees are planted densely in a street canyon, it can lead to air pollution trapping in a certain area, due to the fact that the canopy blocks ventilation circulation [36]. Consequently, it induces negative impacts on human health.

Vertical greenery contributes to the improvement of social well-being by providing great visual engagement and aesthetic values [37]. Lachowycz and Jones [38] emphasize physical activity, involvement and relaxation in nature, and social activities and interactions as important health pathways. Villeneuve et al. [39] propose a model that prioritizes physical activity, respiratory health, and resistance to heart disease. However, little research has been done on the impact of urban green space and its positive effects on the sense of community. A well-designed landscape distribution can provide a gathering place for recreation while also breaking the connectivity of landscape design and isolating the community.

2.3.2 Economic aspect

Increasing urban greenery can help transition to a green economy. A green economy, in general terms, is one that seeks to improve human well-being and social equity while significantly reducing environmental risks and ecological cities [40]. A green economy can be an important component of a complex socio-ecological system. Regarding social well-being, related benefits are difficult to quantify and compare the results. On larger scales, functional connections (e.g., connecting different communities) and more diverse types of green space create new opportunities. However, it poses new challenges simply by broadening the pool of potential beneficiaries and investors.

Green roofs and green walls add value to the properties of buildings, but can also reduce the value of the property due to lack of maintenance and damage [37, 41]. The cost of installing vertical greenery includes several components, both short- and long-term. The costs of growing, pruning, and replacing trees are direct budgetary expenses for stakeholders. Costs for facilitating materials (e.g., tree-transported equipment) and paid labor (e.g., arborists) are also included. Regular pruning and monitoring of plants, as well as adequate nutrition and drainage, are required during service life. Living walls often require plant irrigation and replacement of 5-10% of their plant species each year. Water pipes in automated irrigation systems may need to be replaced every 7.5 years due to salt crystallization [10].

Green roofs and green walls on a building scale promote energy savings if installed correctly [42, 43], reduce sound transmission in buildings [44], contribute to storm water treatment [45], and increase the longevity of the envelope. Green walls can shade and protect blank walls, lowering surface and air temperatures. Green roofs and green walls are not only attractive for new buildings, but they are also retrofitting solutions.

The advancement of vertical greenery in buildings can boost technological and research innovation. On the other hand, lack of technical knowledge and experience can lead to a failed implementation, making the benefits of vegetation ineffective.

2.3.3 Environmental aspect

The vertical greenery system provides various benefits through ecosystem services. They improve air quality by allowing trees to deposit, disperse and absorb particulate matter and/or absorb gaseous pollutants. Vegetation leaves have been shown to absorb gaseous pollutants through their stomata and remove atmospheric particles by drying them off on their surfaces. Furthermore, vegetation, especially trees, can play a role in improving air quality in urban areas by increasing the rates of dumping of particles and the absorption of gaseous pollutants [13, 46, 47]. According to a review that summarized the potential magnitude of reducing air pollution through the canopy of urban vegetation, the average published deposition values correspond to an estimated 1% reduction in pollutants in urban areas [48]. However, success depends on how greenery is implemented and designed, as well as how trees are selected and planted.

When extreme rainfall events occur, the total amount of sealed surfaces increases in many urban areas, which poses a challenge for sewerage systems and wastewater treatment plants. The use of urban greenery for water management, such as green roofs and constructed wetlands, is one promising solution that improves storm water management and urban biodiversity. The tools for modeling storm water management and the economics of GI practices are proposed by [49]. Zuniga-Teran et al. [21] investigate the mechanisms and effectiveness of green infrastructure, which is widely used for storm water management.

The presence of urban greenery improves the microclimate of the city by altering ambient conditions such as the temperature and humidity of the air layer, as well as the airflow near the building skin [6, 43, 50–54]. Bowler et al. [6] provide a detailed review of such empirical studies, summarizing the impact of parks, trees, ground vegetation, and green roofs on urban climate. These studies show that vegetation, through evapotranspiration and shading, prevents warming of land surfaces and air. According to their research, an urban park can be up to 1 °C cooler on average than a non-green site; however, the lack of a suitable description and classification of green infrastructure limits the reliability and comparability of studies. Santamouris et al. [19, 55] review simulation studies on the thermal effects of green roofs. Evidence suggests that green roofs, when used at the city level, can reduce average ambient temperatures by 0.3 to 3K. Pastore et al. [56], Koch et al. [9], and Rahman et al. [57] also review several simulations and experimental studies on vertical greenery used to improve thermal comfort and energy savings in buildings. In general, the use of green walls and facades reduced the surface temperatures of the facades of buildings by 1 to 15 °C in studies conducted in temperate climates [58]. According to Zhu et al. [42], on the building scale, vertical greenery can reduce the maximum energy demand of adjacent buildings by up to 10% by lowering surface and air temperatures. Additionally, strategically planted trees adjacent to a building can reduce energy consumption, particularly cooling energy during summer. However, it is also seen that the cooling provided by vegetation depends on the local climate, the species of vegetation, and the amount of vegetation.

The effects of trees on transportation and sewerage may also be significant for stakeholders. Trees can block vehicular and pedestrian traffic on roads and sidewalks, and tree roots can block sewer pipes. Invasive species also disrupt the local ecosystem and have unintended consequences. Planted urban trees are initially net carbon emitters, becoming carbon neutral only after approximately three decades of emissions offset by sequestration [10].

The advantages and disadvantages clearly indicate that the specific characteristics of green infrastructure may be sensitive to local environmental and social circumstances.

Informed design is critical to ensure benefits over negative impacts and maximize the potential of those benefits. Table 2.2 summarizes the benefits and drawbacks discussed.

Table 2.2: Functions of plants, benefits, and drawbacks of the implementation of green infrastructures from environmental, economical, social and technological aspects

Aspects		Explanations
Plant functions		Photosynthesis; transpiration; evaporation; natural barrier; wood growth; soil substrate; shade; pollen; habitats for creatures; aesthetic value; recreation; soothing; connectivity; nutrition to growth; mechanical stability; sufficient drainage; maintenance; dynamic growth; deposit pollutants; disperse pollutants; absorb pollutants.
Environmental	Benefits	Store carbon; reduce air pollutants; reduce noise pollution; stormwater management; regulate temperature; regulate humidity; reduce runoff; wetland restoration; enhance biodiversity.
	Drawbacks	Trap pollutants in street canyons; block sun in winter; increase energy consumption; thermal insulation in summer; block ventilation; water demand for drainage; break original landscape connectivity.
Economic	Benefits	Produce food/product; increase land/housing value; promote tourism; add cultural value; reduce energy consumption; enhance social wellbeing; develop green economy.
	Drawbacks	Added cost in installation and maintenance; added negative costs and effects on house structures due to the shorter service life; increase in property prices; decrease values due to unmanaged degradation; perceive uncertainty regarding costs and benefits; damage property; block original infrastructures; the same benefits from conventional approach; obstruct vehicles.
Social	Benefits	Enhance working environment; provide recreation places; add aesthetic values; boost social communication; provide natural therapy; increase sustainable awareness; improve health level; increase public participation.
	Drawbacks	Induce allergies; cause accidents; bring bad insects; introduce bad bacteria; break community cohesion.
Technological	Benefits	Boost knowledge transfer; enhance collaboration; boost technology innovation.
	Drawbacks	Concerns on safety (falling trees or fires); undesired interaction with wildlife; competing with other plants; require risk management.

2.4 Planting strategies

Trees are not always beneficial. Improper tree planning and planting can have a negative impact on health, safety, and cost. The planting strategy needs to adapt to local environments, which means planting the appropriate tree species in the appropriate location.

2.4.1 Tree traits

Trees in urban areas influence the microclimate by interfering with the movement of momentum, radiation, temperature, moisture, and pollutants [44, 50, 59, 60]. Trees have the potential to reduce both the urban heat island effect and thus improve human thermal comfort. The cooling mechanism of a tree on different scales is presented in Figure 2.2.

Short- and long-wave radiation are absorbed by the leaves and soil layers of a tree as solar energy passes through it. Convective heat transfers occur in the substrate and the foliage layer. Meanwhile, both the soil and the foliage layers experience evaporation and transpiration. The rest of the heat flux is exchanged partly by the soil and partly between the leaves of the plant layer and the envelop layers.

As a result, the cooling benefits of trees on the building scale come from the shading and evapotranspiration mechanisms. Trees reduce air temperature near the building envelopes by converting energy into latent heat flux through transpiration of water released through the leaf stomata. They also reduce the wind velocity near the envelopes of buildings. During this time, the growth substrate acts as thermal insulation for the building envelope. The shading benefits of a tree reduce the input of short-wave radiation into the shaded area by 60-90%. As a result, surface temperature differences of up to 4 °C between shaded surfaces under tree canopies and sunny asphalt have been reported [61]. Transpiration has a direct effect on lowering the air temperature within or beneath the tree canopy that varies from 1 to 8 °C [57].

The effects of tree shading and transpiration are influenced by climate conditions, tree dimensions, and physiological characteristics [44, 60, 62], which is summarized in Table 2.3. Local wind speed, temperature, and humidity influence the performance of stomata in leaves. Specifically, low relative humidity or a high vapor pressure deficit caused by high temperature indicate a high demand for transpiration. However, actual transpiration is constrained by the availability of soil water. Inadequate water supply causes the stomata to close, reducing water uptake and consequently the cooling effect of transpiration. Solar radiation, because the stomata tend to open when radiation is high, and wind speed, which reduces the boundary layer thickness and thus the resistance to water transport from the canopy, are also positively related to evaporation.

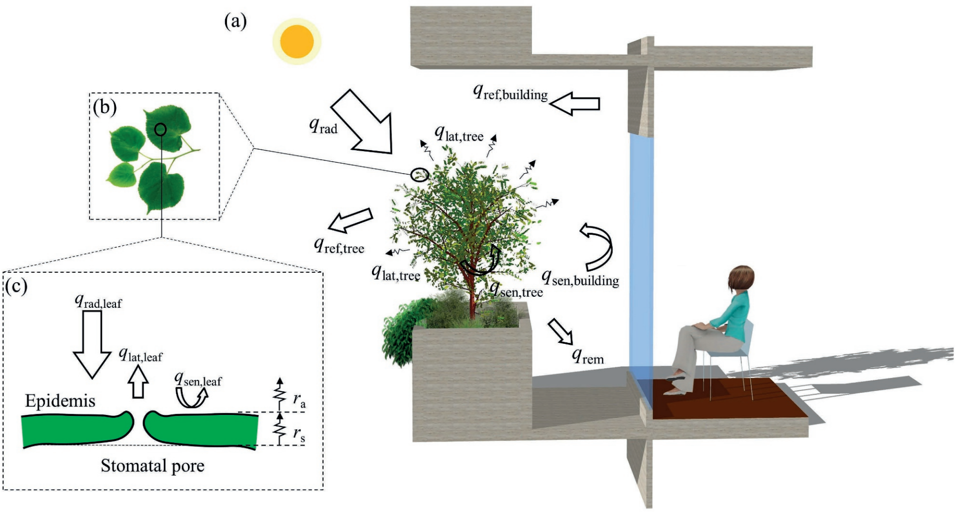

Figure 2.2: Schematic representation of the cooling mechanism of a tree on a balcony. (a) Illustration of radiating exchanges of a tree; on the leaf scale (b), the schematic representation of energy balance in a leaf in given in (c). Note: symbol q denotes for heat flux; footnote symbols rad means radiation; ref means reflection; lat stands for the latent heat; sen is the sensible heat; rem is the remaining heat. The stomatal resistance r_s influences the latent heat flux and the aerodynamic resistance r_a influences both the sensible and the latent heat fluxes.

Regarding tree morphological characteristics, species vary in leaf characteristics (such as leaf thickness, leaf hairiness, leaf color, leaf shape, and specific leaf area), xylem anatomy, and water utilization efficiency. As a result, it can affect the regulation of the air temperature of the boundary layer by regulating their stomata. Previous research has shown that the cooling effect of various tree species, such as *Acer platanoides*, *Crataegus laevigata*, *Pyrus calleryana*, *Robinia pseudoacacia*, *Sorbus arnoldiana*, and *Tilia cordata*, can vary by up to 4 °C [62].

The effectiveness of shading is influenced by canopy characteristics such as leaf area index (LAI), width-to-height ratio, and leaf spatial distribution [60, 63]. Conifers block passive solar heating in winter, so it is preferable to plant deciduous trees around a building. The anatomy of diffuse, porous wood and trees originating from temperate, resource-rich forests exhibited greater cooling capacities. Leuzinger, Vogt, and Korner [64] demonstrate that small leaves have a lower boundary layer temperature by up to 5 °C due to faster loss of convective heat, even if they transpire at the same rate as larger leaves. Among all these factors, the climate is the most important aspect in determining the potential for cooling [57]. Furthermore, the most influential parameter identified is the leaf area index, since it describes the characteristics of the foliage and its density, which is directly related to the transimissivity of solar radiation through the tree crown [60, 63].

Table 2.3: Relationship between growing environments, tree traits, and their influence on thermal performance

Aspects	**Influencing factors**
Climate	Location, wind speed, humidity, temperature
Substrate and drainage	Nutrition level, moisture content, volume, thickness
Surrounding environment	Surrounding objects, green coverage ratio
Tree basics	Origin habitat, species, age, health condition
Tree dimension	Tree height, DBH, stem height
Wood anatomy	Transpiration rate, evaporation efficiency
Canopy	Crown shape, volume, width, leaf area index, drag coefficient
Leaf traits	Growth pattern, longevity, width, shape, thickness, stomatal conductance, optical traits

2.4.2 Planning strategy

The design of integrated green buildings requires the collection of quantitative and qualitative data from various sectors, including the ecological, social, economic, and technological sectors. It is essential that the design aim at long-term benefits by making efficient use of the natural ecosystem rather than human energy subsidies to drive and deliver benefits. The success of greenery construction requires a decision-making system that takes into account relevant aspects. Figure 2.3 provides the considerations from planning to installation and future maintenance.

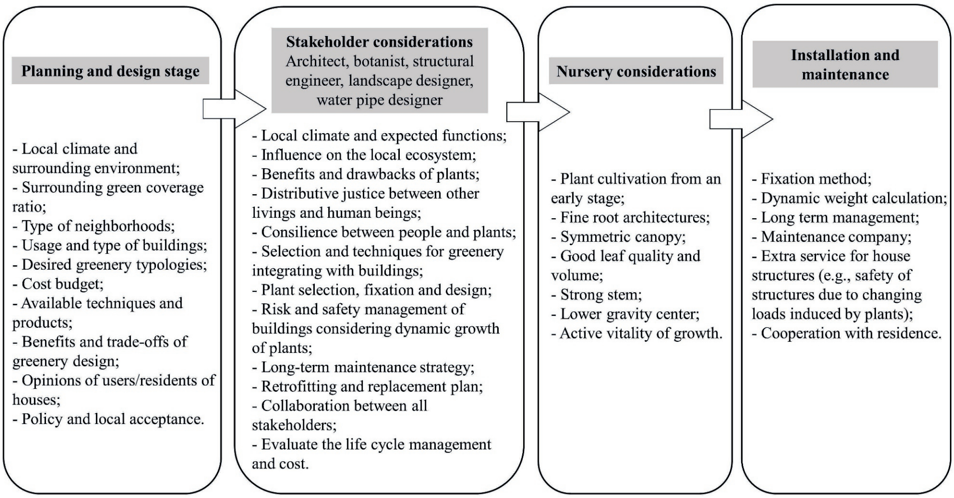

Figure 2.3: Design considerations for building integrated greenery.

2.5 Concluding remarks

This chapter provides current progress on the topic of building integrated greenery. To have a successful implementation of building greenery, a strategic planning, design, and evaluation system is needed.

Since the concept of green infrastructure, nature-based solutions, and vertical forest is relatively new and vague, a clear description of classifications and typologies helps to address the importance of assessing and quantifying them to communicate among different stakeholders. This chapter groups urban greenery methods into several categories according to plant selection and typology: green roof, green wall, elevated forests, green terraces, vertical forests, and green facade, where the form of vertical forests provides the spatial possibility for the future of living tree structures.

The design of a green building requires the collection of detailed information, both quantitative and qualitative. The evaluation of the greenery of the building is discussed both from the benefits and the drawbacks that the system can provide. However, planting trees without considering strategic planning can have negative impacts on the ecosystem. Therefore, this chapter further discusses the cooling mechanism of a tree and its relevant traits, which help regulate the microclimate around buildings. Based on the information studied, this chapter further provides decision-making considerations for the implementation of green buildings from planning to installation.

References

[1] X. Wang, W. Gard, H. Borska, B. Ursem, and J. W. G. Van De Kuilen. Vertical greenery systems: from plants to trees with self-growing interconnections. *European Journal of Wood and Wood Products*, 78:1031–1043, 2020.

[2] United Nations General Assembly. Transforming our world: The 2030 agenda for sustainable development. Goal 11: Make cities inclusive, safe, resilient and sustainable, 2015.

[3] European Union. Green infrastructure (GI) - enhancing europe's natural capital, 2020. URL https://eur-lex.europa.eu/legal-content/EN/TXT/?uri=celex%3A52013DC0249. Last visited 2023-05-20.

[4] European Union. European Union biodiversity strategy for 2030. Bringing nature back into our lives, 2020. URL https://environment.ec.europa.eu/strategy/biodiversity-strategy-2030{_}en. Last visited 2023-05-20.

[5] European Union. Forgoing a climate-resilient europe - the new EU strategy on adaption to climate change, 2020. URL https://eur-lex.europa.eu/legal-content/EN/TXT/?uri=COM:2021:82:FIN. Last visited 2023-05-20.

[6] D. E. Bowler, L. Buyung-Ali, T. M. Knight, and A. S. Pullin. Urban greening to cool towns and cities: A systematic review of the empirical evidence. *Landscape and Urban Planning*, 97(3):147–155, 2010.

[7] N. H. Wong, C. L. Tan, D. D. Kolokotsa, and H. Takebayashi. Greenery as a mitigation and adaptation strategy to urban heat. *Nature Reviews Earth and Environment*, 2(3): 166–181, 2021.

[8] A. Cheshmehzangi, C. Butters, L. Xie, and A. Dawodu. Green infrastructures for urban sustainability: Issues, implications, and solutions for underdeveloped areas. *Urban Forestry and Urban Greening*, 59:127028, 2021.

[9] K. Koch, T. Ysebaert, S. Denys, and R. Samson. Urban heat stress mitigation potential of green walls: A review. *Urban Forestry and Urban Greening*, 55, 2020.

[10] Y. Depietri. Planning for urban green infrastructure: Addressing tradeoffs and synergies. *Current Opinion in Environmental Sustainability*, 54:101148, 2022.

[11] J. Wang and E. Banzhaf. Towards a better understanding of green infrastructure: A critical review. *Ecological Indicators*, 85:758–772, 2018.

[12] F. J. Escobedo, V. Giannico, C. Y. Jim, G. Sanesi, and R. Lafortezza. Urban forests, ecosystem services, green infrastructure and nature-based solutions: Nexus or evolving metaphors? *Urban Forestry and Urban Greening*, 37:3–12, 2019.

[13] A. Jeanjean, R. Buccolieri, J. Eddy, P. Monks, and R. Leigh. Air quality affected by trees in real street canyons: The case of marylebone neighbourhood in central london. *Urban Forestry and Urban Greening*, 22:41–53, 2017.

[14] H. Saaroni, J. H. Amorim, J. A. Hiemstra, and D. Pearlmutter. Urban green infrastructure as a tool for urban heat mitigation: Survey of research methodologies and findings across different climatic regions. *Urban Climate*, 24:94–110, 2018.

[15] L. A. Roman, T. M. Conway, T. S. Eisenman, A. K. Koeser, C. Ordóñez Barona, D. H. Locke, G. D. Jenerette, J. Östberg, and J. Vogt. Beyond 'trees are good': Disservices, management costs, and tradeoffs in urban forestry. *Ambio*, 50(3):615–630, 2021.

[16] K. Tzoulas, K. Korpela, S. Venn, V. Yli-Pelkonen, A. Kaźmierczak, J. Niemela, and P. James. Promoting ecosystem and human health in urban areas using green infrastructure: A literature review. *Landscape and urban planning*, 81(3):167–178, 2007.

[17] C. Bartesaghi Koc, P. Osmond, and A. Peters. Towards a comprehensive green infrastructure typology: A systematic review of approaches, methods and typologies. *Urban ecosystems*, 20:15–35, 2017.

[18] N. Dunnett and N. Kingsbury. *Planting green roofs and living walls.* Timber press Portland, 2008. Pages 91–101.

[19] M. Santamouris, G. Ban-Weiss, P. Osmond, R. Paolini, A. Synnefa, C. Cartalis, A. Muscio, M. Zinzi, T. E. Morakinyo, N. G. Edward, et al. Progress in urban greenery mitigation science–assessment methodologies advanced technologies and impact on cities. *Journal of Civil Engineering and Management*, 24(8):638–671, 2018.

[20] S. Vera, C. Pinto, P.C. Tabares-Velasco, and W. Bustamante. A critical review of heat and mass transfer in vegetative roof models used in building energy and urban environment simulation tools. *Applied energy*, 232:752–764, 2018.

[21] A. A. Zuniga-Teran, C. Staddon, L. de Vito, A. K. Gerlak, S. Ward, Y. Schoeman, A. Hart, and G. Booth. Challenges of mainstreaming green infrastructure in built environment professions. *Journal of Environmental Planning and Management*, 63:710–732, 2019.

[22] A. B. Besir and E. Cuce. Green roofs and façades: A comprehensive review. *Renewable and Sustainable Energy Reviews*, 82:915–939, 2018.

[23] S. Knapp, S. Schmauck, and A. Zehnsdorf. Biodiversity impact of green roofs and constructed wetlands as progressive eco-technologies in urban areas. *Sustainability (Switzerland)*, 11:5846, 2019.

[24] L. Gattie. Personal communication. 2019.

[25] L. Pérez-Urrestarazu, R. Fernández-Cañero, A. Franco-Salas, and G. Egea. Vertical greening systems and sustainable cities. *Journal of Urban Technology*, 22(4):65–85, 2015.

[26] P. Y. Tan, J. Wang, and A. Sia. Perspectives on five decades of the urban greening of Singapore. *Cities*, 32:24–32, 2013.

[27] C. Tan, N. Wong, and S. Jusuf. Effects of vertical greenery on mean radiant temperature in the tropical urban environment. *Landscape and Urban Planning*, 127:52–64, 2014.

2

[28] B. Timur and E. Karaca. Vertical gardens. In *Advances in Landscape Architecture*. IntechOpen, 2013. Pages 587–645.

[29] K. Perini, M. Ottelé, A. Fraaij, E. Haas, and R. Raiteri. Vertical greening systems and the effect on air flow and temperature on the building envelope. *Building and Environment*, 46:2287–2294, 2011.

[30] V. Serra, L. Bianco, E. Candelari, R. Giordano, E. Montacchini, S. Tedesco, F. Larcher, and A. Schiavi. A novel vertical greenery module system for building envelopes: The results and outcomes of a multidisciplinary research project. *Energy and Buildings*, 146:333–352, 2017.

[31] C. Marugg. Vertical forests: The impact of green balconies on the microclimate by solar shading, evapotranspiration and wind flow change. 2018. TU Delft thesis.

[32] R. Fernández-Cañero, L.P. Urrestarazu, and K. Perini. Vertical greening systems: Classifications, plant species, substrates. In *Nature based strategies for urban and building sustainability*, pages 45–54. 2018.

[33] World Health Organization. World health statistics, 2011. URL https://apps.who.int/iris/handle/10665/44552. Last visited 2023-05-20.

[34] Å.O. Sang, P. Thorpert, and A. M. Fransson. Planning, designing, and managing green roofs and green walls for public health – an ecosystem services approach. *Frontiers in Ecology and Evolution*, 10:804500, 2022.

[35] J. Felappi, J. Sommer, T. Falkenberg, and T. Terlau, W.and Kötter. Green infrastructure through the lens of 'one health': A systematic review and integrative framework uncovering synergies and trade-offs between mental health and wildlife support in cities. *Science of The Total Environment*, 748:141589, 2020.

[36] P. Kumar, A. Druckman, J. Gallagher, B. Gatersleben, S. Allison, T. S. Eisenman, U. Hoang, S. Hama, A. Tiwari, A. Sharma, K. V. Abhijith, D. Adlakha, A. McNabola, T. Astell-Burt, X. Feng, A. C. Skeldon, S. de Lusignan, and L. Morawska. The nexus between air pollution, green infrastructure and human health. *Environment International*, 133:105181, 2019.

[37] O. Ogut, N. J. Tzortzi, and C. Bertolin. Vertical green structures to establish sustainable built environment: A systematic market review. *Sustainability (Switzerland)*, 14(19): 12349, 2022.

[38] K. Lachowycz and A. P. Jones. Does walking explain associations between access to greenspace and lower mortality? *Social Science and Medicine*, 107:9–17, 2014.

[39] P. J. Villeneuve, M. Jerrett, J. G. Su, R. T. Burnett, H. Chen, A. J. Wheeler, and M. S. Goldberg. A cohort study relating urban green space with mortality in ontario, canada. *Environmental research*, 115:51–58, 2012.

[40] S. Pauleit, B. Ambrose-Oji, E. Andersson, B. Anton, A. Buijs, D. Haase, B. Elands, R. Hansen, I. Kowarik, J. Kronenberg, T. Mattijssen, A. Stahl Olafsson, E. Rall, A. P. N. van der Jagt, and C. Konijnendijk van den Bosch. Advancing urban green infrastructure in Europe: Outcomes and reflections from the GREEN SURGE project. *Urban Forestry and Urban Greening*, 40:4–16, 2019.

[41] H. Toxopeus and F. Polzin. Reviewing financing barriers and strategies for urban nature-based solutions. *Journal of Environmental Management*, 289:112371, 2021.

[42] S. Zhu, Y. Yang, Y. Yan, F. Causone, X. Jin, X. Zhou, and X. Shi. An evidence-based framework for designing urban green infrastructure morphology to reduce urban building energy use in a hot-humid climate. *Building and Environment*, 219:109181, 2022.

[43] N. H. Wong, Y. He, N. S. Nguyen, S. V. Raghavan, M. Martin, D. J. C. Hii, Z. Yu, and J. Deng. An integrated multiscale urban microclimate model for the urban thermal environment. *Urban Climate*, 35:100730, 2021.

[44] T. Grylls and M. van Reeuwijk. Tree model with drag, transpiration, shading and deposition: Identification of cooling regimes and large-eddy simulation. *Agricultural and Forest Meteorology*, 298:108288, 2021.

[45] V. Venkataramanan, A. I. Packman, D. R. Peters, D. Lopez, D. J. McCuskey, R. I. McDonald, W. M. Miller, and S. L. Young. A systematic review of the human health and social well-being outcomes of green infrastructure for stormwater and flood management. *Journal of Environmental Management*, 246:868–880, 2019.

[46] M. Moradpour and V. Hosseini. An investigation into the effects of green space on air quality of an urban area using CFD modeling. *Urban Climate*, 34:100686, 2020.

[47] C. N. Hewitt, K. Ashworth, and A. R. MacKenzie. Using green infrastructure to improve urban air quality (GI4AQ). *Ambio*, 49(1):62–73, 2020.

[48] T. Litschke and W. Kuttler. On the reduction of urban particle concentration by vegetation-a review. *Meteorologische Zeitschrift*, 17(3):229–240, 2008.

[49] V. M. Jayasooriya and A. W. M. Ng. Tools for modeling of stormwater management and economics of green infrastructure practices: A review. *Water, Air, and Soil Pollution*, 225:1–20, 2014.

[50] M. Robitu, M. Musy, C. Inard, and D. Groleau. Modeling the influence of vegetation and water pond on urban microclimate. *Solar Energy*, 80(4):435–447, 2006.

[51] M. O. Mughal, A. Kubilay, S. Fatichi, N. Meili, J. Carmeliet, P. Edwards, and P. Burlando. Detailed investigation of vegetation effects on microclimate by means of computational fluid dynamics (CFD) in a tropical urban environment. *Urban Climate*, 39: 100939, 2021.

2

[52] S. Zhu, F. Causone, N. Gao, Y. Ye, X. Jin, X. Zhou, and X. Shi. Numerical simulation to assess the impact of urban green infrastructure on building energy use: A review. *Building and Environment*, 228:109832, 2023.

[53] I. Susorova, P. Azimi, and B. Stephens. The effects of climbing vegetation on the local microclimate, thermal performance, and air infiltration of four building facade orientations. *Building and Environment*, 76:113–124, 2014.

[54] Y. Yang, E. Gatto, Z. Gao, R. Buccolieri, T.E. Morakinyo, and H. Lan. The "plant evaluation model" for the assessment of the impact of vegetation on outdoor microclimate in the urban environment. *Building and Environment*, 159:106151, 2019.

[55] M. Santamouris. Cooling the cities–a review of reflective and green roof mitigation technologies to fight heat island and improve comfort in urban environments. *Solar energy*, 103:682–703, 2014.

[56] L. Pastore, R. Corrao, and P. Heiselberg. The effects of vegetation on indoor thermal comfort: The application of a multi-scale simulation methodology on a residential neighborhood renovation case study. *Energy and Buildings*, 146:1–11, 2017.

[57] M. A. Rahman, C. Hartmann, A. Moser-Reischl, M. F. von Strachwitz, H. Paeth, H. Pretzsch, S. Pauleit, and T. Rötzer. Tree cooling effects and human thermal comfort under contrasting species and sites. *Agricultural and Forest Meteorology*, 287:107947, 2020.

[58] G. Pérez, L. Rincón, A. Vila, J. M. González, and L. F. Cabeza. Behaviour of green facades in mediterranean continental climate. *Energy Conversion and Management*, 52(4):1861–1867, 2011.

[59] R. Pace, M. A. Rahman, S. Pauleit, D. J. Nowak, and R. Grote. A single tree model to consistently simulate cooling, shading, and pollution uptake of urban trees. *International Journal of Biometeorology*, 65:277–289, 2021.

[60] M. A. Rahman, L. M. F. Stratopoulos, A. Moser-Reischl, T. Zölch, K. Häberle, T. Rötzer, H. Pretzsch, and S. Pauleit. Traits of trees for cooling urban heat islands: A meta-analysis. *Building and Environment*, 170:106606, 2020.

[61] M. A. Rahman, A. Moser, T. Rötzer, and S. Pauleit. Within canopy temperature differences and cooling ability of *Tilia cordata* trees grown in urban conditions. *Building and Environment*, 114:118–128, 2017.

[62] A. Moser-Reischl, M. A. Rahman, S. Pauleit, H. Pretzsch, and T. Rötzer. Growth patterns and effects of urban micro-climate on two physiologically contrasting urban tree species. *Landscape and Urban Planning*, 183:88–99, 2019.

[63] S. Zhu, Y. Li, S. Wei, C. Wang, X. Zhang, X. Jin, X. Zhou, and X. Shi. The impact of urban vegetation morphology on urban building energy consumption during summer and winter seasons in Nanjing, China. *Landscape and Urban Planning*, 228:104576, 2022.

[64] S. Leuzinger, R. Vogt, and C. Körner. Tree surface temperature in an urban environment. *Agricultural and Forest Meteorology*, 150(1):56–62, 2010.

3

Macroscopic characterization of self-growing connections and structures

The ability of trees to adapt and grow in response to external loads benefits their survival in the natural environment. In response to external stimuli, the process of adaptive growth involves physiological and chemical changes that occur on various scales, from the cellular level to the entire plant organ. For research on the use of self-growing connections as structural elements, most studies are still in the qualitative stage. This chapter focused on the quantitative characterization of self-growing connections on the macroscopic scale. The aspects studied included density variations, geometric changes, and fiber structures within a self-growing connection. The self-growth connections examined were fused by Ficus benjamina L. (weeping fig). Examinations and analyses were primarily based on data from X-Ray scanning and optical microscopy.

Analyses on density variations found that the intersected region presents a higher density compared to the stem region. The fiber structures of a connection were mainly characterized by three fiber bundles, namely merged fiber bundles connecting two stems, deviated fiber bundles, and normal fiber bundles in each individual stem. The group of merged fiber bundles primarily determined the structural integrity and mechanical properties (e.g., strength) of a self-growing connection. Regarding geometric changes, the fused region showed a larger area than the stem region. The location of the maximum area related to the best merged fiber structure. The relationship between the identified characteristics and the mechanical properties of a self-growing connection was further discussed.

3

3.1 Introduction

3.1.1 Adaptive growth of trees

In nature, as plants grow and develop, they constantly encounter complex internal and external mechanical loads. External loads are imposed by the wind, physical barriers (such as Figures 3.1 a and b), and neighboring plants, such as in Figure 3.1 c. In response to loads or constraints, this phenomenon of tree accommodating activity has been recorded and described as adaptive growth since ancient times. In studies by Mattheck [1, 2], numerous qualitative examples are given to illustrate how trees interact adaptively with external loads. However, less studies have been done on the structural potential of such natural connections. From the perspective of engineers and designers, structures built directly from living trees can be realized (examples such as a living tree pavilion [3] and a living tree bridge [4]). As introduced in Chapter 1, the implementation of living structures is proposed as a nature-based solution to improve urban sustainability in the future.

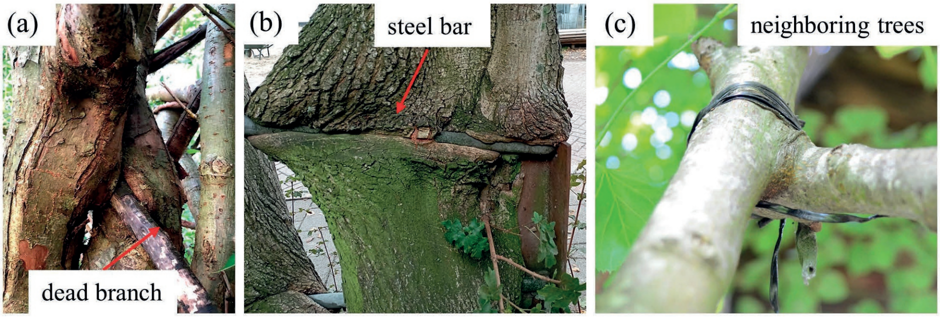

Figure 3.1: Adaptive growth of trees to environmental constraints. (a) Dead branch growing within willow (*Salix alba*) tree stems; (b) maple (*Acer pseudoplatanus*) stems growing within steel bars; (c) fusion of two lime (*Tilia cordata*) stems into a living connection (photo taken in June 2019), referred to as a self-growing connection in this study.

3.1.2 Mechanism behind adaptive growth

In biology, this adaptive growth and development was first termed 'thigmomorphogenesis' by Jaffe in 1973 [5], which described how plants respond to mechanical stimuli. It is now well established that most plants can perceive mechanical signals. Plants respond to external stimuli by modifying their growth, morphology, and material compositions [5–14]. In trees, unlike the Venus flytrap (*Dionaea muscipula* J.Ellis), mechanical responses to morphological changes are not apparent immediately after stimuli. It requires long-term measurements and investigations.

The mechanism of thigmomorpphogenesis has been studied by many researchers [6–12]. Plants respond to mechanical loads on many scales, from plant organs to gene expressions. Meanwhile, it is an integrative development process that involves different structures and functions in a plant. This process can be generalized as the mechanical structure that carries and distributes loads, the mechanosensitive structure that detects stimuli, and the reactions that create the responsive morphogenetic structure [8, 9]. At the tissue level, the mechanical structure mainly involves stiff tissues, that is, the xylem. The mechanosensitive structure is mostly parenchyma (and phloem), and the morphogenetic structures are the primary and second meristems. Therefore, changes in a plant in response to mechanical perturbations result from cooperation between these structures. At the cellular or molecular level, the mechanosensing mechanism involves changes in the cytoskeleton that connects to the plasma membrane and the cell wall [11, 15, 16]. The plasma membrane contains mechanosensitive ion channels, which facilitate signaling through the movement of Ca^{2+} between the apoplast and the symplast [17, 18]. Following mechanoperception, a cascade of physiological responses occurs, involving the regulation of gene expressions and plant growth regulators [19–21]. These physiological and chemical changes, such as plant hormones [22] further influence cell expansion and division in meristematic regions. In the end, this process alters the developing anatomy and morphology; and it eventually changes the biomass allocations within the entire plant. The common thigmomorphogenetic characteristics of the stem and root are outlined in Figure 3.2.

Experimental research on thigmomorphogenesis is generally conducted in the laboratory by subjecting plant stems to static and vibrating loads [24]. Advances in non-destructive imaging and micromechanical techniques are ways of providing more information at the molecular and genetic level to precisely assess plant behavior [25, 26]. Moreover, mathematical modeling methods are also implemented to explain the mechanisms [8, 9, 27]. However, for trees, performing quantitative studies and thus comparing results pose some challenges. First, the experiment protocols may differ due to the variation in tree species. Second, since most trees grow at relatively slow speeds, long-term observations and measurements are needed, which cost effort and time investment. Third, even though a controlled laboratory condition and utilizing standard tree species can be realized, the results obtained would be difficult to apply directly in reality and universal cases. Therefore, research on trees' thigmomorphogenetic responses remains mostly statistical and lacks generalized studies. Regarding self-growing connections, although this type of natural connection has been recorded for a long time, relevant studies focus mainly on qualitative description and empirical observations [2, 4]. To the best of the author's knowledge, no quantitative and systematic research has been conducted to characterize the features of self-growing connections and further to understand their mechanical values.

3.1.3 Effects of adaptive growth

When it comes to the specific consequences in trees caused by thigmomorphogenesis, four aspects are mostly studied: morphological changes, anatomical compositions, fiber structures, and material properties [13, 28–30]. This is mainly because these features are associated with the mechanical functions of trees and the hydraulic conductivity of their growth. Within these four aspects, anatomical compositions focus on the cellular and tissue level, which will be studied in Chapter 4. The other three aspects are investigated in this chapter.

Regarding geometric changes, in general, the response of trees to wind-induced bending results in a reduction in height growth, an increase in radial growth with a tapered shape, and an increase in below-ground biomass for better anchorage [30, 31]. Size modification and area enlargement are the result of deposition and acclimatization of the wood material. The spatial distribution of materials in the region subjected to loads is regulated by tree

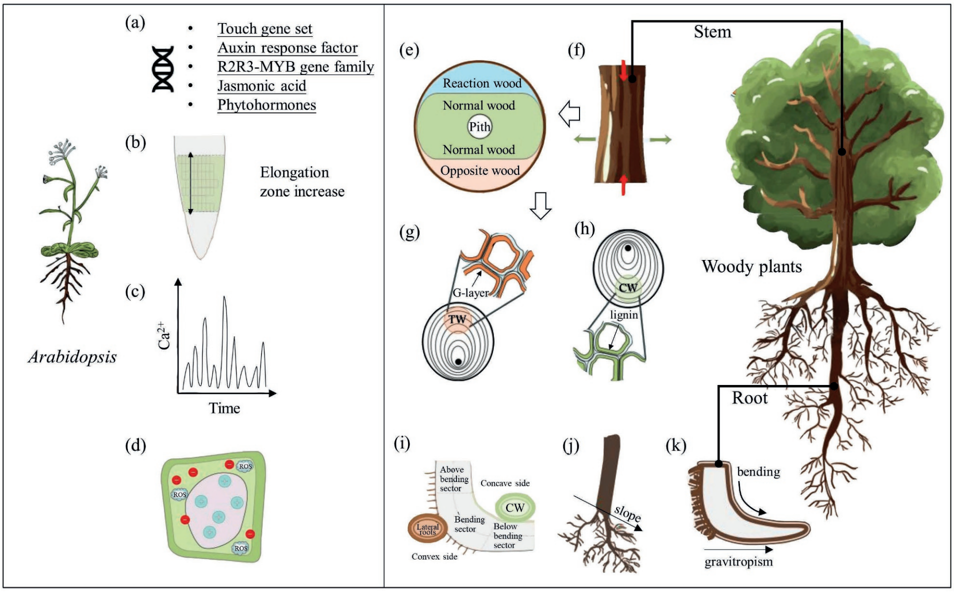

Figure 3.2: Summary of the mechanical stress response in *Arabidopsis* (left) and woody plants (right). (a) Mechanical stress-related molecular responses in *Arabidopsis* stem; (b) increase in the elongation zone with radially symmetric changes in cell expansion and elongation in the root of *Arabidopsis*; (c) stimulus-specific rapid and transient increase in cytosolic calcium in *Arabidopsis* root; (d) apoplastic alkalinization, cytoplasmic acidification, and the production of apoplastic reactive oxygen species (ROS); (e) zones of differentiated growth in woody plant stems subjected to mechanical stress (reaction wood, RW; normal wood, NW; opposite wood, OW); (f) reduction in elongation growth and increase in the radial thickness in the stem of woody plants; (g) location and characteristics of the tension wood (TW) formation, i.e., the RW in the stem of the Angiosperm species; (h) location and characteristics of the compression wood (CW) formation, i.e., the RW in the stem of the Gymnosperm specie; (i) asymmetric response of three root bending sectors on the concave and convex side of bent woody roots; (j) ‘bilateral-fan shape’ lateral roots root distribution in slope conditions; (k) lateral root initiation as a response to either gravitropic curvature or manual woody root bending. Figure modified from [23].

growth, which in turn affects load redistribution within the plant [32]. Changes in geometry mainly influence the stiffness of the structural member. For example, increasing the diameter at the base of the tree benefits the flexural stiffness of the tree stem in response to wind loads. Therefore, the geometric changes caused by the fusion activity on self-growing connections will be investigated.

For the aspect of material properties, the density of wood is the characteristic that is commonly investigated. It is widely used as a key functional trait that indicates the life history of trees and biomechanical and physiological properties [33]. In the field of timber engineering, wood density is usually used when cell walls are partially dried. In this case, the properties of the wood can be better performed. In contrast, in living trees and tree structures, the cell walls are fully saturated. Water within the cell walls and lumen favors plant growth, but reduces the mechanical properties of the cell wall compared to dried conditions. The stiffness and strength of wood are generally assumed to vary linearly with its density [33–35]. It should be noted that the microfibril angle in each layer of the wood cell wall is another important factor that can influence the mechanical properties of the wood [36], Moreover, it is a factor independent of the density of the wood. Studies [37, 38] on tree branches indicate that in the joint region, this area tends to show higher density and interlocking fiber patterns, which may benefit tree structure safety. To this end, density variations within a self-growing connection are another aspect to investigate.

Regarding the last aspect of fiber structures, trees are able to acclimate the internal structure of their trunks and branches according to the stress they experience [39]. This acclimatization leads to specific structures that favor the efficiency and safety function of trees. Since wood is an anisotropic material, spatial distributions and orientations of stiff tissues, i.e. fiber structures, usually indicate the better loading direction of a structure. Studies [38, 40] have shown that trees tend to develop curl, interlocked, and deviated fiber patterns in regions when the original growth was disturbed. Thus, it is assumed that the fiber patterns of self-growing connections would be optimized by adaptive growth. Fiber structures within a self-growing connection will be examined.

Therefore, based on the knowledge and understanding from biology studies on thigmomorphogenesis, at the macroscopic level, self-growing connections are investigated from three aspects, namely density variation, geometric changes, and fiber structures. The studied connections are fused by *Ficus benjamina* L.. Results are obtained by facilitation with the techniques of X-Ray scanning and optical microscopy. The influences of the identified characteristics on the mechanical properties of a self-growing connection are discussed further.

3.2 Materials and methods

3.2.1 Description of braided tree structures

Ficus benjamina, whose common name is the weeping fig, is one of the most popular ornamental foliage plants. It is mainly distributed in the tropical and subtropical area [41]. To add aesthetic values, single trees are usually braided together in certain patterns. Figure 3.3 shows several commonly found patterns: cylinder (Figure 3.3 a), planar (Figure 3.3 b), and ponytail (Figure 3.3 c). Fully braided trees with connections growing in one pot can be considered as a tree structure, which can be divided into three regions from top to bottom:

3

canopy, net, and root/pot regions.

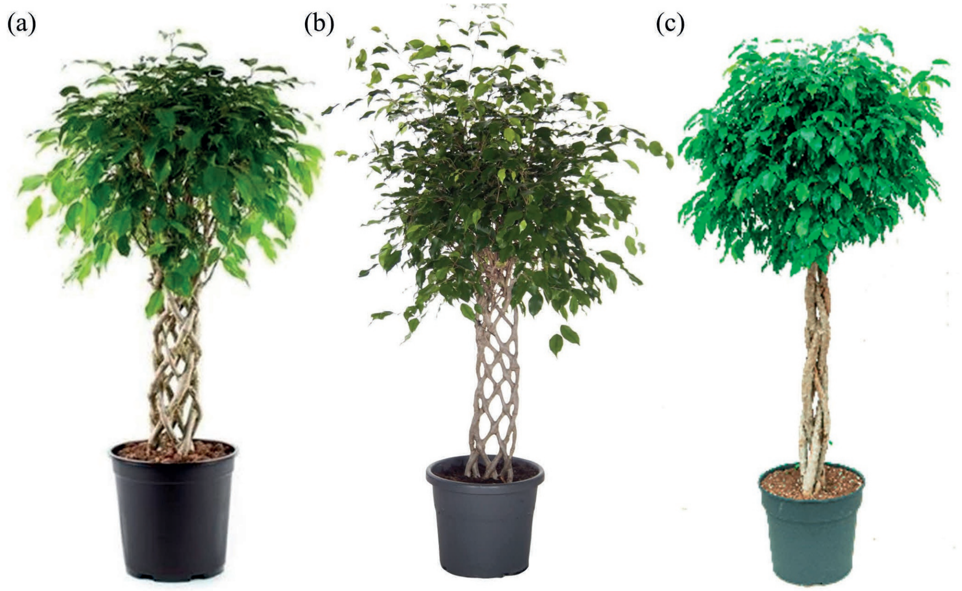

Figure 3.3: Braided tree structures by *Ficus benjamina*. (a) Circular pattern; (b) planar pattern; (c) ponytail pattern. Take the circular pattern as an example, in one pot, eight single stems with relatively same size (approximately 20 mm in diameter) are braided in pairs to form self-growing connections.

Investigations on self-growing connections fused by weeping figs have some advantages: (i) the method to fuse a connection is similar to the one in Figure 3.1 c, which enables further comparisons between tree species; (ii) *Ficus benjamina* is a fast growing tree species, which allows connections to fuse in a relatively short time period (approximately a growing season of six months); (iii) most braided trees are grown in a nursery, which allows the tree to develop in a stable growth condition with sufficient nutrition and less influence from environments. The circular pattern is used in this chapter. The planar pattern is used in Chapter 5.

3.2.2 Definition of self-growing connections

As shown in Figure 3.4 a, in the net region (the region between the canopy and the roots within the black rectangle), eight individual stems in a pot are braided in pairs to fuse a self-growing connection. The self-growing connection is formed by two single stems and fused an intersected surface in a saddle shape outlined by the edge of the bark joint (Figure 3.4 b where the interface is marked in the dashed line). The cross-angle is measured between the center line of the stems. To better describe the self-growing connection, a local coordinate system is located in the middle of the intersected area, x axis is aligned with the direction of the relatively larger stem (denoted as stem1). The first quadrant of the plane xy includes the smaller cross angle, and thus the z direction points out the interface.

As an example of the loading case in Figure 3.4 b, when loads from z direction (F_z) act perpendicular to the interface, it refers to the load out of the plane (Figure 3.4 c). On the contrary, when loads (F_x, F_y) are applied parallel to the plane of the interface (i.e., plane xy), it is defined as loading in the plane (Figure 3.4 d). Following the direction of each axis, a connection can be seen based on three cutting planes: plane xy, xz and yz, which is also in the viewing directions of axis z, y and x respectively. These three viewing directions are used to observe the spatial distribution of fibers.

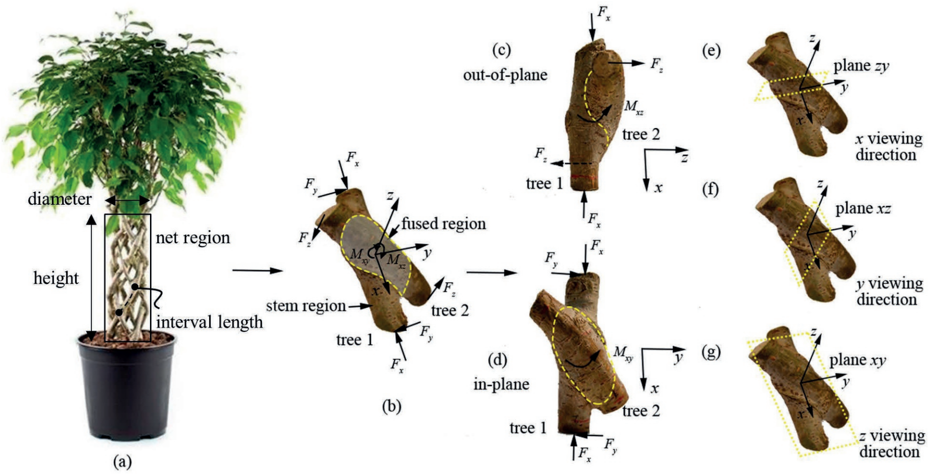

Figure 3.4: Feature definitions of braided tree structures and self-growing connections. (a) Circular braided weeping figs. From the top to the bottom, it is divided into canopy, net, and root/pot regions. Within the rectangle net region, the diameter of the circular net is measured between the outermost distance, and the height is measured from the base of the stem to the location of the last connection; (b) the local coordinate system is located at the center of the fused region. x axis aligns with the relatively larger stem, denoted stem1. The cross angle is measured between the center lines of two stems. The positive direction of y axis is determined when the smaller cross-angle projects in the first quadrant of the plane xy. Therefore, z direction is perpendicular to the intersected surface. The region of interest is the fused area where the stems touch, whereas the other region belongs to the stem region. The direction of loading scenarios is classified based on the plane xy, thus (c) is the out-of-plane loading and (d) the in-plane loading. To inspect internal structures, three viewing planes are defined based on the local coordinate, (e) x viewing direction, (f) y viewing direction, and (g) z viewing direction.

To make the qualitative description clear when explaining the results obtained, a hypothetical illustration of the process of developing a self-growing connection is presented in Figure 3.5. This is a conceptual model. The description is based on three levels of comprehension. (i) The first level is based on the mechanism of tree growth [42]. Wood production comes from the cambium layer of the stems, and the geometry expands in the radial direction of the stem. (ii) The second inference is based on extensive quantitative observations in [1, 2, 43], where the general pattern of self-growing connections is sketched.

(iii) The success of the formation of a connection is signaled by the formation of the shared cambium [44], from which the wood is produced for the connection. This production is added in the fused region.

As defined in Figure 3.4, a connection is divided into the stem and the fused region. As shown in Figure 3.5 a, the fused region is also the intersected (joint/bonded/connected) region of a connection. This region is outlined by the merging edge of the bark in the outer layer of a connection (as the dashed line in Figure 3.4 b). This curve forms the interface or the intersected surface. When observing a connection in a cutting cross section, such as the cross section in the dashed line (in the axis x direction), a point at the inside location within this cross section is selected and named Point P. As the stems grow and expand in their radial direction in Figure 3.5 b, the interface becomes larger and two stems grow deeper into each other. When the locations marked inside the cross sections and at the interface of a connection are compared, the material at Point P involves fusion activity earlier than that at Point E and F which are located at the edge of the fused region. Thus, it may be stated that the cross sections at Point E and F have young fusion (low fusion level), whereas the cross section at point P has old fusion (deep fusion level). As the stems continue to develop, the fusion involves more complex stages. As a result, in Figure 3.5 c, the stems grow much deeper with each other. The cross sections selected at Point M and N have younger fusion (lower fusion level) than those at Point E and F. Therefore, in the fusion region, in the viewing cross section as in Figure 3.5, the cross sections present different stages of fusion, which also indicates the growth history of a self-growing connection.

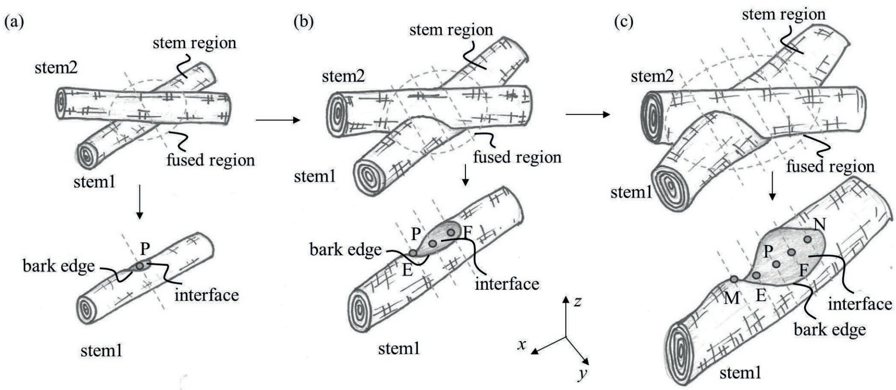

Figure 3.5: Sketch description of growth stages in a self-growing connection. The development of a connection can be assumed to have several stages, as depicted in (a), (b), and (c). Comparing these stages, it is evident that the interface is expanding. Consequently, the material initially involved in this fusion activity, such as at Point P in (a), gradually becomes the oldest fusion point in (b) and (c). Material at Point M and N is the youngest in the fusion activity. Additionally, material at Point E and F is older than Point M and N but younger than Point P.

Three braided tree structures (Tree_T, Tree_B, and Tree_S) with different net sizes were studied. Geometric information about each tree structure was listed in Table 3.1. The diameter of the net region was measured as the horizontal distance between the outermost locations of the entire braided net. The height of the net region was measured as the vertical distance between the top of the pot and the location of the last connection, as shown in Figure 3.4 a. The interval length between the connections was measured between the middle location of two neighboring connections on the same stem.

Table 3.1: Basic information of investigated braided trees: geometric dimensions in the net region, numbers of stems and connections within the braided trees.

ID	Net region		Number of stems	Number of connections	Interval length between connections (mm)
	Diameter (mm)	Height (mm)			
Tree_T	200	800	8	24	50-150
Tree_B	160	900	8	27	50-200
Tree_S	120	600	8	17	30-100

Note:
(1) Tree_T, Tree_B, and Tree_S are braided in circular patterns with varying net sizes. The symbols T/B/S denote the differences and do not have additional meaning.
(2) The net dimension and interval length are measured according to Figure 3.4 a.

3

3.2.3 Density variations

In order to minimize damage to living trees, the density variation within a connection was inspected by the calibrated medical computer tomography (CT) scanner (Siemens Somatom Volume Zoom CT scanner). The mechanism of CT scanning was based on information on how much scanned materials absorb X-ray radiations. The scanned results were translated into pictures where each pixel was represented by a gray value and the gray value was associated with the density of the material. In this chapter, the output gray value, known as the Hounsfield unit [45, 46], was calibrated with the air and water density for the equipment used. Thus, the Hounsfield unit at -1000 was calibrated with air density (apply 0 kg/m^3), and the value at 0 was calibrated with water density (1000 kg/m^3). Following the method used in [47], the obtained Hounsfield values were linearly calibrated. Thus, the linear calibration function can be expressed as Equation 3.1.

$$\rho = h + 1000, \tag{3.1}$$

where h stands for the Hounsfield unit of CT scanning, ρ is the corresponding material density, in kg/m^3. In this case, the density refers to the fresh density of the living tree materials.

The braided trees were scanned only within the net region and the results were constructed from slices at 0.6 cm intervals with a resolution of 0.6 mm. Medical CT scanning had advantages in density calibration, but due to the limits in resolution, no further detailed structure could be displayed. The calibration and analysis of the density variations were performed by ImageJ.

3.2.4 Geometric changes

As shown in Figure 3.6, the geometric variation within the braided tree structure was measured at two levels, specifically at the level of the braided tree structure and at the connection level. The first level of measurement was to understand and compare the variation in diameters caused by the presence of connections in a braided tree structure. The second was to further measure the changes in geometry within a connection caused by the fusion activity.

Measurements along stems

As shown in Figure 3.6 a, a total of eight stems were interconnected in pairs. The stems were sequentially assigned IDs in a counterclockwise manner. The first connection was denoted as the C1 joint by stems 1 and 2, located at the lowest position within the net region. The remaining connections were sequentially assigned numbers counterclockwise, from the lowermost point of the net region to the uppermost point. Along stem1, it involved connections 1, 5, 9, 17, and 21. Measurements along each stem were made at the midpoint of each interval between neighboring connections. Measurements were taken to avoid the presence of knots, branches, and other defects (such as uneven surfaces). Measurements were made in the middle of each interval, and the mean value was used from three measurements. The taper ratio of a stem was determined by calculating the ratio between the top diameter and the base diameter of a stem. For example, the tapering ratio of stem1 was the ratio between D_{18} and D_{11}.

Measurements within connections

Quantification of geometric changes within a connection was achieved by comparing area variations at several spatial locations. As shown in Figure 3.6 b, in the same viewing direction (z direction), within the fused region, a total of seven locations were uniformly chosen. The area of each cross section was quantified using ImageJ based on the results of the scan in section 3.2.3. The mean value was calculated by averaging the values of two adjacent slices at each point. The area in the fused region was further compared with the area in the stem region. The area in the stem was measured at an interval position located above the connecting point. Similarly, the mean value was derived considering three adjacent cross sections. To ensure comparability of the results across connections, the difference between the fused and stem regions was additionally normalized by the area within the stem region. Therefore, the difference in area between the stem and the fused region described the amount of additional wood produced within the fused region. The difference in area was further divided by the area in the stem region. Thus, the obtained area ratio could be used to compare among connections. The assumption of this analysis is that when two stems fuse, there is no removal of material in the fused region. The area ratio was defined as the *overgrown ratio*. The formula is expressed in Equation 3.2.

$$r = \frac{A_i - A_0}{A_0}, \tag{3.2}$$

where r stands for the overgrown ratio of a self-growing connection; A_i is the area of a cross section in the fused region, i from 1 to 7; and A_0 is the area of a cross section in the stem region. In total, 27 connections were measured in the braided tree structure Tree_B

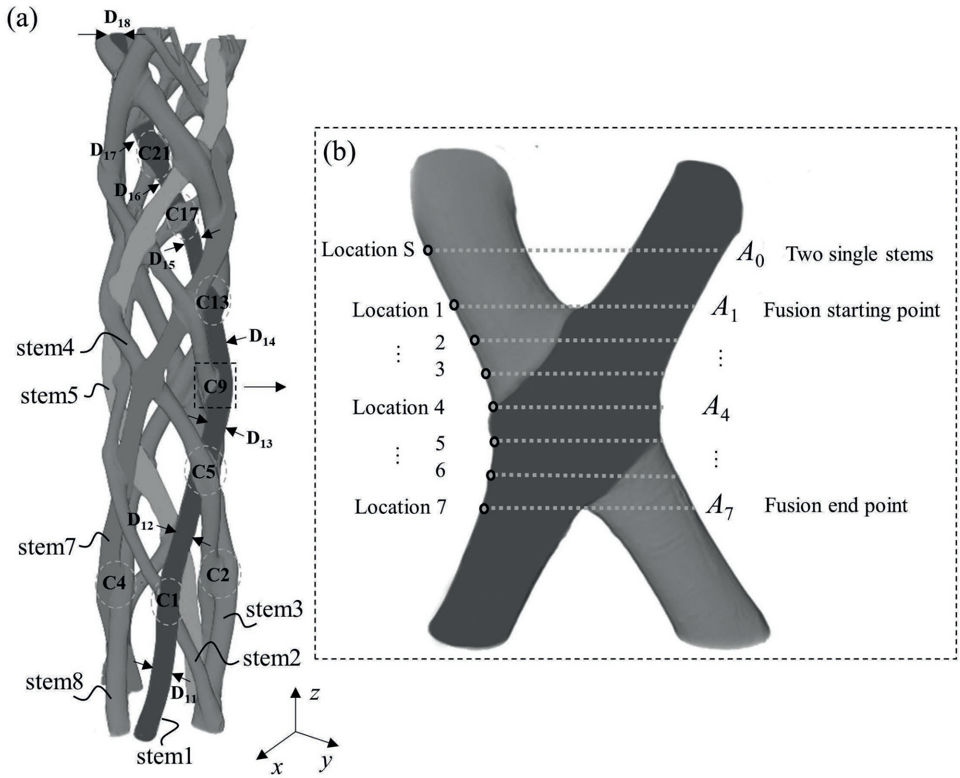

Figure 3.6: Illustration of geometric measurements on the braided tree structure and self-growing connections. (a) Within a braided tree structure, the denotations of stems, connections and measured intervals; (b) within a self-growing connection, the area comparison between the cross section in the stem region and a total of seven cross sections in the fused region. The model is reconstructed from the result of CT scanning. Note: A_i is area of a cross section in the fused region, i from 1 to 7; and A_0 is area of a cross section in the stem region.

and 17 connections in Tree_S. Information about braided tree structures is listed in Table 3.1.

3.2.5 Fiber structures

The internal structures of a connection were inspected by Nano-CT (Micro-CT) scanning (Phoenix Nanotom, 180 kV, 0.5 mA, with a resolution of 60 µm). In total, ten connections from three braided trees were taken. In Tree_T (Tr_T), the selected connections included Tr_T_C1, Tr_T_C2, and Tr_T_C12. In Tree_B (Tr_B), the selected connections included Tr_B_C4, Tr_B_C5, Tr_B_C8, and Tr_B_C17. In Tree_S (Tr_S), the selected connections included Tr_S_C1, Tr_S_C6, and Tr_S_C12. They were cut and immediately performed a scan. The reconstructed scanning results were inspected from three view directions, as illustrated in Figure 3.4. This inspection focused on the fiber patterns within a connection.

Moisture influence

The identification of fiber structures within a self-growing connection was carried out mainly when the connection was cut directly from the braided tree structure. The presence of water within the connections might influence the identification of the material. In addition, some cracks may not be detected when the structure was saturated. Therefore, one (Tr_T_C1) of the ten selected connections was further scanned twice when the moisture contents were under partially (88%) and fully dried (0%) conditions. The calculation of the moisture content was made according to EN13183 [48], and was expressed as the percentage of the water mass to the fully dried wood mass. Comparable inspections of changes in internal structures were also viewed in three directions as in Figure 3.4. Nano-CT had the advantage of investigating internal structures without causing damage to the sample. The shortcoming was that the density was not calibrated, but the relative brightness values might indicate a higher density value. For example, the brighter gray scale indicated a higher density than the darker color. However, the results of the CT scan could not provide detailed information about tissue types due to the limits of resolutions.

Optical microscopic observation

Interpretations of the information provided from the CT scan were further verified by visual identifications. The composition of the material in the stem region and fused area was identified by a digital microscope (VHX-7000, Keyence, Germany) at low magnification (20-30 times). The connection was cut using a microtome (HistoCore Microtome, Leica, Germany) to expose a smooth surface for observations.

3.2.6 Relation between fiber structures and geometric variations

From Tree_T in Table 3.1, five connections (Tr_T_C1, Tr_T_C2, Tr_T_C4, Tr_T_C5 and Tr_T_C8) were cut out to investigate the relation between fiber structures and geometric variations. An accurate structural pattern was difficult to identify directly without damage to the connection. However, fiber production was usually accompanied by an increase in geometric dimensions. Thus, changes in the geometric dimensions of a connection could be used to infer the structural pattern of a connection. The fiber structures were examined by Nano-CT scanning as described in Section 3.2.5. Measurement of cross-sectional area followed the approach described in Section 3.2.4.

3.3 Results and analyses

3.3.1 Density variations

The reconstructed tree and the results analyzed are shown in Figure 3.7. Because three trees are found to have similar patterns, in the main text, only one sample (Tree_T) is included. The rest can be referred to Appendix A for further confirmation.

The reconstructed net region is built on the basis of slices of cross sections. Each slice contains information on four cross sections of joints at different locations, as shown in Figure 3.7 a. Taking this into account, two cross sections are selected and analyzed. One

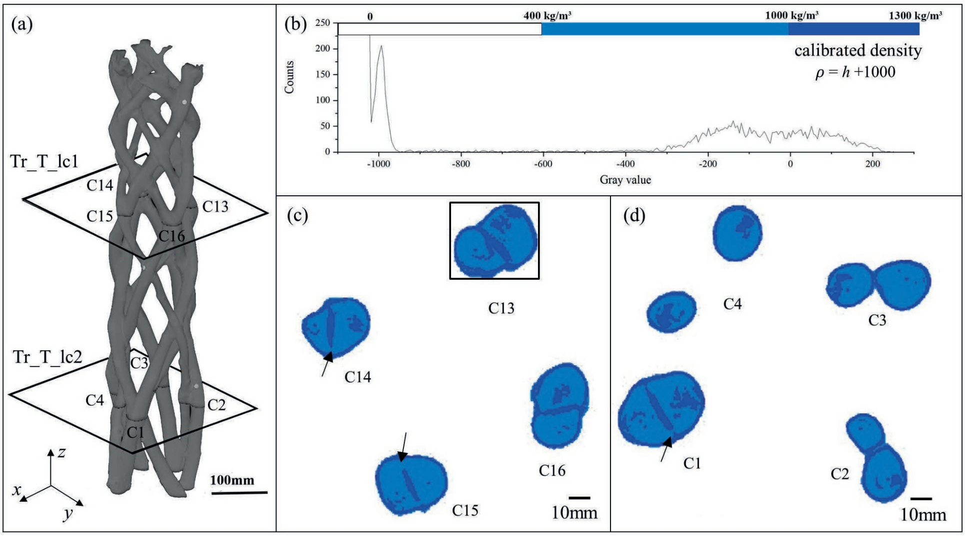

Figure 3.7: (a) Reconstruction of the braided tree structure 'Tree_T' from CT scanning, along with its inspected locations (Tr_T_lc1 and Tr_T_lc2). (b) Histogram of gray values derived from scanning results within the rectangular area shown in (c); the color map is distinguished based on thresholds of 400 and 1000 kg/m^3. (c) Density map at location Tr_T_lc1 indicated in (a); colors correspond to those in (b). (d) Density map at location Tr_T_lc2 indicated in (a); colors correspond to those in (b).

(Tr_T_lc1) is the cross section of the net that includes the middle region of four connections. As described in Figure 3.5, this is considered as in the old fusion stage. Second (Tr_T_lc2) is the location where four fusion cross sections are involved from the young (edge) to the old (middle) fusion stage. It can be seen as shown in Figure 3.6 a, cross sections in the stem region, the starting point of the fusion, the middle location and in between. In this case, four fusion stages and information at the middle location can be compared and displayed at the same time. In Figure 3.7 b, within the rectangular area in Figure 3.7 c, the Hounsfield value frequency diagram is plotted. This value is further calibrated using Equation 3.1. To better highlight regions with higher density, two threshold values are established at 400 and 1000 kg/m^3. The density threshold at 1000 kg/m^3 is the focus of the analysis, as it represents the density of water. Materials with a density higher than that of water can be seen, mainly distributed in the outer layer and the inner fused area. The outer layer is the bark area. In contrast, the inner stem region has a relatively lower density. Within a connection, when the cross section is at the location where the fusion stage is still young, the density distribution appears as a combination of two single stems. On the contrary and interestingly, at the middle location of a connection, where the fusion is supposed to mature, the density distribution is different. The shape of the cross section tends to become round and smooth. The density regions less than 1000 kg/m^3 in each stem gradually merge, following the black arrow in Figures 3.7 c and d. It can be inferred that the outer layer material might be mainly bark, but so far it is not clear whether the internal material is composed of bark.

To better understand density variations, the cross sections within Figure 3.7 d are further plotted using four probe lines, as shown in Figure 3.8. On a single stem (line1 in Figure 3.8), the density of the wood can be considered relatively homogeneous. Within the distance between 1 mm and 28 mm, the density of the stem has an average of 889.7 kg/m^3 with a coefficient of variation (CoV) of 11.4%. The rectangles marked the intersected areas within a fused region in Figure 3.8 a, which corresponds to the same region in Figure 3.8 b. It can be seen that when the fusion is in the young fusion stage (line2 and line3 in Figure 3.8 b), the density profile decreases when the probe lines pass the intersected locations. This indicates that there is discontinuity in the local materials in this region. On the contrary, in the middle fused region, line 4, the density distributions appear relatively stable. This information from density maps and variations explains that the intersected area within a connection has a higher density than the stem region, but the compositions of local material need to be investigated further.

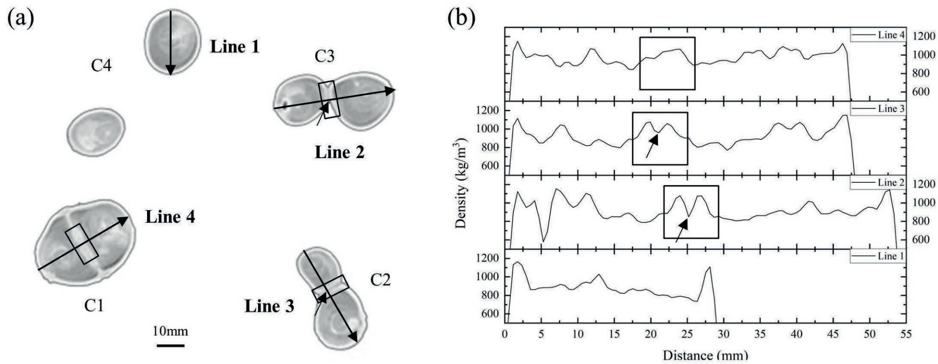

Figure 3.8: Density line profiles within cross-section in Figure 3.7 d. (a) Locations of probe lines in the selected cross-section; (b) density variations along the probe lines.

3.3.2 Geometric changes

In braided tree structures, along the height of each stem, the variation of diameters is recorded and compared at each interval. Figure 3.9 presents the results from Tree_T; results from the other two tree structures (Tree_B and Tree_S) can be referred to Appendix A. To be specific, for example, in Figure 3.6 a, in stem1, the diameters from D_{11} to D_{18} are measured. Stem1 has an average diameter of 20.9 mm with a CoV of 10.0%, and has a taper ratio of 0.91.

It is observed that the existence of connections in the stem influences its diameter size. In stems, the diameter variations measured at the intervals are slightly larger than the diameter difference between top and bottom (e.g., stem2 and stem5 in Figure 3.9). To be specific, in stem2, the difference in diameters caused by fusion of connections is 4.4 mm, but the diameter of D_{18} is 3.3 mm less than D_{11}.

When the taper ratio of a stem is not considered, the focus is to compare the area change between the fused area and the stem area within a connection. Figure 3.10 shows

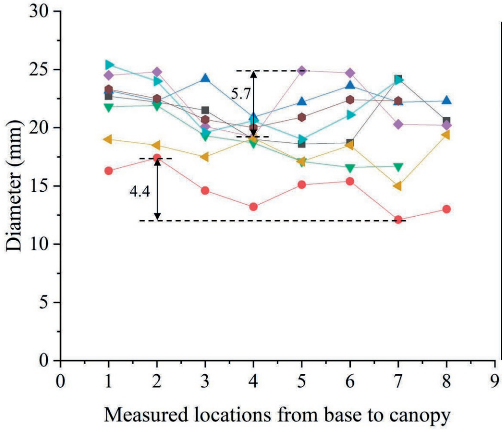

Tree T	Avg. Diameter (mm)	CoV (%)	Taper ratio
Stem1	20.9	10.0	0.91
Stem2	14.6	12.3	0.80
Stem3	22.6	4.4	0.96
Stem4	18.9	12.2	0.77
Stem5	22.3	11.7	0.82
Stem6	18.0	8.3	1.02
Stem7	22.0	11.4	0.95
Stem8	21.7	5.5	0.96

Figure 3.9: Diameter variations in the braided tree structure Tree_T. Left: Diameter variations at 1 to 7 intervals as depicted in Figure 3.6 a; right: the average stem diameter with its coefficient of variation (CoV) and calculated taper ratio.

the variation of the overgrown ratio as defined in Equation 3.2. Here, only connections from one stem (stem1 from Tree_T) are presented. The measured locations correspond to the description in Figure 3.6 b.

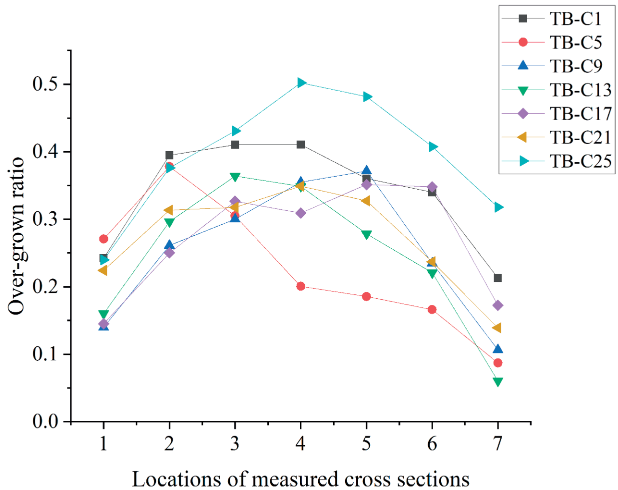

Figure 3.10: Along stem1 of Tree_B, area variations in the fused region, measured locations following Figure 3.6 b, where the naming rules of 'TB_C' stands for connections from Tree_B.

Figure 3.10 presents the analyzed overgrown ratios. The first observation from Figure

3.10 is that the overgrown ratio is always positive. This means that the fused area produced more wood than the stem region within a self-growing connection. Second, when looking at the trend line of variation, the peak value most likely appears in the middle region (locations 3 to 5). As trees grow and develop, an increase in area is always accompanied by an increase in the amount of fibers. Therefore, a relationship between geometric changes and fiber structures is expected to be established.

3.3.3 Fiber structures

To understand the fiber structures within a self-growing connection, the results are presented first from the observations in the stem region. Then, using this information, the deviation and distribution of the fiber bundles in the intersected region are analyzed. Because CT scanning results are given as grayscale images, fiber deviations are justified further on the basis of information from optical microscopy.

In the stem region, the identification and comparison of the directions of the fibers are illustrated in Figure 3.11. In both optical examinations (Figures 3.11 a and c) and CT images (Figures 3.11 b and d), the boundary between the xylem and bark regions (in dashed line) is distinguished. However, in the transverse direction of a stem, in Figures 3.11 a and b, within the xylem region, the growth increment is not composed of early wood and late wood, as usual hardwood. Instead, it consists of parenchyma cells and fibers that alternate in pairs. It forms the growth increment, shown as white rings in Figure 3.11 b. In contrast, in the longitudinal direction as in Figures 3.11 c and d, the white bands in Figure 3.11 d give information about the direction of the fiber.

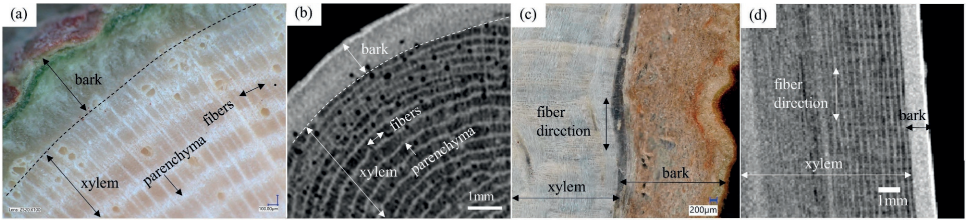

Figure 3.11: Comparison and validation of scanning results and optical microscopy in the stem region of a self-growing connection. (a) Transverse optical appearance; (b) transverse X-Ray appearance; (c) longitudinal optical appearance; (d) longitudinal X-Ray appearance.

In the fused region, the fiber structures observed by optical microscopy are shown in Figure 3.12. After the bark is removed, the fiber bundles in the outer layer of the connection are exposed. Figure 3.12 a shows the bundles of merged fibers (following the direction of the arrow), which connect two stems, distributed in the outer layer of the connection. In particular, this group of fiber bundles was observed primarily at the larger cross-angle between two stems. In contrast, as shown in Figure 3.12 b, within steeper regions at the lower cross angle, no continuous bundles of fiber were observed. Figure 3.12 c shows a cross section within a connection as a representation. This cross section is taken in the x viewing direction (Figure 3.4 e), and it is in the middle location within this fused region. Within this cross section, in the outer area, fused fiber bundles were observed, whereas following the direction of the arrow, in the inner region, few continuous fiber bundles are observed. Furthermore, in this region, these tissues were identified as bark tissues. The pointed spots may be perceived as defects when considering the structural integrity of a self-growing connection.

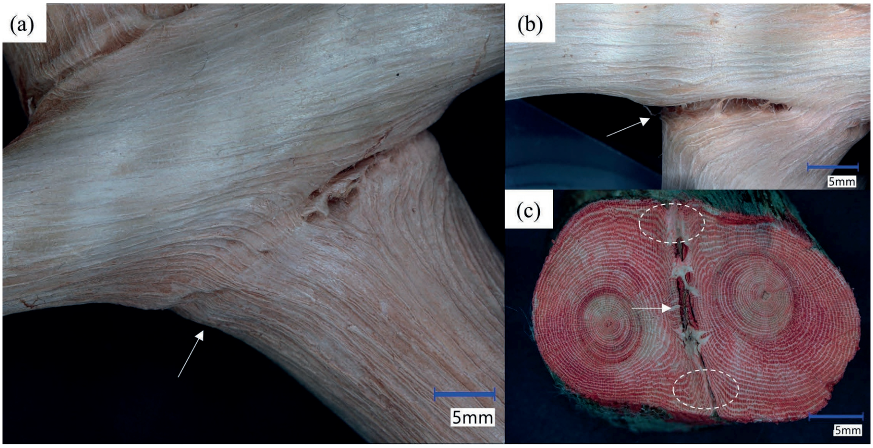

Figure 3.12: Fiber structures of a self-growing connection under optical microscopy. Merged fiber bundles distribute in the outer layer (a). This group of fibers mainly distributes at the larger cross angle of a connection; however, in the smaller cross angle (b), no continuous fibers appears; (c) in the middle location within the fused region in x direction, few fiber bundles connects inside the connection.

In addition to the results in Figure 3.12, Figure 3.13 provides more detailed information on the internal fiber structures within a self-growing connection. In accordance with the definitions in Figure 3.4, Figure 3.13 a shows the reconstructed scanning model according to the defined viewing axes. The appearance of a cross section depends on different viewing directions of the axis; however, in the same viewing direction, the appearance of a cross section differs from the locations of the cutting planes. Thus, in each direction, the fused region is evenly subdivided into segments, as illustrated in Figure 3.13 a, with an interval of approximately 12 mm. In the x viewing direction, as shown in Figure 3.13 b, the cross section consists of two transverse sections of two stems. In the y viewing direction (Figure 3.13 c), the cross section is a combination of a longitudinal section of stem1 and a transverse section of stem2. In the z viewing direction (Figure 3.13 d), the cross section consists of two longitudinal sections of two stems.

In the x viewing direction, the cross-sectional profiles exhibit a relatively symmetric arrangement. In particular, at locations 2 and 4 within this viewing axis, the group of merged fibers is apparent (following the direction of the arrow). This group of fiber bundles presents continuous growth increments that interconnect the two stems. In contrast, the presence of merged fibers is less obvious in the y direction (Figure 3.13 c) and z direction (Figure 3.13 d). In the y viewing direction, continuous growth increments are found in locations 1 and 3, while in the z viewing direction, few increments are observable in locations 1 and 2. The synthesis of insights obtained from both Figure 3.12 and Figure 3.13 will be elaborated on in the Discussion section.

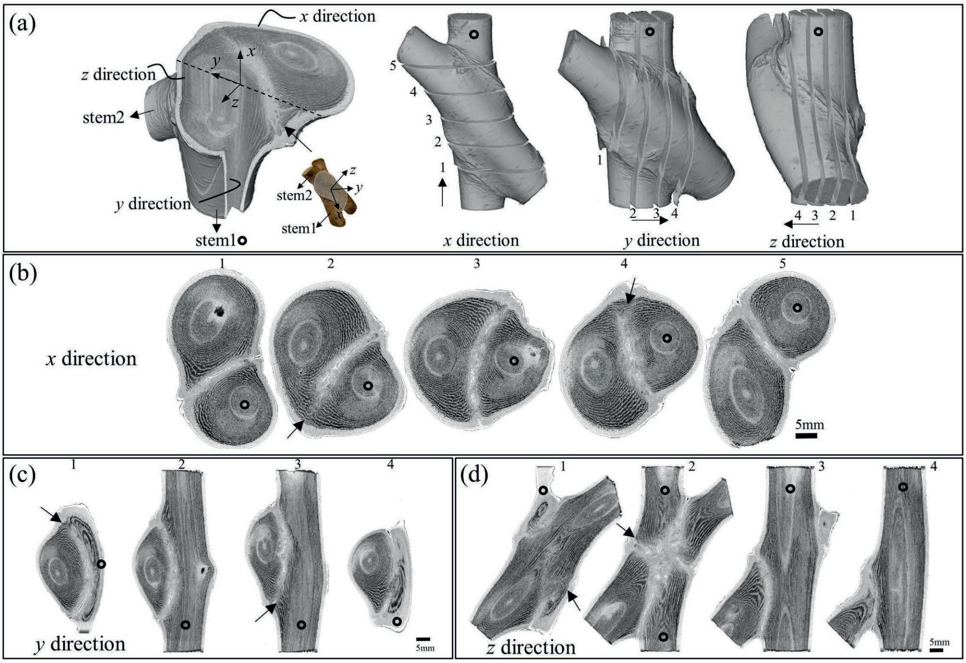

Figure 3.13: Internal fiber structures within a self-growing connection from CT scanning. (a) Reconstructed internal structures of a self-growing connection and the viewing directions according to three axes; (b) the x viewing direction; (c) the y viewing direction; (d) the z viewing direction. Note: The coordinate system aligns with the one in Figure 3.4.

Influence of moisture contents on fiber structures

Following inspections on fiber structures of ten connections, the connection Tr_T_C1 is selected to study the influence of water contents on the fiber structures. Changes in moisture content and mass are shown in Figure 3.14. The fiber structures are displayed in three-dimensional mode at the same position for comparison. The changes are presented in Figure 3.15.

Following the arrows in Figure 3.15, it can be seen that the fiber bundles merged in the outer layer of a connection are not affected by drying. What is influenced the most is the internal fused region. The degree of gray values can give an idea of the density relevance. Brighter white indicates higher density, while black indicates lower density. However, it should be noted that this work does not calibrate the value for the Nano-CT scanner. Although the connection is fully dried (Figure 3.15 c), in the internal region, it still shows a brighter color, which indicates a higher density. However, during the drying process, the internal cracks develop gradually. Only a few materials connect in the fused region when the sample is fully dried. The reason might be that the main composition of the interconnected material is the bark tissue. Further identifications will be made in Chapter 4. This result could suggest that merged fiber bundles in the outer layer of a connection are essential for the structural integrity of a self-growing connection.

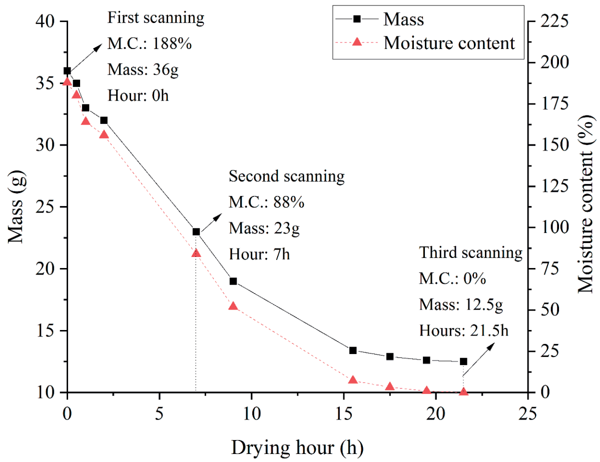

Figure 3.14: Drying process of a self-growing connection. Mass changes with drying hours, during which first scanning was performed at 188%, second scanning at 88%, and third at fully dried 0%.

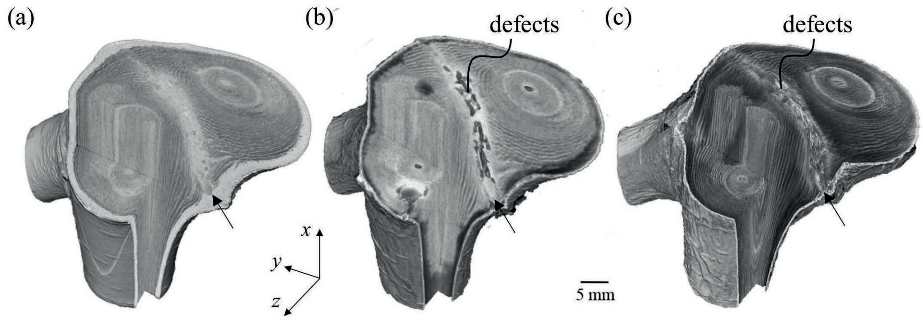

Figure 3.15: Influence of moisture content on the internal structure of a self-growing connection. (a) 3D structure in wet condition as the one in Figure 3.13 a; (b) structure at 88% water content; (c) fully dried structure. Arrows point to the locations of fused fibers.

3.3.4 Relation between fiber structures and geometric variations

The variation of areas at different locations within the intersected region is also correlated with the characteristic of the fiber structures. Nano-CT scanned connections are measured in the same way as in Figure 3.6. The variation of areas is plotted in Figure 3.16. In Figure 3.17, fiber structures of the connection Tr_T_C4 and Tr_T_C8 are presented to explain the relation between fiber structures and geometric changes.

As shown in Figure 3.17, in connection Tr_T_C4, the overgrown ratio peaks at the fourth

3

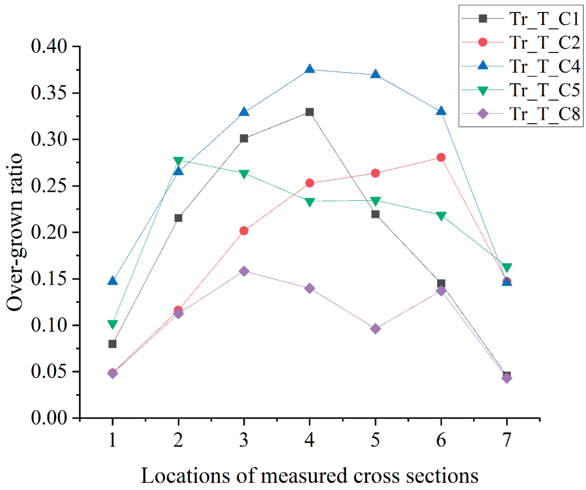

Figure 3.16: Area variations of Nano-CT scanned connections. Measured method follows Figure 3.6.

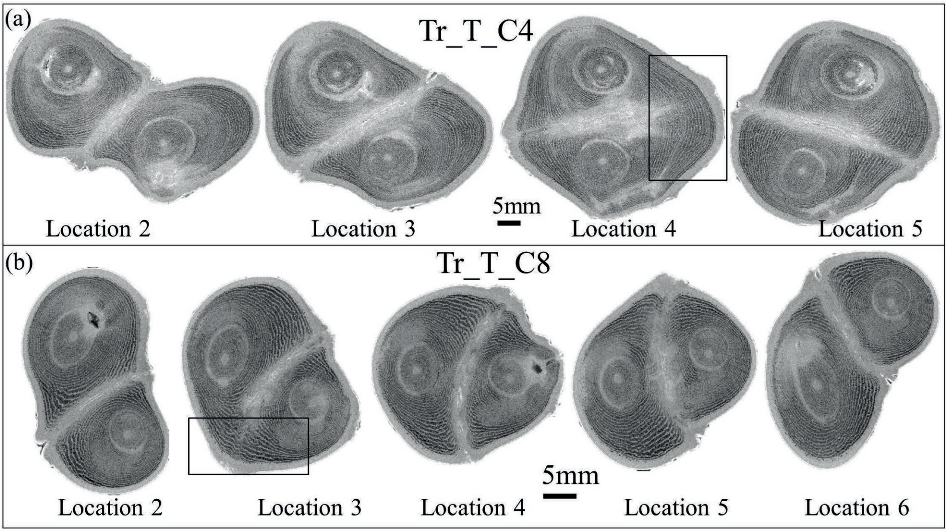

Figure 3.17: Internal changes at measured cross-sections in connection Tr_T_C4 and Tr_T_C8. The rectangular area indicates the place where merged fibers are the most.

measured location. Compared to the fourth location with the other locations (locations 2 to 5), when the area reaches the maximum value (location 4), the fiber structures show the most fused fibers in the cross section. The same finding is identified in connection Tr_T_C8 at location 3. This observation shows the fiber structures at different fusion stages. The changes in area are coupled with the spatial distributions of the fibers. The relationship between the location of the maximum area and the section that has the most merged fibers provides a practical method for evaluating the fusion condition of a self-growing connection. It can be performed by directly measuring the area variations within the fused region.

3.4 Discussion

The mechanism of fusion of a self-growing connection is understood from studies of thigmomorphogenesis, which describe the responsive link between mechanical perturbations and plant growth. The interest of this study is in the effects after tree acclimatization to physical constraints, i.e., after the fusion occurred. However, after the starting point of fusion, this research does not cover how wood is produced over time. This process of development as an entire connection is based on the assumption and illustration in Figure 3.5. Although the process of how this fusion occurs is beyond the scope of this research, it is useful to further discuss how stems fuse together. Based on the results in Sections 3.3.2 and 3.3.3, a conceptual model is proposed to describe the fiber structures within a self-growing connection. Furthermore, it is discussed how the identified features influence the mechanical performance of a connection.

3.4.1 Connection formation process

Understanding the fusion process means knowing how mechanical stresses and physical constraints translate into a certain pattern of growth. One way to explain and interpret the process is from the perspective of thigmomorphogenesis, as has been explained in the Introduction. The shapes of self-growing connections are regulated by the feedback cycles of mechanosensing, mechanotransduction, and mechanoresponse in trees.

Another similar method to explain the process could be the concept of graft [49, 50]. The main difference between the fusion method used in this work and the general grafting method is that the latter usually involves damage to the plants. Thus, the grafting process is considered an analogy to the wound healing situation, and thus successive growth is triggered. The grafting mechanism is usually explained by wound response and wound repair mechanisms, during which it involves the production of plant hormones (e.g., auxin transportation) and the expression induction of defense-related genes [51]. Most plants will graft to themselves; fewer will graft to very closely related species; and plants only rarely successfully graft to more distant relatives. The success of grafting depends on the compatibility of two species, in other words, the recognition between cells [52, 53]. To achieve successful grafting, the grower commonly increases the physical pressure around a graft formation by using a clip or wrapping tape around the graft junction, which has been proven to be helpful for the growth process [54, 55].

The mechanisms behind both thigmomorphogenesis and grafting involve physiological, biochemical, and biomechanical changes at many scales, from gene expression to plant hormone movement to overall shape changes or reunion. It is likely that the process of fusion of self-growing connections could be interpreted from the combination of these two biological activities.

3.4.2 Conceptual model of a self-growing connection

By combining the insights obtained from Sections 3.3.2 and 3.3.3, a simplified model is presented to describe a connection in Figure 3.18.

3

As identified in Figure 3.10, the size of the fused region is enlarged compared to the stem region. This feature is reflected in the enlarged diameter close to the interface. The diameter measured at the interface D_{1m} is greater than the diameter measured at the bottom of stem1 D_{1b}. The diameters (topside of stem1 D_{1t}, bottom side of stem1 D_{1b}, left side of stem2 D_{2l}, and the right side of stem2 D_{2r}) measured on the four sides of two stems may differ from each other.

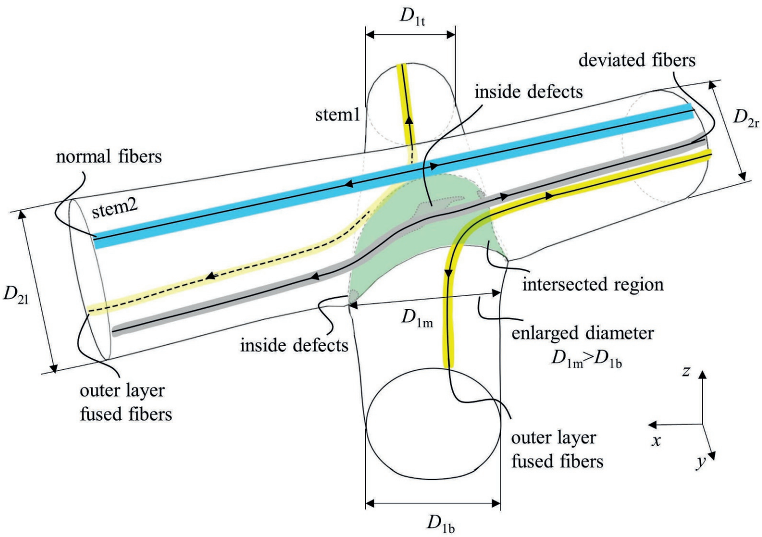

Figure 3.18: The conceptual model of fiber structures of a self-growing connection.

Fibers in a self-growing connection can generally be grouped into three categories: outer merged fiber bundles (in yellow), deviated fibers (in gray), and normal fibers (in blue). The outer merged fibers are distributed mainly in the outer layer of a connection, as shown in Figure 3.13 b. This group of fibers serves as the primary means of bonding two stems to one entity, which is inferred to be the main contribution to the mechanical capacity of a connection. Furthermore, the direction of this group of fibers has a pattern, as presented in Figure 3.12 b. In the smaller cross-angle with a sharp transition, very few merged fibers are identified. In most cases, the direction of these merged fibers originates from one stem, passes across the larger cross-angle, and then connects with the other stem. The distribution pattern of the merged fibers can be explained by the mechanism of wood formation. In several studies [42, 56, 57], it has been found that wood production and grain direction are determined by the distribution and gradients of the plant hormone auxin. The flow of auxin, which is unidirectional on both stems, is based on the direction of growth of the tree. The transportation of auxin within the plant always follows the principle of minimizing energy consumption [58, 59]. The flow of auxin in the path of the larger cross angle is an efficient option instead of the smaller cross angle within the fused region. Schematically illustrated in Figure 3.18, assume that auxin flows from D_{1b} to D_{1t} in stem1 and D_{2l} to D_{2r}, the efficient path of transport is in the yellow line, which also indicates the production of merged fibers.

The distribution of inside defects is difficult to quantify. As understood in Figure 3.12 c, the inner defects are marked at the smaller cross angle and the internal area of the fused region. The group of deviated fibers is located mainly near the edge of the edge of the bark joint of the stem. Groups of deviated fibers and normal fibers are those that do not serve as bonding links within a self-growing connection.

3.4.3 Mechanical effects of macroscopic characteristics

The adaptive growth of a self-growing connection is a dynamic interaction between geometric changes and load redistribution. Meanwhile, this process is accompanied by changes in wood properties (e.g., wood strength) and fiber structures. Currently, it is still challenging to perfectly predict how a tree will acclimate or optimize its internal structure to support its various functions under different environmental conditions [10]. However, how fibers are structured can reveal the growth and loading history to some extent [11, 60]. In this section, we discuss how each identified feature affects the mechanical properties (e.g., strength) of a self-growing connection.

The first finding in this work is the higher density displayed in the intersected area. Reasons leading to higher density may be (i) dense cell accumulation; (ii) water influence; or (iii) a combination of two cases. When water was excluded from the intersected area in Figure 3.15, the dried condition of a connection also showed a relatively higher density in the intersected region; thus, the influence of water can be excluded. If dense cells account for this effect, when relating high density to better strength, three other factors should also be considered: microfibril angle (MFA), fiber direction, and tissue composition. As seen in Figure 3.12, the inner side was composed of soft tissues, which are easy to shrink when water is lost. The wood produced in the fused region is considered the result of a mechanical response, which is the tension wood for the hardwood species [61, 62]. Tension wood exhibits a higher cellulose content than normal wood in chemical compositions; and it is distinguished by its G-layer within fiber cells [62, 63]. Furthermore, tension wood has a smaller MFA [64, 65], which contributes to increased tensile strength and stiffness of the wood. Therefore, the identification of tension wood needs to be confirmed from anatomical features, such as G-layer within fiber cells. This will be conducted in Chapter 4.

The second finding in this work is the spatial distribution of the fused wood. The enlarged area in the fused region increases the stiffness of the cross section, which is beneficial for the mechanical capacity of the cross section. Furthermore, fused fiber patterns are identified from inspections of fiber structures. As depicted and conceptualized in Figure 3.18, the distributed location of the merged fibers prevents the connection from splitting. However, defects at the edge of the young fusion area are also obvious (Figure 3.12 c), which is the risky and weak point of the interface. Thus, the number of continuous merged fiber bundles in the outer layer contributes the most to the integrity and quality of a self-growing

3

connection.

Furthermore, a relationship is found between the fiber structures and the changes in the area. To investigate fiber structures within a connection, current approaches, such as Nano-CT scanning, cause damage to the connection as the connections have to be cut out to ensure the resolution of scanning. However, to monitor and assess the fusion process of a connection in the living condition, non-destructive methods are necessary. For example, as shown in Figure 3.19, the diameters close to the fusion area are larger than those of the stem region ($D_{1m} > D_1$). The distance in the middle location (I_e) of the fused region between the two outermost stems is less than the sum of the diameters of the two stems ($I_e < D_1 + D_2$). It means that the enlarged diameter and fused width are important features because of fusion and should not be neglected or simplified. When the fused width is measured at the center location in the intersected area, it may provide information on the quality of the fusion.

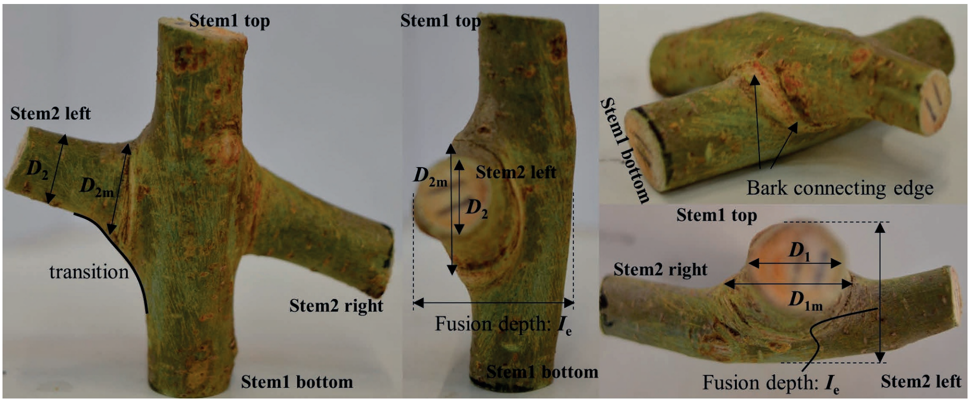

Figure 3.19: Illustration of a self-growing connection; definitions follow Figure 3.4.

It is difficult to conclude whether the fusion improved the mechanical properties. The fusion technique used in this work is to compress two stems without the removal of the bark. This makes the bark of the original stems in the contacted area included with the following growth. Since bark is considered mainly composed of soft tissues, the unavoidable existence of barks in the inner region can be regarded as defects or discontinuities when analyzing mechanical performance. However, continuous merged fiber bundles might compensate for the weakness. Therefore, further anatomical studies are required at the cellular level (in Chapter 4) and mechanical tests at the structural level (in Chapter 5).

3.5 Summary of macroscopic characteristics of self-growing connections

The analysis of the macroscopic features of self-growing connections is summarized in this section, which provides the basis for the mechanical analysis in Chapter 5. The characterization of a self-growing connection in three aspects (density distribution, geometric variation, and fiber structure) is summarized in Table 3.2. The density and geometry of a connection can be measured directly, but the fiber structure is difficult to inspect directly without damaging the connection. Thus, the fourth aspect, which describes the relationship between the fiber structure and geometry variation, is a method of indirectly inferring fiber structures. Fiber structures can be inferred from geometric features, such as the fusion depth as discussed in Section 3.3.4. As presented in Figure 3.18, the fusion depth can be used to estimate the fiber structure and therefore to infer the level of fusion of a connection.

Table 3.2: Macroscopic characterization of self-growing connections

Studied aspects	Remarks	Mechanical influences
Density distribution	- The intersected region has a higher density than the stem region within a connection. (Figure 3.6 and 3.7)	Strong strength is thought to be predicted by high density.
Geometric variation	- The diameter near the interface is enlarged. - When viewing in the defined x direction, the cross-sectional area at the fused region is larger than that in the stem region. (Figure 3.9 and 3.18)	The increased area influences the moment of inertia, which further affects the stiffness.
Fiber structure	- Three main groups of fiber bundles are identified, namely merged fiber bundles in the outer layer connecting two stems, deviated fibers and normal fibers in original stems. (Figure 3.11 and 3.12)	It is concluded the structural integrity and mechanical properties of a connection are determined by the group of merged fibers.
Relation between fiber structure and geometry variation	- The deep level of fusion is found in the middle location of the fused region. (Figure 3.4, 3.16, and 3.18)	This relation provides a method to estimate the level of fusion of a connection by measuring its geometry.

3.6 Concluding remarks

The ability to adapt and respond to mechanical stimuli is crucial for the survival of trees in nature. Due to their adaptive growth, two trees can fuse into a natural connection (i.e., a self-growing connection) to further resist external loads. As a starting point, this chapter aims to characterize macroscopic features of a self-growing connection from three aspects: density variations, geometric changes, and fiber structures. It helps to better understand and further assess the structural value of the self-growing connection for practical applications. The key findings of this chapter can be concluded as follows:

1. Within a self-growing connection, the intersected region presents a higher density than the stem region.
2. The fused region has a larger size than the stem region.
3. The fiber structures of a self-growing connection can be characterized into three groups: the merged fiber bundles in the outer layer connecting the two stems, the deviated fiber bundles, and the normal fiber bundles in each individual stem.

4. In the internal region, it is composed mainly of bark tissues, and fewer fibers fuse together. The group of merged fibers contributes the most to the structural integrity of a self-growing connection.

5. In the fused region, the location of the largest area can be related to the better fused location, which is represented by more merged fiber bundles.

After understanding the macroscopic features of self-growing connections from morphological analysis, Chapter 4 will further investigate the microscopic features from the cellular and tissue level.

References

[1] C. Mattheck. Wood—the internal optimization of trees. *Arboricultural Journal*, 19(2): 97–110, 1995.

[2] C. Mattheck. *Design in nature: Learning from trees*. Springer Science & Business Media, 1998. Pages 29–65.

[3] X. Wang, W. Gard, H. Borska, B. Ursem, and J. W. G. Van de Kuilen. Vertical greenery systems: from plants to trees with self-growing interconnections. *European Journal of Wood and Wood Products*, 78(5):1031–1043, 2020.

[4] F. Ludwig, W. Middleton, F. Gallenmüller, P. Rogers, and T. Speck. Living bridges using aerial roots of *Ficus elastica*–an interdisciplinary perspective. *Scientific reports*, 9(1):1–11, 2019.

[5] M. J. Jaffe. Thigmomorphogenesis: The response of plant growth and development to mechanical stimulation. *Planta*, 114:143–157, 1973.

[6] M. J. Jaffe, A. C. Leopold, and R. C. Staples. Thigmo responses in plants and fungi 1. *American Journal of Botany*, 89:375–382, 2002.

[7] J. Braam. In touch: Plant responses to mechanical stimuli. *New Phytologist*, 165: 373–389, 2005.

[8] C. Coutand. Mechanosensing and thigmomorphogenesis, a physiological and biomechanical point of view. *Plant Science*, 179:168–182, 2010.

[9] B. Moulia, C. Coutand, and J. L. Julien. Mechanosensitive control of plant growth: Bearing the load, sensing, transducing, and responding. *Frontiers in plant science*, 6: 52, 2015.

[10] E. Badel, F. W. Ewers, H. Cochard, and F. W. Telewski. Acclimation of mechanical and hydraulic functions in trees: Impact of the thigmomorphogenetic process. *Frontiers in plant science*, 6:266, 2015.

[11] O. Hamant, M. G. Heisler, H. Jönsson, P. Krupinski, M. Uyttewaal, P. Bokov, F. Corson, P. Sahlin, A. Boudaoud, E. M. Meyerowitz, Y. Couder, and J. Traas. Developmental patterning by mechanical signals in *Arabidopsis*. *Science*, 322:1650–1655, 2008.

[12] O. Hamant. Widespread mechanosensing controls the structure behind the architecture in plants. *Current Opinion in Plant Biology*, 16:654–660, 2013.

[13] F. W. Telewski and M. J. Jaffe. Thigmomorphogenesis: Anatomical, morphological and mechanical analysis of genetically different sibs of *Pinus taeda* in response to mechanical perturbation. *Physiologia Plantarum*, 66:219–226, 1986.

[14] F. W. Telewski. Mechanosensing and plant growth regulators elicited during the thigmomorphogenetic response. *Frontiers in Forests and Global Change*, 3:147, 2021.

[15] G. B. Monshausen and E. S. Haswell. A force of nature: Molecular mechanisms of mechanoperception in plants. *Journal of Experimental Botany*, 64:4663–4680, 2013.

[16] V. Vogel and M. Sheetz. Local force and geometry sensing regulate cell functions. *Nature Reviews Molecular Cell Biology*, 7:265–275, 2006.

[17] T. Kurusu, K. Kuchitsu, M. Nakano, Y. Nakayama, and H. Iida. Plant mechanosensing and Ca^{2+} transport. *Trends in Plant Science*, 18:227–233, 2013.

3

[18] C. E. Morris and U. Homann. Cell surface area regulation and membrane tension. *The Journal of Membrane Biology*, 179:79–102, 2001.

[19] E. W. Chehab, E. Eich, and J. Braam. Thigmomorphogenesis: A complex plant response to mechano-stimulation. *Journal of Experimental Botany*, 60:43–56, 2009.

[20] M. Uyttewaal, A. Burian, K. Alim, B. Landrein, D. Borowska-Wykrt, A. Dedieu, A. Peaucelle, M. Ludynia, J. Traas, A. Boudaoud, D. Kwiatkowska, and O. Hamant. Mechanical stress acts via katanin to amplify differences in growth rate between adjacent cells in *Arabidopsis*. *Cell*, 149:439–451, 2012.

[21] K. Jonsson, O. Hamant, and R. P. Bhalerao. Plant cell walls as mechanical signaling hubs for morphogenesis. *Current Biology*, 32:334–340, 2022.

[22] N. Nakayama, R. S. Smith, T. Mandel, S. Robinson, S. Kimura, A. Boudaoud, and C. Kuhlemeier. Mechanical regulation of auxin-mediated growth. *Current Biology*, 22: 1468–1476, 2012.

[23] M. Kouhen, A. Dimitrova, G. S. Scippa, and D. Trupiano. The course of mechanical stress: Types, perception, and plant response. *Biology*, 12(2):217, 2023.

[24] F. W. Telewski and M. L. Pruyn. Thigmomorphogenesis: A dose response to flexing in *Ulmus americana* seedlings. *Tree Physiology*, 18:65–68, 1998.

[25] P. Milani, S. A. Braybrook, and A. Boudaoud. Shrinking the hammer: Micromechanical approaches to morphogenesis. *Journal of Experimental Botany*, 64:4651–4662, 2013.

[26] A. C. Oates, N. Gorfinkiel, M. González-Gaitán, and C. Philipp Heisenberg. Quantitative approaches in developmental biology. *Nature Reviews Genetics*, 10:517–530, 2009.

[27] A. Geitmann and J. K. E. Ortega. Mechanics and modeling of plant cell growth. *Trends in Plant Science*, 14:467–478, 2009.

[28] M. Fournier, J. Dlouhá, G. Jaouen, and T. Almeras. Integrative biomechanics for tree ecology: Beyond wood density and strength. *Journal of Experimental Botany*, 64: 4793–4815, 2013.

[29] K. J. Niklas. Differences between *Acer saccharum* leaves from open and wind-protected sites. *Annals of Botany*, 78:61–66, 1996.

[30] F. Danjon, T. Fourcaud, and D. Bert. Root architecture and wind-firmness of mature *Pinus pinaster*. *New Phytologist*, 168:387–400, 2005.

[31] B. C. Nicoll and D. Ray. Adaptive growth of tree root systems in response to wind action and site conditions. *Tree Physiology*, 16:891–898, 1996.

[32] D. Sellier, T. Fourcaud, and P. Lac. A finite element model for investigating effects of aerial architecture on tree oscillations. *Tree Physiology*, 26:799–806, 2006.

[33] J. Chave, D. Coomes, S. Jansen, S. L. Lewis, N. G. Swenson, and A. E. Zanne. Towards a worldwide wood economics spectrum. *Ecology Letters*, 12:351–366, 2009.

[34] K. J. Niklas and H. C. Spatz. Worldwide correlations of mechanical properties and green wood density. *American Journal of Botany*, 97:1587–1594, 2010.

[35] M. Borrega and L. J. Gibson. Mechanics of balsa (*Ochroma pyramidale*) wood. *Mechanics of Materials*, 84:75–90, 2015.

[36] I. D. Cave. Theory of X-ray measurement of microfibril angle in wood. *Wood Science and Technology*, 31:225–234, 1997.

[37] D. Slater and A. R. Ennos. Determining the mechanical properties of hazel forks by testing their component parts. *Trees - Structure and Function*, 27:1515–1524, 2013.

[38] D. Slater, R. S. Bradley, P. J. Withers, and A. R. Ennos. The anatomy and grain pattern in forks of hazel (*Corylus avellana* L.) and other tree species. *Trees - Structure and Function*, 28:1437–1448, 2014.

[39] F. Brüchert and B. Gardiner. The effect of wind exposure on the tree aerial architecture and biomechanics of Sitka spruce (*Picea sitchensis*, Pinaceae). *American Journal of Botany*, 93:1512–1521, 2006.

[40] B. Gardiner, J. Barnett, P. Saranpää, and J. Gril. The biology of reaction wood. Springer, 2014. Pages: 13–36.

[41] D. Scuderi, F. Giuffrida, S. Toscano, and D. Romano. Growth, physiological response, and quality characteristics of weeping fig in response to shading levels and climatic conditions. *HortScience*, 47:1586–1592, 2012.

[42] C. Plomion, G. Leprovost, and A. Stokes. Wood formation in trees. *Plant physiology*, 127(4):1513–1523, 2001.

[43] F. Ludwig, H. Schwertfreger, and O. Storz. Living systems: Designing growth in baubotanik. *Architectural Design*, 82(2):82–87, 2012.

[44] A. N. Rao. Developmental anatomy of natural root grafts in *Ficus globosa*. *Australian Journal of Botany*, 14(3):269–276, 1966.

[45] U. Schneider, E. Pedroni, and A. Lomax. The calibration of ct hounsfield units for radiotherapy treatment planning. *Physics in Medicine & Biology*, 41(1):111, 1996.

3

[46] R. A. Brooks. A quantitative theory of the hounsfield unit and its application to dual energy scanning. *Journal of computer assisted tomography*, 1(4):487–493, 1977.

[47] C. Freyburger, F. Longuetaud, F. Mothe, Thiéry Constant, and J. Leban. Measuring wood density by means of X-ray computer tomography. *Annals of forest science*, 66(8): 804, 2009.

[48] European standard EN 13183-1. Moisture content of a piece of sawn timber. Determination by oven-dry method, 2002.

[49] C. W. Melnyk and E. M. Meyerowitz. Plant grafting. *Current Biology*, 25:183–188, 2015.

[50] C. W. Melnyk. Plant grafting: Insights into tissue regeneration. *Regeneration*, 4:3–14, 2017.

[51] M. Asahina and S. Satoh. Molecular and physiological mechanisms regulating tissue reunion in incised plant tissues. *Journal of plant research*, 128:381–388, 2015.

[52] M. Notaguchi, K. Kurotani, Y. Sato, R. Tabata, Y. Kawakatsu, K. Okayasu, Y. Sawai, R. Okada, M. Asahina, Y. Ichihashi, K. Shirasu, T. Suzuki, M. Niwa, and T. Higashiyama. Cell-cell adhesion in plant grafting is facilitated by b-1,4-glucanases. *Science*, 369: 698–702, 2020.

[53] O. Zarrouk, Y. Gogorcena, M. A. Moreno, and J. Pinochet. Graft compatibility between peach cultivars and prunus rootstocks. *HortScience*, 41:1389–1394, 2006.

[54] J. Ko, K. Han, S. Park, and J. Yang. Plant body weight-induced secondary growth in *Arabidopsis* and its transcription phenotype revealed by whole-transcriptome profiling. *Plant Physiology*, 135:1069–1083, 2004.

[55] A. Rasool, S. Mansoor, K. M. Bhat, G. I. Hassan, T. R. Baba, M. N. Alyemeni, A. A. Alsahli, H. A. El-Serehy, B. A. Paray, and P. Ahmad. Mechanisms underlying graft union formation and rootstock scion interaction in horticultural plants. *Frontiers in Plant Science*, 11:1778, 2020.

[56] R. S. Smith and E. M. Bayer. Auxin transport-feedback models of patterning in plants. *Plant, cell and environment*, 32(9):1258–1271, 2009.

[57] E. M. Kramer. Wood grain pattern formation: A brief review. *Journal of Plant Growth Regulation*, 25:290–301, 2006.

[58] E. M. Kramer. A mathematical model of pattern formation in the vascular cambium of trees. *Journal of theoretical biology*, 216(2):147–158, 2002.

[59] E. M. Kramer. A mathematical model of auxin-mediated radial growth in trees. *Journal of theoretical biology*, 208(4):387–397, 2001.

[60] J. Dumais. Can mechanics control pattern formation in plants? *Current Opinion in Plant Biology*, 10:58–62, 2007.

[61] A. B. Wardrop and H. E. Dadswell. The nature of reaction wood. IV. Variations in cell wall organization of tension wood fibres. *Australian journal of botany*, 3(2):177–189, 1955.

[62] T. E. Timell. The chemical composition of tension wood. 1969.

[63] W. A. Côté, A. C. Day, and T. E. Timell. A contribution to the ultrastructure of tension wood fibers. *Wood Science and Technology*, 3(4):257–271, 1969.

[64] B. Clair, T. Alméras, H. Yamamoto, T. Okuyama, and J. Sugiyama. Mechanical behavior of cellulose microfibrils in tension wood, in relation with maturation stress generation. *Biophysical journal*, 91(3):1128–1135, 2006.

[65] J. R. Barnett and V. A. Bonham. Cellulose microfibril angle in the cell wall of wood fibres. *Biological reviews*, 79(2):461–472, 2004.

4

Microscopic characterization of self-growing connections

In Chapter 3, the macroscopic features of self-growing connections induced by adaptive growth were investigated. This chapter further studied the material composition of self-growing connections at the microscopic (i.e., tissue and cellular) level. The stem and fused regions were studied separately within a connection. The stem region was used to understand the basic tissues that make up the wood material. The fused region was studied according to different stages of fusion. This investigation was performed by digital optical microscopy with prepared glass slides.

This chapter provided evidence and support at the microscopic level to support the macroscopic observations in Chapter 3. In the inner part of a self-growing connection, it was observed that few continuous merged fibers were present, organized mainly by parenchyma cells. The merged fiber bundles were produced primarily in the outer layer of a connection and were characterized by deviated directions that connected two stems together. Tension wood with a G-layer and crystals within cells were observed in the fused region. The influence of tissue compositions on the mechanical capacity of a self-growing connection was further discussed.

4.1 Introduction

Trees demonstrate an adaptive response to external loads that can be examined from the molecular to the structural level. The macroscopic characteristics (density variations, geometric changes, and fiber structures) of self-growing connections have been investigated in Chapter 3. However, since wood is a highly hierarchical material, macroscopic features are integral features based on microscopic properties. For example, the high density of wood in a local region might result from the accumulation of wood cells with thick cell walls. Thus, this chapter explores the material compositions in deeper depth and performs the characterizations of self-growing connections at the microscopic level to support and explain the observations found at the macroscopic level. Based on the understanding from the micro-scale, we will discuss further how the identified features can potentially affect the mechanical properties (e.g., strength and stiffness) of a self-growing connection.

4.1.1 Hierarchical structure of wood

Numerous researchers have examined the hierarchical structure of wood for a long time [1–5]. As adapted in studies [2, 5] and presented in Figure 4.1, the hierarchical structure of wood can be divided into four levels, namely the macroscopic scale, microstructure, ultrastructure and molecular scale. The macroscopic level, including the tree and wood bulk (Figures 4.1 a and b) with a size of 10^{-2} m up to 100 m, representing the stem and branch of the tree, as well as processed wood products. Wood is made up of various types of tissue at the microscopic level (as in Figures 4.1 c and d), with a size range of 10^{-5} m to 10^{-1} m. The next scale represents the ultrastructure of the cell wall, with a size range of 10^{-8} m to 10^{-5} m. In the cell wall structure, it consists of primary and secondary cell walls. Within the secondary cell wall, it can be divided into three layers, namely S_1, S_2, and S_3, in which S_2 contributes the most to the mechanical strength of the cell wall. The chemical makeup of cell walls is described at the molecular level (Figure 4.1 g), which is typically between 10^{-10} m and 10^{-8} m in size.

The microfibril of wood is composed of three main chemicals, cellulose, hemicellulose, and lignin, in which cellulose contributes the most to the strength, especially tensile strength, of the wood material. As illustrated in Figures 4.1 f and g, at the molecular level, it can be considered that the cellulose fibers are reinforced by a matrix made of hemicellulose and lignin, organized into layers of cell walls with different percentages and volumes. For the growth of plants, various tissues structure and form themselves in a systematic way to perform various tasks. At every level of the structural hierarchy of wood, the complicated arrangement gives rise to a broad range of mechanical properties.

In nature, trees can develop adaptive growth in response to external and internal stresses, as reviewed in Chapter 3. The effects of adaptive growth are evident at every level of the hierarchical structure. Tension wood in angiosperms is a typical example of wood development from adaptive growth (Figure 3.2 g). At the molecular level, it is discovered that tension wood contains more cellulose in comparison to normal wood. One of the main predictors that tension wood is present, acknowledged by most scholars [6–8], is the production of G-layer (gelatinous fibers) at the microscopic level. When tension wood is produced, the geometry of the stem or branch generally appears in an oval shape.

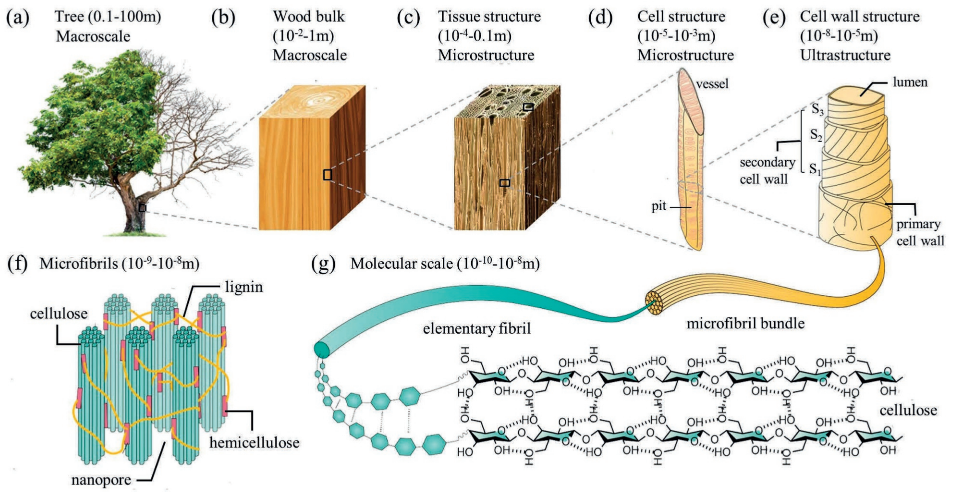

Figure 4.1: Hierarchical structure of wood. The macroscale of wood includes (a) the tree structure and (b) wood bulk and its products. (c) and (d) are the microstructure of wood that represents the tissue compositions and cell morphology. (e) The ultrastructure is the structure of cell wall layers. (f) and (g) represent the chemical and molecular compositions of microfibrils at the molecular level. Figure modified from [5].

4.1.2 Relation between microstructures and mechanical properties

In this chapter, the motivation for studying the microstructure of self-growing connections is to connect the relation between microcharacteristics (e.g., tissue type, fraction, and organization pattern) and mechanical properties (e.g., strength and stiffness).

To identify the microstructural characteristics of wood, depending on inspection resolution and desired information, common experimental techniques include optical microscopy, scanning electron microscopy, X-ray diffraction, and others [9]. Due to the size of the samples, it is challenging to conduct experimental studies on the mechanical characteristics of wood at the microscopic level. Additionally, separating the interactions of various tissues to examine the influence of each on mechanical properties is a challenge compared to experiments considering the scale of the tissues [10]. To understand the mechanical contribution of each tissue component, theoretical approaches have been developed, such as cellular theory [1, 11]. This theory simplifies the geometry of cells into a hexagon with different geometric parameters. Numerical analysis [12–14] has been incorporated with the facilitation of finite element analysis within the theoretical framework of the cellular structure. However, with regard to self-growing connections, a theoretical and numerical analysis cannot be performed without understanding of material compositions.

Regarding the mechanical contribution of specific tissues, Onoda et al. [15] discovered that although most species have a thick outer bark, including the phloem and cambium, the contribution of these tissues to the stiffness of the stem was minimal. Rays have been found to increase the mechanical rigidity of wood in the radial direction, due to their perpendicular alignment with the wood ring [16, 17]. At a constant overall density, vessels that form large conductor pipes and are designed for effective water transport reduce the stiffness of wood [17]. As illustrated in Figure 4.2, the mechanical stiffness and strength of wood are expected to decrease as a significant proportion of thin-walled parenchyma cells replace thick-walled fibers [1]. Fibers are considered the main component of tissue to provide stiffness and strength to the wood. However, there is approximately 10 times the difference between the strength parallel and perpendicular to the fiber direction, as shown in Figure 4.2. Therefore, anatomical characterization focuses on identifying the direction of the wood fibers and distinguishing the types and proportions of the composed tissues.

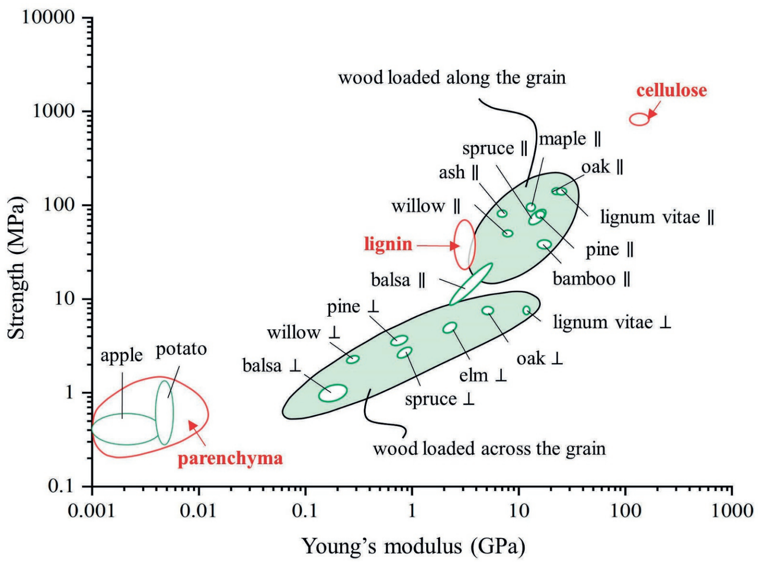

Figure 4.2: Strength plotted against Young's modulus for selected plant materials. Note the large range in properties produced by varying the arrangement of the three main building blocks (cellulose, hemicellulose and lignin) in the cell wall as well as the cellular structure. Figure adapted from Gibson et al. [1].

4.1.3 Fusion condition and stage

In Chapter 3, the merged fiber bundles were identified as the primary component to form a connection. The amount and distributive structure of this group of fibers has been associated with the condition of fusion. Additionally, the merged fibers are distributed in a pattern that can be related to the location of observation. Furthermore, the location of observation reflects the growth stage of a connection. Consequently, the characteristics of this group of fibers determine the mechanical strength and stiffness of a connection. This information can be referred to Figures 3.18. The focus of the study is on bundles of fibers, which does not consider detailed tissue organizations. However, at the microscopic level, discontinuities and inhomogeneities in the material affect the full realization of the mechanical properties of a connection.

To the best of the author's knowledge, relatively little study has been done on the anatomical analysis of fused living connections. The focus of this chapter is on anatomical examination of the self-growing connections of *Ficus benjamina* L. With this information, it is further to understand the tissue organization patterns of a self-growing connection and to compare the anatomical differences between the fused and stem regions. The mechanical properties that could be affected will be discussed on the basis of understanding of the tissue organizations within a self-growing connection.

4.2 Materials and methods

In Chapter 3, the study objects include both the braided tree structure and the self-growing connection. In this chapter, the study focuses only on the connection.

4.2.1 Sample description

As defined in Figure 3.4, a self-growing connection can be divided into stem and fused regions. Figure 4.3 separates the two regions further to give a detailed explanation. In Figure 4.3 a, the three viewing directions (x, y, and z directions) determine the observation cross sections within a self-growing connection, especially for the fused region.

In the stem region (Figure 4.3 b), the anatomy could be inspected in three sections, namely transverse (X), tangential (T) and radial (R) sections. To facilitate the identification of different tissues and provide more information, the clipping (C) cut was also made. In this cut, primarily the ray cells were shown in different appearances according to the angle of the clipping cut. Rays were usually produced in companion with fiber cells. In this way, depending on the appearance of the ray cells, the angle of the fibers surrounding them could be inferred. Figure 4.3 c shows the trimmed region of the intersected area from the scan results in Chapter 3. It was observed from the figure that the tissue types at the interface of a connection were difficult to distinguish from each other due to the limitation of the resolution. This also proved the necessity of investigating the fused region with a magnified optical microscope.

The stem region and fused region were studied separately in a self-growing connection. The stem region was used to understand the basic tissue components of the wood material. The fused region was studied by comparing anatomical organizations at different view locations. These locations represented different levels of fusion, as discussed in Chapter 3, Section 3.3.4. From understanding of the distribution of the merged fibers, it could be assumed that at the edge location of the fused region, the merged fibers were less than those near the center of the fused region.

4.2.2 Anatomical observation methods

In Figure 3.12, it was discovered that the fused fiber bundles spread mainly in the outer layer of the connection. This group of fibers was usually found to be produced mainly in the larger cross-angle of a connection. When viewed from three different directions (x, y, z viewing directions), the identification of the direction of the fibers involved identifying the original direction of the fibers from two stems, as well as the direction of the fused fiber at the interface. Furthermore, although observed in the same viewing direction, the cross sections exhibited a varied organizational pattern depending on the location of the

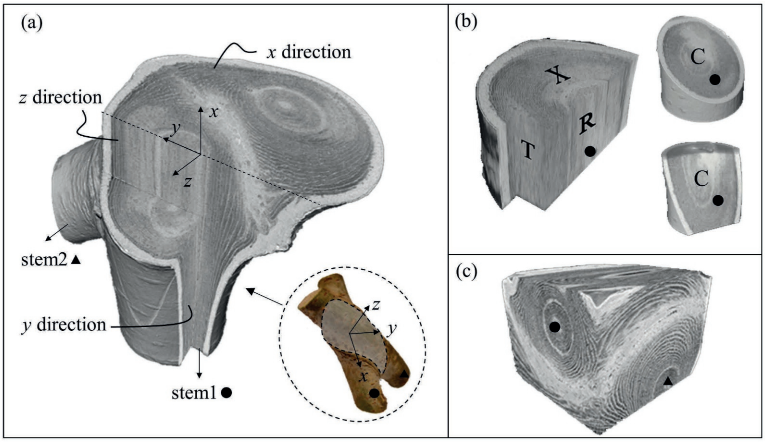

Figure 4.3: Internal structure, stem and fused regions of a self-growing connection. (a) The internal structures and cross sections in three (x, y, z) viewing directions; (b) the stem region, this region can be viewed from transverse (X) and longitudinal directions, including tangential (T) and radial (R) directions. Additionally, the clipping plane (C) is the fourth cutting direction. (c) The cropped fused region within a self-growing connection.

cut (e.g., in Figure 3.13 b). This pattern was thought to be related to the fusion stage. As sketched in Figure 3.5, the middle location of a fused region was considered to be in an older stage of fusion, which meant that this part had been growing longer and had deeper fusion than the other locations. At the periphery of the fused area, it was considered the early or young stage of fusion.

To this end, to understand the organizational patterns of tissues in different locations, as shown in Figure 4.4, a self-growing connection was cut into several partitions in the fused region. Figure 4.4 a was an example of a self-growing connection. In the viewing direction of y, the fused region was uniformly divided into six zones as in Figure 4.4 b. The cross sections obtained (Figure 4.3 c) in this viewing direction were made up of a longitudinal cut in stem1 and a clipped cut in stem2, with an unclear organization of tissues at the interface. Similarly, in the x viewing direction, six partitions were made evenly (Figure 4.4 d). The cross sections obtained in this direction were made up of the transverse cut of stem1 and the clipping cut of stem2. Thus, in z direction, the fused region of a connection was uniformly divided into 4 parts (Figure 4.4 e). The cross sections in z direction contained two longitudinal cuts in stem1 and stem2.

The thickness of each partition was determined to be approximately 5 mm. This was because in the subsequent process of making microscopic slices, for better observation, at least five slices were made in each partition. Because during the cutting process, two factors influenced the preparation of the slices with a complete cross section: (i) the bluntness of the cutting knife; (ii) the thickness of the cross section. From experience, when the thickness was set at 5 mm, sufficient slices could be prepared.

Therefore, 15 cross-wise connections from braided Tree_B and 15 cross-wise connections from Tree_S were chosen and cut for inspection. Tree_B and Tree_S were described

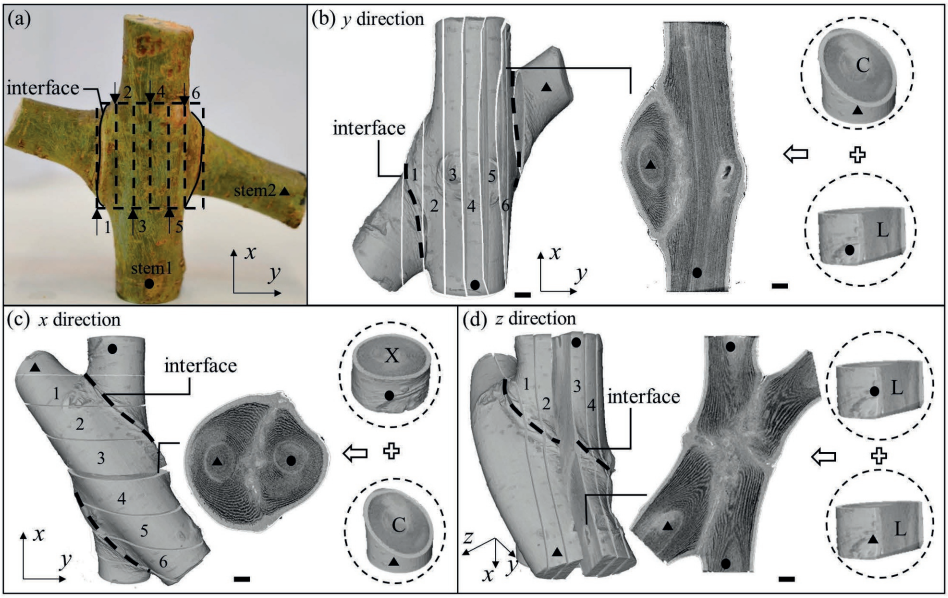

Figure 4.4: Anatomical analysis of self-growing connections: structural composition and division in x, y, z directions. (a) Example of a self-growing connection cut in y direction. (b) In the y cutting direction, within the fused region, the connection is divided uniformly in six zones. The cross sections exposed are composed of a clipping (C) cut in stem2 and a longitudinal (L) cut in stem1. (c) The six uniform partitions cut in x direction, where the cross sections are composed of a transverse (X) cut in stem 1 and a clipping cut in stem2. (e) The four uniform partitions cut in z direction, where the cross sections are composed of two longitudinal cuts in stem 1 and in stem2. Scale bar = 5 mm.

in Table 3.1. For three different evaluation directions (x, y, z directions), these connections were further separated into three groups, respectively. Thus, it had ten connections in each cutting direction. The study focused on investigating general and comparable patterns among connections because it was not possible to investigate a connection in three directions at once when performing destructive anatomical analysis. The generalized patterns in this chapter were considered to also apply to other connections.

4.2.3 Microscopic slides preparation

Glass slides for microscopic investigations were prepared according to the instructions [18]. All self-growing connections investigated in the chapter were in fresh condition, which meant that the anatomical study was performed immediately after the connection was cut out of the living braided tree structure. As listed in Table 4.1, in the stem region, 40 samples were prepared in total. Three cross sections, namely transverse, radial and tangential sections, were cut with a thickness of 20 μm.

In the fused region, as shown in Figure 4.5, a fresh connection was first cut and left only the fused region. The fused region was then mounted on a microtome (Leica Histocore, Germany) to prepare slices for specific uses. In the example of Figure 4.5 b, the connection was cut in the x direction based on the six divided zones. In each divided zone, eight slices were made as in Figure 4.5 c. The slices ranged in thickness from 35 to 45 μm. Table 4.1 provided information on the number of partitions in each direction and the number of slices prepared in each partition. Note that when the thickness of the microscopic slice was thin (less than 35 μm) in the connected region, it was very difficult to keep the slice intact. This was because this region contained a variety of tissues with varying hardness; for example, the xylem tissues were stiffer than the phloem tissues.

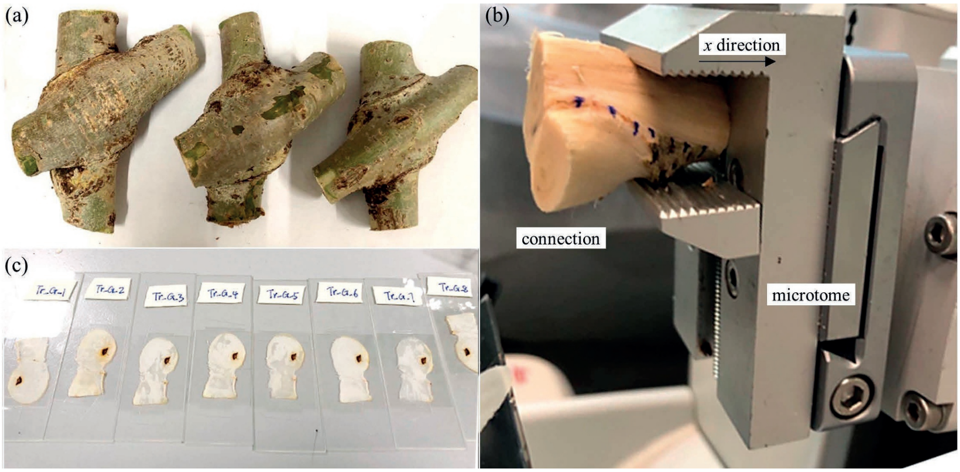

Figure 4.5: Preparation process of glass slides for microscopy. (a) Examples of self-growing connections; (b) the fused region mounted on the microtome for slicing; (c) glass slides prepared for microscopic observations.

Table 4.1: Preparation of microscopic slices: Cutting directions in the stem and fused region, the thickness and quantity of slices in a self-growing connection

Stem (40 samples)		**Connection** (10 samples for each direction)			
Cross section	Thickness (μm)	Cutting direction	Partition	Thickness (μm)	Number of slices in each partition
Transverse (X)	20	x direction	6	35 ~ 45	8
Radial (R)	20	y direction	6	35 ~ 45	8
Tangential (T)	20	z direction	4	50 ~ 60	5

Note: (1) Cutting cross sections for stems can be found in Figure 4.3.
(2) Cutting directions (x, y, z directions) for connections are referred to Figure 4.4.

After the slices were prepared, they were rinsed and dehydrated by a series of ethanol solutions (50%, 70%, and 90%) and then fixed to microscopic glass. They were then immediately examined under a microscope without being stained. The optical microscope (Keyence VHX7000, Germany) was used at magnifications from 20x to 2000x for characterization at different resolutions. Quantitative parameters such as vessel diameter, fiber diameter, wall thickness, and tissue proportions were studied in cross sections. The area fraction of a tissue was calculated by the ratio of the area of a tissue type taken up in the total inspected region. This analysis was carried out with Keyence communication software. Anatomical features were studied and quantified using the IAWA approach [19].

4.3 Results and analyses

4.3.1 Fundamental tissues in the stem region

Figure 4.6 gives an overview of the cross section of the stem. *Ficus benjamina* does not show distinct sapwood and heartwood. Bark tissues are easy to collapse when dried since most cells are thin-walled parenchyma cells and not fully lignified. Wood is diffuse porous without distinct growth rings. Instead, growth increments consist of fibers and banded parenchyma alternating with each other. Quantitative information about general characteristics, including the width of the bark, the cambium zone and growth increment, and the area fractions of each tissue, is listed in Table 4.2.

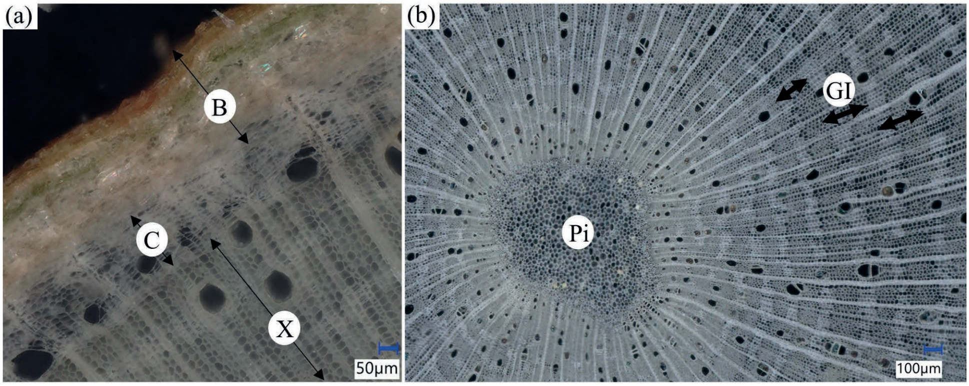

Figure 4.6: Anatomical overview of *Ficus benjamina* in cross-section of a stem, (a) in bark area and (b) in xylem (wood) region. Tissue types: Bark (B), xylem (X), cambium zone (C), growth increment (GI), and pith (Pi).

In three cross sections (transverse, tangential, and radial) in Figure 4.7, it can be seen that the vessels of the weeping figs are circular or oval in outline and mostly solitary or some in a radial multiple of two to four in the transverse section. The fibers that make up the ground tissue are square or polygonal in outline. The rays are multi-seriate. They are mostly heterocellular and composed of procumbent cells and square / upward cells. The banded parenchyma is present and the cells are brick-shaped. Sectional appearance in clipping planes is not presented in the main content; for further information, it can be referred to the Appendix B.

Morphological data is measured and recorded after identifying the qualitative characteristics of the tissue in the wood region. The characteristics of the fibers recorded included

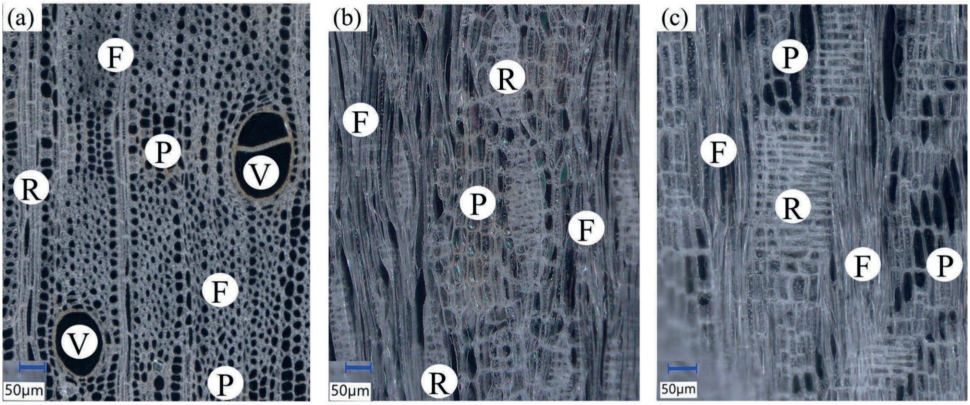

Figure 4.7: Cross-sectional appearance of a single stem. (a) Transverse section; (b) tangential cross section; (c) radial section. Tissue types: Fibers (F), parenchyma cells (P), rays (R), and vessel (V).

Table 4.2: Quantitative information about general features of wood in stem region

General information				
Region	Bark (B)	Cambium zone (C)	Growth increment (GI)	
N	20	30	49	
Width mean (CoV, %), μm	946.0 (6.0)	118.3 (18.4)	218 (21.1)	
Xylem				
N	30	30	30	30
Tissue	Fibers (F)	Parenchyma (P)	Rays (R)	Vessel (V)
Area proportion mean (CoV, %), %	46.3 (18.1)	31.7 (15.2)	10.0 (20.2)	12.0 (12.0)

Note: N stands for counting numbers.

cell size, length, and thickness of the cell wall. Rays are measured in radial and transverse sections. The height and diameter of a fusiform formed by the accumulation of ray cells in radial sections are measured. In addition, the thin cell wall thickness is measured in the transverse sections. The vessels are only measured in diameter. The cell wall thickness and dimension of the brick-shaped axial parenchyma cells in the xylem are measured in three orientations. Table 4.3 shows the morphological information on each tissue cell.

4.3.2 Tissue organizations in the fused region

At the periphery locations in x, y, and z directions as well as in the center of the fused region in x direction, patterns of tissue organization are shown in the fused area. Cross sections between the edge and middle locations are appended in Appendix B. Additionally, some anatomical changes at the cellular level are presented in this section.

Table 4.3: Morphological statistics of cells (fiber, ray, vessel, and parenchyma) in xylem

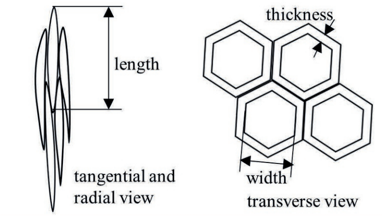

Fiber			
Dimension	Width	Thickness	Length
N	103	121	50
Mean (μm)	12.4	3.2	255.9
CoV(%)	30.1	17.2	17.4

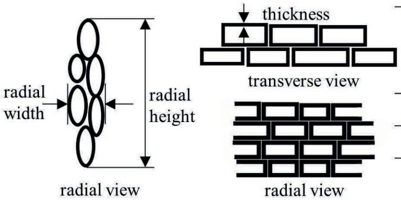

Ray			
Dimension	Thickness	Radial width	Radial height
N	50	50	50
Mean (μm)	2.5	33.1	246.6
CoV(%)	20.0	31.3	24.8

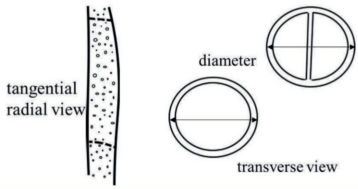

Vessel	
Dimension	Diameter
N	50
Mean (μm)	60.8
CoV(%)	25.7

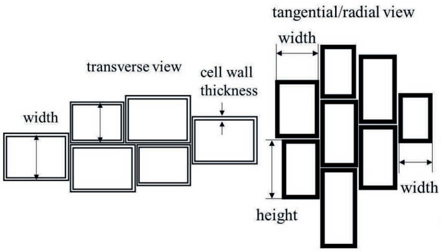

Parenchyma				
Dimension	Width in transverse view	Cell wall thickness	Height in tangential/ radial view	Width in tangential/ radial view
N	50	50	50	50
Mean (μm)	18.9	2.2	50.8	16.0
CoV(%)	19.6	17.1	19.1	23.0

Note: N stands for counting numbers.

Edge location in the fused region

The tissues in the periphery in the x direction are shown in Figure 4.8. This location is taken in the first partition within the fused region, as shown in Figure 4.4 d and Figure 4.8 a. The slice made for this location is shown in Figure 4.8 b. The tissue organizations at this location are zoomed in in Figure 4.8 c. The interface at this location is found to consist primarily of bark tissues. When this region is exposed to the room environment, the tissues in this area are easy to wrap and shrink, and consequently prone to cracking. The direction of the fibers is further identified. However, only parallel fibers are easy to identify, marked as $F_{\parallel}$. Inclined fibers (F_{α}) are mainly identified based on the appearance of the rays around them. Compared to the direction of the fiber in stem1, stem2 and the intersected region in Figures 4.8 b and c, when the fibers are close to the interface, the direction of the fibers in stem1 changes from the perpendicular direction to the parallel direction.

Figure 4.9 provides two other locations in y and z directions to show how tissues connect and organize in the periphery location. The locations presented correspond to the first partition in Figures 4.4 b and e. Similarly to Figure 4.8, the bark and parenchyma tissues make up the most connected space at the intersection. A few fibers are spotted, but they are not continuously connected between two stems. The interface is the location where the fibers deviate and extend from one stem to the other stem.

Middle location in the fused region

The anatomical characteristics of the middle location are presented in the fourth partition of Figure 4.4 d in the x direction. The cross-sectional appearance at locations of y and z directions can be found in Appendix B for more information. As shown in Figure 4.10 b, four local areas are taken in the cross section and zoomed in for further research. In local areas, Figures 4.10 c and f, peripheral regions are chosen. In this area, tissues are observed to be continuously organized and free of flaws. Fibers that smoothly transfer from one stem to the other stem are marked by the dashed line in Figure 4.10.

When comparing the outer locations (Figures 4.10 c and f) with the inner locations (Figures 4.10 d and e), the tissues in this inner region are less organized and the fiber bundles do not show a continuous merged pattern. Furthermore, this region is made primarily of bark parenchyma tissues, which are easy to crack when the sample is dehydrated.

Fused fiber bundles

As illustrated in Figure 4.10, continuous and merged fiber bundles are produced primarily in the outer part of a cross section. The magnified regions in the middle of a fused region in the other two directions are shown in Figure 4.11 to provide more details on the fused tissue bundles. The locations in Figures 4.11 a and b correspond to the third partitions in Figures 4.4 b and e. The shifting orientations of the fibers are marked in dashed lines. This outer layer in the middle is characterized by continuous and structured tissues free of flaws.

4.3.3 Cellular changes in the fused region

Crystals in parenchyma cells can be seen under the polarized light of a microscope. Bright particles in parenchyma cells are clearly visible in the intersected region in Figures

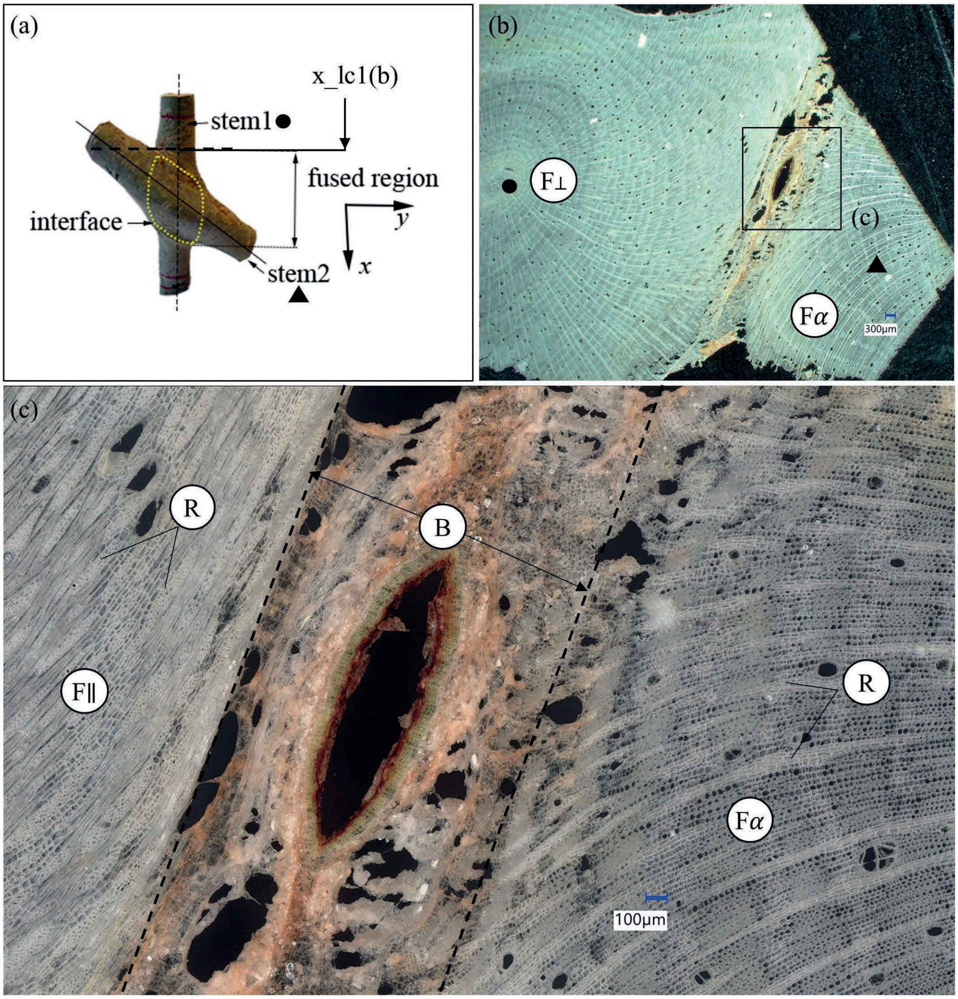

Figure 4.8: Tissue organization at the edge location of the fused region in x direction. (a) The inspection location (x_lc1) in a connection; (b) cross-sectional appearance of the inspected section, where the rectangular is magnified for further examination in (c). Tissue types: Fibers (F), parenchyma cells (P), rays (R), and vessel (V). Parallel fibers are marks as $F_{\parallel}$, inclined fibers are F_{α}. The angle reference is the plane of the paper.

4

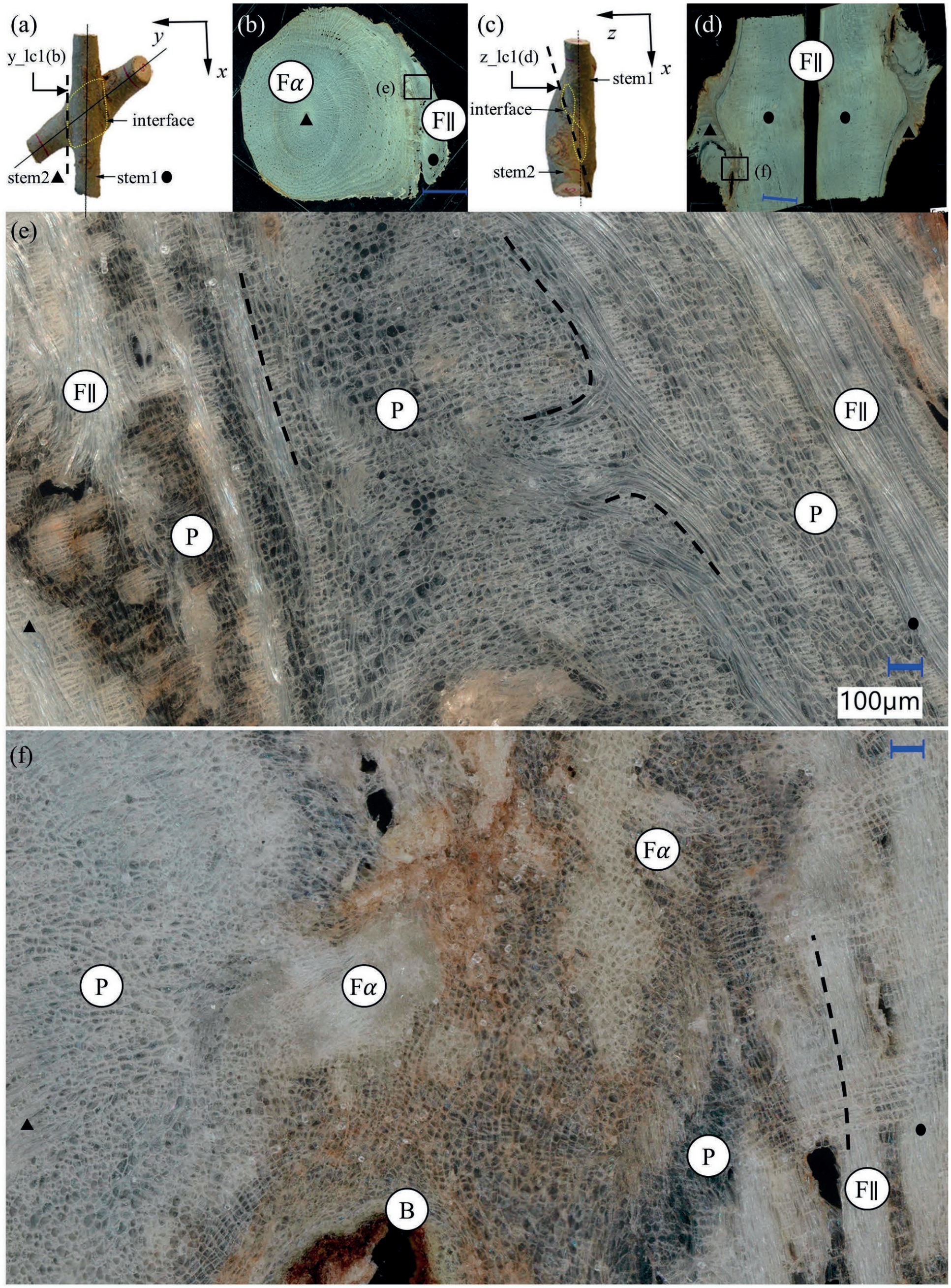

Figure 4.9: Tissue organization at the edge location of the fused region in y and z direction. (a) The inspection location y_lc1 in a connection; (b) cross-sectional appearance at location y_lc1, where the rectangular area is magnified for further examination in (e). (c) The inspection location z_lc1 in a connection; (d) cross-sectional appearance of the inspected section at z_lc1, where the rectangular area is magnified for further examination in (f). Tissue types: Fibers (F), parenchyma cells (P), rays (R), and vessel (V). Parallel fibers are marks as $F_{\parallel}$, inclined fibers are F_{α}. The angle reference is the plane of the paper. Dashed lines indicate the fiber directions.

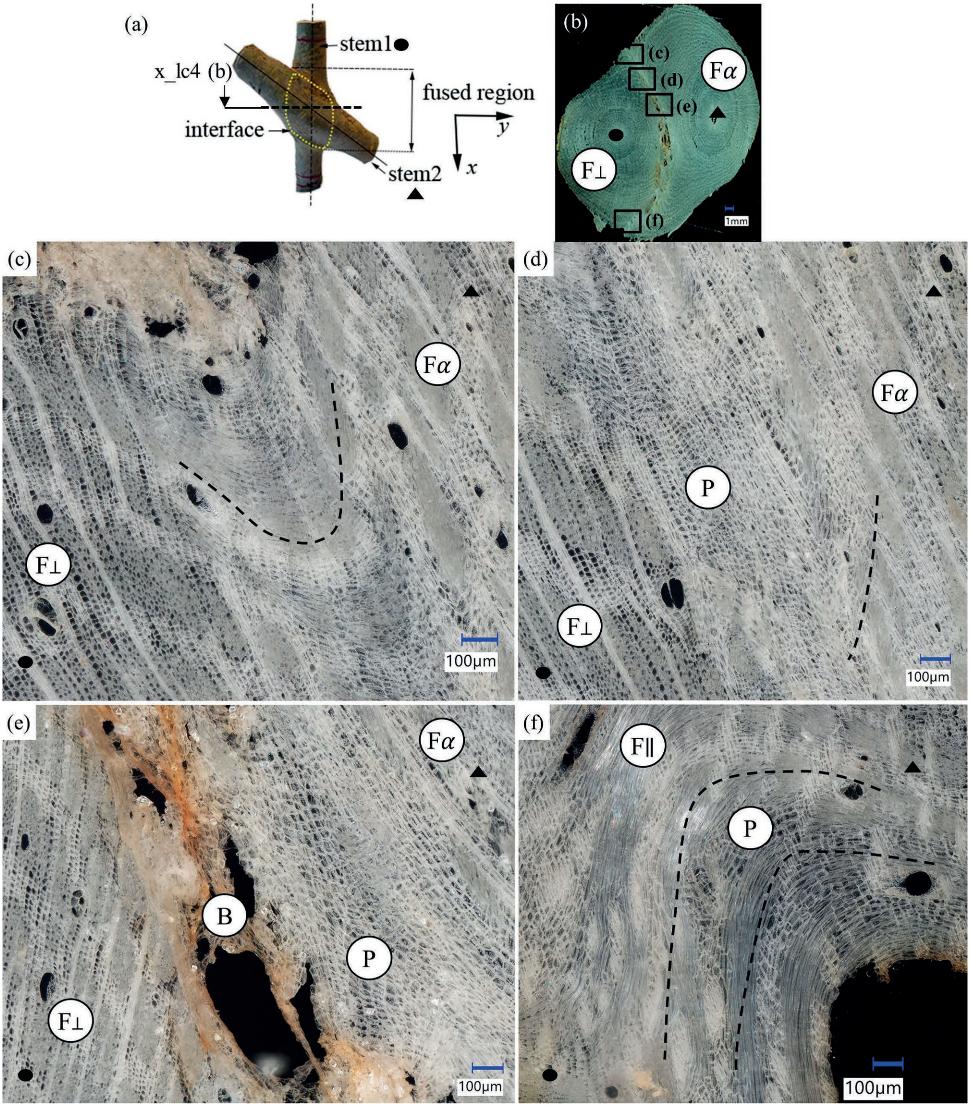

Figure 4.10: Tissue organization at the middle location of the fused region in x direction. (a) The inspection location (x_lc4) in a connection; (b) cross-sectional appearance of the inspected section, where the rectangular area is magnified for further examination in (c), (d), (e) and (f). Tissue types: Fibers (F), parenchyma cells (P), rays (R), and vessel (V). Parallel fibers are marks as $F_{\parallel}$, perpendicular fibers are $F_{\perp}$, inclined fibers are F_{α}. The angle reference is the plane of the paper.

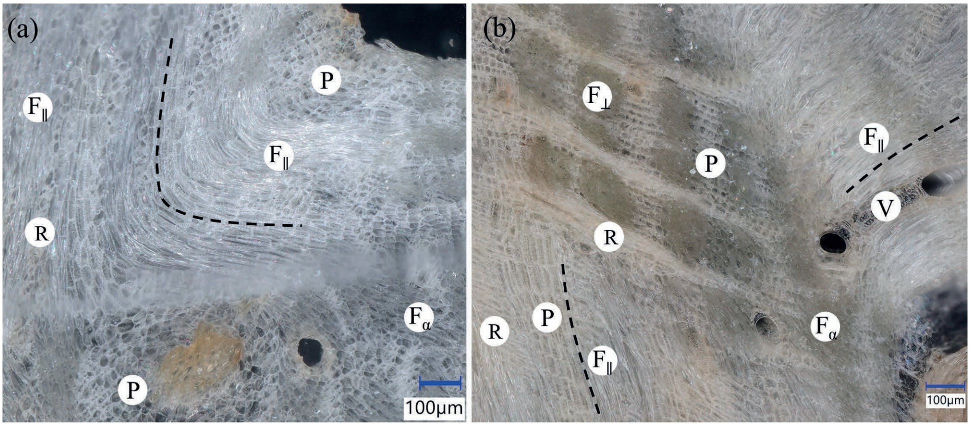

Figure 4.11: Continuous merged fiber bundles in the outer layer of a connection. Fused fiber bundles in the middle location of the outer layer of a cross section (a) from y direction, and (b) from z direction. Tissue types: Fibers (F), parenchyma cells (P), rays (R), and vessel (V). Parallel fibers are marks as $F_{\parallel}$, inclined fibers are F_{α}. The angle reference is the plane of the paper.

4.8, 4.9, and 4.10. To examine these traits more closely, Figure 4.12 shows the detailed features of the crystals in the intersected region.

In addition to the crystals found at the interface, tension wood is also spotted according to the description in [8]. In Figure 4.13, it is easy to detect fiber cells with a G-layer in the intersected area following the direction of the arrows.

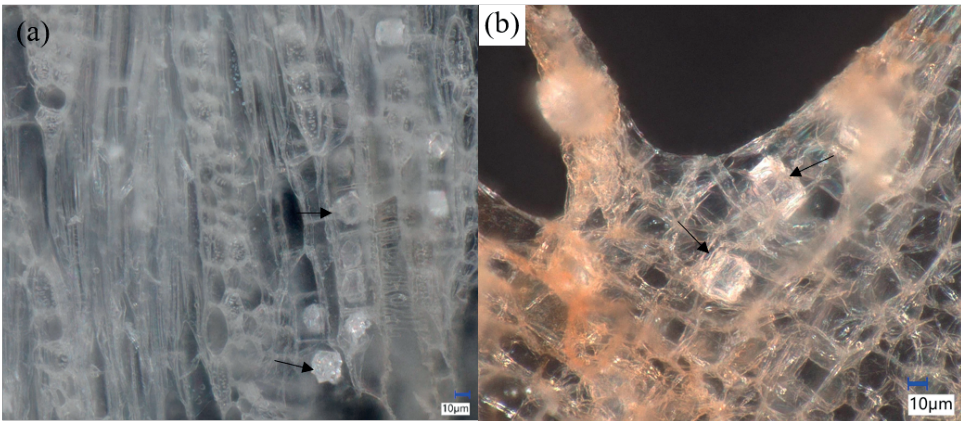

Figure 4.12: Crystals identified in the fused region. Black arrows point to the formed crystals.

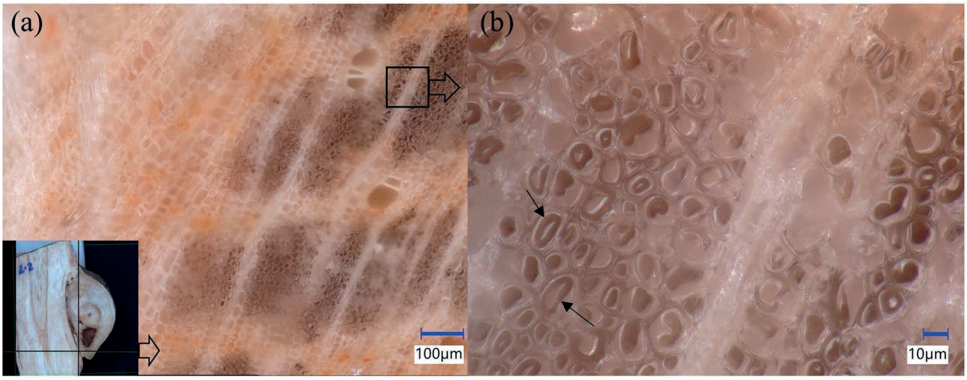

Figure 4.13: Tension wood in the fused region. (a) Intersected region, where the region outlined by the black rectangle is magnified in (b).

4.4 Discussion

4.4.1 Hierarchical changes from cells to tissue patterns

The mechanism of adaptive growth was reviewed and explored with reference to studies on thigmomorphogenesis in Chapter 3. Changes in tissues during the process can be referred to early work by Rao [20]. Additionally, changes in the chemical composition and ultrastructural level are not covered. In other words, the impact of the chemical fractions that affect the microfibril angle is not taken into account.

At the cellular level, the presence of crystals, G-layers, and deviated fibers is found, see Figures 4.12, 4.11 and 4.13. With respect to the presence of crystals, *Ficus* species have evolved physical or chemical defense mechanisms to cope with a variety of conditions and pests. The development of minerals is the foundation of physical defenses [21, 22]. The mineral crystal that is formed the most frequently in the *Ficus* family is the calcium oxalate crystal [22]. Thus, cystals identified in this work might be a type of calcium oxalate crystals in reaction to physical activities. However, the chemical compostion and relevant mechanism need to be investigated further.

The formation of tension wood is mainly due to the stresses experienced by the local wood [23]. It is signalled by the presence of G-layers, as described in [8]. In response to internal and external stresses at the interface during the fusion process, the presence of tension wood proved the physical interaction between growth and conditions.

In the work by Hamant et al. [24], the cell development pattern is related to experienced stresses. The elongation of the cell growth axis follows the direction of maximum principal stress. When this is taken into account, the deviation fiber bundles between two stems might depend on the stress state in the fused region. Another statement is that the direction is controlled by the auxin gradients within the stem [25]. This statement is explained from the hydraulic function of a tree based on the theory of fluid dynamics. The most likely possibility could be the interaction and trade-off between multiple functions: transportation of water and nutrition, growth and evolution, and mechanical supports. The formation and development of the fiber pattern need to be studied from different disciplines and perspectives.

4.4.2 Relationship between tissue organizations and mechanics

In the periphery of the fused area, soft tissues are spotted, which have little mechanical strength and stiffness as reviewed in the introduction (Figure 4.1), as seen in Figures 4.8 and 4.9. When there is a lack of water, this area is prone to cracking and shrinking. In the middle section (Figures 4.10 d and e) of the fused region, this area is made up of a combination of parenchyma cells, bark, and fewer continuous fiber bundles. In contrast, continuous fiber bundles are detected in the outer layer, as shown Figures 4.10 c and f, as well as Figure 4.11. This group of fibers plays an important role in connecting two stems and is assumed to mainly contribute to the overall mechanical properties of the connection.

The extent to which two stems fused together is described in this work by the terms 'fusion degree' and 'fusion stage'. The existence of a shared cambium region, from which merged fiber bundles emerge, indicates the fusion of two stems. The young fusion stage is used to describe stems that have freshly fused bark and that have an appearance similar to that of the periphery of the fused region. When additional fused fiber bundles are seen in the outer layer of the middle region, where the two stems are first touched, it is thought to be an older stage of fusion. The degree of fusion is related to the mechanical strength of the section. Smooth and continuous fiber bundles in the outer layer are a sign of good fusion quality.

Another observed feature is that the growth increment gets narrower the closer it gets to the crossed area. In Chapter 3, it was discovered that the fused region had a higher density than the stem region, which may be related to the narrow growth increment. However, more research is needed, for example, to quantify the size of cells close to the interface.

4.5 Summary of microscopic characteristics of self-growing connections

The analysis of the microscopic features of self-growing connections is summarized in this section, which provides the basis for the mechanical analysis in Chapter 5. Table 4.4 summarizes the results observed at the microscopic level. Compared to macroscopic features, microscopic features are difficult to measure when the study is performed at the connection level to explain the macrophenomena.

Together with the conceptual model illustrated in Figure 3.19, the complete characterization of a self-growing connection can be understood. From both Tables 3.2 and 4.4, it can be inferred that the most important component within a connection for its mechanical properties are the merged fiber bundles. When the connection is subjected to out-of-plane tensile forces, the amount and direction of the merged fibers determine its loading response. Therefore, in Chapter 5, two parameters are proposed to quantify merged fibers, namely fusion degree and the interface curvature, which will be explained in Section 5.2.

Table 4.4: Microscopic characterization of self-growing connections

Studied aspects	Remarks	Mechanical influences
Outer merged fiber bundles	- Continuous fibers are mostly organized in the outer layer. - Less continuous merged fibers are seen in the inner area of the fused region. (Figure 4.10 and 4.11)	It supports the statement that the structural integrity and mechanical properties of a connection are determined by the group of merged fibers.
Inner soft tissues	- Bark tissues are identified in the inner area of the fused region. (Figure 3.11 and 4.10)	This area can be considered as imperfections that diminish the mechanical strength.
Edge soft tissues	- Few merged fibers emerge at the edge location in the outer layer. (Figure 4.8 and 4.9)	This area can be regarded as imperfections that reduce the mechanical strength.
Tension wood	The over-grown wood in the fused region is identified as tension wood, characterized by the presence of G-layers. (Figure 4.13)	Tension wood is considered to have high tensile strength.

4.6 Concluding remarks

Microscopic features of self-growing connections have been characterized in this chapter. The purpose is to understand and compare the organization of the tissue in the stem region and the fused region of a self-growing connection, thus analyzing the potential mechanical behavior. The tissue patterns and potential influence are identified and generalized as follows.

1. At the cellular level, crystals and tension wood characterized by G-layers are found in the fused region, which might reflect the mechanical stress the interface has experienced.
2. At the periphery of the fused region of a self-growing connection, the interface is mainly made up of bark tissues.
3. Continuous merged fibers are primarily produced in the outer layer of a connection and are characterized by deviated directions joining two stems together.
4. In the inner part of a connection, fewer continuous merged fibers are found, mainly organized by parenchyma cells.

This chapter provides some evidence at the microscopic level to support the conceptual model (Figure 3.18) proposed in Chapter 3. The relation between the location of the observation and the amount of merged fibers is further discussed. It shows that by observing at a certain location, the growth condition of a self-growing connection can be evaluated. This provides the possibility of evaluating the fusion condition of a connection with minimal damage, which will be discussed in Chapter 5.

4

References

[1] L. J. Gibson. The hierarchical structure and mechanics of plant materials. *Journal of The Royal Society Interface*, 9:2749–2766, 2012.

[2] T. Speck and I. Burgert. Plant stems: Functional design and mechanics. *Annual Review of Materials Research*, 41:169–193, 2011.

[3] K. de Borst, T. K. Bader, and C. Wikete. Microstructure–stiffness relationships of ten European and tropical hardwood species. *Journal of Structural Biology*, 177:532–542, 2012.

[4] L. Salmén. Micromechanical understanding of the cell-wall structure. *Comptes Rendus Biologies*, 327:873–880, 2004.

[5] C. Chen, Y. Kuang, S. Zhu, I. Burgert, T. Keplinger, A. Gong, T. Li, L. Berglund, S. J. Eichhorn, and L. Hu. Structure–property–function relationships of natural and engineered wood. *Nature Reviews Materials*, 5(9):642–666, 2020.

[6] W. A. Côté, A. C. Day, and T. E. Timell. A contribution to the ultrastructure of tension wood fibers. *Wood Science and Technology*, 3(4):257–271, 1969.

[7] T. E. Timell. The chemical composition of tension wood. 1969.

[8] J. Ruelle. Morphology, anatomy and ultrastructure of reaction wood. 2014. Pages 13-35.

[9] E. Toumpanaki, D. U. Shah, S. J. Eichhorn, E. Toumpanaki, S. J. Eichhorn, and D. U. Shah. Beyond what meets the eye: Imaging and imagining wood mechanical–structural properties. *Advanced Materials*, 33:2001613, 2021.

[10] H. C. Spatz, L. Köhler, and K. J. Niklas. Mechanical behaviour of plant tissues: composite materials or structures? *Journal of Experimental Biology*, 202:3269–3272, 1999.

[11] L. J. Gibson. Biomechanics of cellular solids. *Journal of Biomechanics*, 38:377–399, 2005.

[12] A. Bergander and L. Salmén. Cell wall properties and their effects on the mechanical properties of fibers. *Journal of Materials Science*, 37:151–156, 2002.

[13] S. Malek and L. J. Gibson. Multi-scale modelling of elastic properties of balsa. *International Journal of Solids and Structures*, 113-114:118–131, 2017.

[14] C. S. Modén and L. A. Berglund. Elastic deformation mechanisms of softwoods in radial tension - cell wall bending or stretching? *Holzforschung*, 62:562–568, 2008.

[15] Y. Onoda, A. E. Richards, and M. Westoby. The relationship between stem biomechanics and wood density is modified by rainfall in 32 Australian woody plant species. *New Phytologist*, 185:493–501, 2010.

[16] I. Burgert, A. Bernasconi, K. J. Niklas, and D. Eckstein. The influence of rays on the transverse elastic anisotropy in green wood of deciduous trees. *Holzforschung*, 55: 449–454, 2001.

[17] K. De Borst and T. K. Bader. Structure–function relationships in hardwood – insight from micromechanical modelling. *Journal of Theoretical Biology*, 345:78–91, 2014.

[18] J. C. Tardif and F. Conciatori. Microscopic examination of wood: Sample preparation and techniques for light microscopy. In *Plant microtechniques and protocols*, pages 373–415. Springer, 2015.

[19] E. A. Wheeler, P. Baas, and P. E. Gasson. IAWA list of microscopic features for hardwood identification. 1989.

[20] A. N. Rao. Developmental anatomy of natural root grafts in *Ficus globosa*. *Australian Journal of Botany*, 14(3):269–276, 1966.

[21] J. W. Hudgins, T. Krekling, and V. R. Franceschi. Distribution of calcium oxalate crystals in the secondary phloem of conifers: A constitutive defense mechanism? *New Phytologist*, 159:677–690, 2003.

[22] M. Pierantoni, R. Tenne, B. Rephael, V. Brumfeld, A. van Casteren, K. Kupczik, D. Oron, L. Addadi, and S. Weiner. Mineral deposits in ficus leaves: Morphologies and locations in relation to function. *Plant Physiology*, 176:1751–1763, 2018.

[23] M. H. Zimmermann, A. B. Wardrop, and P. B. Tomlinson. Tension wood in aerial roots of *Ficus benjamina* L. *Wood Science and Technology 1968 2:2*, 2:95–104, 1968.

[24] H. Morris, M. A. F. Gillingham, L. Plavcova, S. M. Gleason, M. E. Olson, D. A. Coomes, E. Fichtler, M. M. Klepsch, H. I. Martínez-Cabrera, and D. J. McGlinn. Vessel diameter is related to amount and spatial arrangement of axial parenchyma in woody angiosperms. *Science*, 322:1650–1655, 2008.

[25] E. M. Kramer. Wood grain pattern formation: A brief review. *Journal of Plant Growth Regulation*, 25(4):290–301, 2006.

5

Biomechanical properties of the self-growing connection

This chapter focused on the study of the tensile out-of-plane properties of self-growing connections based on the knowledge obtained from the macroscopic and microscopic characterizations in Chapters 3 and 4. This study consisted of several steps, which included quantifying the influencing factors, designing and performing tensile out-of-plane tests, analyzing the correlation between the influencing factors and the mechanical properties, and establishing a predictive model to estimate the strength of a connection.

In order to describe the fusion level of a self-growing connection, fusion degree and interface curvature were first proposed and defined. In addition, other parameters that can influence the mechanical performance of a connection were quantified, including density, moisture content, diameter, cone ratio, and cross-angle. The calculated mechanical properties of a connection included tensile strength, stiffness, and load-carrying capacity.

The results showed that the average diameter of a connection had a strong positive correlation with its tensile strength and stiffness. The interface curvature had a negative and moderate correlation with the strength. The fusion degree was used to distinguish the failure modes of connections. When the fusion degree was greater than approximately 15%, the connection failed in the shape of 'Y', otherwise the failure occurred at the interface. The predictive model to estimate the tensile strength of a connection was established based on the approach of an artificial neural network.

5

5.1 Introduction

The self-growing connection, as a basic structural element, can be used to form many different types of living structure, such as a chair (Figure 1.2 c) and a living root bridge (Figure 1.2 d). The fused living structure has three main advantages compared to traditional structures such as those made of wood, concrete, and steel.

1. Pure nature. This living structure is made exclusively from natural materials, which makes it not only sustainable but also capable of absorbing carbon dioxide during its growth.

2. Growth potential. As a tree progresses from a juvenile to a mature state, the mechanical properties of the wood undergo significant changes. Research has indicated that juvenile wood exhibits lower density and modulus of elasticity when compared to mature wood [1]. During this growth process, the geometry of the structure also expands as wood accumulates, resulting in increased stem stiffness. Therefore, with the increased strength and stiffness resulting from dynamic growth, tree structures can support higher loads and reduce corresponding load deformations.

3. Self-optimization. An additional advantage of this living structure lies in its adaptive nature, which allows it to modify its fiber structure and optimize material properties in response to changes in external loads.

4. Contribution to urban envrionment. Tree structures can utilize canopy space, increasing available space and contributing to urban greening and space utilization.

However, fused living structures also have some drawbacks as in the following.

1. Time consuming. Trees grow slowly, which requires a significant amount of time for structures to form.

2. Structural safety and stability. Living structures are susceptible to weather and tree growth, especially in the early stage of fusion, which can compromise stability and require special attention to safety.

3. Maintenance challenges. Living structures require regular maintenance, such as pruning and pest control, which results in high maintenance costs.

4. Limitations in design and applicability. The design of tree structures is constrained by the growth of the tree, which may not meet all design requirements. Tree structures may not be suitable for all environments and applications, which requires evaluation and selection based on specific circumstances.

Nevertheless, the application of self-growing connections and living structures in the field of engineering structures has not yet been explored. Before the start of this study, the available studies were limited mainly to observational records [2] and qualitative analyses [3, 4] of the natural phenomenon from the fields of horticulture and architectural design. In recent years, some studies [5, 6] have been carried out to explore the biological and mechanical properties of living structures. However, to the best of the author's knowledge, few have analyzed the correlation between fusion characteristics and mechanical properties of living structures and further explored the structural value. The existing groundwork and progress in this direction are limited and thus have posed challenges in both the experimental testing and theoretical development.

The mechanical loading cases are categorized into two groups, namely in-plane loading and out-of-plane loading, as defined in Figures 3.4 c and d. The plane refers to the projected interface to the defined plane xy at the local coordinate. As discussed in Section 1.2.3, the interface of the self-growing connection is the most critical and vulnerable area in the natural environment, especially with regard to the interface's ability to withstand perpendicular tensile and shear forces. This chapter focuses on the study of the tensile perpendicular situation, which is the out-of-plane loading in Figure 3.4. The applied loads focus on the tensile forces on the interface. In other words, the mechanical properties of the connection include the tensile strength, stiffness, and load-carrying capacity under tension. However, to fully understand the biomechanical performance of a connection, there are still some gaps. For example, it is not clear how to obtain and analyze the mechanical properties of a connection. Meanwhile, no method has been developed to measure and quantify the growth characteristics of a connection. Therefore, this chapter is organized into five steps with the motivation to measure, analyze, and predict the performance of a self-growing connection.

1. Quantify and measure parameters that can describe the level of fusion and have effects on mechanical properties.

2. Design tensile out-of-plane experiments to obtain the mechanical performance of the self-growing connection.

3. Determine and analyze mechanical properties, including tensile strength, stiffness, and load-carrying capacity.

4. Understand the correlation between the measured influencing parameters and the mechanical properties.

5. Construct a model to predict the strength of a self-growing connection.

In the first step, quantification of fusion related parameters is based on the macroscopic features in Chapter 3, Section 3.5, as well as microscopic features in Chapter 4, Section 4.5. Through the second and third steps, the mechanical properties of the connections can be obtained. These parameters can be analyzed as the output variables influenced by the quantified input parameters from the first step. Therefore, in the last step, on the basis of the input and output variables, the tensile strength of a connection is predicted using the artificial neural network (ANN) approach. How the tensile experiments are designed and how the ANN approach is implemented will be elaborated in Section 5.2.

5.2 Materials and methods

5.2.1 Braided tree structures and self-growing connections

In this chapter, the braided tree structures and connections of each tree structure were the two levels of samples for measurements. The braided tree structures were fused with weeping figs (*Ficus benjamina* L.). The braided pattern was planar as shown in Figure 3.3 b. A detailed description and definitions of braided tree structures could be found in Section 3.2.2. Mechanical tests were performed at the connection level. However, from one braided tree structure, it provided approximately 20 connections suitable for tests. To add more variations to the dataset (for example, different diameters), nine braided tree structures with different net sizes were used.

A braided tree structure could be divided into three regions, namely the canopy, net, and pot regions, as seen Figure 5.1 a. Front and side views of the braided tree structure can be found in Figures 5.1 a and b. In one braided tree structure, six stems were braided in pairs. Self-growing connections were created along the stem at intervals ranging from 50 to 200 mm. Table 5.1 provided basic details on the braided tree structures. The size of the braided tree structure was described by its full height and net size. The width of the net was measured between the outmost locations of the planar net. The net height was measured between the basal location of the stem and the upper location of the first branch. The small braided tree structures had a relatively smaller net size and mean stem diameters (approximately 16 mm). On the contrary, large braided tree structures had larger mean stem diameters (greater than 20 mm).

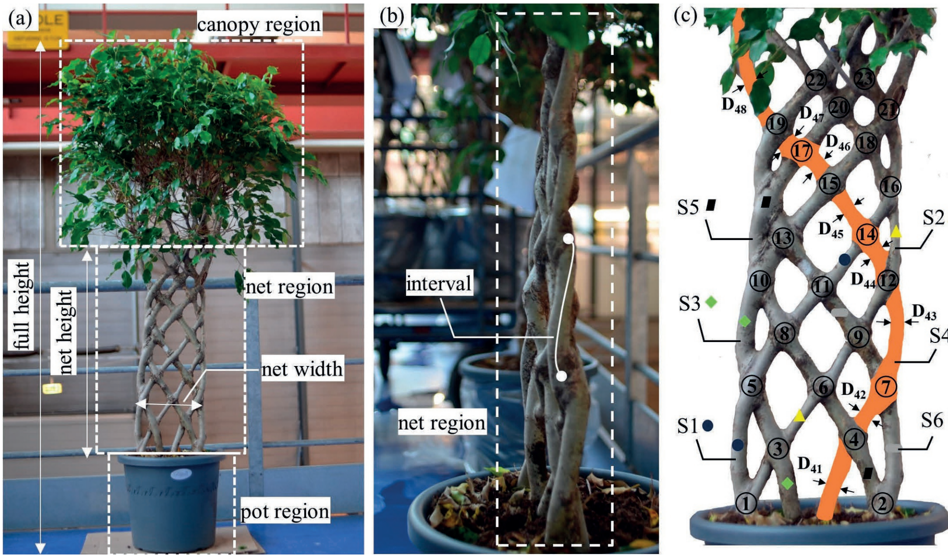

Figure 5.1: Illustration of braided tree structures and measured information. (a) Front view of a braided tree structure (Tree C); (b) side view of Tree C; (c) labels of connections and measured locations along stems.

As shown in Figure 5.1 c, in the braided tree structure C (Tree C), the stem was labeled in order from left to right. For example, the stem on the left side was labeled stem 1 (S1). Thus, self-growing connections were labeled in order from left to right and bottom to top. The labeling rule was similar to the description in Section 3.2.4. In this case, along stem 4 (S4 in orange), seven connections were formed, which included connections 4, 7, 12, 14,

Table 5.1: Morphological information of investigated braided tree structures

General description		Six stems braided in pairs into a planar net.			
		Connections are created at every 100-200 mm interval for big-sized braided tree structures, and 50-150 mm interval for small-sized braided tree structures.			
General information	**ID**	**Full height (mm)**	**Net size**	**Number of total connections**	**Number of connections tested**
Small-sized braided tree structures	Tree A1	1200-1300	net width 200-250 mm net height 600-650 mm	18	3
	Tree A2			20	3
	Tree B1			17	6
	Tree B2			21	6
Big-sized braided tree structures	Tree C	1800-2000	net width 300-350 mm net height 800-850 mm	23	14
	Tree D			22	16
	Tree H			26	18
	Tree I			25	18
	Tree K			27	18
Total	9	-	-	-	102

15, 17, and 19. C4 was an abbreviation for Connection 4 in Tree C. Within a braided tree structure, not all connections were suitable for testing; for example, connections 10 and 13 in Tree C, these connections were filtered out. In total, 102 connections were harvested from the prepared braided tree structures.

5.2.2 Measurements of braided tree structures

In Section 3.3.2, the results showed that the formation of connections along the stem greatly influenced the diameter of the stem. Furthermore, each connection in the braided tree structure had its spatial location. The consideration of spatial location was prompted by two key factors. In general, first, along the height of individual tree stems, the growth distribution and biomass allocation were considered different. As a result, the overall shape of the stem was considered parabolic with the oldest cambium age in the basal area [7, 8]. The second point was to consider the process of braiding the self-growing connection into a braided tree structure. The process might be carried out gradually from the bottom row of connections to the top row as the stems grew vertically. These two factors might result in the fact that self-growing connections in different spatial locations had different material properties and fusion conditions. For example, in Figure 5.1 c, connection 15 was at a higher location than connection 4. This spatial difference might influence its growing properties (e.g. density) and fusion condition. However, in studies [7, 8], it was also argued that in the branch-free stem, the growth distribution in the stem would be the same. The samples studied in this chapter considered connections below the canopy and within the branch-free area to avoid growth influences due to branches, i.e., in the net region in Figure

5.1 a. To this end, the location of each self-growing connection was recorded, but the variations caused by different spatial locations were not further analyzed in the results.

In addition to recording spatial locations, the diameter variation along the stem was also measured in the braided tree structure. In addition, the taper ratio of each stem was calculated. The taper ratio was calculated as the diameter ratio of the stem between the diameter of the last interval and that of the first interval. To be specific, in Figure 5.1 c, eight intervals were divided by seven connections. The diameter of each interval was measured at its middle location. In this case, eight diameters were obtained. The taper ratio was the division of the diameter of the eighth interval (D_{48}) and that of the first interval (D_{41}).

The schematic illustration of Tree C, along with the changes in diameter, was shown in Figure 5.2. The spatial location and origin of the stems of each connection were noted in Figure 5.2 a. Variations in diameter in each stem were recorded and shown in Figures 5.2 b and c. The coefficient of variation (CoV) in each stem reflects the influence of connections on diameter variation. This also illustrates the variability in diameter among the four stem regions of the connection. Even within the same stem, the diameters on two sides of the connection exhibit different sizes. The small-sized braided tree structures were difficult to measure because their intervals were short. Only the five big-sized braided tree structures were recorded. Detailed information on the other tree structures can be found in the Appendix C.

After measurements of the braided tree structures were made, the connections for tests were cut out. The connection was kept in its wet and fresh condition during the testing period, by controlling its moisture content. The moisture content of a connection was controlled to be higher than 120%. The moisture content of a freshly cut connection was measured to be approximately 150%. Due to the duration of the testing, it was difficult to perform the tests immediately after cutting. Therefore, after cutting the connections, they were stored in a refrigerator in a temperature range of 0 to 7 °C and covered with moist clothing that was soaked in a 50% ethanol solution. This method of treatment was used to prevent water loss and also to avoid the production of fungi.

5.2.3 Measurements of self-growing connections

Measurements of self-growing connections were classified into three groups. The first group was related to the physical parameters, which included density (ρ) and moisture content (MC). The second group was geometric parameters, which involved the diameters (D) of two stems, the cone ratio (R_{cone}) of each stem, the area of the interface (A), and the cross-angle (α) of a connection. The parameters related to the fusion, which included the fusion degree (F_d) and interface curvature (C), were the third group. The definitions of the local coordinate system and the viewing planes could be found in Figure 3.4 in Chapter 3.

Physical parameters

Mass The green mass and the fully dry mass of a connection were measured. The green mass was measured immediately after the connection was cut from the tree. After mechanical tests, the connections were dried in the oven until the mass reached a constant value. The dry mass, which was also the wood mass, was then weighed. The drying process was carried out according to EN13183 [9].

(a)

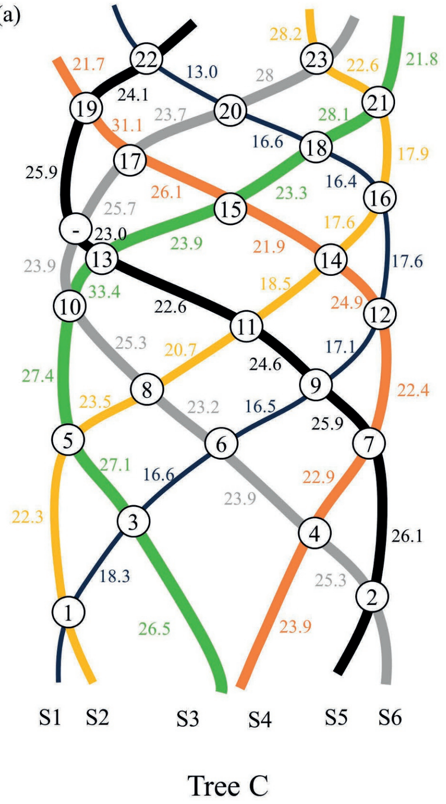

(b)

Stem (S) ID	Average diameter (mm)	CoV (%)	Taper ratio
S1	16.5	9.5	0.71
S2	21.4	16.6	1.26
S3	26.4	13.6	0.82
S4	24.4	12.8	0.91
S5	24.9	6.2	1.11
S6	24.5	5.7	0.90

(c)

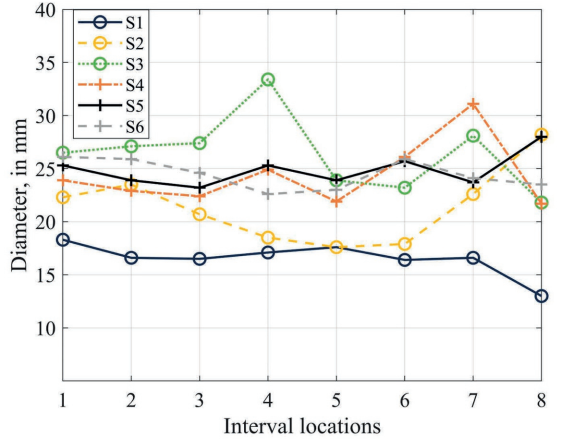

Figure 5.2: Geometric information on the braided tree structure Tree C. (a) Schematic illustration of the braided tree structure Tree C; (b) diameter variations in Tree C; (c) diameter variations along stems.

Volume Since a connection had an irregular shape, the water displacement approach was a suitable way to measure the volume of a connection. Volume was measured when the connection was cut from the braided tree structure. This meant that the measured volume was the green volume of a connection. The connection was inserted into a beaker filled with water. As the connection was embedded in the beaker, the equivalent volume of water was displaced. The volume of water displaced was considered to be the green volume of the connection.

Basic density (ρ) The basic density used in this work was calculated as the ratio of the dry mass (i.e., wood mass) to the green volume, expressed by Equation 5.1. The reason for using the dry wood mass to calculate the density was to exclude the effect of varying moisture contents between connections, and thus to compare the effect of the amount of wood content on the connections.

$$\rho = \frac{M_d}{V_w}, \tag{5.1}$$

where ρ is the basic density of a connection, in kg/m^3; M_d mean the dry mass; V_w represents the green volume.

5

Moisture content (MC) was measured by dividing the mass of water by the mass of wood, expressed as a percentage in Equation 5.2.

$$MC = \frac{M_w - M_d}{M_d} \times 100\%, \tag{5.2}$$

where MC is the moisture content of a connection, in %; M_w and M_d mean the green mass and the dry mass, respectively.

Geometric parameters

Figure 5.3 presented the geometry information of a self-growing connection. The geometric parameters measured included the diameters at two sides of two stems, cross-angle, fusion depth, and area of interface.

Cross-angle (α) was measured between the center lines of the stems. The lower angle was described as the cross-angle of a connection, while the higher angle was equal to 180°-α. The cross-angle of the selected samples ranged from 25° to 90°due to the angle limitation of the clamp space in the mechanical setup.

Diameter (D) As shown in Figure 5.3, the geometric information of a connection was marked. The diameters of each stem were measured on four sides of a connection: D_{1l}, D_{1r}, D_{2l}, and D_{2r}. The measured location was selected 2 to 3 cm from the interface. The measured diameters in one stem were averaged as the diameter of this stem, the same as that of the other stem. This meant that the diameter of stem 1 (D_1) was the mean of D_{1l} and D_{1r}. The diameter (D_{avg}) of a connection was the mean diameter of stem1 (D_1) and stem2 (D_2).

Cone ratio (R_{cone}) was calculated as the diameter difference ratio in a stem on two measured sides. The ratio was the division of the smaller diameter into the larger diameter, for example, the ratio of D_{1l} and D_{1r} in Figure 5.3 a. Two cone ratios could be obtained from a connection. In this work, the smaller was taken for later analysis, because the difference in cone ratios in the tested connections was less than 5%.

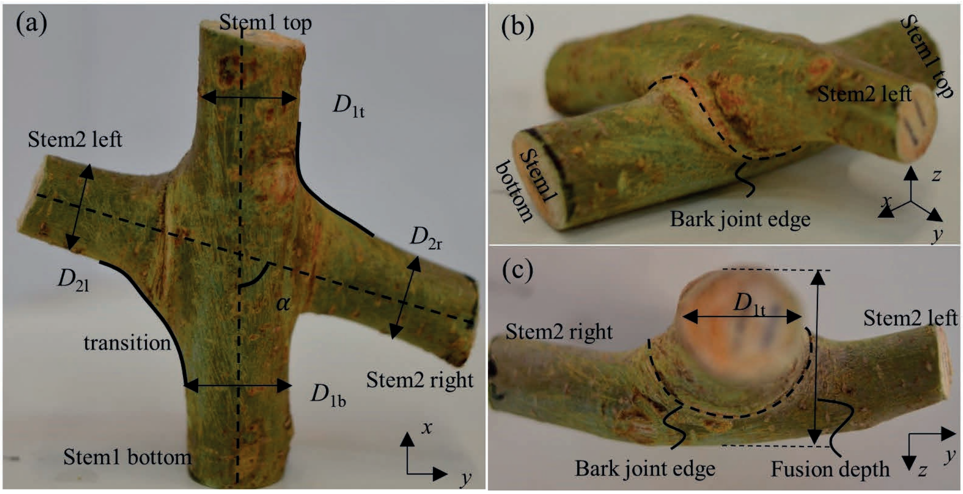

Figure 5.3: Geometry of connection **I**11 as an example. (a) Diameters at four sides of stems; (b) the interface outline merged by bark from two stems; (c) illustration of measuring fusion depth of connection **I**11.

5

Diameter ratio (R_{dia}) As defined in Section 3.3.2, the stem with the largest diameter was denoted stem1. The diameter ratio was defined as the division of the maximum stem size (stem1) divided by the minimum stem size (stem2).

Fusion depth (F) As in Figure 5.3 c, the distance at the center and between the edges of two stems in the xy plane was referred to as the fusion depth (F). In Chapter 3, it was discussed that at this location, the depth of fusion might be related to the better distribution of fused fibers and the extent to which a connection has fused. The difference between the sum of the diameters of two stems and the fusion depth was then referred to as the net fusion depth.

Curved area (A_{curved}) It was difficult to measure the curved area directly from the sample, as the shape of the interface was similar to a saddle. As a result, handy scan equipment (HandyScan 3D, Creaform) was utilized. The resolution of the scanning was 1 mm. It first scanned the connection, followed by the application (VXElement) which created a mesh model from the point-cloud data. The model obtained was the reconstruction of the outer surface of a self-growing connection. Figure 5.4 presented the approach applied in this work on how to measure the interface of the connection based on the reconstructed scanning model. The edge of the connected area (bark joint edge in Figure 5.3 b) was easily located. When the outline was manually picked as a cutting curve to divide two stems, the interface was exposed. The 3D surface was reconstructed by manually selecting the nearest three points to produce a mesh with a resolution of no less than 5 mm^2. Consequently, the curved area was formed and the area was measured.

Projected area (A_{proj}) The mapped plane xy was the mechanical loading plane constructed by the center line of one stem with a normal vector perpendicular to the other center line of another stem. The curved interface was then projected to this plane, and the

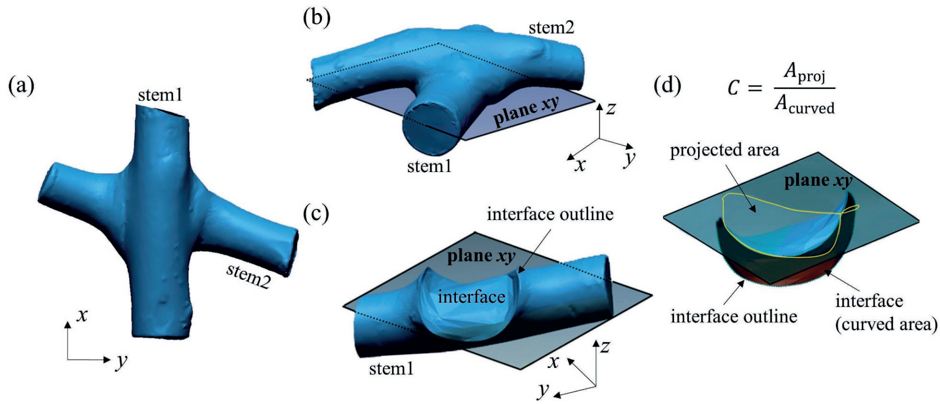

Figure 5.4: Illustration of the approach to derive the interface curvature of a self-growing connection in Figure 5.3. (a) Reconstructed model from the surface scanning; (b) plot of the reference plane, plane xy, according to the loading situation; (c) separation of two stems based on the outline of interface; (d) projection of the curved interface to the reference plane xy, forming a projected area.

5

obtained planar surface was the projected area.

Fusion related parameters

Fusion related parameters also belonged to geometric factors. The differences were that they indicate the fusion condition of a connection. They were quantified from distance and area measurements, expressed as a percentage.

Fusion degree (F_d) was defined as the percentage of fusion depth (F) taken from the mean diameter in a connection, expressed in 5.3. Individual stems developed over time when two stems fused together, so it was assumed that combined growth was achieved at the interface. As a result, there was a size difference between the interface and the diameter of the stem. This size difference indicated how much combined growth had developed. In other words, the degree of fusion revealed the extent to which one stem fused into the other. This distance could also indicate the number of merged fibers that connected two stems, as explained in Section 3.3.4. As a result, it could be assumed that the higher the degree of fusion, the better the quality of the fusion.

$$F_d = \frac{D_1 + D_2 - F}{D_{avg}} \times 100\% \tag{5.3}$$

where F_d means fusion degree of a connection, in %; D_1, D_2 and D_{avg} means the diameters of stem1, stem2 and the mean of two stems' diameters; and F is the fusion depth measured.

Interface curvature (C) was derived from the division between the projected area and the curved area, expressed as Equation 5.4. It was proposed as a parameter to describe the shape of the interface. It explained the percentage of the area that a connection could mobilize when resisting an external force.

$$C = \frac{A_{\text{proj}}}{A_{\text{curved}}}, \tag{5.4}$$

where C means the interface curvature of a connection which is the area ratio without a unit; A_{proj} and A_{curved} mean the measured areas of the projected and curved surfaces as explained in Figure 5.4.

Fiber structure could only be examined after the tensile test. To understand the level of fusion of a connection, it was also necessary to look at the structural patterns of the fused fibers in addition to measuring the degree of fusion and the interface curvature. After the tensile test and the oven drying process, the connection was fully dried. The bark tissue was then placed in water for about 12 hours. After that, it was easy to remove and see the fiber structures in the outer layer of the connection. The examination was focused on the fused fiber in the failure plane after the tests.

5.2.4 Tensile out-of-plane tests

After the measured parameters were collected, the investigation proceeded to the design of the tensile tests and the determination of the mechanical properties of the self-growing connections. The design of the experimental setup and the calculation of mechanical properties were first proposed in this dissertation.

5

Test setup description

Tensile tests on irregular self-growing connections presented numerous challenges. The initial concern was raised by the misaligned center lines of the stems, which resulted in a certain eccentricity between the two stems. Moreover, variations in cross-angle and diameter required the design of flexible clamps. Additionally, the loading scheme should effectively transfer forces to the interface and generate tensile forces to split the connection. Finally, selecting a suitable measurement tool required careful evaluation.

Consequently, the tensile setup was designed with adjustable load-transfer clamps, as depicted in Figure 5.5 a. Two adjustable rails were fastened to the moving platform at the bottom and with the load cell at the top, providing a spatial four-point loading system, as illustrated in Figures 5.5 b and c. The analysis included the use of three-dimensional digital image correlation (3D DIC) cameras to gauge the interfacial region, with the ARAMIS (GOM, Germany) program used to assess deformations.

The schematic explanation of the load transfer pathway was visually presented in Figure 5.6. The tensile forces exerted by the supports (A, B, C, and D) were transferred to shear forces and moments at the interface of a connection. The distance between AB and CD in Figure 5.6 was designated as L_{AB} and L_{CD}, representing the load span in two stems. The loading spans (L_{AB} and L_{CD}) were limited to twice of the diameter size. This limitation ensured that the forces conveyed to the interface were effectively treated as tensile forces acting on it. Although moments transferred to the interface were inevitable, the influence from moments was not taken into account in the current analysis. Controlled by a bottom loading platform, tensile testing was performed by applying displacements, with the platform moving at a constant velocity of 0.02 mm/s. During testing, the top clamp (located in A and B) remained immobile. The deformations of the connection were quantified by averaging the displacements in the loading points C and D.

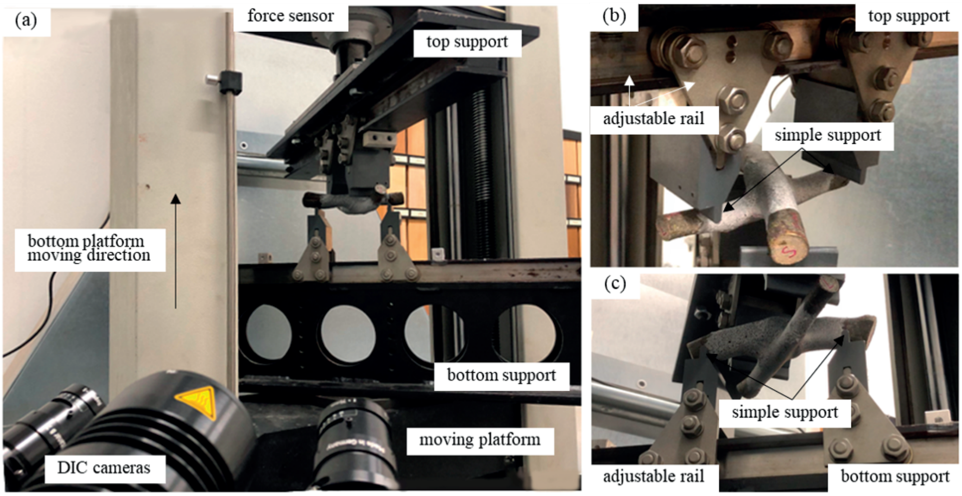

Figure 5.5: Setup of tensile out-of-plane tests. (a) Overview of the loading equipment, supports, and measuring cameras; The bottom support is placed on the moving platform, which moves in a vertical direction. The top support has been clamped to the top. The top support can only rotate horizontally, while the bottom support can move in the vertical direction and rotate. (b) Details of the top support. Two adjustable wheels locates at the rail to enable the adjustment of load spanning. (c) Details of the bottom support with similar setup to the top support.

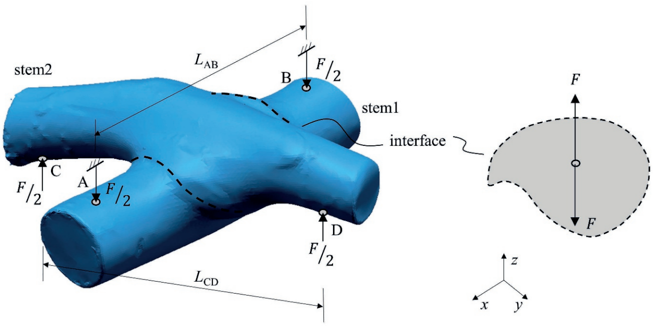

Figure 5.6: Schematic illustration of loads transfer in a self-growing connection. Forces (F) applied from the load cell are transferred evenly to the four supports: A, B, C, and D. The upper clamps A and B are not movable in the vertical direction. Loads are applied at CD at a rate of 0.02 mm/s.

5

Determination of mechanical properties

This section focused on determining the mechanical behavior of the connection subjected to tensile forces perpendicular to the interface. The description was divided into two parts, namely, the description of the loading stages and the determination of the mechanical properties (tensile strength, stiffness, and loading capacity).

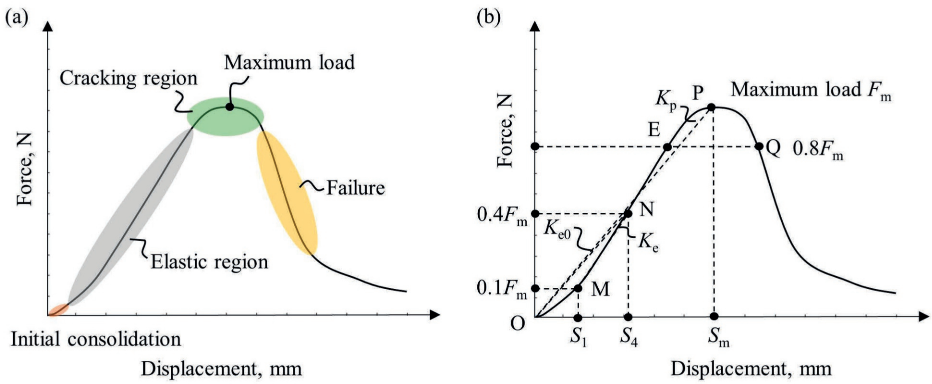

Figure 5.7: Determination of mechanical properties of a self-growing connection. (a) General description of the deformation behavior of a connection; (b) calculations of mechanical properties: maximum load F_m, elastic stiffness K_e, initial stiffness K_{e0}, and peak stiffness K_p.

Loading stage In Figure 5.7 a, the results of the tensile tests provided the force versus deformation curve. This deformation curve of a connection could be generally divided into four regions, namely, initial consolidation, elastic region, cracking region, and failure region. The stage of initial consolidation was the period when the connection adjusted its position within the loading space. Meanwhile, the free water and soft tissues in the connection were compressed. This happened before the elastic stage when the deformation increased proportionally with the applied force. After the elastic stage and within the force range between approximately $0.8F_{\mathrm{m}}$, this stage was the gradual cracking stage. It should be noted that in the force decent region, the cracks kept extended. The difference between the crack region and failure was that after approximately $0.8F_{\mathrm{m}}$. When the cracks extended to around half of the interface, the connection experienced a sudden load drop and failed.

Stiffness, tensile strength, and loading capacity The maximum load was denoted as the maximum load (F_{m}) for a connection under tension, marked as point P in Figure 5.7 b. Points E and Q represented the 80% maximum loads during the ascending and descending stage on the deformation curve. The point M was at the location where the force reaches $0.1F_{\mathrm{m}}$, while the point N corresponds to $0.4F_{\mathrm{m}}$. The tangent drawn between the points M and N was calculated as the elastic stiffness (K_{e}) of a connection. In addition, the initial stiffness (K_{e0}) was determined and calculated as the scant value from point M to the original point O. Furthermore, from the peak point P to the original point O, the scant value of this region was determined as the peak stiffness (K_{p}). The expression of three stiffnesses could be found in Equation 5.5.

5

$$
\begin{aligned}
K_{\mathrm{e}} &= \frac{0.4F_{\mathrm{m}} - 0.1F_{\mathrm{m}}}{S_4 - S_1}, \\
K_{\mathrm{e0}} &= \frac{0.4F_{\mathrm{m}}}{S_4}, \\
K_{\mathrm{p}} &= \frac{F_{\mathrm{m}}}{S_{\mathrm{m}}},
\end{aligned}
\tag{5.5}
$$

where K_{e}, K_{e0}, and K_{p} represent the elastic stiffness, initial stiffness, and peak stiffness, respectively. F_{m} is the maximum force and its corresponding deformation is S_{m}. S_4 and S_1 are the deformation correspond to the force at 40% of the maximum force and 10% of the maximum force during the ascending process, respectively.

The tensile strength of a connection was the division of the maximum force by the projected area of the connection. It was expressed as the Equation 5.6. It should be noted that the determined strength was the effective tensile strength. Tensile stresses were assumed to be uniformly distributed over the projected interfacial area.

$$
f = \frac{F_{\mathrm{m}}}{A_{\mathrm{proj}}},
\tag{5.6}
$$

where f denotes the strength of a connection, in MPa; F_{m} refers to the maximum force from the loading curve, and A_{proj} means the projected area of the test connection.

5.2.5 Statistical analysis

ANOVA analysis

Self-growing connections for mechanical tests were harvested from different braided tree structures, as described in Table 5.1. The braided tree structures were grown in nurseries to ensure a stable growth environment. However, different braided tree structures might still have different growth conditions, such as nutritional level. This resulted in different properties (e.g., density and moisure content) of connections depending on the origin of the braided tree structures. Furthermore, this might further affect the performance of a connection under loads.

To this end, self-growing connections from the five large braided tree structures were first performed by means of a one-way ANOVA analysis. The parameters studied included density, moisture content, and cross-angle. This analysis aimed to understand whether there was a significant difference between different braided tree structures. If the results analyzed were not significant, the connections of the tree structures were mixed for further studies without considering the difference in the origin of growth.

K-S test

To describe the characteristics of the parameters measured from the connection, K-S tests were implemented. This analysis was aimed at examining the statistical distribution of the data. Nine parameters were examined, including the cone ratio, average diameter, diameter ratio, projected area, fusion degree, interface curvature, tensile strength, stiffness, and maximum load. This analysis was prepared for further development of the prediction model.

5

Pearson correlation coefficient

The correlation coefficient (r) of the variables is a measure of their linear dependence. Given paired data $(x_1, y_1), ..., (x_n, y_n)$ consisting of n pairs, r is defined as Equation 5.7.

$$r = \frac{\sum_{i=1}^{n}(x_i - \overline{x})(y_i - \overline{y})}{\sqrt{\sum_{i=1}^{n}(x_i - \overline{x})^2}\sqrt{\sum_{i=1}^{n}(y_i - \overline{y})^2}}, \tag{5.7}$$

where n is the sample size; x_i and y_i are the individual sample points indexed with i; $\overline{x} = \frac{1}{n}\sum_{i=1}^{n} x_i$ is the sample mean value and analogously for $\overline{y}$.

Before establishing the strength prediction model for the connection, the correlation between the measured parameters was analyzed and quantified by r. The negative value of r indicate the negative relationship between two variables. When r is equal to 0, it is considered that there is no relation between two variables. When the absolute value is between 0.25 and 0.5, the relationship is considered weak. Between 0.5 and 0.75, it is considered a moderate relationship. If the absolute value of r is greater than 0.75, the correlation between two variables is considered strong.

5.2.6 Tensile strength prediction using ANN

ANN model development

The ANN approach has been used recently in predictive models for the field of materials engineering [10, 11] due to its specific features such as adaptively (i.e., learning from input parameters) and model independence. The objective of this section was to develop a neural network model to predict the tensile strength of a self-growing connection. The development of an ANN model to predict tensile strength was outlined in this framework (Figure 5.8). The first step is to collect data on tensile strength from the measurements and analyses. These data were then used in the ANN model. Next, the ANN model was designed and trained using input data. Finally, the model was tested and evaluated to determine its accuracy and reliability.

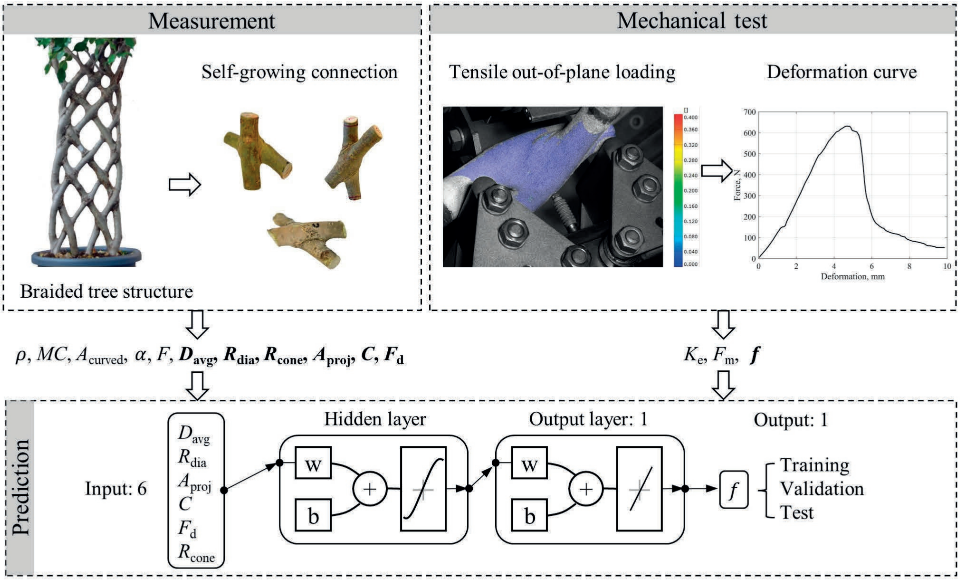

Figure 5.8: Framework of the development process of the ANN model for the prediction of tensile strength of self-growing connections.

In order to set up an ANN, it needs to define: (i) the architecture of the ANN; (ii) the training algorithm, which is used for the ANN learning phase; and (iii) the mathematical functions describing the mathematical model. The architecture or topology of the ANN describes the way artificial neurons are organized in the group and how information flows within the network. As described in Figure 5.8, training and testing data for the development of the ANN model were prepared using 102 sets of data from tensile tests. The model used six input parameters, namely diameter ratio (R_{dia}), cone ratio (R_{cone}), average diameter (D_{avg}), projected area (A_{proj}), interface curvature (C), and fusion degree (F_d). Density and MC were not considered, because the correlation coefficient (r) to tensile strength was nearly zero. The ANN model was developed in MATLAB and applied to predict the tensile strength of a self-growing connection of the given input features. The training algorithm used was the Levemberg-Marquardt algorithm for quick calculations.

The ANN model learns the underlying physics of the system of interest from the training samples, which are basically the cause-effect samples. Therefore, the number of training samples significantly influences the predictive performance of the network. Increasing the number of training samples provides more information and thus increases the potential level of accuracy that the network can achieve. Having too few data samples will lead to poor generalization by the network. In this work, the fraction of the data set for training and validation varied to compare performance. The train validation test portion was decided as 70%, 65%, and 60%. The portion of the test data remained the same as 15%. Thus, the validation portion was 15%, 20%, and 25%. Different cases are listed in Table 5.2.

Since the output parameter was tensile strength f only, the model architecture had one output layer. ANN models with different hidden layers were compared, including 5, 10, and 15 hidden layers. In total, 9 cases were included and listed in Table 5.2.

Table 5.2: Cases studied for ANN prediction of tensile strength of a self-growing connection

Case	Hidden layer	Training	Validation	Test
H5-I	5	70%	15%	15%
H5-II	5	65%	20%	15%
H5-III	5	60%	25%	15%
H10-I	10	70%	15%	15%
H10-II	10	65%	20%	15%
H10-III	10	60%	25%	15%
H15-I	15	70%	15%	15%
H15-II	15	65%	20%	15%
H15-III	15	60%	25%	15%

5

Performance indicators

The reliability and precision of the developed neural networks were evaluated using Pearson's correlation coefficient (r in Equation 5.7) and the root mean square error (RMSE). The lower the RMSE, the more accurate the evaluation. The equations to determine RMSE can be found in Equation 5.8.

$$\mathrm{RMSE} = \sqrt{\frac{1}{n}\sum_{i=1}^{n}(y_i - y_i^{\mathrm{pre}})} \tag{5.8}$$

where y_i is the tensile strength of a self-growing connection obtained from experiments; y_i^{pre} is the predicted value from NN model; n is the total number of data points.

5.3 Results and analyses

5.3.1 Parameter data description

ANOVA analysis is performed on the density, cross-angle, and moisture content of the connections from five braided tree structures listed in Table 5.1. The analyzed results are presented in Table 5.3. Among the five large braided tree structures, the cross-angle has no difference; and the density shows weak significance. From this information, it can be assumed that it has no differences between the five braided tree structures. In contrast, the moisture content shows an obvious difference. However, considering that the fibers within a connection are above the fiber saturation point, the influence of MC on the material properties is assumed to be negligible. Therefore, it is assumed that the origin and source of the connections from different braided tree structures may not affect connections' material properties, so the connections were mixed together to analyze them in a broad manner.

K-S tests are performed to test whether the measured data come from a normal standard distribution. The results are presented in Table 5.4. The variables tested include the cone ratio, diameter ratio, average diameter, projected area, fusion degree, interface curvature, tensile strength, elastic stiffness, and maximum load. The results of the K-S test proved that all the collected data are present in a normal distribution. The parameter distributions are plotted. The empirical and standard cumulative distribution functions (CDF) are compared in Figure 5.9.

Table 5.3: ANOVA statistical analysis among braided tree structures

Description	- Null hypothesis: no differences among tree structures; - Significance level: 5%.		
Parameters	**F-value**	**p-value**	**Test decision**
Density, kg/m^3	2.42	0.060	Accept
MC, %	38.58	2.3e-15	Reject
Cross-angle, degree	0.54	0.705	Accept

Table 5.4: K-S analysis of geometric and mechanical parameters

Description	- Null hypothesis: tested data comes from a standard normal distribution; - Significance level: 5%.				
Parameters	**Mean**	**CoV(%)**	**[min, max]**	**p-value**	**Test decision**
Cone ratio	0.91	7.7	[0.80, 1.00]	0.087	Accept
Average diameter, mm	20.1	15.9	[12.3, 26.8]	0.753	Accept
Diameter ratio	1.22	12.3	[1.00, 1.68]	0.150	Accept
Projected area, mm^2	964.8	36.4	[293.1, 2109.1]	0.253	Accept
Fusion degree, %	24.8	56.9	[-14.6, 73.2]	0.919	Accept
Interface curvature, %	56.9	18.5	[35.2, 89.8]	0.784	Accept
Tensile strength, MPa	0.75	29.3	[0.23, 1.38]	0.323	Accept
Elastic stiffness, N/mm	139.8	26.7	[55.3, 254.5]	0.992	Accept
Maximum load, N	718.3	44.6	[32.4, 1559.8]	0.332	Accept

5.3.2 Force-deformation behavior

In this section, the deformation of a connection in response to tensile forces is presented. Connection **I**11 is used as an example to illustrate the tensile behavior and the failure mechanism. For further clarification and support, the descriptions of two other connections D5 and K11 are placed in the Appendix C. The crack initiation and propagation process is explained in combination with the DIC measurements.

Tensile behavior stages

To explain more clearly the deformation of the connection **I**11, in Figure 5.10 a, three locations are selected at the interface of the connection **I**11. Three 20 mm long virtual strain gauges are installed at locations of lc1-middle, lc2-edge, and lc3-inside. Lc1-middle is made at the middle location of the interface, with a length of 20 mm. Parallel to this lc1-middle, lc-edge and lc3-inside are placed 10 mm away from the middle gauge. The

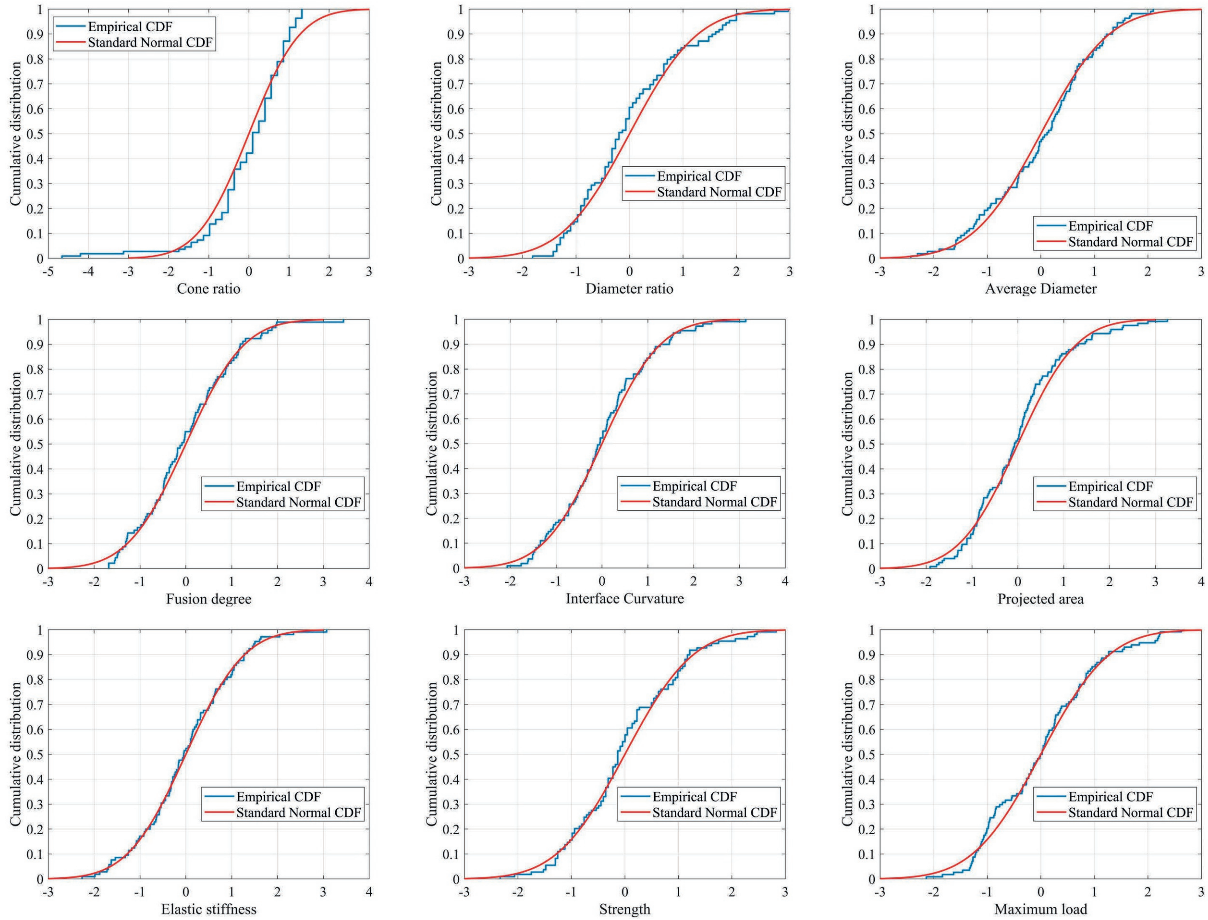

Figure 5.9: Empirical and standard cumulative distribution functions (CDF) comparision of diameter, fusion degree, curvature and strength.

5

elongation of the virtual gauges is measured from the DIC results. Connection **I**11 has an average diameter of 19.7 mm, a fusion degree of 12.3%, an interface curvature of 53.6%.

The deformation curve of how the connection I11 responds to tension out-of-plane is plotted in Figure 5.10 b. In this figure, three dashed lines are drawn at the points when the forces reach $0.8F_m$ (501.6 N, 3.3 mm), F_m (631.5 N, 4.7 mm), $0.8F_m$ (501.6 N, 5.5 mm), respectively. The elongations measured on the three strain gauges are plotted in Figure 5.10 c. The three dashed lines are marked at the same force location. The name of the dashed line corresponds to the development stage (a, c, and e) in Figure 5.11.

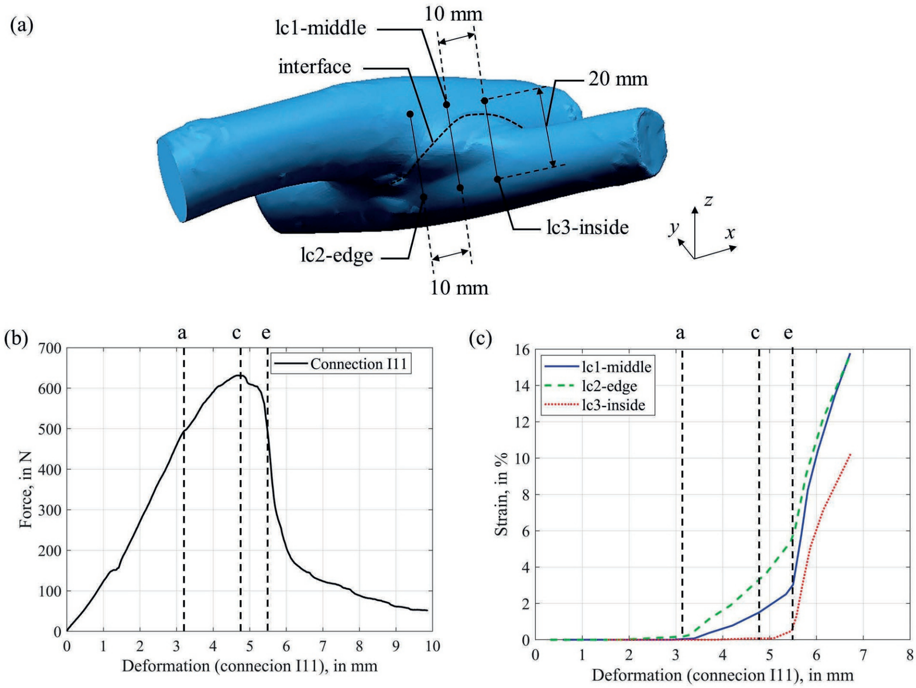

Figure 5.10: Force-deformation responses of connection **I**11. (a) Locations to measure the elongation of the interface; (b) overall deformation of connection **I**11, measured at the loading locations C and D as in Figure 5.6; (c) interface elongation of connection **I**11. Dashed lines a, c, and e in (b) and (c) correspond to the stages a, c, and e in Figure 5.11.

- Initial consolidation stage

After being subjected to tensile forces, the connection initially experiences a consolidation stage. This stage has a displacement of less than 1 mm. During this period, the bark at the supporting location is compressed, and the water in the stems is compressed. Meanwhile, the connection adjusts its position due to its irregular shape until it reaches the new equilibrium. The consolidation stage of connection **I**11 is short.

- Elastic stage

Following the consolidation stage, the connection undergoes a subsequent linear elastic phase characterized by a proportional increase in forces with displacement. This region can be divided into two parts. The first displacement part of the connection occurs at the four ends of the stem region. Although the distance between the loading point and the edge of the interface is controlled to be less than 2 cm, the bending moments transferred from the support to the interface still exist. Strictly speaking, the tensile out-of-plane test is a four-point bending tensile to the interface. Thus, the four supporting ends of the stems of the connection first bend, and this is observed until the deformation reaches approximately 1.5 mm. The second part is the deformation of both the intersected region and the stem region. Analyzing the deformation characteristics of wet connections, it reveals that this linear elastic range can span approximately one third of the diameter of the stem. The elastic stiffness K_e of the connection **I**11 is 141.7 N/mm.

- Cracking region

After the linear region, the connection starts to crack and progresses to the cracking region from approximately 501.6 N, which is also $0.8F_{\mathrm{m}}$. Figure 5.11 gives the observations and measurements from the DIC. Figures 5.11 a to e are within the cracking region. At this stage, the crack occurs first at the edge of the fused region (Figures 5.11 a and b) with a deformation of approximately 3.3 mm. Before then, the elongation of the interfacial region is minimal. This can be further confirmed by the local elongation in Figure 5.10, the connection **I**11 starts to crack at the lc2-edge. Meanwhile, the stiffness starts to reduce and becomes soft.

As stated in Table 4.4, found in Chapter 4, the edge location of the fused region is mainly composed of bark tissues with minimal fused fibers. At around 600 N, visible cracks are obvious to see. With increasing forces, the crack spread to the interface. This can be observed in the increase in elongation in the middle of the interface (lc1-middle) in Figure 5.10 b.

Before the loading force reaches its peak, the cracks extend in the interface in both x and y directions (the coordinate system in Figure 5.11 a). The length of the crack in the x direction is found to be less than half of the interface (Figure 5.11 c). It is spotted when the crack extends to approximately half of the interface area, around 0.8 F_{m}, the connection has a sudden load drop and subsequent failure.

However, depending on the fusion condition, some connections have a sudden load drop, which corresponds to brittle behavior, directly after the peak load. For example, for the connection K1 in Figure 5.12, the connection is brittle. Connection K1 cannot deform after peak load. In Appendix C, the connection K11 also presents a brittle behavior after peak load.

Failure modes

Among all samples, in general, two failure modes are identified: (i) Interface failure: the failure occurs at the interface. (ii) Interface to stem failure: the failure occurs at the interface and extends across stems. They are mainly differentiated by their degree of fusion (F_{d}). In the main content, two example groups are given here to show the two failure modes, as in Table 5.5. In the first group (Group 1), it is observed that when the degree of fusion is less than approximately 15%, this meant that only 15% of the diameter of the

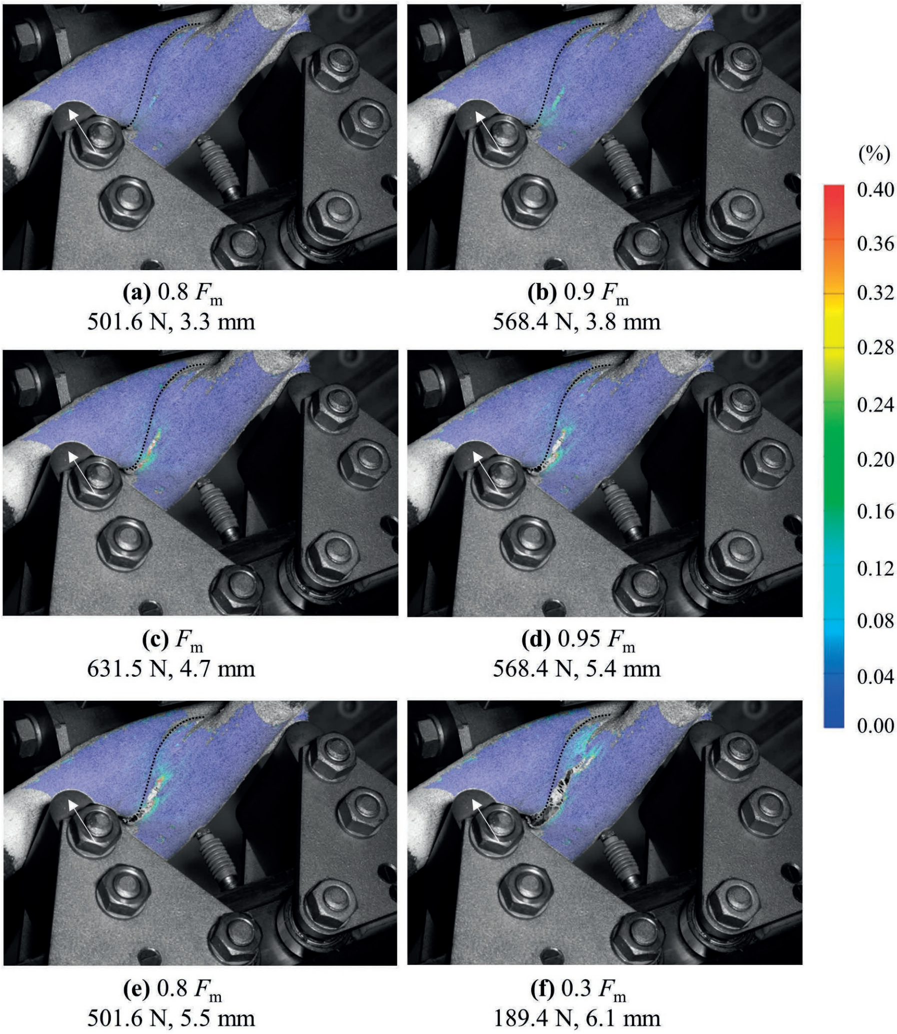

Figure 5.11: Development of surface strain in connection **I**11. Black dashed lines indicate the outline of intersected region.

stem was connected with the other stem, the failure is observed to occur and develop in the intersected plane (failure mode i: interface failure). This is mainly because the fused fibers are less in this group of connections. Furthermore, the interfacial curvature of the connection is low and it is difficult to mobilize material in the stems, see Figures 5.13 a and b.

Table 5.5: Examples of two groups of failure: Group 1 interface failure and Group 2 interface to stem failure

Group	Connection ID	D_{avg} (mm)	F_d (%)	C (%)	f (MPa)	K_e (N/mm)	F_m (N)
Group 1	K1	21.3	-14.6	60.2	0.50	101.2	648.0
	D4	16.1	4.4	78.4	0.47	65.8	324.4
	B8	16.9	-7.7	66.1	0.65	99.2	394.1
	K10	15.7	-2.7	82.0	0.41	76.6	250.0
	K12	14.9	-0.3	59.6	0.36	55.3	129.2
Group 2	C4	24.0	11.0	57.1	0.72	187.0	1000.3
	D13	21.9	20.1	72.4	0.54	133.6	659.7
	H4	25.0	24.6	41.0	1.30	216.3	1559.8
	I15	22.6	42.3	42.8	1.26	187.3	1260.7
	C17	26.7	73.2	45.7	1.01	118.2	1077.6

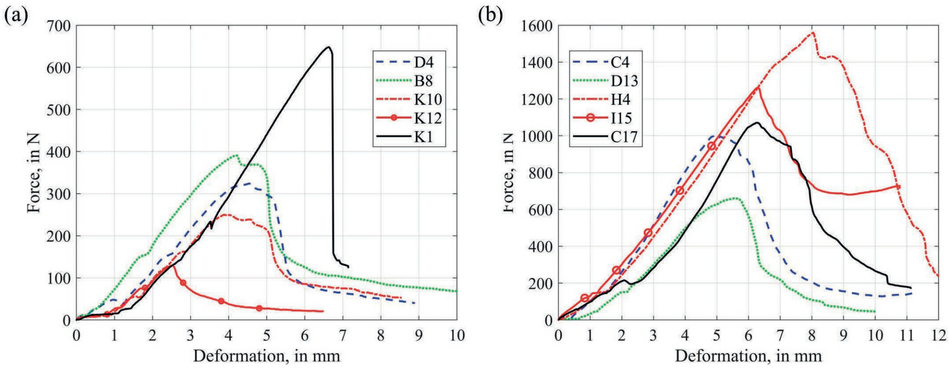

Figure 5.12: Deformation curves of two example groups. (a) Group 1: interface failure. (b) Group 2: interface to stem failure.

In the second group (Group 2) in Table 5.5, as the stems grow deeper in each other, the failure mode is similar to that of the connection **I**11. The cracks extends to the connecting stems, forming a failure plane in the shape of 'Y' (failure mode ii: interface to stem failure). The failure plane of the second group is shown in Figures 5.13 c, d, and e. Regarding mechanical properties, the second group has a relatively higher strength and load capacity than Group 1.

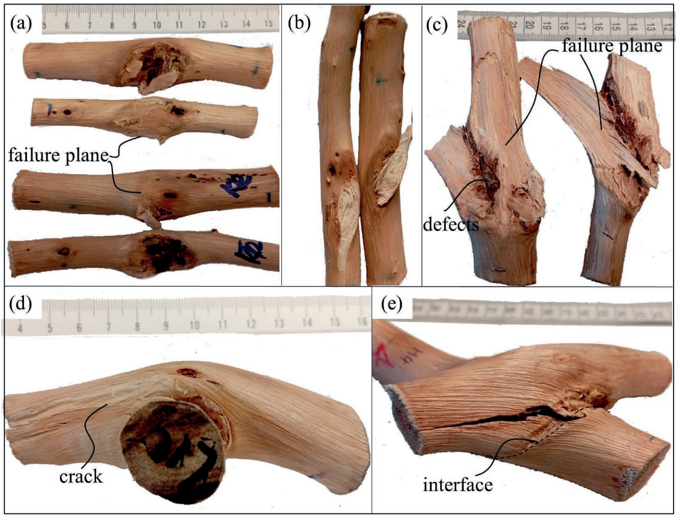

5

Figure 5.13: Failure modes of two example groups. (a) Top connection K10, bottom K12; (b) connection K1; (c) and (e) H4; (d) connection C17.

At the microscopic level, in Figure 5.14, the illustration presents the cracks that occur within the cross sections as the cracks propagate throughout the extension process for failure mode i. Figure 5.15 gives the illustration of failure mode ii.

In failure mode i (Figure 5.14 a), the failure surface (black dashed line) overlaps the interface (red dashed line), and a small number of merged fibers (yellow dashed line) are found on the upper side of the connection in Figure 5.14 a. The merged fibers can also be seen in Figures 5.14 b to c following the yellow arrows. The cracks start at the corners of the connection and then propagate mainly on the lower side of the interface. Meanwhile, the stem2 of the connection experiences a rotation in the z direction. As a result, the cracked surface opens on the lower side of the connection.

In failure mode ii (Figure 5.15 a), the failure surface (black dashed line) only partially overlaps the interface (red dashed line). Connections that fail in mode ii have more merged fibers and form a more curved interface. As in the failure pattern of failure mode i, cracks occur first at the corners and then extend along the interfaces (Figure 5.15 b to c). However, when the crack extension encounters the merged fibers (Figures 5.15 c to e), the crack extension path no longer follows the interface, but rather follows the direction of the wood grain (Figures 5.15 f and g). The red circle marks the region of the interface, and the yellow arrows point to the merged fibers. Compared with the failure plane with the interface and fiber directions in Figures 5.13, 5.14, and 5.15, it shows that the failure occurs mainly due to a combination of the limit of the tensile strength of soft tissues, the limit of the shear strength, as well as the limit of the tensile strength perpendicular to the wood grain.

Stiffness comparison

In this section, among all samples, the stiffness is compared among elastic stiffness K_e, initial stiffness K_{e0}, and peak stiffness K_p. The results are presented in Figure 5.16.

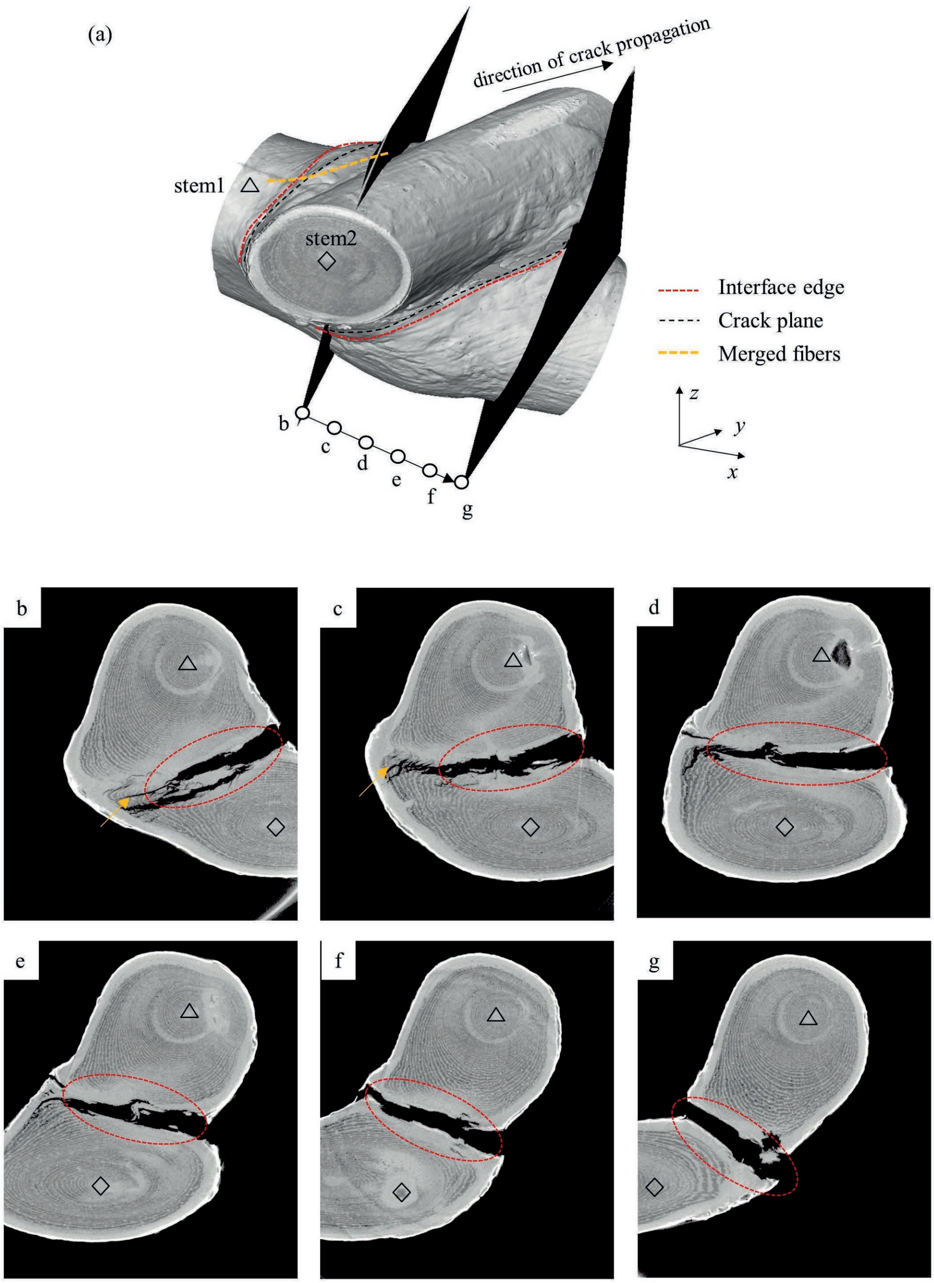

Figure 5.14: Failure mode i: interface failure.

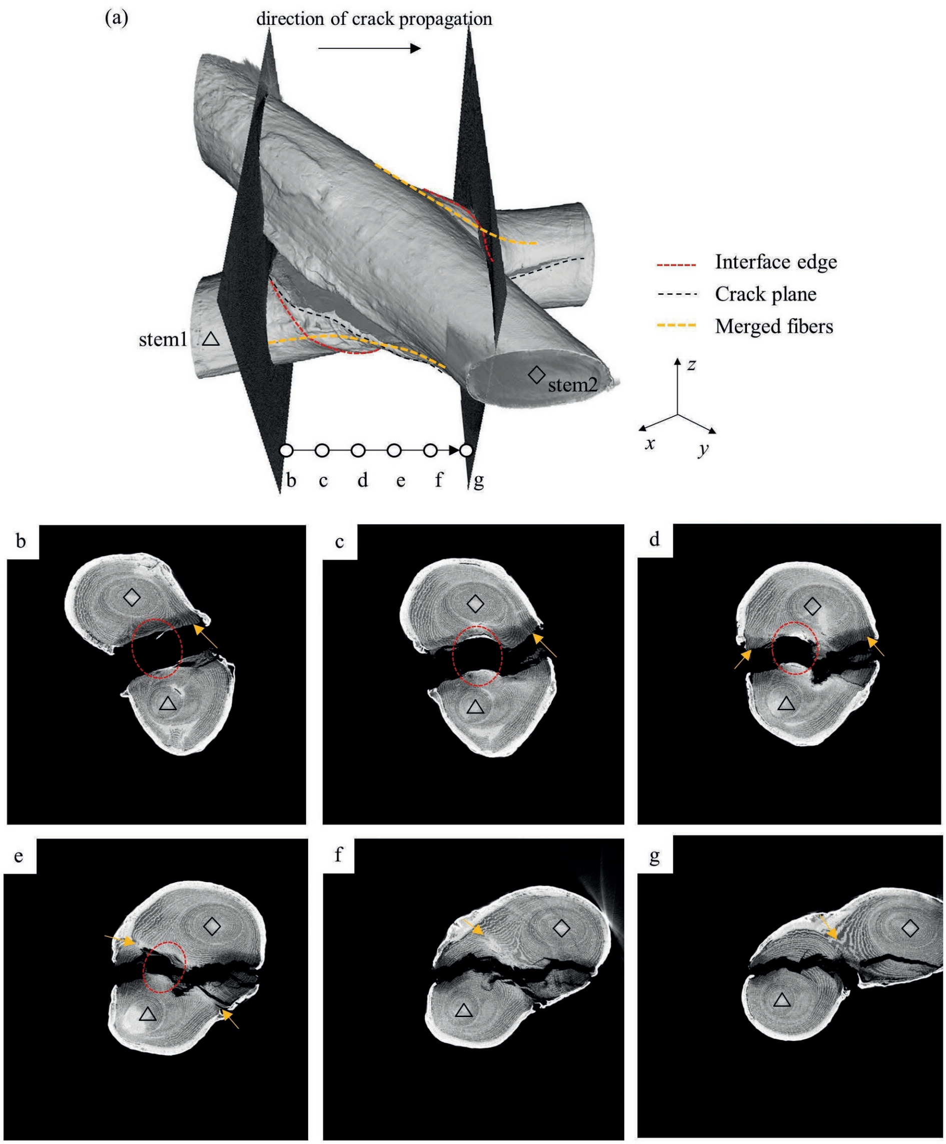

Figure 5.15: Failure mode ii: interface to stem failure.

Figure 5.16 a compares the relative magnitude between the elastic stiffness and the initial stiffness. The initial stiffness K_{e0} is generally lower than the elastic stiffness K_{e1}. It shows that most connections experience a consolidation stage when loading begins. In Figure 5.16 b, it shows that the elastic stiffness is slightly higher than the peak stiffness K_p. However, in Figure 5.16 c, the peak stiffness K_p is higher than the initial stiffness K_{e0}.

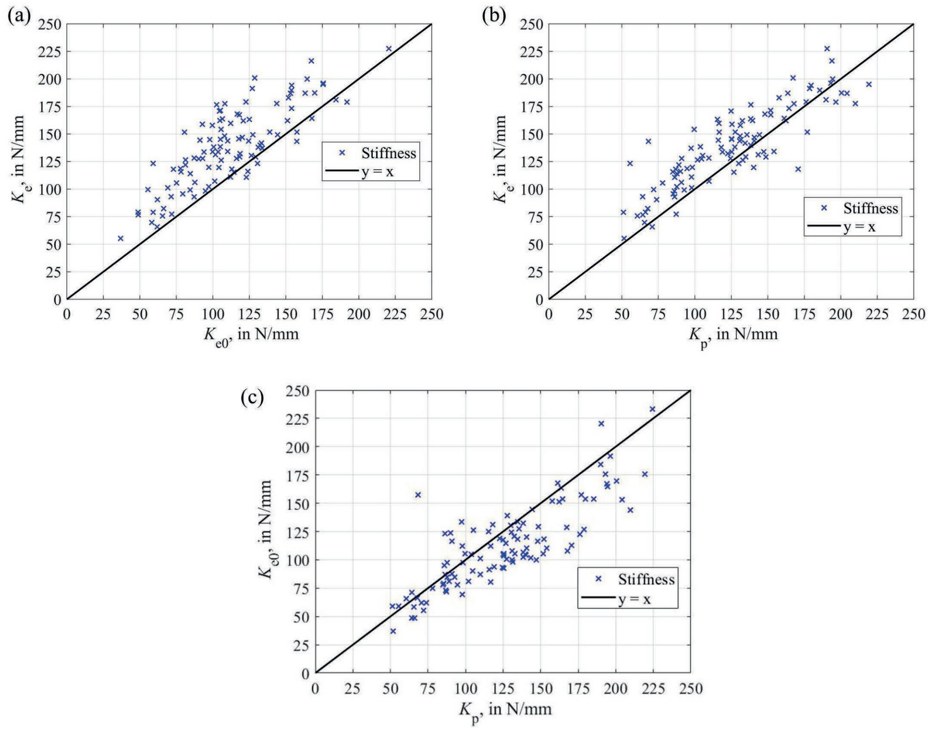

Figure 5.16: Comparison between stiffness. (a) Comparison between elastic stiffness (K_e) and initial stiffness (K_{e0}); (b) comparison between elastic stiffness (K_e) and peak stiffness (K_p); (c) comparison between initial stiffness (K_{e0}) and peak stiffness (K_p).

Correlation among factors

The correlation matrix between the parameters is analyzed and listed in Figure 5.17. Mechanical properties include tensile strength (f), elastic stiffness (simplified as K), and maximum load (F_m). Geometric and fusion-related parameters include cone ratio (R_{cone}), diameter ratio (R_{dia}), average diameter (D_{avg}), projected area (A_{proj}), fusion degree (F_d), and interface curvature (C).

When considering the tensile strength of a connection, the interface curvature, cone ratio, and diameter ratio have negative correlations. The projected area influences the least tensile strength (r = - 0.05). However, the projected area correlates weakly (r = 0.33) with the interface curvature and almost strongly (r = 0.72) with the average diameter.

The influence of the diameter ratio on the tensile strength is weak (r = - 0.15). The degree of fusion and the average diameter have a positive correlation with the tensile strength. The interface curvature has a negative and mediate correlation (r = - 0.53) with the tensile strength, but the fusion degree has a positive and weak correlation (r = 0.24). The average diameter influences the strength weakly (r = 0.43), as well as the cone ratio (r = - 0.33).

5

Regarding elastic stiffness (K), it is mainly influenced by two parameters, namely average diameter (r = 0.70) and projected area (r = 0.66). Fusion depth has a weak correlation with a r = 0.21. The cone ratio, diameter ratio, and interface curvature have the least influence on stiffness.

Regarding the maximum load (F_m), average diameter and the projected area are found to have a strong and positive correlation, with a r is 0.84 and 0.74, respectively. Cone ratio, diameter ratio, and interface curvature have the least influence on maximum load. In particular, the degree of fusion and the curvature of the interface have a negative weak correlation (r = - 0.40) with each other.

5.3.3 Strength prediction model for self-growing connections

As described in Section 5.2.6, the results of the development of the prediction model for the strength of a connection are presented in this section. Based on the correlation matrix in Figure 5.17, six input parameters are used as input variables to establish the ANN model. According to the designed cases in Table 5.2, the compared performance based on RMSE and r is presented in Table 5.6.

When comparing the hidden layers, it shows that the cases with 10 hidden layers have the best RMSE of training (0.008) and the best RMSE of test (0.011). When the training set is assigned 75%, the training result has a best r of 0.91 and the overall result has a best r of 0.84. The performance results of the case H10-I are presented in Figures 5.18 and 5.19. When training the model as in Figure 5.19 a, it stops at Epoch 6. This means that the network has completed the designated number of training cycles and that the parameters have been updated accordingly. Training has been stopped because no further improvement in model performance is observed beyond a certain number of epochs and because of the risk of over fitting.

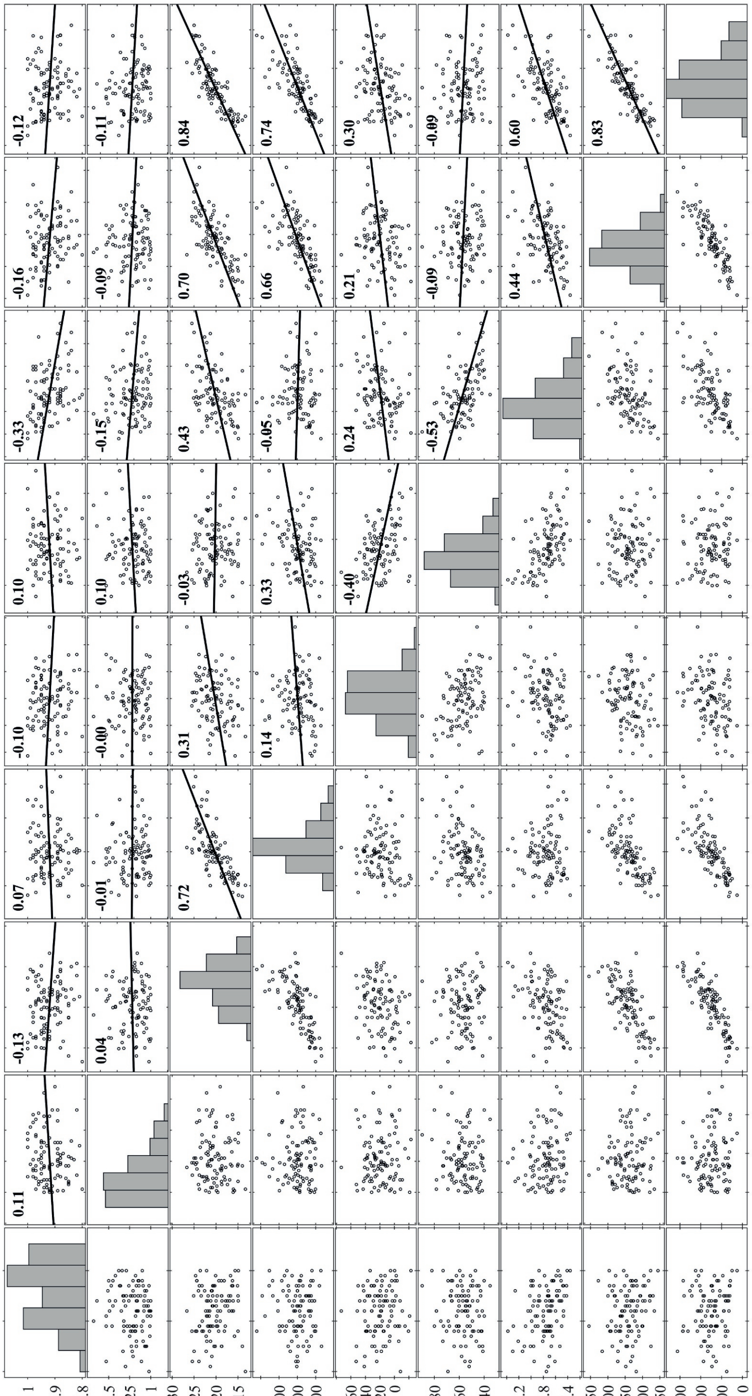

Figure 5.17: Correlation matrix among parameters: cone ratio (R_{cone}), diameter ratio (R_{dia}), average diameter (D_{avg}), projected area (A_{proj}), fusion degree (F_{d}), interface curvature (C), tensile strength f, elastic stiffness K, and maximum load F_{m}.

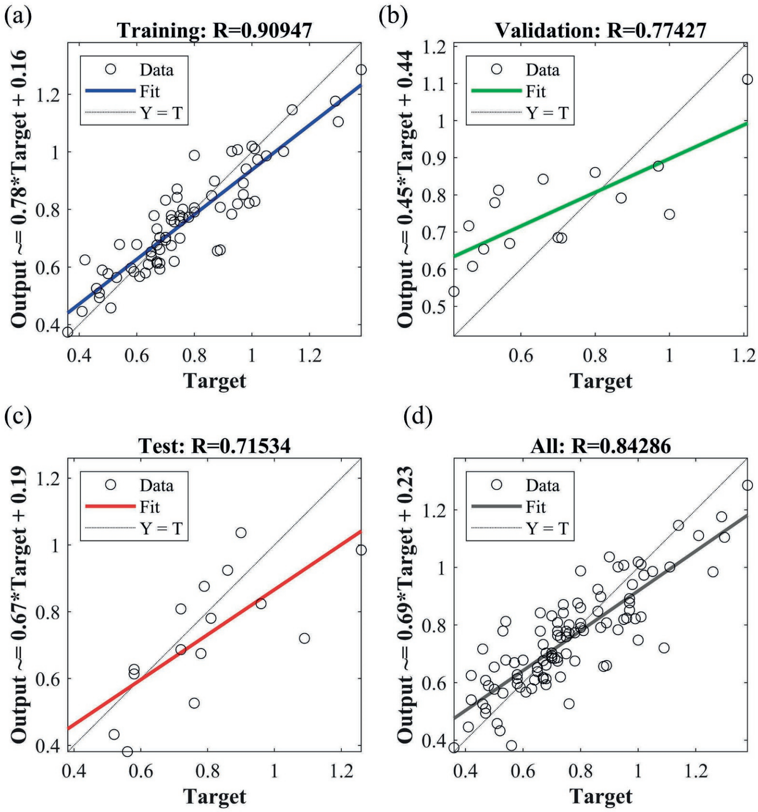

Figure 5.18: ANN model prediction results in case H10-I in Table 5.6.

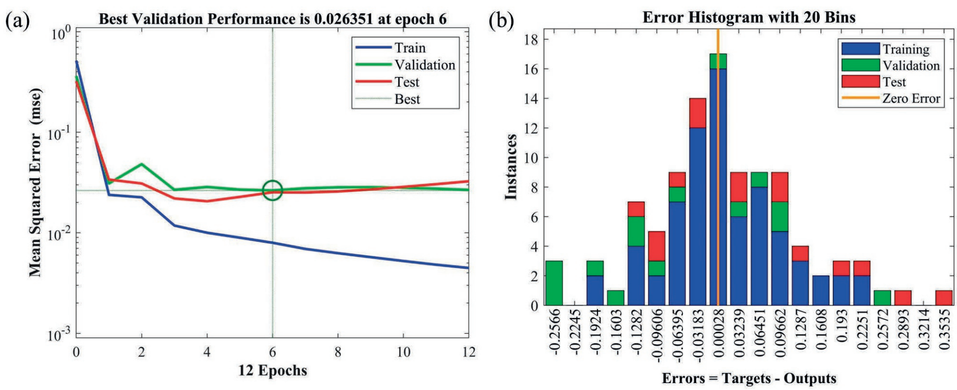

Figure 5.19: ANN model performance in case H10-I in Table 5.6.

Table 5.6: The ANN model performance in studied cases

Case	RMSE			*r*			
	Training	Validation	Test	Training	Validation	Test	All
H5-I	0.015	0.033	0.022	0.77	0.82	0.83	0.77
H5-II	0.013	0.026	0.029	0.84	0.79	0.75	0.79
H5-III	0.009	0.024	0.032	0.86	0.81	0.75	0.81
H10-I	0.008	0.026	0.025	0.91	0.77	0.72	0.84
H10-II	0.014	0.023	0.021	0.85	0.66	0.74	0.8
H10-III	0.013	0.035	0.011	0.85	0.75	0.77	0.78
H15-I	0.014	0.019	0.018	0.85	0.75	0.79	0.82
H15-II	0.011	0.027	0.018	0.86	0.67	0.83	0.81
H15-III	0.016	0.021	0.036	0.83	0.62	0.76	0.78

5.4 Discussion

5.4.1 Comparison between fusion degree and interface curvature

The fusion condition of a connection is mainly described and measured using the proposed parameters of the fusion degree and the interface curvature without damaging connections. Another approach is to observe the fiber structure after destruction.

The fusion degree is easier to measure and compare without damaging the connection. However, given the natural process of tree growth and the fact that the measurement was made only in the middle (Figure 5.3 c), the precision of using the parameter to infer the amount of fused fibers may not be sufficient. This is because the distribution of the merged fibers is not uniform in the fused region. The interface curvature has the advantage of taking into account the shape of the loading area. The 3D saddle-shaped interface is measured from the reconstructed model by surface scanning. By analyzing the curved interfacial area and its projected area to the loading plane, the area ratio is used to reflect the amount of effective area that the fused connection can mobilize. However, measurement must be facilitated by scanning equipment. The fiber structures of a connection are the most accurate way to inspect the structure of the merged fibers and thus be related to the fusion situation, but can only be examined after failure.

Each of these three parameters, used to describe the extent of fusion, comes with its own advantages and disadvantages. Which one to use in practice depends on the accuracy required for the problem. When the interface curvature and degree of fusion are measured, the results can provide information on the tensile strength of a self-growing connection. However, the correlation coefficient of both factors was less than 0.6. This means that there are still random variations that cannot be explained for some reason. One reason is that the proposed parameters may not fully quantify the degree of fusion and require additional parameters for supplementation. Another reason is the uncertainties in plant growth, which lacks quantifiable information.

5.4.2 Mechanical properties

The tensile force on the connection induces a non-uniform stress distribution at different locations on its interface. This mainly results from the complexities of the structures in the interfacial region. The edge of the bark joint forms a 3D saddle-shaped interface, while the fiber bundles are distributed around the interface (Figure 3.19). In addition, when calculating the strength of a connection, it is assumed that the tensile stresses are evenly distributed over the projected area of the connection. Since wood is an anisotropic material, the loading capacity in parallel and perpendicular to the fiber direction has a large difference. Taking into account the direction of the merged fibers within a connection in Figure 5.20, the resultant stresses can be decomposed according to the tangent lines at the locations loaded along the interface. Consequently, the decomposed stresses can be considered, respectively, as the rolling shear stress and the tensile stress perpendicular to the direction of the fiber (as shown in Figures 5.20 a, b and c). Stress failure at the loading location is a combined limit of both the perpendicular tensile capacity and the shear capacity of the local wood. In addition, the propagation of failure also depends on the direction of the local fibers. When the stress profile changes from Figures 5.20 a to d, the combined limits vary. In particular, at the lower cross angle as in Figure 3.12 b and in Figure 5.20 a, cracks were first initiated due to the few fused fibers. In contrast, the merged fibers produced the most at the location in Figure 5.20 c, providing the primary resistance to the connection.

To the best of the author's knowledge, few studies [12, 13] have been found on the mechanical properties of wood in weeping figs, and it is then difficult to compare the results obtained accurately with studies under the same loading conditions. In this work, the average tensile strength of a self-growing connection is 0.75 MPa. The derived strength is an effective strength of the entire interface that is modeled as an equivalent planar surface. If strength is considered similar to the stress components in engineered wood, the longitudinal shear of the wood can be compared with the study by Van de Kuilen et al. [14] and the rolling shear strength by Ehrhart et al. [15]. It is assumed that the rolling shear capacity primarily controls the failure. Therefore, it further compares the average value of tensile strength (0.75 MPa) in this chapter with the shear strength (1.88 MPa) in the lowest density interval in the study [15]. However, the test material in this chapter is in fresh condition, which is above the fiber saturation point (30%). In engineered wood, a moisture content of 12% or less is usually used. As suggested in studies [15–17], the shear strength of [15] was reduced due to the high moisture content (above the fiber saturation point), and the result was further multiplied by a factor of 0.3 to obtain 0.56 MPa. The tensile strength (0.75 MPa) obtained in the chapter is slightly greater than the calculated strength (0.56 MPa). However, the approach to obtain the strength is different from each other in two comparable studies. In this study, strength is a combined effect of both rolling shear and longitudinal shear. Whether or not this comparison is reasonable is in doubt. It requires relevant studies in the future. However, some limitations must be pointed out. The weeping fig in this research is a juvenile tree around eight years old, whereas the data discussed and compared from the references are mainly from mature trees whose strength is usually

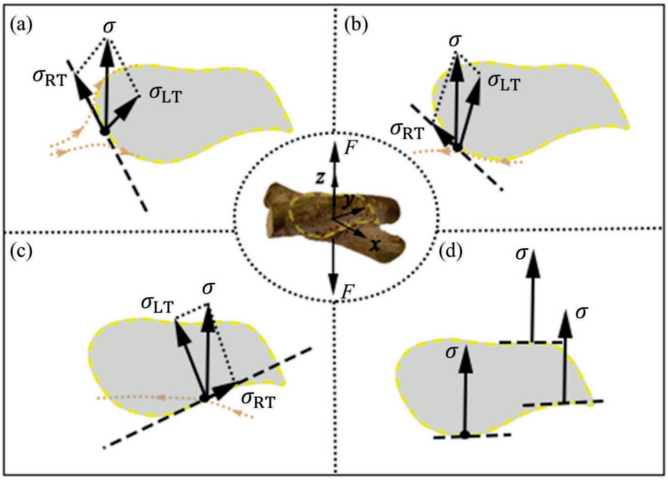

Figure 5.20: Stress components along the interface of a self-growing connection under tension. (a) Stress components at the location where the merged fibers are few and the fusion level is low. (b) Stress components at the location where the merged fibers are greater and the fusion level is higher than that in (a). (c) Stress components at the location where the fusion level is the highest within the connection. (d) Stress components at locations where the scant of the interface is perpendicular to the tensile forces. The yellow dashed lines indicate the interface surface, whereas the brown dotted lines indicate the local fiber direction. The resultant tensile stress σ is decomposed according to the local tangent line along the interface. The symbols L, R, and T represent the longitudinal, radial, and tangential directions, respectively. Merged fibers are shown on a brown dot line; interface in yellow dashed line.

higher than their juvenile trees. Additionally, during mechanical tests, the tension-induced moments transferred to the interface are not considered, but these moments affect the tensile strength of a connection. To what extent the transferred moments influence the strength of a connection, it needs to be further examined.

The design of tensile tests for connections involves a spatial four-point bending test. Shear is used to transfer the load to the interface. The stem is inevitable to bend during the process, resulting in complicated stress distributions at the interface. Both shear and tension deformations appeared in the outline of the interface. Combining the limits of both mechanical strength, a connection can fail. The test's design is nevertheless challenged by the irregular shape of the self-growing connection.

5.5 Concluding remarks

In this chapter, the biomechanical characteristics of self-growing connections were examined. Information from Chapters 3 and 4 was used to quantify the fusion characteristics of self-growing connections. The measured parameters included density, moisture content, cross-angle, cone ratio, diameter ratio, average diameter, fusion degree, and interface curvature. When a customized four-point bending set-up was designed and conducted, the tensile out-of-plane behavior of self-growing connections was obtained. Mechanical properties included tensile strength, stiffness, and load carrying capacity. With the measured date set, an ANN model was developed to predict the tensile strength of the self-growing connection. The main findings of this chapter are summarized below.

1. The fusion related parameters proposed in this chapter, namely fusion degree and interface curvature, can be utilized to estimate of the fusion condition of a self-growing connection without inducing any damage.

2. The force versus deformation curves of the tensile tests show a gradual cracking region in the 0.8 peak load range, which is mainly related to the shape of the interface and the portion of merged fibers. When the fusion degree is less than approximately 15%, the failure occurs at the interface of a connection, but when the fusion degree is greater than approximately 15%, the failure plane crosses the stems to form a 'Y' shape. This failure process is mainly controlled by the combination of rolling shear and the tensile perpendicular strength of the wood material.

3. The tensile strength of a connection has negative correlations with the cone ratio and interface curvature, while it has positive correlations with the average diameter and fusion degree. Among these parameters, the interface curvature has a negative and mediate correlation with the tensile strength (r = - 0.53).

4. Average diameter and projected area have better correlations with the stiffness and load-carrying capacity compared to other parameters.

5. The fusion degree is weakly correlated with the tensile strength (r = 0.24), stiffness (r = 0.21), and maximum load (r = 0.3). In comparison, the interface curvature can better predict the tensile strength of a connection.

6. With 10 hidden layers and using the input dataset, the ANN model can provide a good prediction of the tensile strength of a self-growing connection.

With an understanding of the biomechanical properties of self-growing connections, geometrical and fusion-related parameters can be evaluated to design, monitor and predict the mechanical properties of self-growing connections. After the discussion on *Ficus* connections in this chapter, Chapter 6 will further investigate the larger-scale interconnected tree systems formed by the tree species *Tilia*.

References

[1] F. C. Bao, Z. H. Jiang, X. M. Jiang, X. X. Lu, X. Q. Luo, and S. Y. Zhang. Differences in wood properties between juvenile wood and mature wood in 10 species grown in China. *Wood Science and Technology*, 35:363–375, 2001.

[2] C. Mattheck. *Design in nature: Learning from trees.* Springer Science & Business Media, 1998. Pages 29–65.

[3] F. Ludwig, H. Schwertfreger, and O. Storz. Living systems: Designing growth in baubotanik. *Architectural Design*, 82(2):82–87, 2012.

[4] F. Ludwig. Baubotanik: Designing with living material. In *Materiality and Architecture.* Routledge, 2016. Pages 182–191.

[5] W. Middleton, H. I. Erdal, A. Detter, P. D'Acunto, and F. Ludwig. Comparing structural models of linear elastic responses to bending in inosculated joints. *Trees*, 37(3):891–903, 2023.

[6] M. D. Mylo, F. Ludwig, M. A. Rahman, Q. Shu, C. Fleckenstein, T. Speck, and O. Speck. Conjoining trees for the provision of living architecture in future cities: A long-term inosculation study. *Plants*, 12(6):1385, 2023.

[7] F. Biondi. From dendrochronology to allometry. *Forests*, 11(2):146, 2020.

[8] P. R. Larson. Stem form development of forest trees. *Forest science*, 9:1–42, 1963.

[9] BSI. BS EN 13183-1: Moisture content of a piece of sawn timber. Determination by oven-dry method, 2002.

[10] F. Khademi, S. M. Jamal, N. Deshpande, and S. Londhe. Predicting strength of recycled aggregate concrete using artificial neural network, adaptive neuro-fuzzy inference system and multiple linear regression. *International Journal of Sustainable Built Environment*, 5(2):355–369, 2016.

[11] M. A. Getahun, S. M. Shitote, and Z. C. A. Gariy. Artificial neural network based modelling approach for strength prediction of concrete incorporating agricultural and construction wastes. *Construction and Building Materials*, 190:517–525, 2018.

[12] D. E. Kretschmann. Wood handbook, Chapter 5: Mechanical properties of wood. *Forest Products Laboratory*, pages 1–46, 2010.

[13] L. Wessolly and M. Erb. Manual of tree statics and tree inspection. *Irish Forestry*, 74, 2017. Pages 94–129.

[14] J. W. G. Van de Kuilen, W. Gard, G. Ravenshorst, V. Antonelli, and A. Kovryga. Shear strength values for soft-and hardwoods. In *CIB-W18 Proceedings*, 2017. Pages 49–70.

[15] T. Ehrhart and R. Brandner. Rolling shear: Test configurations and properties of some european soft-and hardwood species. *Engineering structures*, 172:554–572, 2018.

5

[16] J. M. Dinwoodie. Timber—a review of the structure-mechanical property relationship. *Journal of Microscopy*, 104(1):3–32, 1975.

[17] R. Brandner, W. Gatternig, and G. Schickhofer. Determination of shear strength of structural and glued laminated timber. In *CIB-W18 Proceedings*, 2012. Pages 239–254.

6

Biomechanical behavior of interconnected tree systems

This chapter investigated the mechanical characteristics of interconnected tree systems that were fused by self-growing connections from lime trees (Tilia cordata Mill.). Cases studied included single-standing trees, cross-connected trees, and parallel-connected trees. The mechanical characteristics of the tree system were described by its loading capacity, the deformation of the stem and root system, and the rigidity of the interconnected system. This study was conducted by improved pulling tests performed on different defined loading cases, namely, loading in the connected plane (in-plane) and out of the connected plane (out-of-plane). Investigations were carried out in two consecutive years with the aim of understanding the effects of two-year growth on the mechanical behavior of connected trees. The analyzes were based on the results obtained from pulling tests in combination with finite element modeling.

The results revealed that tree growth induced a reduction in deformation, rotation, and local elongations, and in turn, increased the rigidity of the whole system. With respect to cross-connected trees, they showed a significant bracing effect in the plane. Regarding parallel connected trees, the parallel self-growing connection in the lower region increased the basal stiffness but presented an asymmetric behavior under loads.

6

6.1 Introduction

6.1.1 Interconnected tree system

Through the self-growing connection fused naturally by two independent trees, the two connected trees are able to carry and share loads together, and thus act as an intact structural system, which is further defined as *an interconnected tree system.* According to the findings in Chapters 3 and 4, a self-growing connection is formed by the merged fibers that are produced from both of the connecting tree stems. This group of fibers serves as a load-sharing and nutrition-transporting path between two living trees. Furthermore, according to the results of the mechanical tests in Chapter 5, the ability of a connection to transmit loads and its strength are further examined. In principle, these findings provide evidence and support for the applicability of interconnecting living trees.

Chapters 3, 4, and 5 have focused on self-growing connections fused by weeping figs (*Ficus benjamina*). The main reason to choose this species is its fast growing feature, as well as its material availability for research. However, the object studied is limited to a single species only. Furthermore, weeping figs in the study grow in a container, which is a confined condition compared to trees that grow in open soil. To be specific, compared to larger commonly planted trees (e.g., birch, oak, and lime), the studied fig trees have a much smaller size, which has a stem height of approximately 2 m and a diameter at breast height of approximately 25 mm. To this end, this chapter investigates a second species of tree, which is *Tilia cordata.* As shown in Figure 6.1, the *Tree Pavilion* is the object studied in this chapter. It contains two types of interconnected tree system, i.e., parallel connected trees (Figure 6.1 b) and cross connected trees (Figure 6.1 c). In Section 6.2, a more detailed description of the research object will be provided.

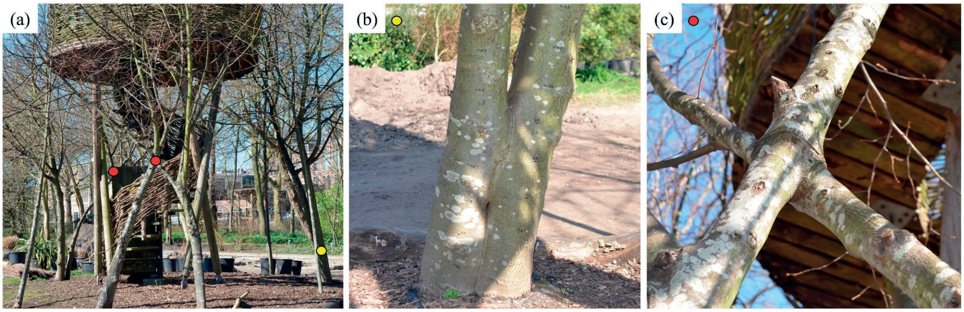

Figure 6.1: Pictures of the living tree pavilion and self-growing connections. (a) The *Tree Pavilion* is surrounded by several pairs of interconnected trees, where red and yellow dots indicate the locations of cross and parallel self-growing connections; (b) parallel self-growing connection; (c) cross self-growing connection. Photos made in January 2022.

Unlike single-standing trees, when two trees are fused together, they form a structure with an asymmetric distribution of biomass with reference to the formation plane which includes the connection. As a result of growth development in geometry and material properties, the interconnected system reacts differently depending on the direction of the applied forces. For example, as shown in Figure 6.1 b, parallel connected trees present a larger value of moment of inertia in the connecting plane but a lower value outside the connecting plane. Thus, this type of interconnected tree system may be at risk of being loaded outside the connecting plane, but it is reinforced within the connecting plane. To the best of the author's knowledge, there is little research on the interconnected trees, especially on their mechano-physical properties, but relevant studies on single trees can provide a foundation for understanding the interconnected tree systems. For example, experimental design approaches, methods of calculating mechanical responses, and the prediction of damage can be referred to studies on single trees, as elaborated in the following section.

6.1.2 Interaction between trees and external loads

Regarding trees, whether they are single-standing or interconnected, they grow in a natural environment. The main source of external disturbances and damage comes from the wind. Most studies on tree risk assessment due to wind usually focus on trees that grow in forests [1–5]. In addition to wind damage, other external loads from nature, such as heavy rain, snow and ice, fire, and excessive heat, as well as soil movement, should also be considered to evaluate the risk of trees in forests. Regarding open trees in urban environments, due to complex growing conditions, the characteristics of trees are difficult to parameterize and less work has been published [6, 7].

The interaction of wind with trees and the processes that lead to tree failure are complex and depend on many factors. Plant damage under wind loading occurs on different scales, as shown in Figure 6.2. The scales range from single needle or leaf damage to individual plants, plant communities, and the regional level. Regarding the wind damage on single trees, the common failure studied includes branch breakage (Figure 6.2 b), stem breakage (Figure 6.2 c) and uprooting failure (Figure 6.2 d).

To evaluate the performance of trees during wind loading, a variety of techniques have been proposed. At an early stage, many researchers [9–11] applied mechanical theory to a simplified tree structure to understand the deformation and stress distribution of the tree stem. In the theoretical approach, a tree is modeled as a fixed tapered beam to the ground, and the applied calculated method is based on the mechanical theory of a cantilevered beam. This approach provides theoretical foundations for understanding the interaction between trees and loads, but it is impossible to directly quantify the variations from many factors, such as tree species, crown shape, and root characteristics.

The second group of techniques, which has also been widely applied in forestry, is called mechanistic models such as GALES, HWIND, and FOREOLE [1, 3, 12]. The susceptibility of a forest stand and trees within a stand to wind damage is controlled by many factors. They include properties of wind climate (i.e., wind speed, duration and gustiness), forest and tree structures and characteristics, such as tree species, tree height and diameter, crown area and shape, root mass and architecture, soil properties, etc. In addition to the general parameters, in response to wind, trees move dynamically and with consequent short-term vibration and oscillatory motion. Meanwhile, their crowns are streamlined and the stem may be deflected. Trees also respond to the prevailing wind load by growing compression or tension wood. When aiming to predict the wind threshold and damage to trees accurately, all the parameters mentioned above should be taken into account both in the static condition and in the dynamic condition. However, it is not realistic to make a decision to obtain accurate mechanical performance at the expense of extensive

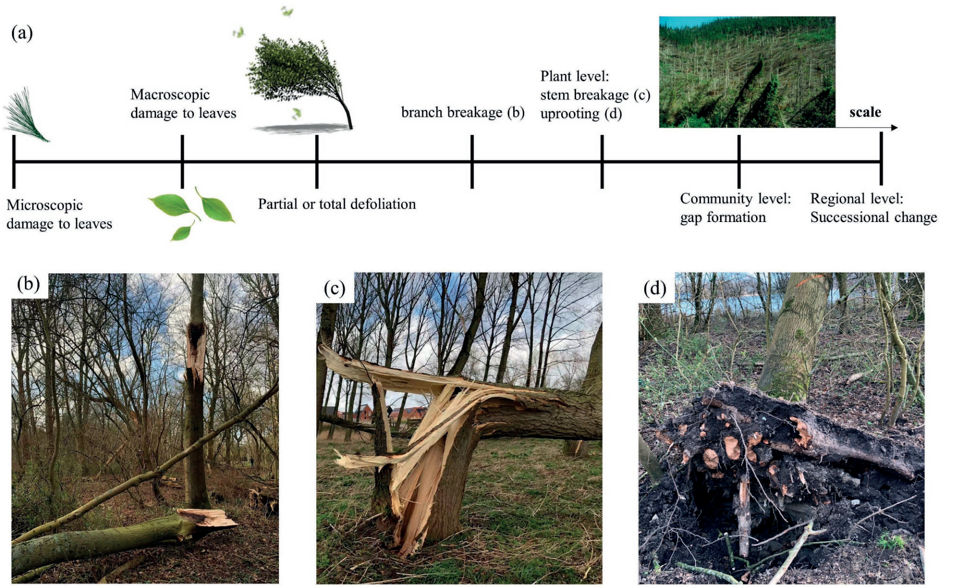

Figure 6.2: Tree damage caused by wind loads. (a) Wind damage to trees at different scales, modified from [8]; (b) branch breakage; (c) stem breakage; (d) uprooting failure.

6

measurements of every parameter.

The general approach of mechanistic modeling is a combination of empirical pulling results and mechanical analysis in terms of the simplified tree shape. In the mechanistic modeling, the wind profile is determined based on the characteristic and climate of the studied site. Wind loading and gravity forces on a tree are calculated at each height segment based on predefined distributions. Theoretically, it is assumed that a tree deflects to a point of no return as a result of static loading where the wind is assumed to have a constant speed, and thus is considered as static loads. In this circumstance, it is assumed that a tree has failed (i.e., lose its stability) when the applied bending moment of a tree exceeds the maximum resistance of the tree stem to breakage (Figure 6.2 c) or of the root system to overturning (Figure 6.2 d). Thus, the stability of a tree is affected by external loads and gravity, which include the mass and mass distribution of the stem and crown. The resistance of the stem to failure depends on the strength limits of the wood. Similarly, the resistance of the roots to uprooting depends on the characteristics and properties of the root and soil system.

In Figure 6.3, the interaction between trees and wind loads is summarized. Figures 6.3 a and b explain the forces applied to the tree structure and the resisting forces that reacted. The factors influencing the vulnerability of trees to wind damage are summarized in Figure 6.3 c.

Although the development of the mechanistic approach is based both on mechanical theory and on test results, an accurate prediction of failure is still limited by the complexity of the factors involved. Therefore, practical measures have been taken to directly predict the safety of trees. For example, with regard to the resistance to stem breakage, Gardiner [1] and Peltola [3] suggested that the third power of the diameter of the stem at breast height best predicted the maximum resistance to bending, regardless of the species of trees. For resistance to uprooting, they also suggested that the best predictor is stem volume (i.e., the product of tree height and the second power of diameter of breast height). These indicators are decided based on allometric relationships [13] between the weight of the crown, stem, and roots of the tree. Furthermore, these simplifications make sense on the basis of casual relationships between tree geometry characteristics and maximum resistance moments.

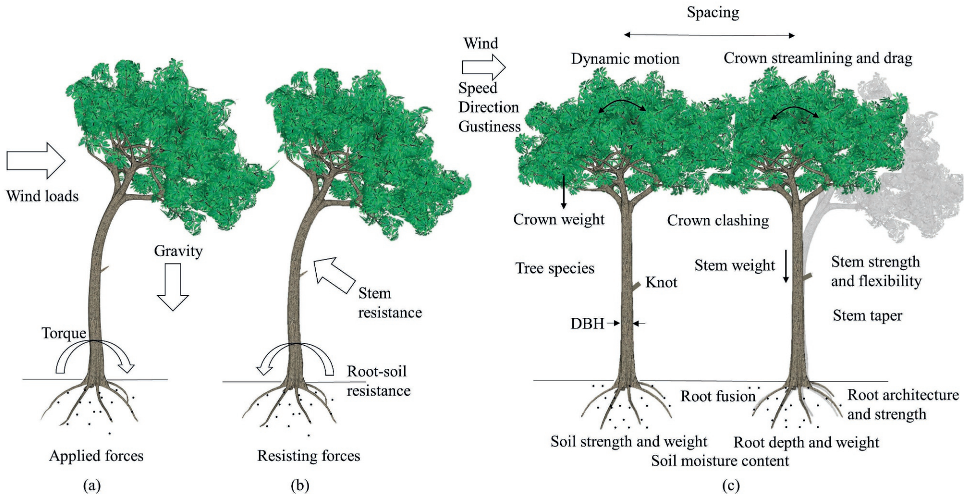

Figure 6.3: Interaction between wind and trees. (a) Applied forces; (b) resisting forces; (c) factors influencing the vulnerability of trees to wind damage (critical wind speed). (a) and (b) are modified from [4]; (c) is modified from [14].

However, from these predictive relationships by using stem information, it suggests that when a tree grows older, it becomes relatively easier to be uprooted, as the tree stays at the same height when it matures, which is not always the case in reality. As stated in the comparison between different models [2], this mechanistic modeling approach is very practical and feasible to use in forestry by providing information on the evaluation and management mechanism of wind risk. However, it is limited by tree species, as it focuses mainly on softwood forests (e.g., Sitka spruce in [15], Norway spruce in [3]). Moreover, it is also limited by the analysis of the dynamic interaction of wind and trees. Furthermore, although this approach has been attempted to extend from the stand level to individual trees [12], it is still not able to provide accurate performance for individual trees.

To understand the method and process of tree uprooting, several researchers further investigate the root anchorage of individual trees [16–22]. The anchorage stability of a root system can be understood in terms of the degree to which the root systems respond to the mechanical forces transmitted to them. To better quantify this reaction, the rotation angle is usually measured and considered as a function of the turning moment [21]. Previous

6

studies suggest that the resistance moment reaches its maximum when the base deflection angle is around 2 to 4 degrees [17, 21, 23, 24]. In the mechanistic model [1], it predicts that overturning occurs when the angle of the tree stem is in the range of 5 to 8 degrees from the vertical. Regarding the mechanism of the uprooting process, Coutts [17] was one of the first to investigate the components of the anchorage of tree roots. He correlated the anchorage with several components, such as the mass of the root-soil plate, the strength of the windward roots, the strength of the root hinge, and the soil strength that interacted with the root systems. Stokes [22] investigated the influence of different site conditions, as well as different stages of growth, on the anchorage of softwood trees by pulling tests. Nicoll [18] studied the influence of root depth, soil type, and site characteristics. Deep rooting was found to increase critical turning moments by 10 - 15% compared to trees of equivalent mass with shallower roots.

Understanding root anchorage is developed from empirical studies to numerical modeling. To better understand the influence of root architecture on the root anchorage mechanism, Dupuy [25] used a 2D FEM to simulate overturning processes in trees and to determine the role of individual roots in tree anchorage with respect to root patterns. Furthermore, he developed a 3D FEM by incorporating real root system architectures to characterize anchorage mechanisms during tree regrowth with respect to soil types [26]. With the development of experimental techniques, a combination of the terrestrial lidar scanning approach with FEM [27, 28] has been applied for the analysis of tree dynamics. However, because the parameters involved are many and their interactions are difficult to describe and quantify, it is difficult to draw a generalized conclusion.

6

The most common and widely used experimental method on tree stability as mentioned above is referred to as a static pulling test [4, 5, 8, 22]. Wind loads are simulated by pulling trees with a winch and cable system. Therefore, the critical force, in other words, static wind load is based on the recorded peak of the applied winching force to fail the tree. Traditional pulling tests usually pull a tree to failure in a destructive way. Furthermore, the recorded parameters are only the force history and base rotations. As an improvement, Brudi and Wessolly [24] proposed the elasto-inclino approach to pull a tree within an elastic region without causing further damage to the growth of a tree. During the test, the strain monitored at the positioned locations and the rotation at the base are monitored in the range of elastic deformation. From the collected data, the failure threshold is predicted from the elastic limits of a tree.

6.1.3 Research structure and objective

In this chapter, as stated above, we focus on the biomechanical properties of interconnected tree systems. Three main knowledge gaps have been identified. First, the living system has an irregular connecting shape, which induces different mechanical responses in terms of various loading cases. It is not clear how this system reacts to external loading. Secondly, to quantify mechanical behavior and measure relevant parameters (i.e., stiffness, maximum loads, stress, and strain distributions), there is no standard testing program regarding interconnected trees. Third, when this system grows over time, the influence of enlarged geometry and increased self-weight on the mechanical performance of the system is not known; and there is no predictive method to assess.

Based on the identified challenges, this chapter is organized in several steps.

1. The procedure for pulling tests is designed and improved to customize the measurements on interconnected trees.
2. The mechanical responses of the interconnected trees under different scenarios (loading in the connecting plane and outside the connecting plane) are then analyzed based on a combination of pulling results and FEM estimation.
3. The designed pulling tests are performed in two stages with a growth difference of two years.

In this way, a better understanding of the development over time of the mechanical properties and the influence of growth ring formation of the interconnected trees and their rigidity may be obtained. Furthermore, since the pulling test is a complex method, the repeatability and comparability of this test are an additional aspect under consideration.

6.2 Materials and methods

6.2.1 Interconnected tree systems: Description and measurement

Description of interconnected trees

The object of the study is the *Tree Pavilion* located at the TU Delft Hortus Botanicus. The construction of the living tree pavilion was carried out in November 2010 and the selected trees were small-leaved lime trees (*Tilia cordata*). All trees planted were five years old in 2010. Therefore, in 2020, the studied trees were 15 years old, which included five years of growth before planting and 10 years of growing in the garden. Consequently, in 2022, the trees studied were at age 17. In the following content, the first growth stage studied was termed stage I at the age of 15, as stage I; and the second growth stage was termed stage II, at the age of 17.

In this structure, two types of self-growing connections were created. Parallel and cross connections, as in Figures 6.1 b and c, respectively. The technique used to fuse the connection was simple and straightforward. Two stems were tied together in pairs with an elastic rope after planting in 2010. This group of trees has been maintained regularly to keep a healthy growth condition. As shown in Figure 6.4 a, this group of trees was planted in a circle shape surrounding the middle point 'O', and they were numbered from the bottom right corner clockwise. Thus, as sketched in Figure 6.4 b, the objects studied in this chapter involve three types:

1. Single standing tree 10B;
2. Cross connected tree system 9B-10A;
3. Parallel connected tree system 6A-6B.

The parallel connection (Figure 6.1 b) was fused by trees 6A and 6B. The cross connection (Figure 6.1 c) was formed by tree 9B and tree 10A. The parallel connection was located in the lower part of two trees approximately 0.5 m above ground, and the cross connection formed at a height of 2.2 m, above the location of the first branch in tree 9B. In this chapter, the names of the objects were kept the same as they were labeled in the *Tree Pavilion*, trees 1, 7, 9B, 6A, and 6B will be studied in Chapter 7.

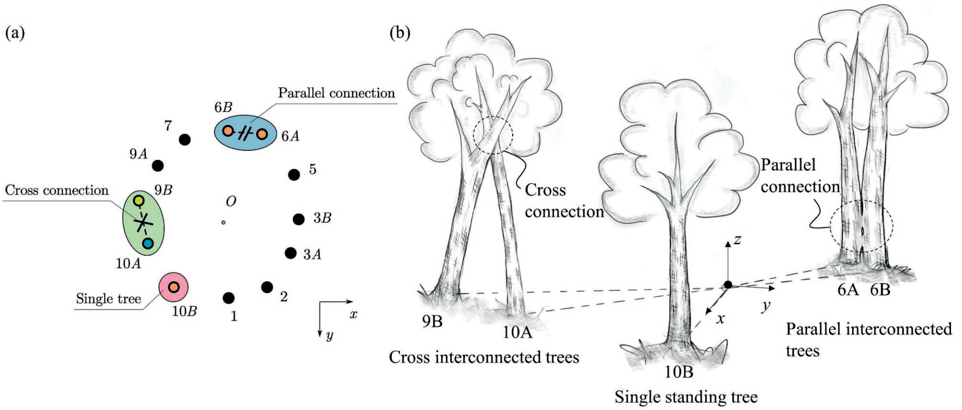

Figure 6.4: Configuration of single and interconnected tree systems. (a) Horizontal layout of tree distributions, where ellipse circles indicate locations of studied trees and dark dots are surrounding planting trees; (b) sketch illustration of appearance of studied trees.

Definition and measuring approach

This work aims to measure and test the mechanical behavior of interconnected trees in response to different loading directions. The definition of the loading plane needs to be clarified. Meanwhile, to understand the stress and strain distributions considering the real geometry of trees, the method to measure and model the irregular shape of a tree (i.e., tapered stem, elliptical cross section, and inclination) needs to be described.

The irregular shape of a tree was measured primarily in the stem region within the height range of 3 m. As sketched in Figure 6.5 a, the cross-connected system was taken as an example. When two independent trees (9B and 10A) fused together, the plane zy contained the cross connection. The centroid of the coordinate system was placed in the middle location of the pavilion (point ‘O’ in Figure 6.4 a). Mechanical loading in plane zy was defined as in-plane loading, while loading outside this plane was referred to as out-of-plane loading.

A tree was first segmented at every 10 cm (H_0 = 10 cm) increment from the base of the stem to the top. As sketched in Figure 6.5 a, the point P_i in the segmented cross section toward the inner centroid O was measured to locate the coordinates ($P_i(x_i, y_i, z_i)$). This point was measured by projecting the location onto the xy plane. The x and y coordinates were determined in reference to the local coordinate system. From this point on, in the cross section containing the point P_i, the diameters (D_{ai} and D_{bi}) in two perpendicular directions and the circumference of this elliptical section were measured.

Figure 6.5 b showed an example of the measurement of P_9. Figure 6.5 c illustrates the approach to construct the shape of the tree by measured points, cross sections, and segments. For example, when the coordinate of point P_9 was determined, three points in the elliptical shape of the cross section could be determined by measuring the diameters in

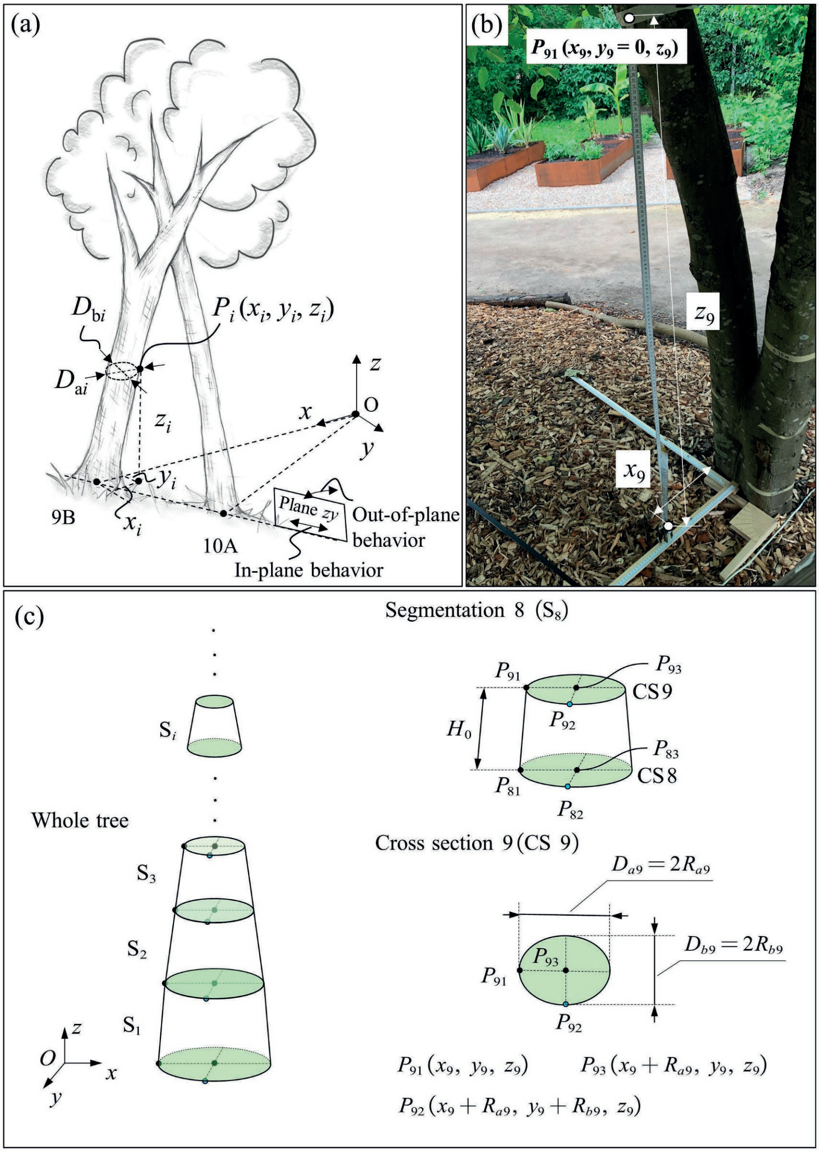

Figure 6.5: Measurement of the geometric shape and reconstruction of a tree. (a) Sketched example of measuring coordinates of P_i. The location of a tree is measured according to the coordinate system located in the planting center O. At every 10 cm (H_0), the diameters are measured in the x (D_{ai}) and y (D_{bi}) directions. The point towards the centroid is specified by its coordinates ($P_i(x_i, y_i, z_i)$). The connected trees are in the plane zy, thus, structural response in the plane zy is the in-plane behavior, and the other perpendicular direction is out-of-plane behavior. (b) Practical example of the measurement of point P_9 in interconnected trees. (c) Reconstruction of the geometric model of a tree based on segments. Segments are constructed based on cross sections that are mapped by edge points together with diameters in the x and y directions, as described in (a) and (b). An example of segment 8 is shown.

two (x and y) directions. Thus, each segmentation could be built up based on the cross sections. With the determined segmentation, the entire tree could be reconstructed.

The perimeter was measured with a soft ruler and the spatial coordinate distances were measured with custom triangle tools and a caliper. The resolution of the measurement was 1 mm, as seen in Figure 6.4 b. All activities were carried out avoiding branches and knots. Measurements of the study objects were made on June 12, 2020 and June 10, 2022 to compare their growth. The measured geometry was recorded and used to reconstruct the finite element model (FEM) for numerical analysis.

In Table 6.1, the geometric information of the measured trees is provided. The diameter at breast height (DBH) of a tree was measured at a height of 1.5 m. The slenderness of a tree was determined by the division between height and DBH. The volume of the stem was calculated to be limited to the measured height, which was within 3 m height.

Table 6.1: Geometric information of investigated single and connected trees

Type	ID	Height (m)		DBH (cm)		Slenderness		Stem volume (cm^3)	
		I	II	I	II	I	II	I	II
Single standing tree	10B	6.2	8.0	10.6	14.0	58.5	57.1	28600	48500
Cross interconnected trees	9B	6.0	7.5	10.0	12.6	60.0	59.5	18400	30100
	10A	5.5	7.0	4.9	6.7	112.2	104.5	7500	12200
Parallel interconnected trees	6A	7.3	8.0	11.9	14.2	61.3	56.3	25500	39000
	6B	7.3	8.0	10.0	12.4	73.0	64.5	18700	29100

Notes:
- Slenderness = Height / DBH;
- I indicates tree age 15 and measured on June 2020; II indicates tree age 17 and measured on June 2022.

6.2.2 Design of pulling tests

The purpose of pulling tests on single and interconnected trees was to investigate the mechanical performance of the tree system under horizontal loads as a static simulation of wind forces, and thus to estimate the loading capacity and influence of the connection to tree stability.

In this work, pulling tests were designed and customized according to the features of living tree systems. The testing program was carried out and repeated in two stages, first in June 2020 (stage I) and second (stage II) in June 2022. The test setup, loading cases, and measured locations for each test piece were the same in the two stages. The primary difference between the two stages was the growth and development of the studied trees. Therefore, in the following content, a brief explanation of each testing program will be presented.

Pulling test setup

Figure 6.6 presented the sketch of the test setup for cross interconnected trees 9B and 10A as an example. The setup consisted of two inclinometers, three elastometers, a forcemeter, an anchored roller, and a data logger. The external force was applied through a winch that was pulled from a roller anchored to a car. A force meter (PiCUS TreeQinetic testing system, Germany) was connected to the winch to measure the tension forces through the cable, which was equal to the pulling force.

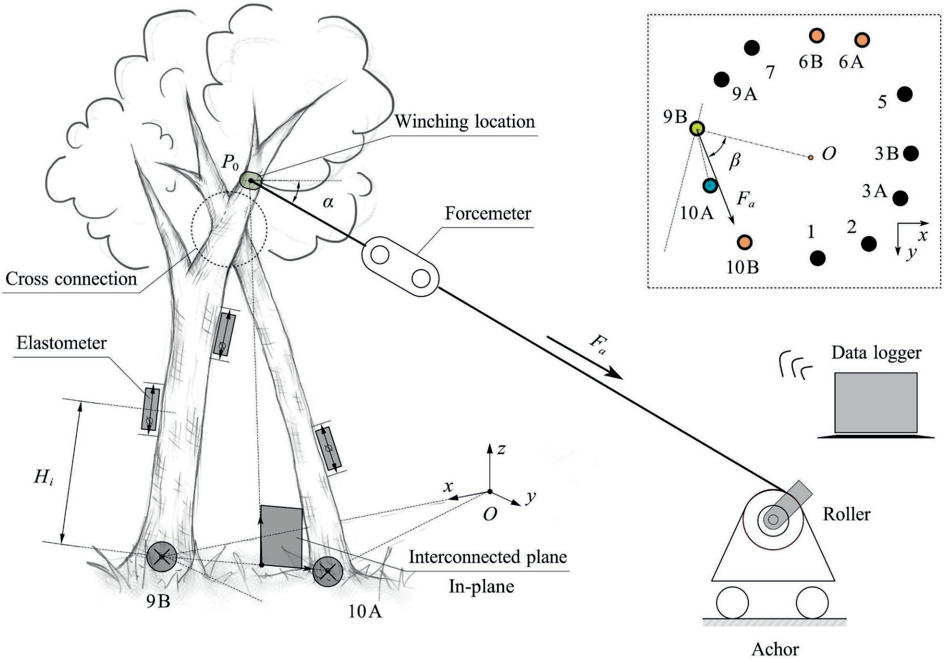

Figure 6.6: Illustration of the setup for pulling tests. This example presents the test on the cross connected tree 9B and 10A, which is defined as the in-plane loading case. Angles α and β indicates the spatial direction of the force (F_a) applied at P_0 in reference to tree plane and vertical direction. Elastometers and inclinometers are positioned along stems and at the base of the tree in respect to the loading direction. For example, in this case, the elastometers are positioned on the compressive and tensile sides along the stem. The vertical location of one example elastometer is measured at height H_i.

The force meter had a resolution of 0.01 kN and an accuracy of 0.3 kN. The rolling speed for each test was controlled by hand, ranging from 50 to 100 mm/min. For each test case, it took approximately 6 to 8 minutes. When the force was applied, the direction of the force was measured in two directions. One direction was the angle to the horizontal direction, denoted as α, and the other angle was measured from the projected direction to the centroid of the coordinates, marked as angle β.

In order to monitor the bending response of the tree, inclinometers and elastometers (PiCUS TreeQinetic testing system, Germany) were positioned. Figures 6.7 a and b showed the measurement setup and the device installation process. The elastometer was used to measure the elongation of the marginal fiber along the tree stem. It had a resolution of 0.1 μm. The mechanism of elastometer measurements was through the detection of movements between two steel pins that were inserted into the marginal fibers of the stem with a depth of approximately 2 cm from the bark. The distance between two steel pins was 198 to 202 mm, averaged 200 mm in this work. In the basal region of a tree, an inclinometer was placed, in which the rotation was measured parallel to the force direction and perpendicular to the force direction. It had a resolution of 0.002°.

For each of the test scenarios, as shown in Figure 6.6, three or four locations were selected to measure the strain distribution along the tree. According to the study by Wessolly and Brudi [23, 24], strains tended to have a relatively higher value within the region of one-third and two-thirds of the height of a stem. Meanwhile, the location at the breast height was the most commonly used location for measurements of tree characteristics and prediction of failure [4, 8]. Therefore, the locations selected to monitor the failure included 0.8 and 1.4 meters, and other measured locations were listed in Table 6.2. The measuring locations were also selected to avoid any knots.

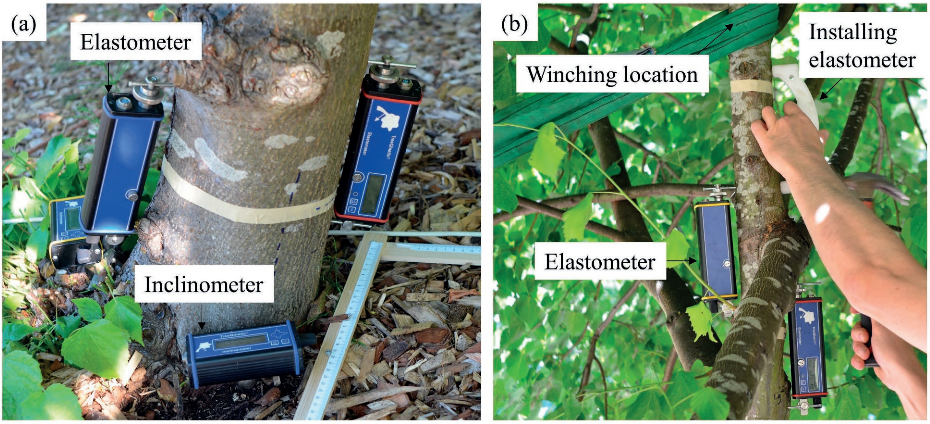

Figure 6.7: Picture of the device for measurements. (a) Example position of elastometers and inclinometers; (b) installation of elastometers.

Testing groups

The pulling tests were first categorized into three groups according to the type of interconnected system. They included single tree 10B, cross interconnected trees 9B and 10A, and parallel connected trees 6A and 6B. The group of trees 9B and 10A was divided into four loading cases. Since only three elastometers were available, three repetitive tests under the same loading case were performed to collect more measurements.

- Group 1: Single standing tree 10B.
  As seen in Figure 6.8 a, the 10B single standing tree was tested using the classic pulling method. It was used as a reference test. The measured locations were selected at heights of 0.2 m (H_1), 1.4 m (H_2) and 1.9 m (H_4); the winch was placed at a height of 2.8 m (H_F). The purpose of this testing group was to understand the strain distribution in a single standing tree while pulling it with a winch. It was also used

to calibrate the FEM model to obtain reaction forces according to the collected strain distributions.

- Group 2: Parallel interconnected trees 6A and 6B.
  As shown in Figure 6.8 b, trees 6A and 6B connected in the lower part, which differed from the single standing tree in increasing biomass and rigidity in the lower region. With respect to this type of system, it was only tested in the out-of-plane direction. The measured locations can be found in Table 6.2.

- Group 3: Cross interconnected trees 9B and 10A.
  The cross-connected trees were tested in two main cases: Out-of-plane (Cases C1 and C2) and in-plane (Cases C3 and C4) tests.

  Cases C1 and C2 of Group 3 were performed in the out-of-plane direction of the connected trees, as in Figures 6.8 c and d. It meant that the loading direction was perpendicular to the connection line of 9B and 10A. The differences between these two cases were that case C1 (Figure 6.8 c) was loaded on the connection directly; while case C2 (Figure 6.8 d) was loaded on tree 9B at the height of 2.5 m. Case C1 focused on understanding the load sharing between two trees; and case C2 simulated the case when the connected trees were subjected to moments and shear force in the in-plane direction.

  Cases C3 and C4 of Group 3 were tests performed in the in-plane direction. In case C3, the force was intentionally applied in the vertical direction in comparison to the resultant force in case C4. Case C4 applied the forces on tree 9B to obtain the strain distributions, as seen in Figures 6.8 e and f.

The measuring locations and the direction of the applied forces in terms of each case are listed in Table 6.2.

Table 6.2: Loading groups and heights at measured locations, symbols correspond to Figure 6.8

Group	ID	Measured location (m)					Force direction (°)	
		H_1	H_2	H_3	H_4	H_F	α	β
Single standing tree	10B	0.2	1.4	1.9	2.5	2.8	12.6	10
Cross interconnected trees, 9B-10A	C1	0.4	0.8	1.5	-	2.2	10.5	50
	C2	0.4	0.8	2.2	2.4	2.5	17.2	50
	C3	0.4	0.8	2.2	-	2.5	90	-
	C4	0.4	0.8	2.4	-	2.5	29.1	65
Parallel interconnected trees, 6A-6B	6A6B	0.2	0.5	0.8	-	1.9	19.2	89

Elastic thresholds

The pulling tests were not intended to cause any damage to the tree during loading. Thus, the tests were performed in the elastic region, which might not disturb the growth of the tested trees in the future. According to studies by Brudi and Wessolly [23, 24], the

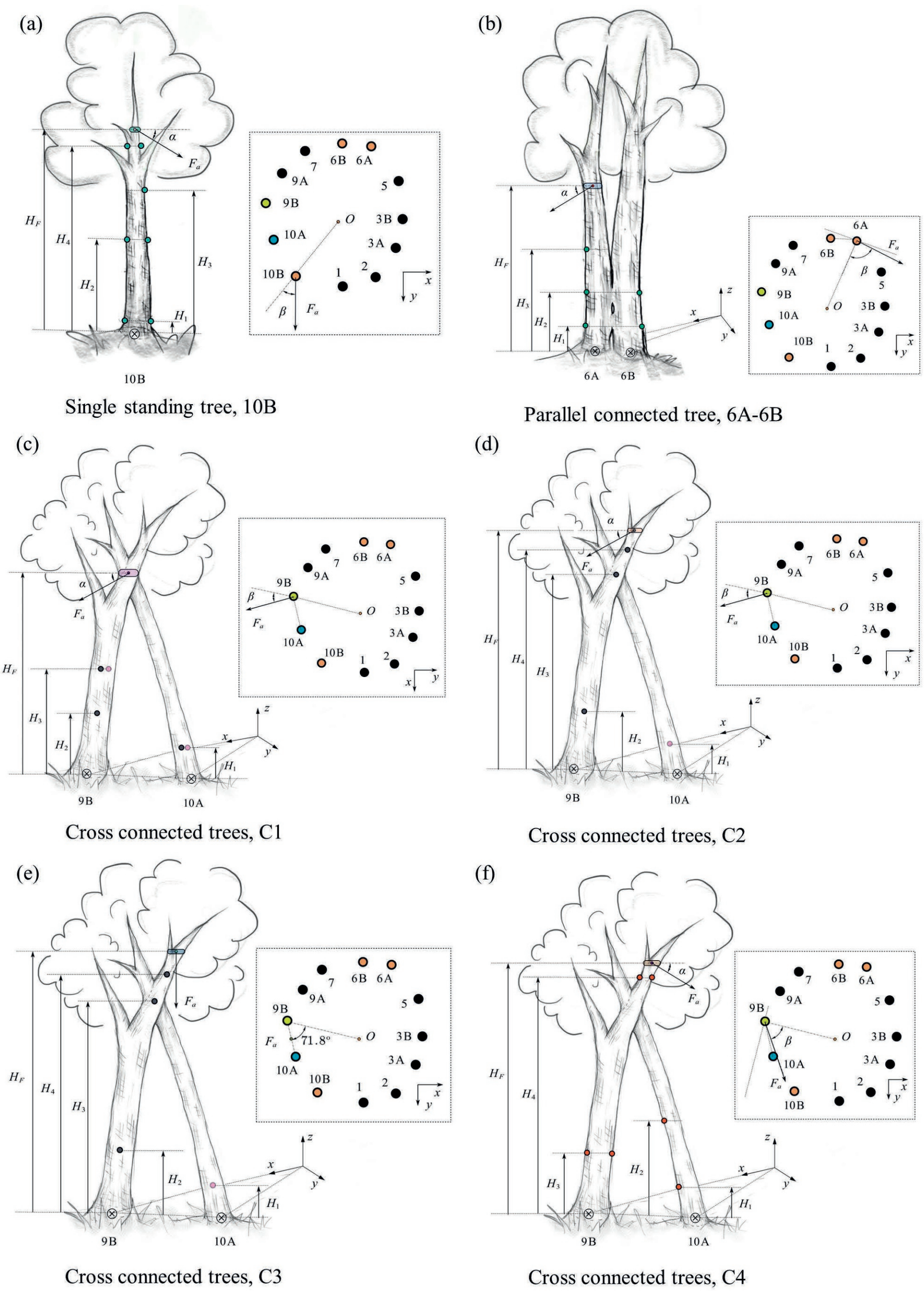

Figure 6.8: Sketch illustration of the loading cases. (a) 10B: Group 1 single standing tree 10B; (b) 6A6B: Group 2 out-of-plane pulling test on parallel connected trees 6A and 6B; (c) C1: Group 3 out-of-plane loading on the connection of cross-interconnected tree 9B and 10A; (d) C2: Group 3 out-of-plane loading above the connection of cross-interconnected tree 9B and 10A; (e) C3: Group 3 vertically in-plane loading above the connection of cross-connected tree 9B and 10A; (f) C4: Group 3 horizontally in-plane loading of cross-connected tree 9B and 10A. The symbol H indicates the height of the measured location; α and β denote the angles of the applied force. Specific magnitudes are referred to Table 6.2.

elastic deformation of a tree can be monitored and controlled by measured instant strains and rotations within the elastic thresholds during tests. Therefore, the strains monitored during the testing were limited by 300 μm maximum, i.e., 0.15% elongation or compression. Meanwhile, the rotational threshold was set at 0.05°. During the test, when any of these measured locations reached the defined thresholds, the test was terminated.

6.2.3 Numerical analysis by FEM

The use of FEM analysis in ABAQUS was to facilitate the analysis of the stress distribution and reaction forces and moments. This was because when the tree reacted and bent due to the external force, the leaning portion of self-weight in the stem and canopy, i.e., the second order of effect, could provide a good estimation from FEM. Taking into account the characteristics of the tree (i.e. irregular cross sections and inclination of the stems), the reconstruction of the model was based on the measurements as stated in Figure 6.5.

The stem region was modeled as stacking solids, which is presented in Figures 6.9 a and b. The centerline of each tree was made by connecting the center points of each segment (e.g., P_{82} and P_{92} in Figure 6.5 c). The direction of the fibers in each tree follows the direction of the constructed centerline. Compared to trees 9B, 6A, and 6B, the direction of the stem of 10A was curved and was defined by the local coordinate system that followed the centerline of the stem. In the region of connection, the stem's position was first established. It was based on measurements of diameters in both directions and the determination of the edge point. After creating the stem, the connection was created by performing a Boolean operation in ABAQUS, from which the two trees were combined together to form a single entity.

In previous chapters, the results showed that the fiber bundles around the fused region were complex and difficult to quantify (Figure 3.18). Figures 6.9 c and d provided detailed information on the connections. The fiber direction of elements in the intersected area was assigned the same direction as the larger stem. In particular, in the cross-connected trees 9B-10A, tree 9B had a larger diameter in the connected region. Thus, the fiber direction in the connected region (overlapped region) was assumed to follow the stem direction of 9B without deviations. The fiber direction of the other part of 10A was assigned the same direction as the stem direction of 10A, as indicated by the red arrows in Figure 6.9 c. In Figure 6.9 d, the fiber direction in the merged region followed the stem direction of 6A; and the other part follows tree 6B.

The modulus of elasticity of the investigated lime tree for the FEM analysis was not measured directly, but was referred to information from [23] and put as 8300 MPa as listed in Table 6.3. Density was put as 1000 kg/m^3 as indicated in [29]. Green wood was modeled as homogeneous solid using element C3D10. The mesh size was determined to be approximately 25 mm in length. According to EN384 [30], the ratio between longitudinal Young's modulus and perpendicular Young's modulus was determined as 15; and the ratio between longitudinal Young's modulus and shear modulus was determined as 16. The crown of the tree was simulated as a mass located at the top of the measured stem. The weight ratio between the crown of the tree and the stem was set as 0.3 following the reference in [31]. All parameters are listed in Table 6.3. It should be noted that in Table 6.3, using single and simplified values to represent mechanical parameters, such as a simplified value for Young's modulus for a living tree, has its advantages and disadvantages. The

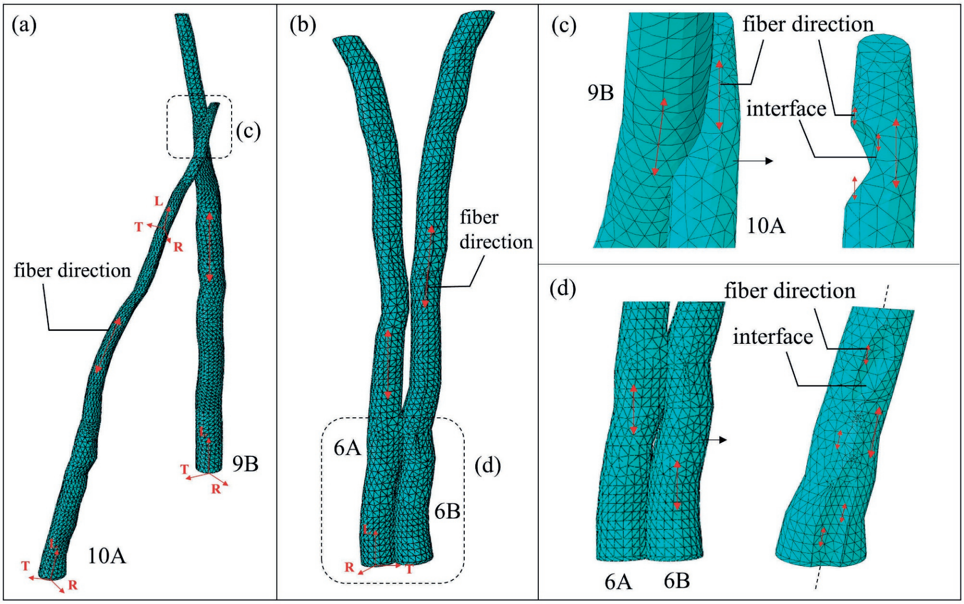

Figure 6.9: Method to reconstruct the tree model in FEM. (a) Generation of cross connected trees 9B-10A based on the measured segments described in Figure 6.5 c; (b) reconstruction of parallel connected trees 6A-6B; (c) determination of the fiber directions of the cross self-growing connection; (d) determination of the fiber directions of the parallel self-growing connection. Two-way arrows indicate the direction of the wood grain.

6

single values can help simplify the models and facilitate understanding of the mechanism. However, this approach overlooks important details and variations in material properties. For example, the Young's modulus in the branch is different from that on the stem of the tree [32]. Moreover, it is also difficult to capture the complex heterogeneous nature of biological materials; and it may not accurately reflect differences in mechanical properties among different types of trees or parts.

Table 6.3: Input parameters for FEM modelling of trees

Density (g/mm^3)	**Stem to canopy weight ratio**	**Young's modulus (MPa)**			**Shear modulus (MPa)**			**Poisson's ratio**		
ρ	W_{canopy}/W_{stem}	E_L	E_R	E_T	G_{LR}	G_{LT}	G_{RT}	μ_{RT}	μ_{RT}	μ_{RT}
0.001	0.3	8300	553	553	519	519	51.9	0.4	0.2	0.2

In general, the loads applied in the FEM model included the gravity of the canopy and stem, and the applied external force of during the tests. The single standing tree 10B was the reference test to calibrate the Young's modulus in the FEM model, and the calibration revealed that the Young's modulus was found to have good agreement with the measured local strains when it was set at 8300 MPa.

It should be noted that in the modeling, the applied force value was set at 1000 N. The main consideration behind this approach is that it allows for convenient comparison of load responses under different loading cases at this specific value. It also enables observation of the region beyond the elastic strength limit reaching 20 MPa. The reaction force and the moment at the base were extracted from the FEM results when the applied force was set at 1000 N. Furthermore, the stress and strain distributions were extracted to facilitate the identification of weak regions. Weak regions mean the area that experiences the relative highest level of stress within the interconnected trees. The advantage of the model was that it can give a relatively accurate value of the reaction moments and the stress distribution. The methodology will be explained in further detail in combination with the experimental results in the following section.

The direction of the forces applied in the FEM modeling was consistent with the measurements of the pulling tests. In the pulling tests, the measured forces were recorded in two directions, namely horizontally and vertically, and were recorded in Table 6.2. In the FEM model, the horizontal and vertical forces were applied separately according to the measured angle. The forces were loaded in linear steps on the loading time. In the chapter, the mentioned 1000 N for comparison was referred to the resultant force considering both vertical and horizontal forces.

In the FEM model, the forces were applied through the reference points coupled with the surface where the rope was tied in the pulling tests. The boundary conditions were applied to the bottom surface of the trees through coupled reference points. Fixed conditions were used. The resisting moments were extracted from the reference points.

6.2.4 Results analyzing method

Figure 6.10 summarizes the framework of the methodology implemented in this chapter using the parallel connected tree 6A-6B as an example. The entire investigation included two stages (stage I and stage II) with a two-year difference in growth. This growth increase was obvious, as observed in Figure 6.10 in the dashed region. The gap between parallel connected trees closed after two years of growth. Experimental investigations were carried out in the two stages with the same setup and measurements.

As explained in previous sections, the collected data had three types. First, the growth information of the investigated trees, i.e., geometric changes. This information was collected and explained in Section 6.2.1. With this information, the FEM models were constructed.

Second, the measured mechanical data from the pulling tests included applied force, force direction, deformations, and basal rotations. The measurement of tree bending deflection was not applicable in these tests. Due to the fact that in these tests, it was not feasible to install measurement points and reference points in the field test. Therefore, only local elongations were collected.

The third type was the estimated results from FEM, including reaction forces and moments, and stress estimates. To this end, the obtained data involved applied force, strains, rotations from experimental tests, and the resisting moment and stresses from FEM analysis. The combination of the two types of data sets could provide a complete picture of the tree system in response to the applied forces.

6

Since the loading process was performed manually by rolling the cable from the anchored roller, the collected data had a certain fluctuation. Furthermore, in the experiments, the tests were stopped by controlling the measured point in the elastic threshold, so that the loads obtained were not the same for different test conditions. To make the cases comparable, the analysis process of the results had several steps.

1. Linear regression. The experimental data were first regressed to a linear function considering that the tests are performed in the elastic region. The regression was performed on forces versus strains, forces versus rotations. The determination of the parameters within the analyzed function was based on the maximum coefficient of determination.

2. Location of the failure indicator. The determination of weak or failing spots was based on the regressed trend of strains from the experimental tests and the stress distributions of the FEM. The point at which the maximum strain, maximum stress, and rotation was reached was the weak point and was used to predict the maximum force. Since the lime trees studied were relatively young, the maximum rotational capacity of the tree was established at 5° according to [17]. The strain and stress limits before failure was set at 0.24% and 20 MPa, respectively, as stated in the table in the Appendix in [23].

3. Extrapolation based on the location of the failure. The load carrying capacity was determined by extrapolating from the weak location. This information was used to compare changes in load capacity in different systems and stages.

4. Comparison between two stages of growth. As shown in the last stage in Figure 6.10. The comparison of stains in two growth stages was based on regressed results from

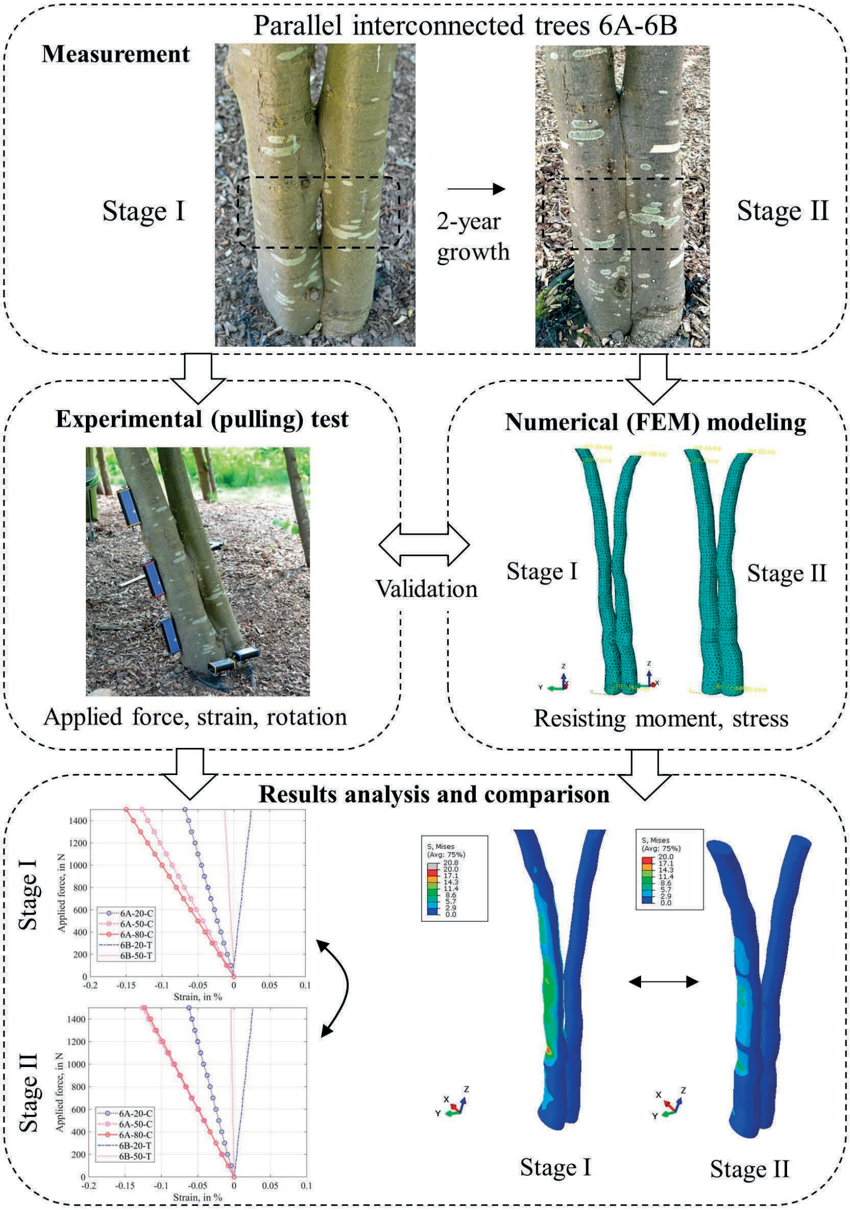

Figure 6.10: Framework of the analysis method and process.

experimental tests. The comparison of the stiffness of the roots was based on the regression between the reaction moments from the FEM and the regressed rotation from the pull tests under the same applied force. The comparison of stresses was based on the results from FEM.

According to the study by Lundstrom et al. [21], the anchorage of the root system was a function of rotation. In this work, the anchorage of the root system in one direction (in-plane or out-of-plane) was defined as the ratio of the reaction moment divided by the measured rotation in this direction, as in Equation 6.1.

$$K_r = \frac{M_r}{\varphi} \tag{6.1}$$

where K_r is the anchorage of the root system, in N·mm/deg; the M_r is the resisting moment obtained from FEM analysis according to the applied force of pulling tests, in N·mm; the φ is the rotation angle measured from pulling tests.

6.3 Results and analyses

The results are presented in the order of the testing groups, i.e., Group 1 single tree 10B, Group 2 cross connected tree 9B-10A from C1 to C4, and Group 3 parallel connected tree 6A-6B. In each group, the results of two repeated stages are compared to better understand the effect of growth on mechanical behavior.

The measured locations are denoted as 'LC-X-T/C', which means the measured location at 'X' height on the tension ('T') or compression ('C') side. The forces analyzed are the resulting forces F_a as in Figure 6.8. The results of each case studied include four parts.

- Geometric growth from stage I to stage II;
- Comparison between the recorded data points and the regressed line according to the coefficient of determination (R^2);
- Comparison between regressed strains in two stages;
- Comparison between root anchorage in two stages.

6.3.1 Single tree 10B

Regarding the loading case of the 10B single tree, the results of growth measurements, pulling tests, and numerical analysis are presented in Figures 6.11 and 6.12.

Figure 6.11 shows the comparison between the experimental and regressed results in stages I and II. As explained in Section 6.2.4, the data is first linearly regressed, as in Figures 6.11a to d. The fitness of the experimental data and regressions is first compared in both the root and the stem area. The resulting moments are obtained from the FEM analysis and plotted against the regressed rotations in the force direction in Figures 6.12 b and d, from which the anchorage value can be calculated. Since the rotation of the root system perpendicular to the force direction is minimal in Figure 6.11 d, it is not considered in Figure 6.12 d when plotting.

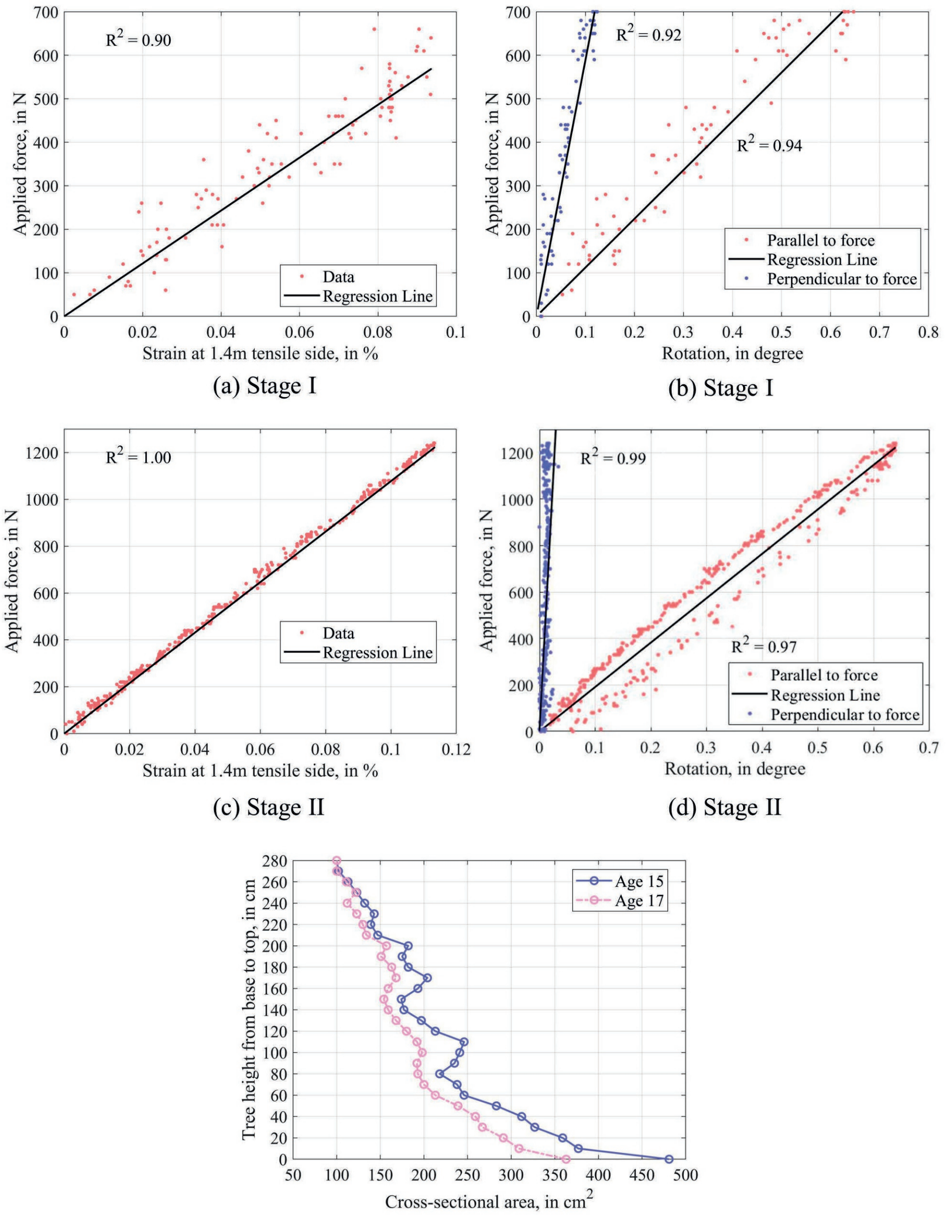

(a) Stage I (b) Stage I

(c) Stage II (d) Stage II

(e) 2-year growth

Figure 6.11: Single tree 10B: Experiment results from two stages and geometric variation diagram of tree 10B. (a) Experimental results and regression at the measured height of 1.4 m in stage I; (b) root rotations from tests and regression lines in the directions of parallel to forces and perpendicular to forces in stage I; (c) experimental results and regression at the measured height of 1.4 m in stage II; (d) root rotations from tests and regression lines in two directions in stage II; (e) geometry as a function of tree height in two years.

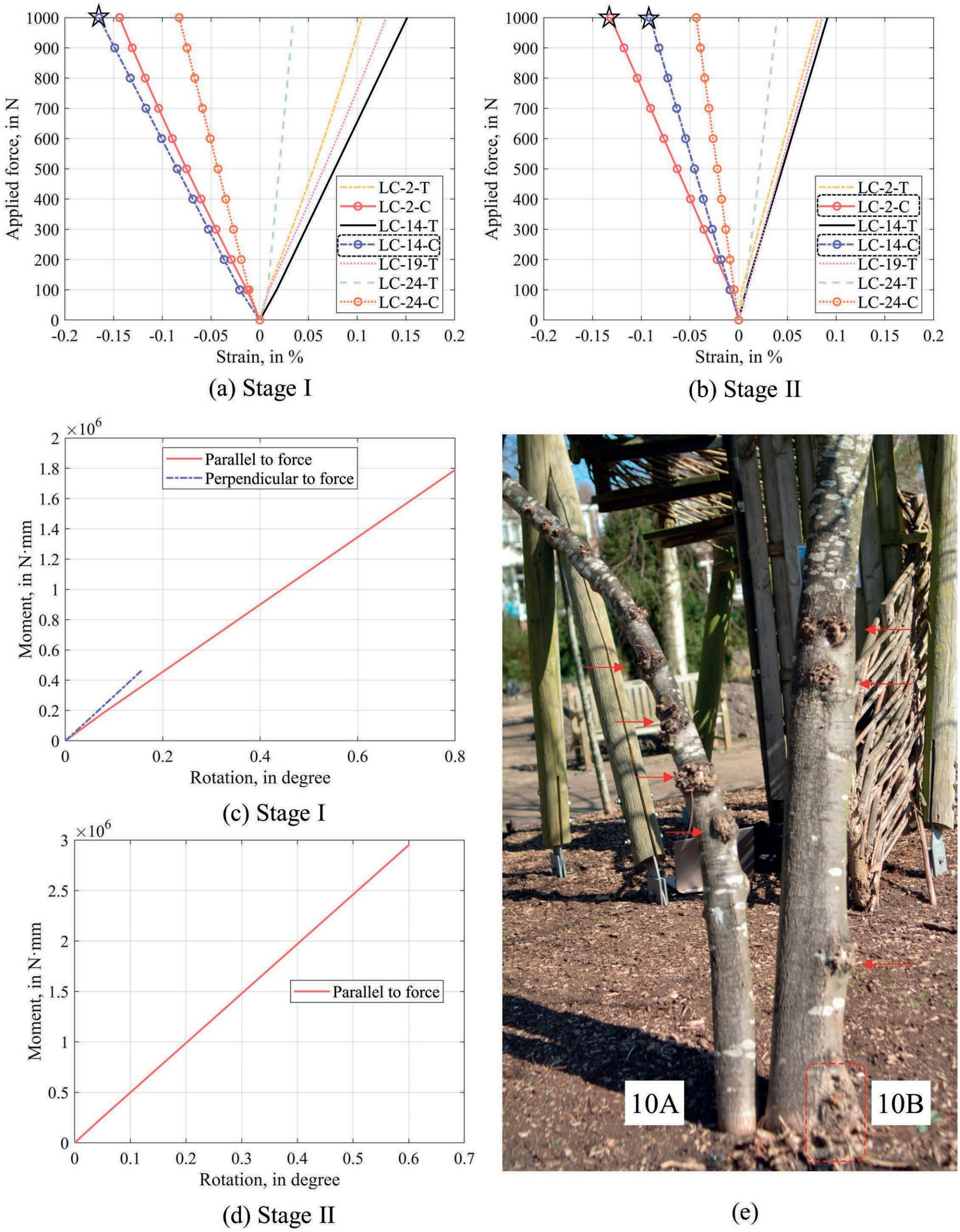

Figure 6.12: Single tree 10B: Comparison between regressed results. Analyzed strains in stage I (a) and stage II (b); analyzed root rotations in stage I (c) and stage II (d); (e) picture of the appearance of tree 10A and 10B.

6

In this test group, this comparison is represented by the measurement at height of 1.4 m. When comparing Figures 6.11 a and c, the quality of the data set in the second testing stage is more accurate than that obtained in the first stage. This is because in the second repeated test, the loading process was more stably controlled by a rolling wheel to apply forces. Since regressed fitness is acceptable ($R^2 > 0.9$) in all measurements, linear functions can be used as extrapolation to indicate weak spots with higher levels of strain.

In Figures 6.11 b and 6.11 d, it can be seen that tree 10B rotated mainly in the force direction, i.e. parallel to the force rotation. Compared to the slopes of the lines in Figure 6.12 c and d, in stage I, the root system shows an anchorage magnitude of 22.4×10^5 N·mm/deg; and in stage II, it shows an anchorage of 49.2×10^5 N·mm/deg, which is doubled due to the growth of two years. Furthermore, the basal area has increased by 30% compared to the area in stage I, and the area at a height of 2.8 m is the same. This can be explained by the development of root systems and the radial growth of the stem.

The further extrapolated strains stages I and II are compared and presented in Figures 6.12 a and b, with the same set of axis limits. According to the geometry measured in Figure 6.11 e, the shape of the cross section from the base to the top along the stem of the tree does not transfer smoothly. Assuming the pipe theory is used to explain tree growth [33], which means that during the divergence of branches from the tree trunk, the volume and mass of the tree remain conserved, then at the upper end of the branches, the volume of the stem is smaller than that of the lower end of the branches, resulting in a smaller diameter. Therefore, the formation of tree knots affects the variation in the diameter of the stem in this area. The turning points in the area variation, located at heights of 0.7 and 1.5 meters, are mainly due to the existence of knots, as shown in Figure 6.12 e following the red arrows. This also explains the absence of a measurement point at 0.8 m.

Figure 6.12 provides a comparison of the regressed results in two stages. Compared to stage I in Figure 6.12 a and stage II in Figure 6.12 b, it can be seen that the strains measured at the locations are reduced after two years of growth. For example, at location 'LC-14-C', the strain was 0.165% in stage I, and reduced to 0.135% in stage II under the same load. Figures 6.12 c and d compare rotations at base locations. The anchorage of the root, which is the slope of the plot, in stage II is higher than that in stage I.

Compared to strain variations, in stage I, it is observed at a height location of 1.4 m that the tree experiences the maximum reaction. However, in stage II, the peak shifts to the base at 0.2 m. This peak shift is considered to be caused by the root bridge (in Figure 6.12 e in the dashed rectangle), because the device is influenced by the movements of the root bridge. In this circumstance, it is assumed that the value at the base of the root bridge predicted the breaking of the stem. However, in terms of the stem failure region, it is still considered that the height of 1.4 m is the indicating location of failure.

6.3.2 Cross interconnected trees 9B-10A

The results of cross-connected trees 9B and 10A are presented in terms of the four loading cases: out-of-plane loading cases C1 and C2 and in-plane loading C3 and C4. The growth of trees 9B and 10A is compared in Figure 6.13. At the height of DBH, within the two-year growth, tree 9B increases 59.2% area compared to stage I, while tree 10A increases 105.2% area. Until stage II, tree 9B is 3.5 times larger than tree 10A. The turning points in the variation line are mainly due to the growth of knots as shown in Figure 6.12 e. It is noted that at the height of 1.9 m of tree 9B, the tree has its first branch, which reflects a decrease in area. The location of the self-growing connection is at a height of 2.2 m. The connection is fused by the main stem of tree 9B, but is located above the location of the first main branch of 9B, as sketched in Figure 6.8. Furthermore, above the connection, tree 10A has one branch that grows from the main stem. Geometry measurements and later model construction are only made and plotted along the main stem of trees 9B and 10A.

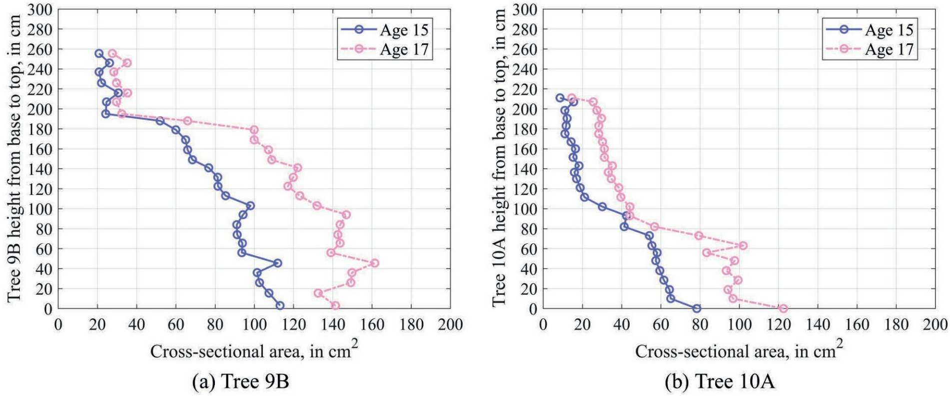

Figure 6.13: Geometry as a function of tree height of 9B and 10A.

Out-of-plane behavior

The results of the 9B-10A cross-connected tree are first given in the out-of-plane loading cases. In this loading condition, the results of case C1 (Figure 6.8 c), which is loaded at the connection (load height 2.2 m), are given in stages I and II, respectively. The results of case C2 (Figure 6.8 d), which is loaded above the connection (at height 2.5 m), are presented and compared between two growth stages. The difference between cases loaded at the connection and above the connection is in the way in which moments and shear forces are transferred through the connection to the supporting stem. In case C1, the connection does not experience transferred moments and shear forces, while in case C2 the connection functions and transfers loads. Case C2 is more likely to be the loading in reality. When the load is 1000 N, the connection is subjected to a moment of 3×10^5 N·mm, and a shear force of 1000 N.

C1: Loading at the connection level

The fitness of the experimental data and the regressions in the stem and root systems is first presented in Figure 6.14. In general, compared to the two test stages in Figure 6.14, the quality of the second performance is better controlled (R^2 = 1.00), but the regressed results of stage I (R^2 = 0.89) are still acceptable. Since two trees are inclined and crossed fused, when they are loaded onto the connection, the trees rotated not only in the force direction but also in the perpendicular direction. Tree 9B reacted more than tree 10A; see Figures 6.14 c and e in stage I and d and f in stage II. For example, at a load of 300 N, tree 9B rotated 0.5° parallel to force and 0.14° perpendicular to force. On the contrary, tree 10A rotated 0.08° parallel to the force direction and 0.07° perpendicular to the force direction.

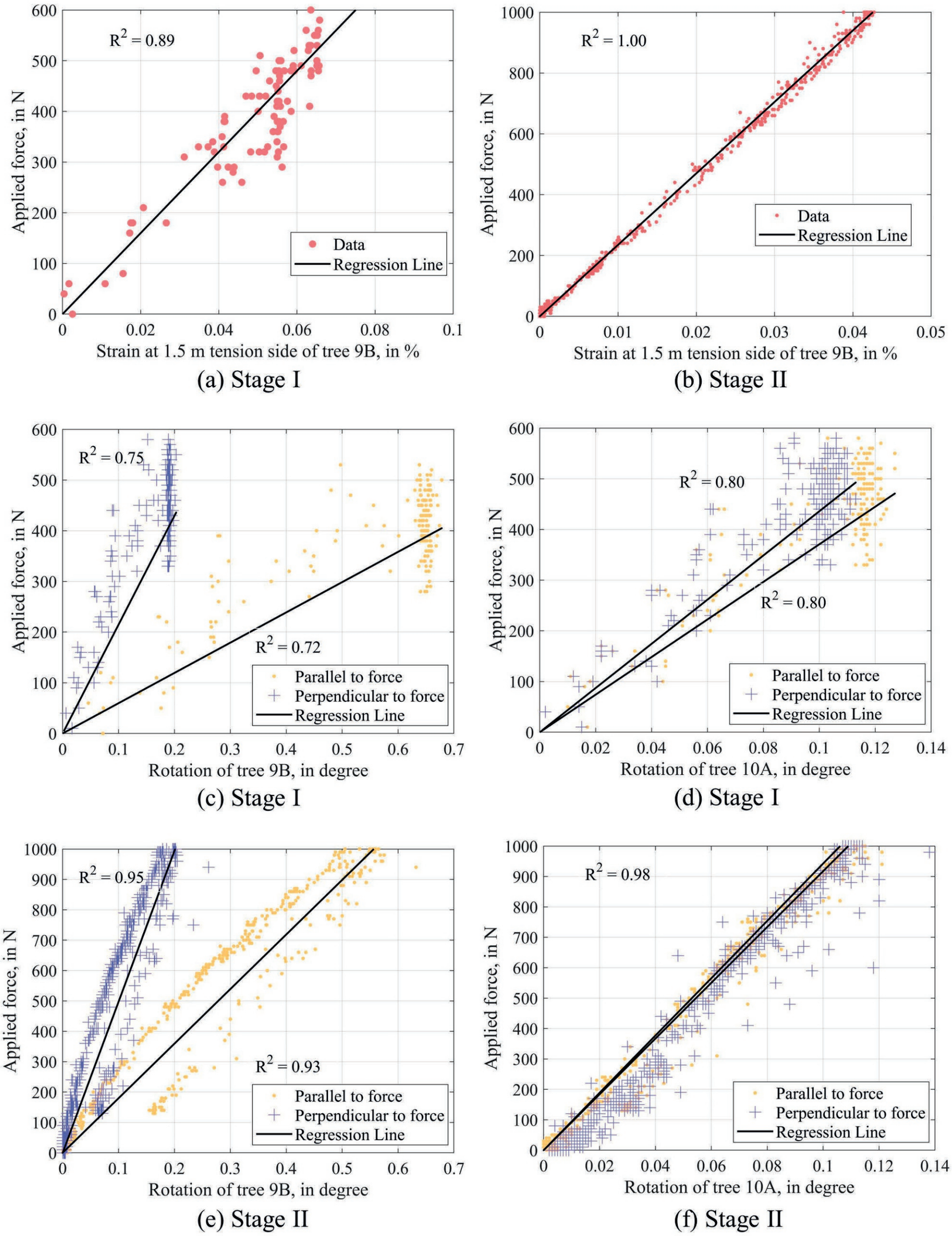

Figure 6.14: C1 cross connected tree 9B-10A: Comparative analysis of strain distributions and root rotations in two experimental stages. Strain results from pulling tests and regression in stage I (a) and stage II (b). Root rotations of tree 9B (c) and 10A (d) in two directions and their regressions in stage I. Root rotations of tree 9B (e) and 10A (f) in two directions and their regressions in stage II.

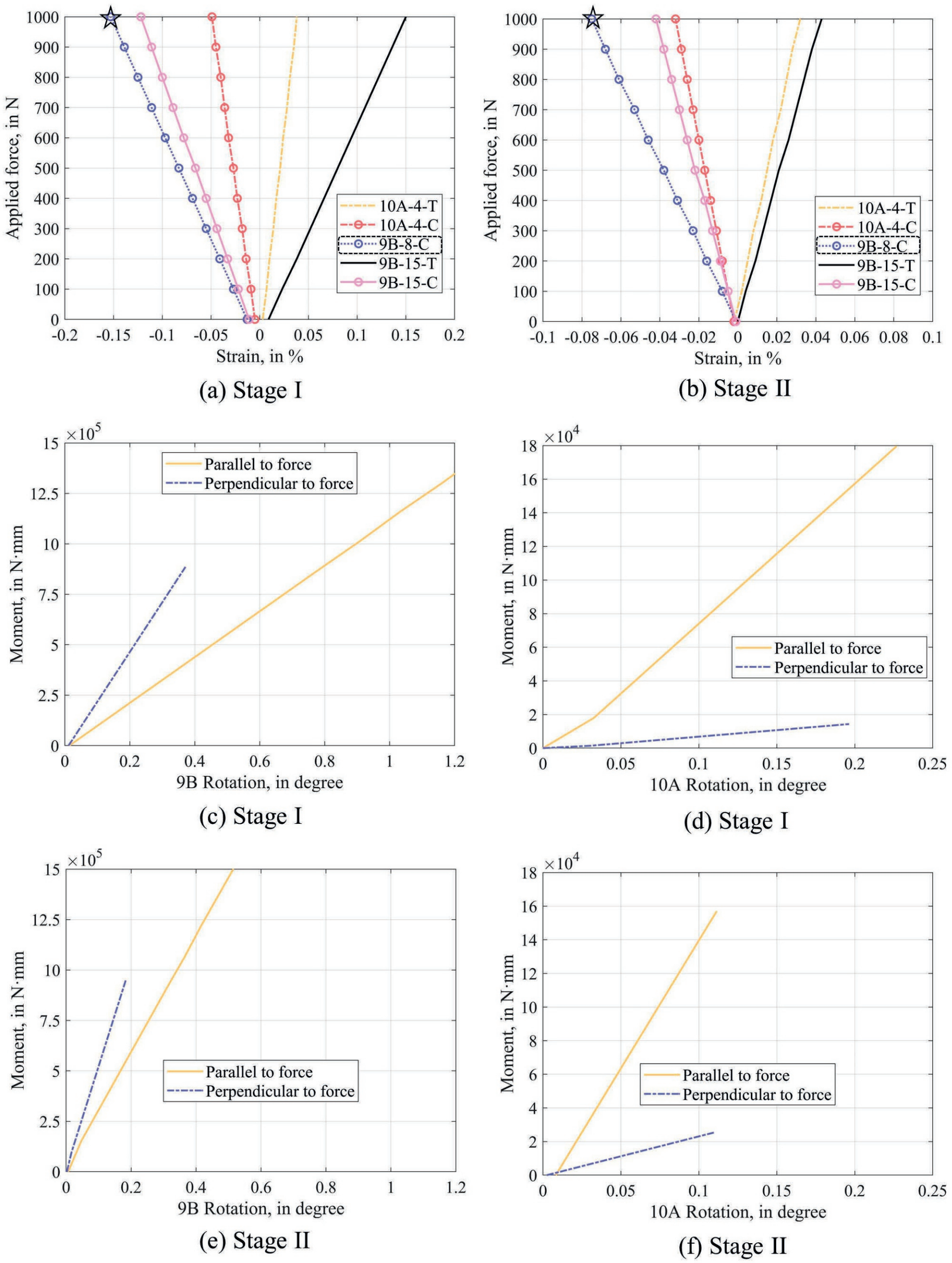

Figure 6.15: C1 cross connected tree 9B-10A: Regressed results of strain distributions and root rotations in two stages. Strain distributions in trees 9B and 10A in stage I (a) and stage II (b). Root rotations of tree 9B (c) and tree 10A (d) in two directions and their regressions in stage I. Root rotations of tree 9B (e) and tree 10A (f) in two directions and their regressions in stage II.

When comparing the strain variations in two stages (i.e., Figure 6.15 a and Figure 6.15 b), it is observed that tree 9B reacts more than tree 10B at the measured locations. The peak value in 9B occurs at height 0.8 m in both growth stages ('9B-8-C'). When trees grow two years older, under the same external forces, they experience lowered elongations in the measured locations. For example, at 1000 N load, at a height of 1.5 m of tree 9B, the strain has a value of 0.150% and 0.043% in stage I and II, respectively.

In stage I, in Figures 6.15 c and d, both trees rotate more in the direction of the applied force, but the anchorage exhibited different values in terms of the loading directions. Under this circumstance, the parallel to the force direction refers to the out-of-plane direction, and the perpendicular to the force direction is the in-plane direction. Thus, tree 9B has a higher anchorage value in the plane (24.6×10^5 N·mm/deg) than that of the out-of-plane (11.3×10^5 N·mm/deg). Regarding tree 10A, in this loading case, it shows a higher anchorage value outside the plane (8.32×10^5 N·mm/deg) than in the plane (0.77×10^5 N·mm/deg). The difference in anchorage may be explained from the roots distribution. Besides tree 10A, as shown in Figure 6.12 e, tree 10B grows closely to tree 10A. Root systems of tree 10B may be involved in the loading process. Moreover, in the direction of the forces (out-of-plane), roots from tree 10B may contribute more than in-plane direction.

In stage II, in Figures 6.15 e and f, with respect to tree 9B, the observed trend is similar to stage I. The anchorage of tree 9B has doubled: 51.2×10^5 N·mm/deg in-plane and 28.8×10^5 N·mm/deg out-of-plane. However, the anchorage derived from tree 10A is reduced compared to the results from stage I: 22.7×10^5 N·mm/deg in-plane and 14.6×10^5 N·mm/deg out-of-plane.

Because the measured locations are limited in the pulling tests, further identification of the weak region is combined with the FEM results. Figure 6.16 illustrates the results of the stress distributions in two stages. The applied forces in the model are set at 1000 N and the assumed mechanical properties of the trees are given in Table 6.3.

Combining the results of pulling tests with the results of the finite element analysis, it can be seen that the weak region (as indicated in Section 6.2.4) occurs mainly in the lower part of tree 9B and the turning location of tree 10A in the dashed circles. The circled region in tree 10A is at a height of 1.4m where knots emerged, as seen in Figure 6.12 e. When comparing the stress distributions in stage I in Figure 6.16 a c and stage II in Figure 6.16 c d, the lower region of tree 9B experiences the higher stress level. Therefore, in this case, it is assumed that the location at the height 0.8 m of 9B ('9B-8-C') predicts the failure.

C2: Loading above the connection

In this section, the results of the test case of loading out-of-plane of tree 9B-10A at a height of 2.5 m of tree 9B, which is above the cross self-growing connection, are given in this section. Figure 6.17 shows the fitness of the regressed results to the recorded data in terms of deformations and rotations. Similarly to case C1, the second stage of the pulling tests has a better quality ($R^2 = 1.00$ in Figure 6.17 b) than the first stage ($R^2 = 0.87$ in Figure 6.17 a). With the regressed functions, Figure 6.18 presents the extrapolations and estimations of the strain and rotation variations.

When comparing the strains analyzed in stage I (Figure 6.18 a) and stage II (Figure 6.18 b), it is observed that, at the location '9B-22' where the connection is formed, the reduction in strain is significant. This provides evidence of the bracing effect of the connection.

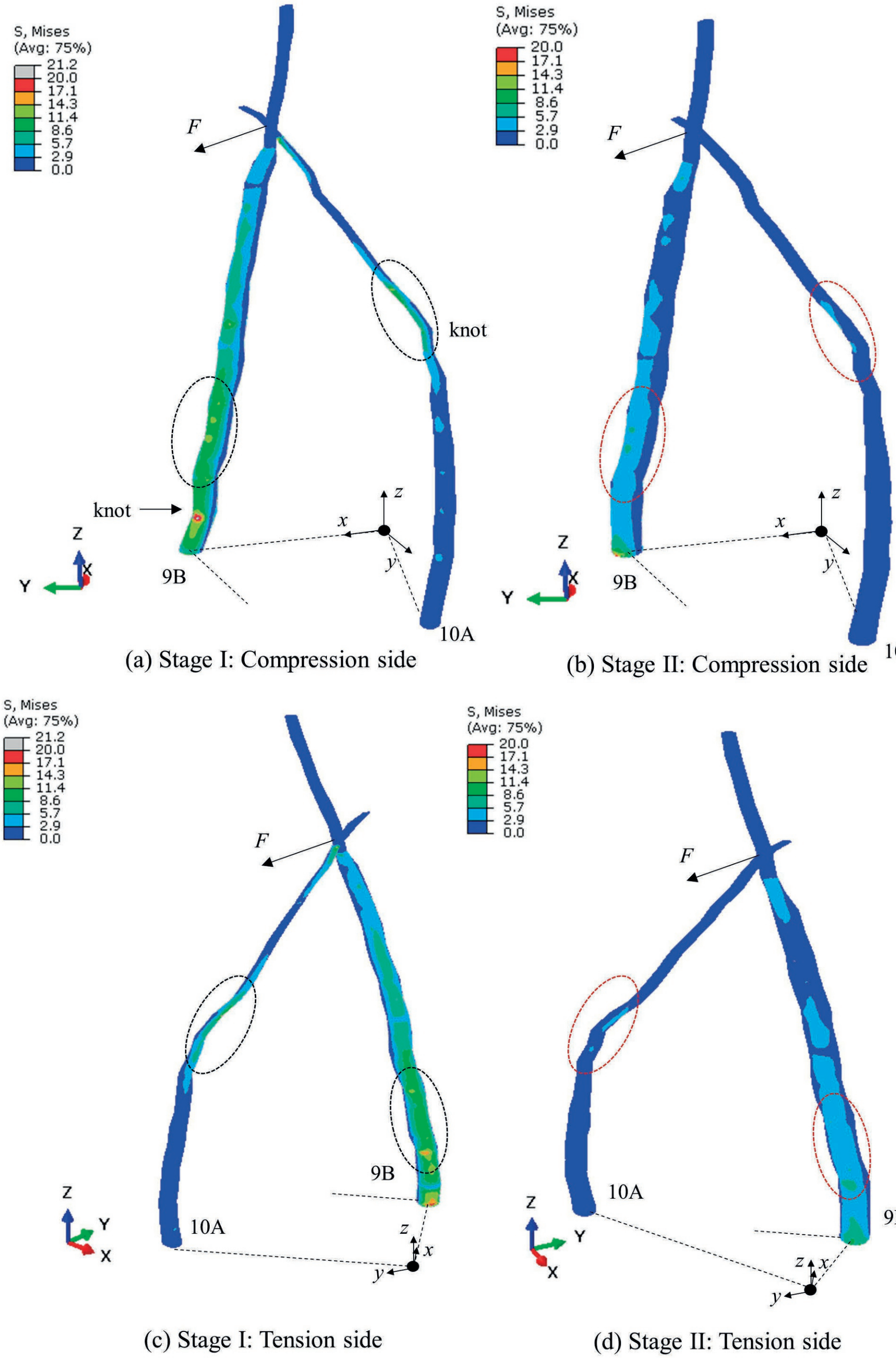

Figure 6.16: C1 cross connected tree 9B and 10A: Stress distributions from FEM calculations. Stress distributions in stage I: (a) Compression side and (c) tension side. Stage II: (b) Compression side and (d) tension side.

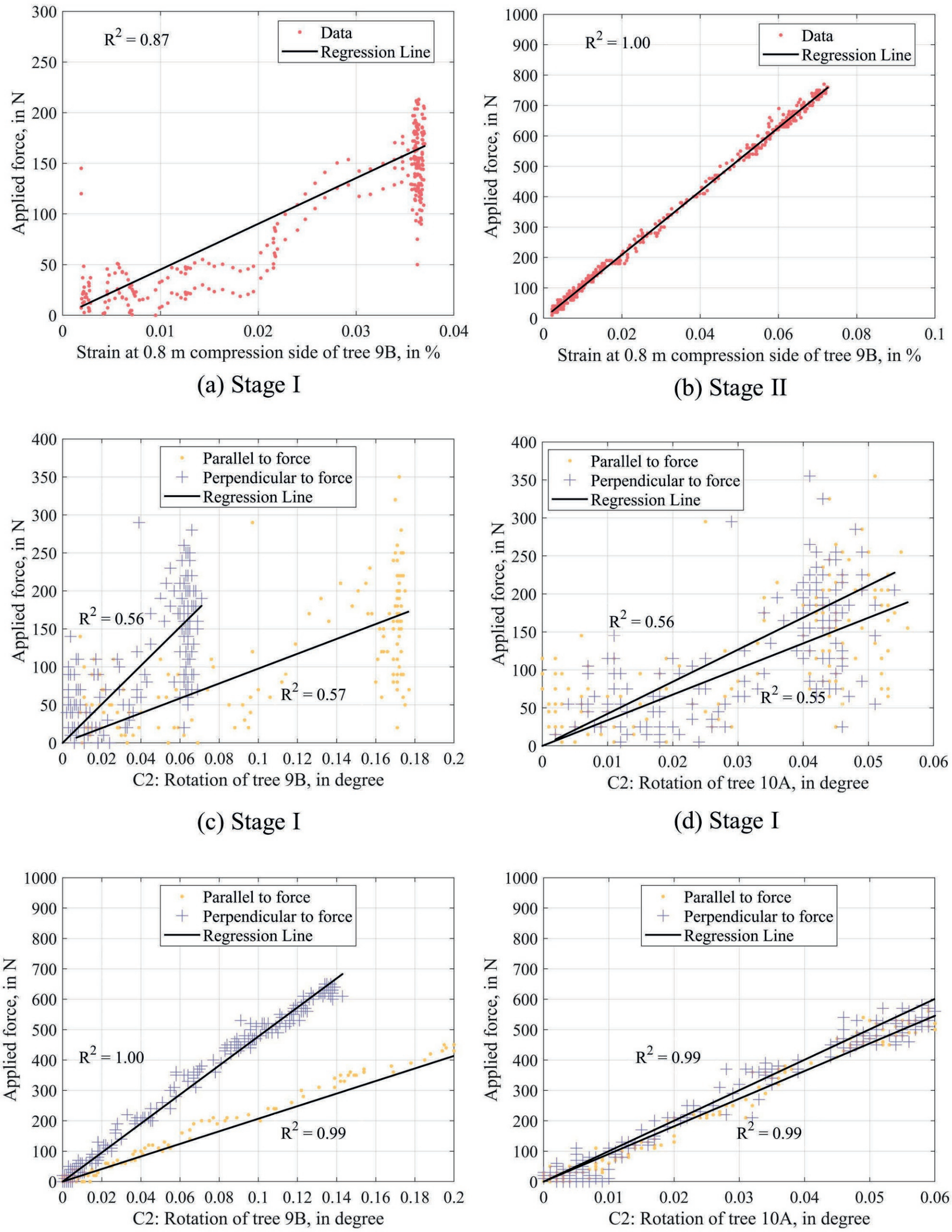

(a) Stage I (b) Stage II

(c) Stage I (d) Stage I

(e) Stage II (f) Stage II

Figure 6.17: C2 cross connected tree 9B-10A: Comparative analysis of strain distributions and root rotations across two experimental stages. Strain results from pulling tests and regression in stage I (a) and stage II (b). Root rotations of tree 9B (c) and 10A (d) in two directions and their regressions in stage I. Root rotations of tree 9B (e) and 10A (f) in two directions and their regressions in stage II.

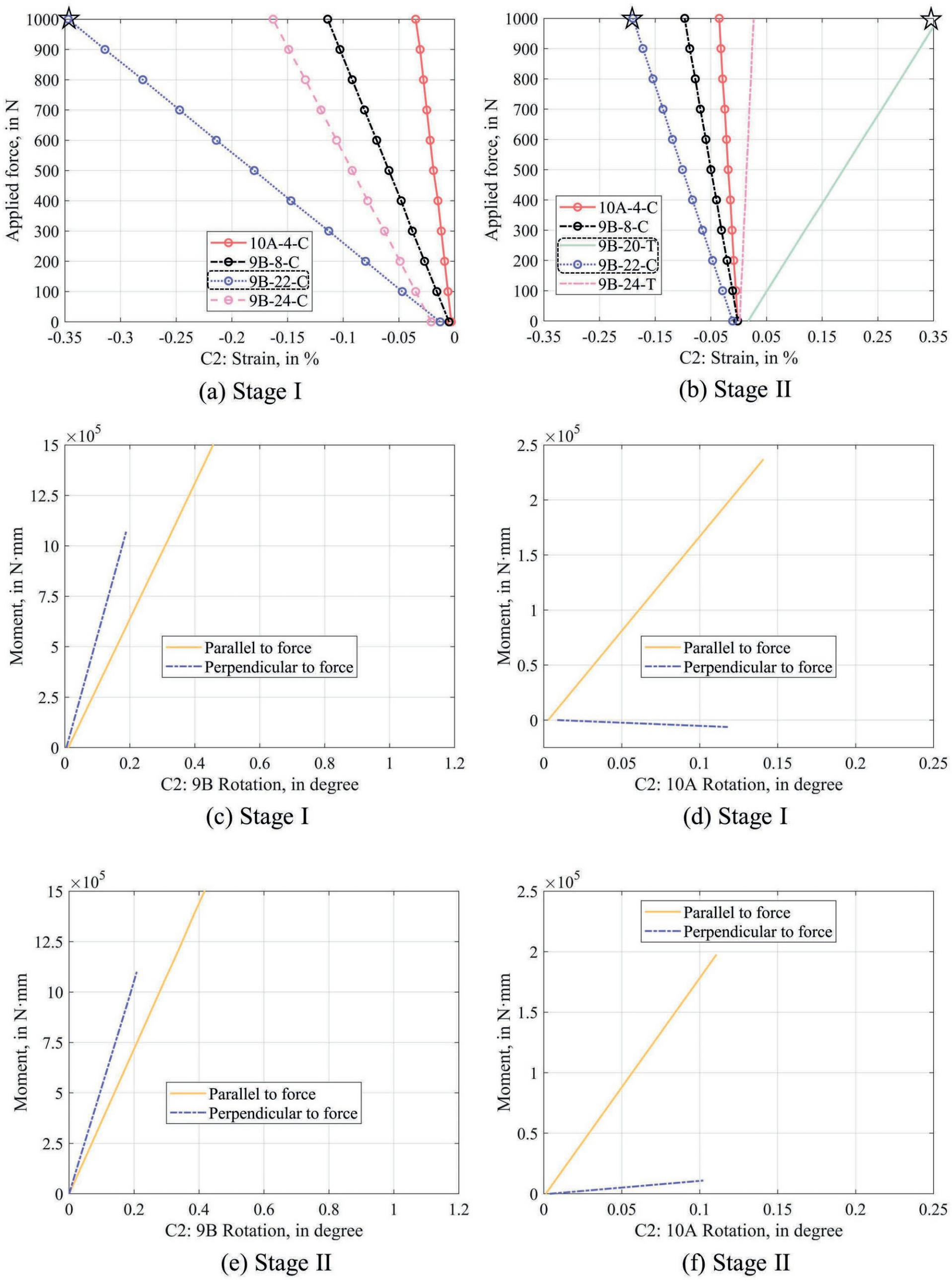

Figure 6.18: C2 cross connected tree 9B-10A: Regressed results of strain distributions and root rotations in two stages. Strain distributions in trees 9B and 10A in stage I (a) and stage II (b). Root rotations of tree 9B (c) and tree 10A (d) in two directions and their regressions in stage I. Root rotations of tree 9B (e) and tree 10A (f) in two directions and their regressions in stage II.

6

Together with the results from FEM, as shown in Figure 6.19, it can be seen that, in the connection region, the stresses are first concentrated. As described in the previous content, the connection located above the first branch, which means that the joint stem of tree 9B in this region (diameter = 53mm, stage I at height 2.2 m) is smaller than the main stem below (diameter = 100 mm, stage I at height 1.4 m). If it is only focused in the region below the connection, apart from the turning region of tree 10A, higher stresses are mainly in the lower part of tree 9B. The reduction in stress is obvious when comparing between stage I (Figures 6.19 a and c) and stage II (Figures 6.19 b and d).

In stage I, in cases C1 and C2, by comparing the rotational relationships, two observations have been identified. First, tree 9B takes most of the deformation at the base (Figure 6.15 d and f, Figure 6.18 d and f). For example, in C1, tree 9B rotated 1.28° maximum and 10A 0.22°, whereas in C2 tree 9B rotated 0.5° maximum and tree 10A 0.14°. Second, tree 9B has a relatively higher anchorage in the plane (57.8×10^5 N· mm/deg) and a lower value outside the plane (33.6×10^5 N·mm/deg). However, although tree 10A rotates similarly in two measured directions, the out-of-plane anchorage is much higher (17.1×10^5 N·mm/deg) than the in-plane anchorage (0.57×10^5 N·mm/deg). In stage II (Figures 6.18 e and f), the rotations and anchorage values are not significantly different from stage I (Figures 6.18 c and d).

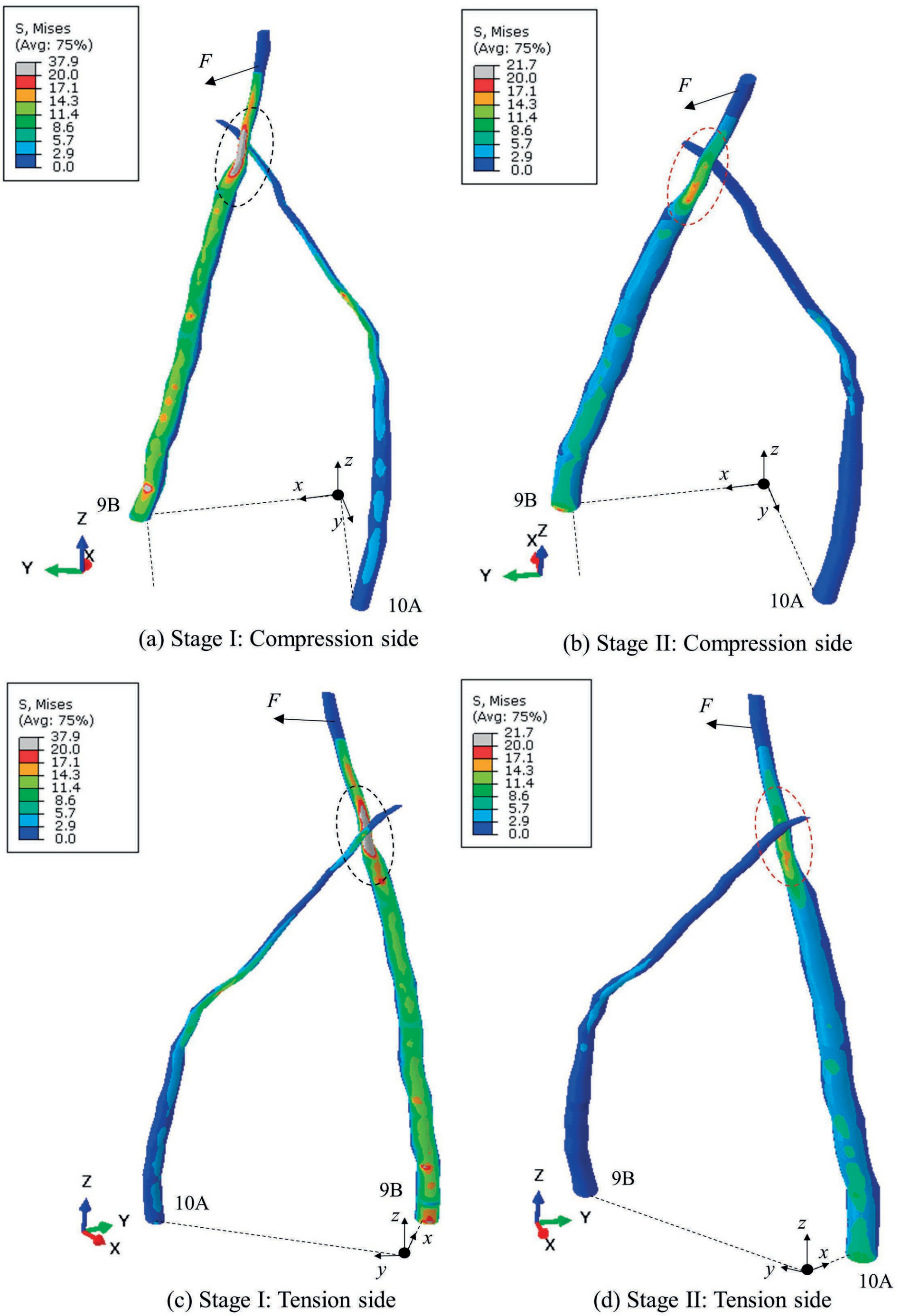

Figure 6.19: C2 cross connected tree 9B and 10A: Stress distributions from FEM calculations. Stress distributions in stage I: (a) Compression side and (c) tension side. Stage II: (b) Compression side and (d) tension side.

In-plane loading

The group of in-plane loading includes the cases of vertical loading (C3 Figure 6.8 e) and horizontal loading (C4 Figure 6.8 f). The vertical loading intends to give results in terms of pure vertical forces; whereas the horizontal loading focuses on the horizontal forces. The results of two cases are presented separately below.

C3: Vertical loading in the plane

Pulling tests in the vertical direction (Figure 6.8 e) is difficult to load by pulling in the vertical direction, so in this direction, it is loaded by hanging several weights of 5 kg (stage I two weights and stage II four weights). However, in the process of hanging the weights, there are a lot of fluctuations due to the movement of the weights. Consequently, as shown in Figure 6.20. The data collected in stage I and II show large scatters. Thus, the comparison does not proceed. The experimental results for this condition are not satisfactory. However, this attempt provides a preliminary study for future improvement.

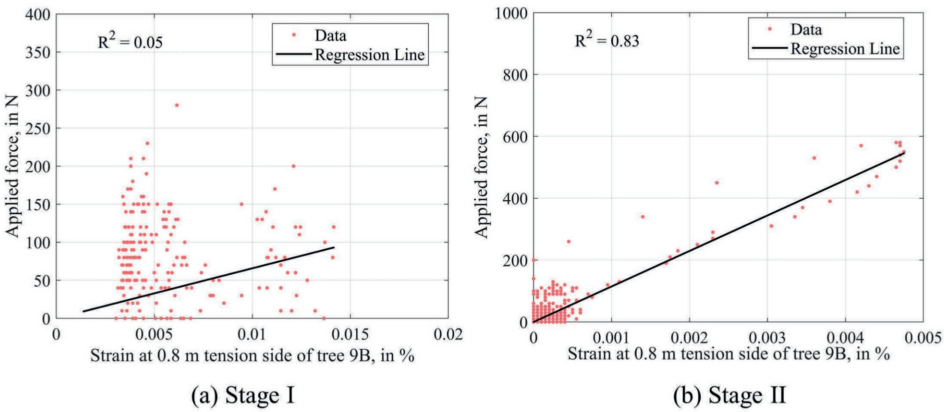

Figure 6.20: C3 cross connected tree 9B and 10A: Experimental results in two stages. (a) Stage I; (b) stage II.

C4: Loading out-of-plane above the connection

The pulling responses of the cross-connected trees 9B and 10A in-plane at a height of 2.5 m are presented in Figure 6.21. This figure compares the collected data with the linear regressed lines. Similarly to previous cases, data collected in stage I show a certain scatter (R^2 = 0.54), but the data in the second stage are better (R^2 = 0.99) due to the improvement of the loading process by a roller.

As shown in Figures 6.21 c to f, although the interconnected system is controlled to pull in the cross-plane, there is inevitably a certain rotation noticed out-of-plane. It is also reflected in the basal rotation of trees 9B and 10A. In stage I (Figure 6.21 c), tree 9B is more likely to rotate in-plane and less out-of-plane; and tree 10A has the opposite behavior (Figure 6.21 d). However, in stage II (Figures 6.21 e and f), both trees 9B and tree 10A rotate more in the plane than out of the plane.

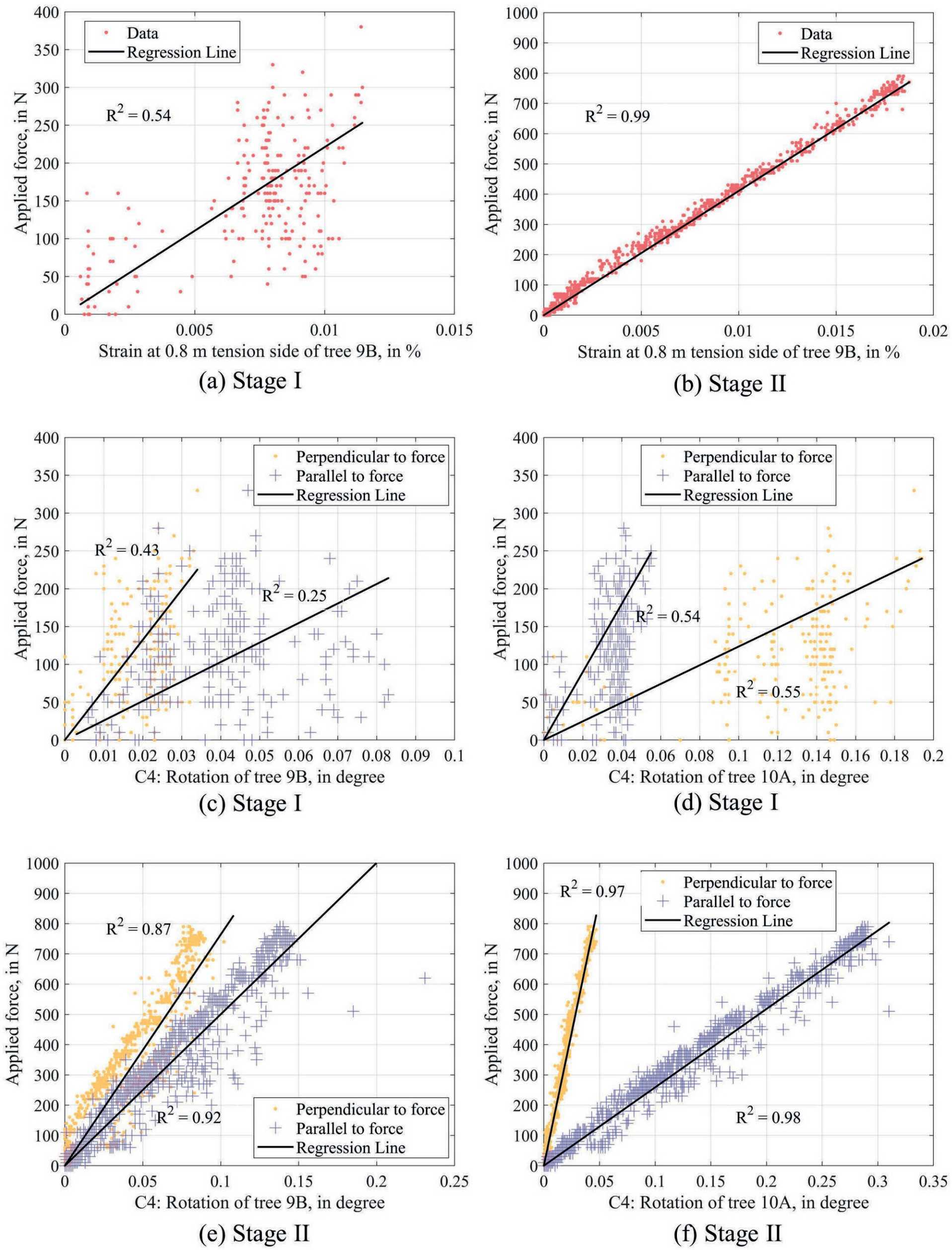

Figure 6.21: C4 cross connected tree 9B-10A: Comparative analysis of strain distributions and root rotations in two experimental stages. Strain results from pulling tests and regression in stage I (a) and stage II (b). Root rotations of tree 9B (c) and 10A (d) in two directions and their regressions in stage I. Root rotations of tree 9B (e) and 10A (f) in two directions and their regressions in stage II.

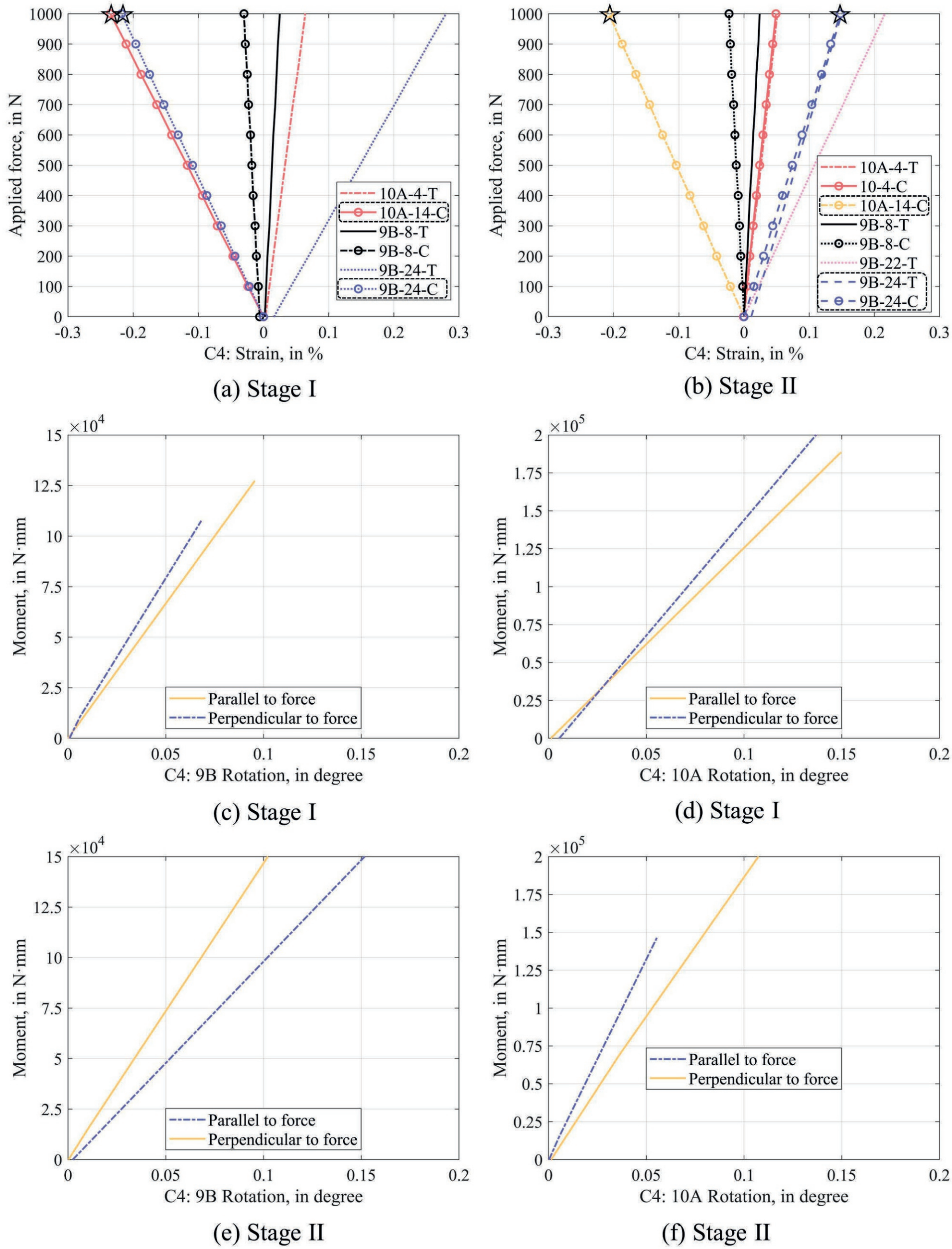

Figure 6.22: C4 cross connected tree 9B-10A: Regressed results of strain distributions and root rotations in two stages. Strain distributions in trees 9B and 10A in stage I (a) and stage II (b). Root rotations of tree 9B (c) and tree 10A (d) in two directions and their regressions in stage I. Root rotations of tree 9B (e) and tree 10A (f) in two directions and their regressions in stage II.

6

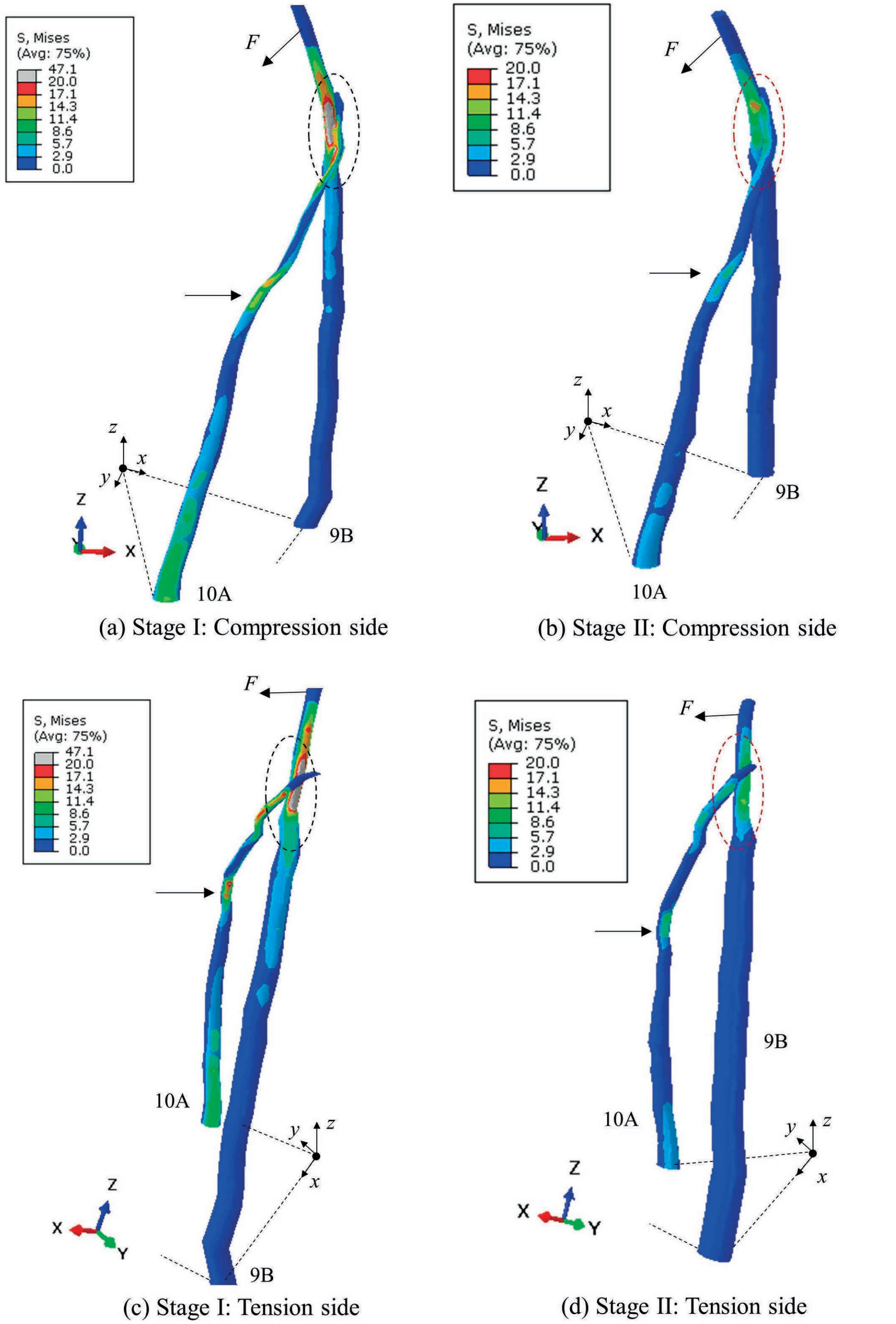

Figure 6.23: C4 cross connected tree 9B and 10A: Stress distributions from FEM calculations. Stress distributions in stage I: (a) Compression side and (c) tension side. Stage II: (b) Compression side and (d) tension side.

During tests, the force is applied with a horizontal angle (α) of 29.1° , and a projected angle to the middle location (β) of 89° , as shown in Table 6.2. The connecting plane of 9B-10A in Figure 6.8 f, together with the middle point 'O' forms a triangle; and the angle between '9B-O' is measured 71.8° , thus the projected force direction is shifted from the connecting plane 6.8°. When the system is loaded in this direction, in stage I, it is observed that tree 10A (Figure 6.22 d: 0.15° parallel and 0.14° perpendicular) takes most of the root rotations compared to tree 9B (Figure 6.22 c: 0.09° parallel and 0.06° perpendicular). In stage II, the rotation difference between tree 9B (Figure 6.22 e: 0.15° parallel and 0.1° perpendicular) and 10A (Figure 6.22 f: 0.05° parallel and 0.11° perpendicular) becomes less. Under this circumstance, the anchorage values do not show much difference. This content will be compared and discussed in the following section.

When comparing the strain variations measured in two stages (Figures 6.22 a and b), it can be seen that at a height of 1.4 m of tree 10A, the system has its maximum resistance. Furthermore, the loads on 9B are reduced. This only takes into account the region below the connection.

As shown in Figure 6.23, compared to the out-of-plane loading reaction, the internal forces are more distributed and share more on tree 10A. It indicates that tree 10A works as a bracing support for tree 9B. Consequently, tree 9B experiences less loads. The connection region is still the most risky area, but considering the 9B perspective, the safety of tree 9B has increased.

6.3.3 Parallel interconnected trees 6A-6B

Trees 6A and 6B are connected in the lower part at a height of 0.4 m, but the connected region develops gradually within a height of 0.2 m to 0.6 m. This interconnected system is tested only in the in-plane loading case. The results are presented in the same order, first growth comparison in Figure 6.24, following the regressed results in Figure 6.25, and Figure 6.26, and then the stress distribution of the FEM analysis in Figure 6.27.

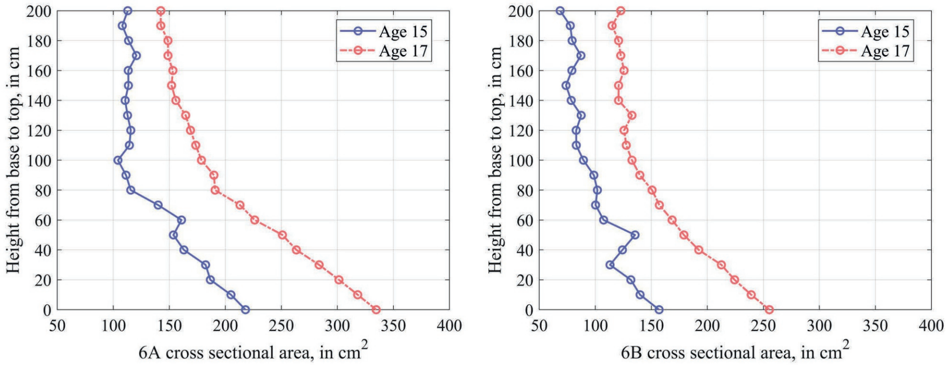

Figure 6.24: Geometry changes as a function of tree height of tree 6A and tree 6B.

In Figures 6.25, it can be seen that tests in two stages both give stable results with R^2 larger than 0.85. From the comparison between root rotations in trees 6A and 6B, in stage I and stage II, it is observed that the two trees move together, but 6B moves less than 6A. Tree 6A is the tree where the forces are applied. For example, in Figures 6.25 c and d, the rotation parallel to the force for 6A is 0.17° at a load magnitude of 1000 N. Regarding tree 6B, the rotation reaches 0.34° under the same load. However, the rotation parallel to the force was much lower than the rotation perpendicular to the force. Differences in anchorage in two directions will be discussed in further detail in the following section.

In the analysis of the strain measurements in Figures 6.26 a and b, it can be seen that of the two measurement stages, the strain decreases in stage II and the trees become stiffer under the same load. Compared to the results of stage I in Figure 6.27 a c with stage II Figure 6.27 b d, the reduction in stress is observed. Furthermore, it is noticed that, in terms of this form of parallel interconnections, internal reaction forces are mainly concentrated in one stem compared to the other. In this system, the height of 0.8 m of tree 6A was identified as the failure indicator.

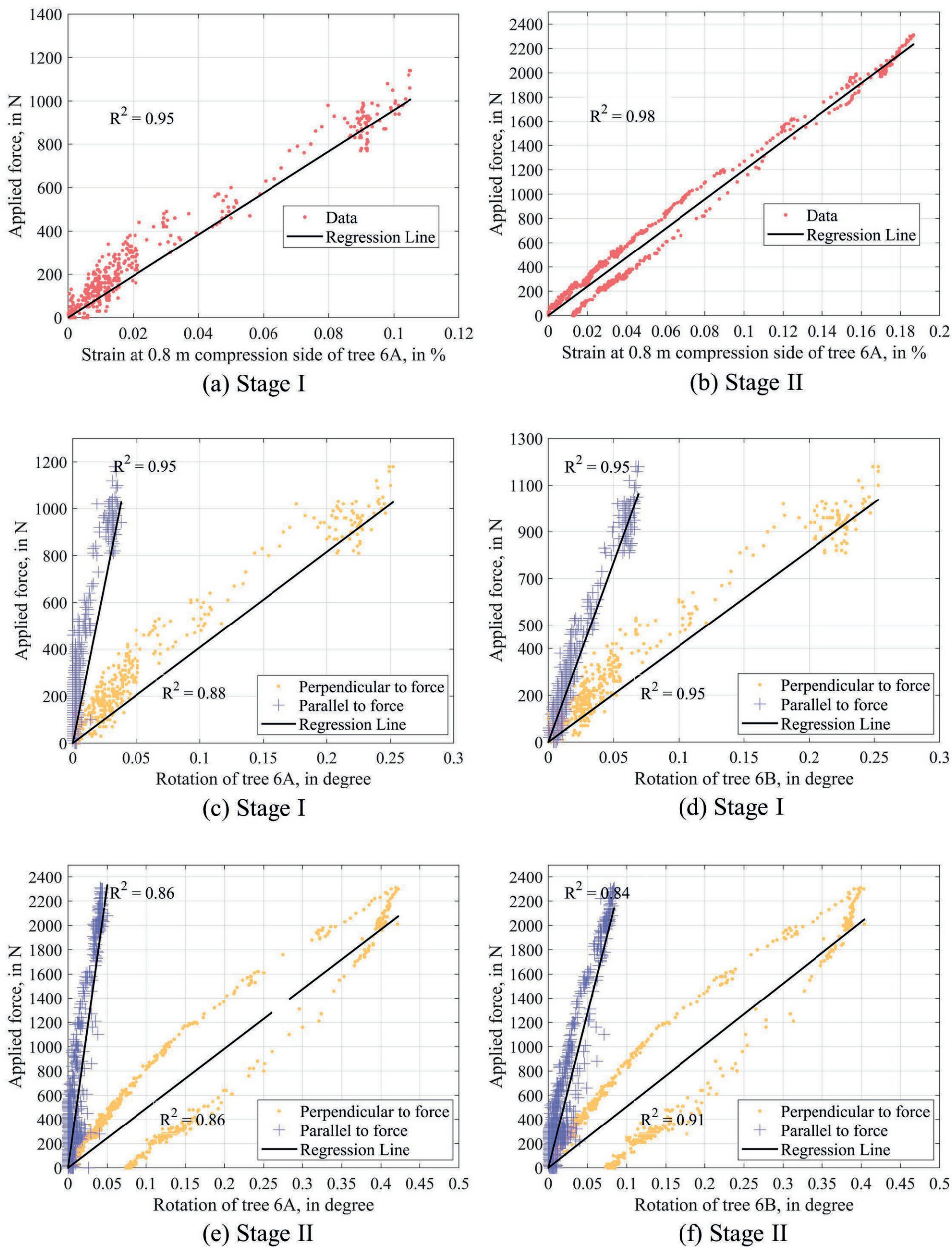

Figure 6.25: Parallel connected trees 6A and 6B: Comparative results in two experimental stages. Results from pulling tests and regression in stage I (a) and stage II (b). Root rotations of tree 6A (c) and 6B (d) in two directions and their regressions in stage I. Root rotations of tree 6A (e) and 6B (f) in two directions and their regressions in stage II.

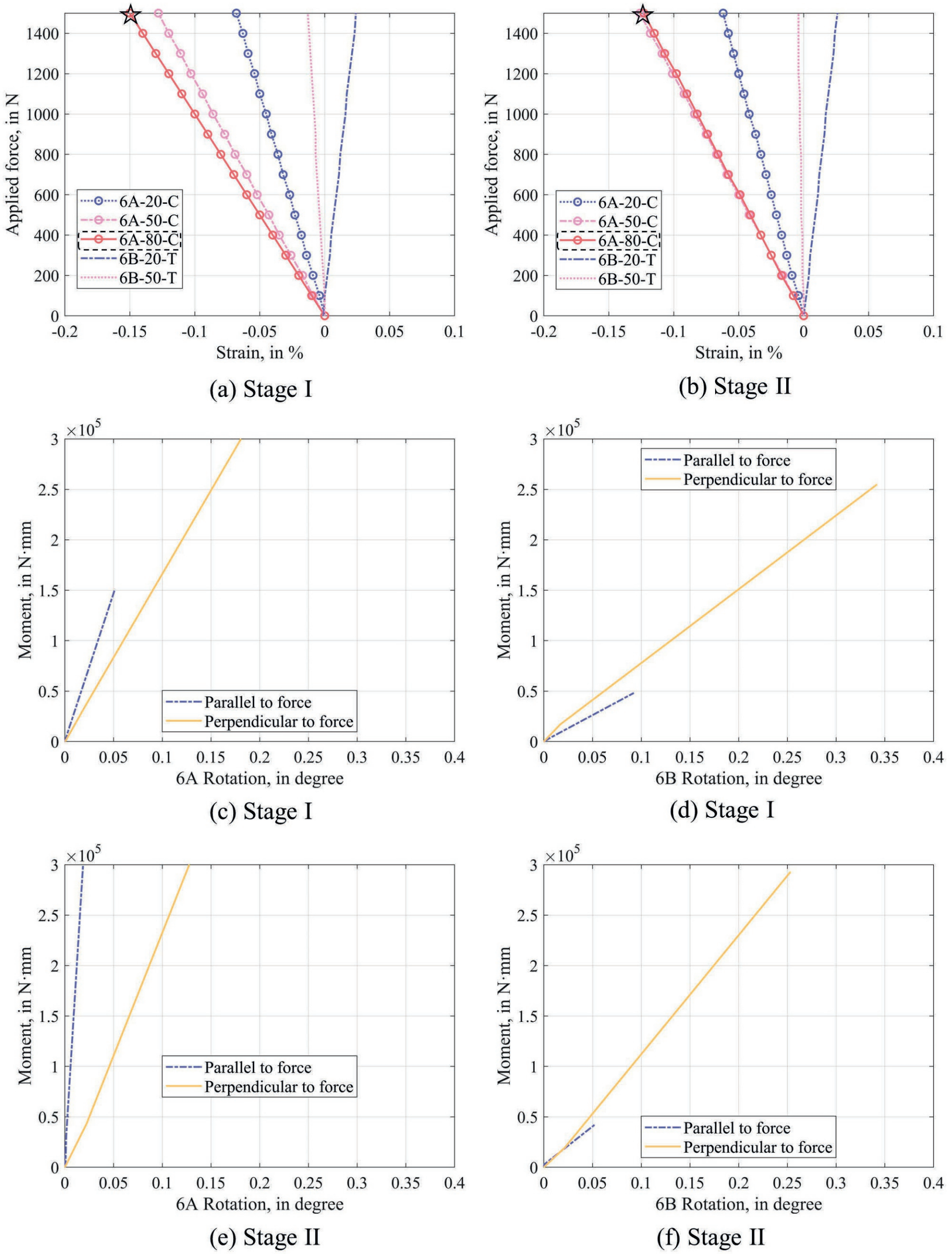

Figure 6.26: Parallel connected trees 6A and 6B: Regressed results of strain distributions and root rotations in two stages. Regressed strain variations from experimental results in stage I (a) and stage II (b); regressed root rotation results of tree 6A (c) and 6B (d) in stage I; regressed root rotation results of tree 6A (e) and 6B (f) in stage II.

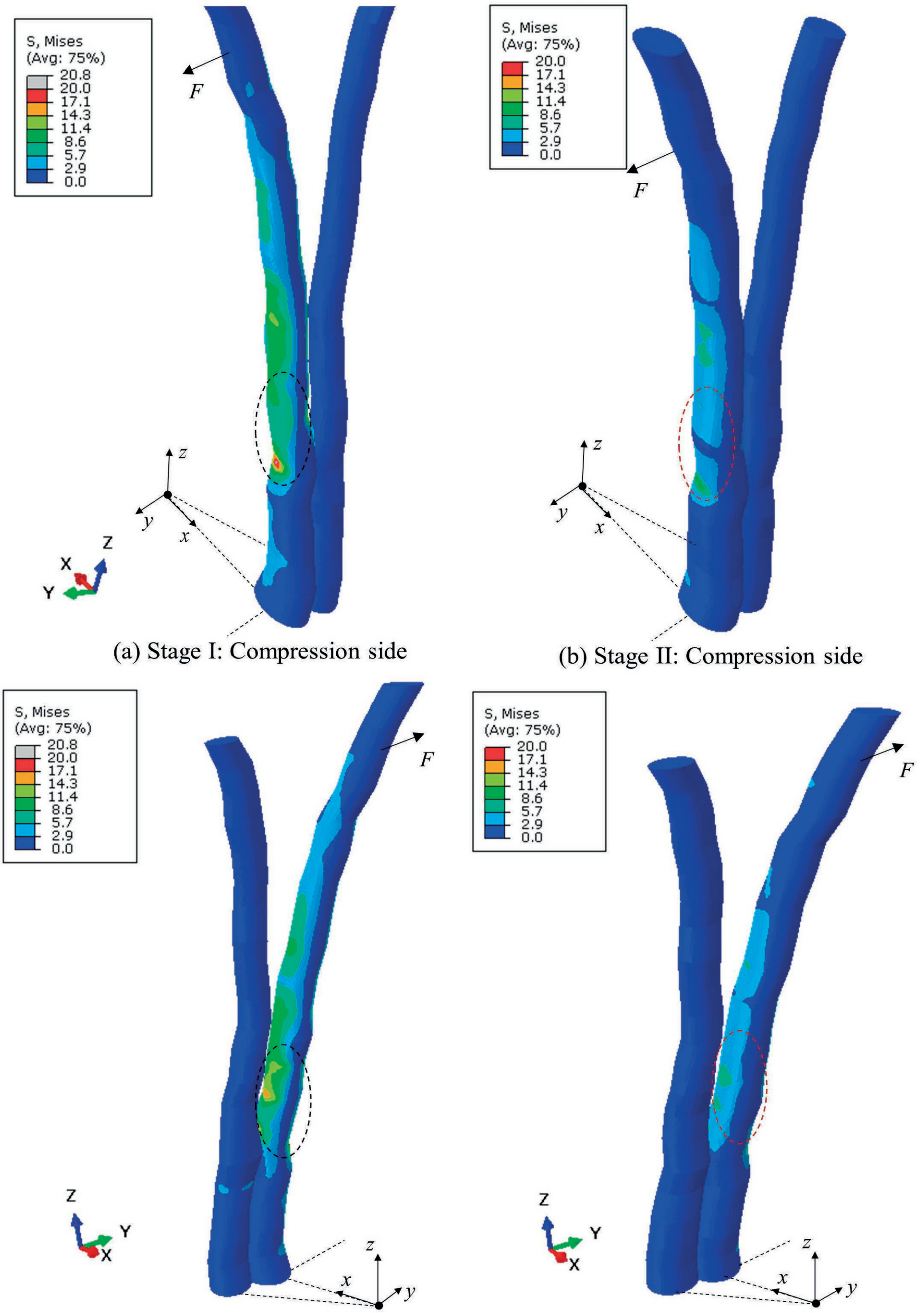

(a) Stage I: Compression side

(b) Stage II: Compression side

(c) Stage I: Tension side

(d) Stage II: Tension side

Figure 6.27: Parallel connected tree 6A and 6B: Stress distributions from FEM calculations. Stress distributions in stage I: (a) Compression side and (c) tension side. Stage II: (b) Compression side and (d) tension side.

6.4 Discussion

In the section of discussion, it first focuses on the discussion and comparison of different tree systems as a result of growth and development. Three mechanical properties are compared: loading capacity, root anchorage, and stiffness. Second, the application potentials of the two types of interconnected trees are discussed in further detail. The limitations of this study are then noted.

6.4.1 Estimation of load carrying capacity

The loading capacity of a tree and an interconnected system is estimated from the approach of extrapolation based on the results tested. The magnitude is determined by identifying the weak region and calculating its failure limits in terms of predefined thresholds. In this way, this extrapolated value is assumed to represent the failure of a structure. In Section 6.2.4, the selection of elastic limits is explained. The elastic limits of the stem are set at 0.24% of strain and 20 MPa of strength. Compared to the mechanical limits with the rotational limit of 5°, it is observed that in our work with young trees, the tree tends to fail mainly due to stem breakage rather than root uprooting. Take tree 10B in stage I as an example. When root rotation reaches 5°, the extrapolated applied force will be approximately 5640 N (or if the threshold is set at 2°, then the estimated force will be 2250 N). However, in the stem region, when using the estimate at the location at 1.4 m height, the stem will fail at 1450 N. Therefore, it is assumed that the load carrying capacity is estimated from the identified weak spot only in the stem region.

6

For convenience of comparison, the extrapolated range is set at 1000 N, as the applied force in FEM modeling. The difference in stage I and stage II is the growth over a period of two years. Table 6.4 gives the strain distributions under 1000 N loads and its corresponding estimated load capacity.

Table 6.4: Comparison of strain distributions and maximum load among loading cases

Case ID	**Stage**	**Stain (%)**								**Failure indicator**	F_{max}
		H_1		H_2		H_3		H_4			
		C	T	C	T	C	T	C	T		N
10B	I	0.140	0.100	**0.160**	0.150	-	0.130	0.080	0.030	10B-14-C	1450
	II	0.130	0.080	**0.090**	0.090	-	0.090	0.040	0.040	10B-14-C	2700
C1	I	0.049	0.038	**0.153**	-	0.122	0.150	-	-	9B-8-C	1650
	II	0.032	0.032	**0.075**	-	0.042	0.043	-	-	9B-8-C	3200
C2	I	0.035	-	**0.114**	-	0.347	-	0.163	-	9B-8-C	2150
	II	0.035	-	**0.097**	-	0.19	-	0.027	-	9B-8-C	2500
C4	I	0.283	0.064	0.03	0.025	**0.283**	-	0.266	0.280	10A-14-C	850
	II	0.049	0.051	0.023	0.024	**0.207**	-	0.148	0.150	10A-14-C	1150
6A6B	I	0.038	0.016	0.072	0.004	**0.087**	-	-	-	6A-8-C	2500
	II	0.042	0.017	0.084	0.003	**0.082**	-	-	-	6A-8-C	2800

Note: (1) H_1, H_2, H_3, and H_4 correspond to the measured locations in Table 6.2. (2) Analysed values with bold fonts indicate the weak locations; and they correspond to the failure indicators in this table, in order to estimate maximum loads; (3) F_{max} means the maximum loads extrapolated from the failure indicator.

Except for the parallel tree system 6A-6B, it can be seen that the strains estimated at the measured locations under a load of 1000 N are reduced after two years of growth. When the external load is kept the same, the elongations that responded along the stem can be considered due to the combined effects of the increase in biomass, cross-sectional expansion, and cell wall maturation. Furthermore, as trees grow, they develop growth stresses to enhance the strength of the growing stems, and during maturation the stresses relax [34]. Therefore, the reduction in estimated strains must be explained by both biological and mechanical factors, such as wood heterogeneity, development of material elasticity, increase in the second moment of inertia and in dead weight, changes in growth stress, and maturation stresses or strains of fiber cells. In addition, stresses caused by environments also play a role.

The maximum force is derived on the basis of the location of the weak spot in the stems. Since the strain is reduced, it makes sense that the maximum load is also increased. It should be noted that the location at the connection (e.g., in C2 H_3) is not considered. However, when the system is loaded above the connection, it is the region with the highest risk. When comparing the loading case out of plane (C2) and in plane (C4), the failure occurs in the supporting tree that determines the capacity.

6.4.2 Comparison between root anchorage

In Table 6.5, it gives the comparison in root deformation and corresponding anchorage. The rotation of roots is derived from the extrapolation of the regressed lines when the external loads are 1000 N. Reaction moments were obtained from the FEM model considering self-weight of both the stem and the crown. The anchorage of the root system is defined as the ratio of the basal moment and the rotation, as studied by Lunstrom et al. [35]. For a single standing tree 10B, there is no difference in-plane or out-of-plane.

From Table 6.5, the first observation is that the root anchorages have developed after two years, which is also reflected in the reduction in root rotations. The second observation is based on the comparison between different loading planes. It seems that the root systems of the interconnected trees are not symmetric. Consequently, the anchorages of the roots vary in different directions. What is still difficult to explain is the increase in anchorage in C2 (loading out-of-plane above connection) compared to C1 (loading out-of-plane at connection).

Table 6.5: Comparison among loading cases in root rotation and anchorage

Case	Stage	Tree	Out-of-plane		In-plane	
			Angle	Anchorage	Angle	Anchorage
			Degree	$\times 10^5$ N·mm/deg	Degree	$\times 10^5$ N·mm/deg
10B	I	10B	0.83	22.4	-	-
	II	10B	0.16	49.2	-	-
C1	I	9B	1.28	11.3	0.36	24.6
		10A	0.22	8.3	0.19	0.8
	II	9B	0.53	28.8	0.19	51.2
		10A	0.11	14.6	0.10	22.7
C2	I	9B	0.5	33.6	0.19	57.8
		10A	0.14	17.1	0.11	0.6
	II	9B	0.48	35.9	0.21	52.6
		10A	0.11	18.0	0.10	1.1
C4	I	9B	0.07	15.8	0.10	13.3
		10A	0.53	15.1	0.15	12.6
	II	9B	0.11	14.7	0.18	10.0
		10A	0.38	18.4	0.55	26.4
6A6B	I	6A	0.03	34.0	0.2	18.1
		6B	0.06	5.2	0.21	7.5
	II	6A	0.02	177.0	0.19	23.1
		6B	0.03	8.1	0.18	11.1

6.4.3 Stiffness comparison

The changes in stiffness of single trees and interconnected trees are compared in Table 6.6. The stiffness is compared on the basis of the deformation obtained from FEM under the same load of 1000 N. When comparing the two stages of growth (I and II), the growth process has increased the rigidity of the tree stems by a factor of more than 30%.

Cases 2 and 4 are loading out-of-plane and in-plane, respectively. At the same growth stage, it can be found that the in-plane deformation was much lower than the out-of-plane loading. This means that the in-plane stiffness is higher than that of out-of-plane.

Table 6.6: Deformation comparison among loading cases

Case ID	Stage	Force location	Deformation	Factor
		H_F, m	mm	(II/I)×100%
10B	I	2.8	180.5	39.5
	II	2.8	71.3	
C1	I	2.2	61.1	62.5
	II	2.2	38.2	
C2	I	2.5	137.7	47.9
	II	2.5	65.9	
C4	I	2.5	43.7	34.3
	II	2.5	15.0	
6A6B	I	1.9	33.7	41.2
	II	1.9	13.9	

6.4.4 Applicability of interconnected tree systems

After comparing the mechanical responses of different systems, parallel connection may suit the condition when the root of trees is weak. By connecting the base, the anchorage will increase, but it may cause asymmetric behavior. When a tree has a weak stem, the strain and stress distribution of a tree usually concentrate in the middle region of the stem; in this case, a cross section might be suitable to act as a bracing to support.

In any case, the addition of a self-growing connection is a way to transfer and dissipate energy within the tree. It increases redundancy by adding one more connecting element to the structure, and thus potentially increases the reliability. However, when the connection is broken, the following growth condition is not considered. This may influence the future development of the tree, which is beyond the scope of our work. In addition, the connection itself is a weak link between two trees. Conclusions from previous studies on the fiber patterns of the connections showed that the interface area experiences mainly tension perpendicular and shear forces, which is risky for wood material.

6.4.5 Testing limitations

In the pulling tests, the pulling process is operated manually. Although it has been controlled very carefully by adding a stable rolling wheel, it still caused fluctuations in the results. In the second stage of the tests, i.e., in stage II, the testing procedure has been improved to obtain better measurements. This improvement is mainly due to the uniform and slow rotation of the winch during loading.

The mechanical properties of the single tree and interconnected tree system are described by parameters which include loading capacity, deformation, strain, stiffness, root rotation, and internal reactions (stress and reaction moments). In the tests, the strain, applied force, and root rotations are measured. The deformation is extracted from the FEM analysis. Stress and reaction moments are also obtained from FEM. The advantage of FEM is that the complexity of the geometry can be taken into account, which includes the elliptical diameter of the tree, the taper shape, and the degree of inclination. FEM can also take into account the uniform distribution of wood biomass and second-order effects. This combined method can give a good estimate of the prediction of failure, but still requires some assumptions.

When constructing the FEM model, the geometry of the structure is built as segments, and at the connecting region, it does not have a smooth connecting shape. Consequently, it resulted in a stress concentration at the points where the segments are constructed, which is not considered in the FEM results. However, analysis can provide some insight into internal reactions. Regarding living trees, the modulus of elasticity is known to vary in trees with respect to height, radial position, and cambial age [36–38]. However, because of the limitation of the test samples, it is assumed that the modulus of elasticity is the same along the stem. Moreover, the modulus of elasticity is assumed to remain unchanged over growth. Modeling the self-growing connection was defined as a merged part and its fiber direction aligned with the dominant tree, which is not in agreement with our findings in Chapter 3. The merged fibers should be produced by combining two stems, and the direction should be across two stems, which was not considered in the modeling of the connection.

6

6.5 Concluding remarks

In this chapter, the biomechanical characteristics of interconnected tree systems are investigated by means of pulling tests and FEM analyses. Some key conclusions from this paper are listed below.

1. Pulling tests together with FEM calculations may act as an applicable tool to provide an informative understanding of the mechanical performance of the tree under loads.
2. In most of the cases studied, the growth of trees induces a reduction in deformation, rotation, and local elongations; additionally, the stiffness of the entire system increases.
3. Regarding the cross interconnected trees, they show a significant bracing effect in the connecting plane, which is reflected by fewer deformations and fewer stress responses compared to out-of-plane loading. However, the loading capacity of the cross interconnected system loaded in plane depends on the strength of the supporting trees.
4. For parallel connected trees, the connected lower region increases the basal stiffness but presents a certain asymmetric behavior due to the uneven distribution of the root anchorage.

With an understanding of the biomechanical properties of interconnected tree systems, it can be further evaluated and applied to the design of living tree structures.

References

[1] B. Gardiner, H. Peltola, and S. Kellomäki. Comparison of two models for predicting the critical wind speeds required to damage coniferous trees. *Ecological Modelling*, 129:1–23, 2000.

[2] B. Gardiner, K. Byrne, S. Hale, K. Kamimura, S. J. Mitchell, H. Peltola, and J. C. Ruel. A review of mechanistic modelling of wind damage risk to forests. *Forestry: An International Journal of Forest Research*, 81:447–463, 2008.

[3] H. Peltola, S. Kellomäki, A. Hassinen, and M. Granander. Mechanical stability of Scots pine, Norway spruce and birch: An analysis of tree-pulling experiments in finland. *Forest Ecology and Management*, 135:143–153, 2000.

[4] H. M. Peltola. Mechanical stability of trees under static loads. *American Journal of Botany*, 93:1501–1511, 2006.

[5] E. de Langre. Plant vibrations at all scales: A review. *Journal of Experimental Botany*, 70(14):3521–3531, 2019.

[6] B. Kane. Determining parameters related to the likelihood of failure of red oak (*Quercus rubra* L.) from winching tests. *Trees - Structure and Function*, 28:1667–1677, 2014.

[7] G. Dahle, K. James, B. C. Kane, and J. Grabosky. A review of factors that affect the static load-bearing capacity of urban trees. *Arboriculture and Urban Forestry*, 3:89–106, 2017.

[8] B. Gardiner, P. Berry, and B. Moulia. Wind impacts on plant growth, mechanics and damage. *Plant science*, 245:94–118, 2016.

[9] J. Morgan and M. G. R. Cannell. Structural analysis of tree trunks and branches: Tapered cantilever beams subject to large deflections under complex loading. *Tree Physiology*, 3:365–374, 1987.

[10] R. Milne and P. Blackburn. The elasticity and vertical distribution of stress within stems of *Picea sitchensis*. *Tree Physiology*, 5:195–205, 1989.

[11] H. C. Spatz and F. Bruechert. Basic biomechanics of self-supporting plants: Wind loads and gravitational loads on a Norway spruce tree. *Forest Ecology and Management*, 135: 33–44, 2000.

[12] V. Cucchi, C. Meredieu, A. Stokes, F. De Coligny, J. Suarez, and B. A. Gardiner. Modelling the windthrow risk for simulated forest stands of Maritime pine (*Pinus pinaster* Ait.). *Forest Ecology and Management*, 213:184–196, 2005.

[13] P.E. Levy, S.E. Hale, and B.C. Nicoll. Biomass expansion factors and root : shoot ratios for coniferous tree species in Great Britain. *Forestry: An International Journal of Forest Research*, 77:421–430, 2004.

[14] B. Gardiner, A. R. T. Schuck, M. Schelhaas, C. Orazio, K. Blennow, and B. Nicoll. *Living with storm damage to forests.* 2013. European Forest Institute, pages: 31–38.

[15] B. A. Gardiner. *Mechanical characteristics of Sitka spruce.* Forestry Commission, 1989. Pages 1–24.

[16] M. J. Crook and A. R. Ennos. The anchorage mechanics of deep rooted larch, *Larix europea* L. japonica. *Journal of Experimental Botany*, 47:1509–1517, 1996.

[17] M.P. Coutts. Components of tree stability in Sitka spruce on peaty gley soil. *Forestry: An International Journal of Forest Research*, 59:173–197, 1986.

[18] B. C. Nicoll, B. A. Gardiner, B. Rayner, and A.J. Peace. Anchorage of coniferous trees in relation to species, soil type, and rooting depth. *Canadian Journal of Forest Research*, 36:1871–1883, 2006.

[19] C. J. Stubbs, D. D. Cook, and K. J. Niklas. A general review of the biomechanics of root anchorage. *Journal of Experimental Botany*, 70:3439–3451, 2019.

[20] T. Fourcaud, J. N. Ji, Z. Q. Zhang, and A. Stokes. Understanding the impact of root morphology on overturning mechanisms: A modelling approach. *Annals of Botany*, 101:1267–1280, 2008.

[21] T. Lundström, T. Jonas, V. Stöckli, and W. Ammann. Anchorage of mature conifers: Resistive turning moment, root–soil plate geometry and root growth orientation. *Tree Physiology*, 27:1217–1227, 2007.

[22] A. Stokes, M. A. Ghani, F. S., F. Danjon, H. Jeannin, S. Berthier, A. D. Kokutse, and H. Frochot. Root morphology and strain distribution during tree failure on mountain slopes. *Eco-and Ground Bio-Engineering*, pages 165–173, 2007.

[23] L. Wessolly and M. Erb. *Tree Statics and Tree Inspection.* 2016. Pages 221–259.

[24] E. Brudi and P. Van Wassenaer. Trees and statics: Non-destructive failure analysis. *ISA Champaign*, pages 1–17, 2001.

[25] L. Dupuy, T. Fourcaud, and A. Stokes. A numerical investigation into factors affecting the anchorage of roots in tension. *European Journal of Soil Science*, 56:319–327, 2005.

[26] L. X. Dupuy, T. Fourcaud, P. L., and A. Stokes. A generic 3D finite element model of tree anchorage integrating soil mechanics and real root system architecture. *American Journal of Botany*, 94:1506–1514, 2007.

[27] T. Jackson, A. Shenkin, A. Wellpott, K. Calders, N. Origo, M. Disney, A. Burt, P. Raumonen, B. Gardiner, M. Herold, T. Fourcaud, and Y. Malhi. Finite element analysis of trees in the wind based on terrestrial laser scanning data. *Agricultural and Forest Meteorology*, 265:137–144, 2019.

[28] T. Jackson, A. Shenkin, J. Moore, A. Bunce, T. Van Emmerik, B. Kane, D. Burcham, K. James, J. Selker, K. Calders, N. Origo, M. Disney, A. Burt, P. Wilkes, P. Raumonen, J. Gonzalez De Tanago Menaca, A. Lau, M. Herold, R. C. Goodman, T. Fourcaud, and Y. Malhi. An architectural understanding of natural sway frequencies in trees. *Journal of the Royal Society Interface*, 16, 2019.

[29] B. Šilinskas, A. Povilaitienė, G. Urbaitis, M. Aleinikovas, and I. Varnagirytė-Kabašinskienė. The wood quality of small-leaved lime (*Tilia cordata* Mill.) trees in an urban area: A pilot study. *Forests*, 12:420, 2021.

[30] CEN. EN 384: Structural timber - determination of characteristic values of mechanical properties and density, 2016.

[31] H. Peltola and S. Kellomäki. A mechanistic model for calculating windthrow and stem breakage of scots pines at stand age. *Silva Fennica*, 27:99–111, 1993.

[32] M. G. R. Cannell and J. Morgan. Young's modulus of sections of living branches and tree trunks. *Tree physiology*, 3(4):355–364, 1987.

[33] H. T. Valentine. Tree-growth models: Derivations employing the pipe-model theory. *Journal of theoretical biology*, 117(4):579–585, 1985.

[34] J. Gril, D. Jullien, S. Bardet, and H. Yamamoto. Tree growth stress and related problems. *Journal of Wood Science*, 63:411–432, 2017.

[35] T. Lundström, M. J. Jonsson, and M. Kalberer. The root-soil system of Norway spruce subjected to turning moment: Resistance as a function of rotation. *Plant and Soil*, 300: 35–49, 2007.

[36] G. A. Dahle and J. C. Grabosky. Variation in modulus of elasticity (E) along *Acer platanoides* L.(Aceraceae) branches. *Urban Forestry and Urban Greening*, 9(3):227–233, 2010.

[37] H. Lindström, J. W. Evans, and S. P. Verrill. Influence of cambial age and growth conditions on microfibril angle in young Norway spruce (*Picea abies* L. Karst.). *Holzforschung*, 52:573–581, 1998.

[38] F. Brüchert, G. Becker, and T. Speck. The mechanics of Norway spruce *Picea abies* L. Karst: Mechanical properties of standing trees from different thinning regimes. *Forest ecology and management*, 135(1-3):45–62, 2000.

7

Resistance micro-drilling inspection for living tree connections

The future vision of this research focuses on the long-term application of living structures created through self-growing connections. It is essential to understand the growth of fusion within the self-growing connection without causing major harm in order to guarantee the sustainability of the living structure. To address this, micro-drilling resistance measurement was employed in this chapter. The technique gave an output resistance profile that was used to estimate the density relevance and anatomical characteristics (e.g., growth ring and decay) of the object studied.

This chapter investigated the self-growing connections fused by Ficus benjamina and Tilia cordata. Ficus connections served as a reference sample to generalize relations between drilling resistance, density variations, and anatomical features. These relations were further utilized to infer the fusion situation from the drilling results of the Tilia connection. Regarding the examinations on the Ficus connections, it was noted that when the drilling needle passes through the intersected region, a drop-down effect was observed. This effect was primarily attributed to the local material, which consisted of bark tissues. Regarding the inference on the Tilia connection, a similar drop-down effect was identified in the intersected area. However, without an informative anatomical analysis, the micro-drilling measurements had limitations to infer more precise information.

7.1 Introduction

7.1.1 Growth assessment of self-growing connections

When a self-growing connection is fused by two individual stems, the development of a connection comes from both trees. Understanding to what extent a connection has fused is the key message in estimating the potential strength of a connection. Monitoring the growth of a self-growing connection without disturbing the future development is a challenge for better assessment of the living tree structure.

As studied in previous chapters (Chapter 3 and 4), the fusion and growth of the self-growing connection shows various growth characteristics in different stages over time (see Figure 3.4). Furthermore, even within the same growth period, in different cutting sections, the cross section of a connection exhibits different levels of fusion stages (Figure 3.13). The characteristics of a connection that can be measured and that can reflect growth conditions include the following aspects.

- The **density profile** close to the merged boundaries exhibits a relative higher magnitude compared to the stem region (Chapter 3, Figure 3.7 and 3.8).
- From a geometric perspective, the **fusion depth and interface curvature** of the interfacial surface are introduced to reflect the fusion condition. The fusion depth is measured in the middle location between two stems, as discussed in Figure 3.19 in Chapter 3, and is defined in Figure 5.3 in Chapter 5. The interface curvature of the interface surface is described and elaborated in Figure 5.4 of Chapter 5. These parameters have been shown to have a moderate correlation with the strength of a connection (r = - 0.54 for the interface curvature to the strength for analysis).
- When investigating the **fiber patterns**, Figure 3.18 in Chapter 3 gives an abstract but thorough illustration of the typical fiber pattern of a self-growing connection. It shows the discontinuities (i.e., included bark tissues, Figure 3.12 c) tend to be present in the interior region of the interfacial area; and fused fibers that join two stems are more likely to be distributed in the smooth transit zone in the outer layer of a connection.

Among the listed aspects, some features are hard to quantify, e.g., fiber pattern and internal discontinuities. The measurable results include the fusion depth and interface curvature, which are the most direct and practical way to infer the growth of the connection. Other aspects, such as fiber structures, have to be further confirmed from destructive anatomical studies. However, the accuracy of the measurements to describe the growth condition is questionable because a deep fusion is determined not only by the amount of continuous fused fibers in the outer layer, but also by the interior discontinuities. Therefore, a practical and feasible approach is needed to indicate the interior profile of a connection.

7.1.2 Resistance drilling measurements

The resistance drilling measurement is a semi/non-destructive and rapid method commonly applied in situ for the inspection of living trees [1–4] and timber buildings [5–8]. It has been used for many applications including tree growth investigations [9–11], wood defect detection (such as decay, insect damage, internal void, and internal cracks, etc.).

[12–15] and evaluation of wood density and mechanical properties [16–20]. The commonly used equipment for wood detection and its drilling needle is shown in Figure 7.1.

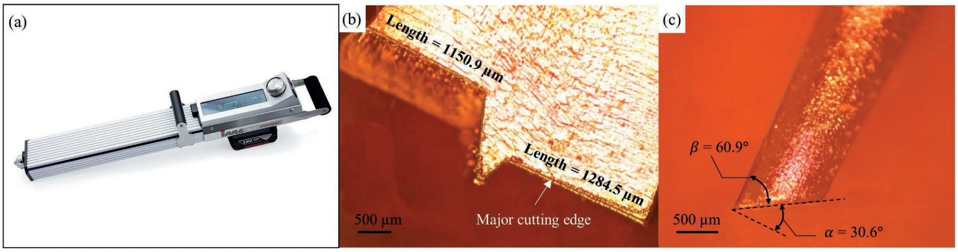

Figure 7.1: Resistance drilling equipment. (a) Equipment IML-RESI Power Drill; (b) drilling needle in the front view; (c) drilling needle in the side view. Modified from [21].

Resistance micro-drilling measures the relative resistance (drilling torque and feed force) of the material as a rotating needle (Figure 7.1 b and c) is driven into the wood at a constant drilling and feed speed. Changes in wood resistance are displayed on a graph plotted against the drilling depth as changes in amplitude. Areas with higher values can be associated with knots and other high-density anatomical variations (e.g., latewood) and lower value extremes pointing towards decays and cracks. Although it requires drilling into the tree, this measurement only results in an opening of 3 mm width and is considered minimally invasive and will not influence the future growth of living trees.

The drilling resistance of a tree is commonly considered as a function of the wood properties (such as density), defect zones, and discontinuities such as open cracks, areas of severe decay [2, 6, 19, 22–25]. Density is one of the most important characteristics of standing trees that affect the properties of many wood products. Many investigations [2, 22–24] found that the resistance to drilling is proportional to the density variations of the wood member. Early research indicated that there was a strong linear correlation between mean drilling resistance and wood density [2]. Recent studies also shows a moderate to strong correlation between the resistance of the drill to wood density, for example, the correlation coefficient is reported to be 0.6 in [22], 0.71 in [23], and greater than 0.8 in [24]. Regarding the correlations between the resistance to drilling and the mechanical properties (compressive strength), the correlation coefficient is not significant, which presents a value less than 0.6 in most tree species [6, 19, 25].

When comparing the drilling profiles measured in dry wood and green wood, Mattheck [1] found that the drilling resistance in dry wood was more or less of the same magnitude as in green wood. Similarly, another work [26] also reports that when the moisture content of the wood is in the range between 55% and 71%, the density and the moisture content are not significantly correlated. However, a positive correlation between moisture content and density is also reported [21]. Sharapove et al. [21] indicates that the variations in the results may be due to different drilling conditions, i.e., drilling speed, feed rate and drilling needle geometry, which are not clearly elaborated in the mentioned works, but have a combined effect on the drilling results.

In some studies [4, 6], the measurement of the resistance of the drilling is recommended as a qualitative approach to interpret the characteristics (e.g., decay zone) of the drilled sample. This is because the forces or torques to which the drill bit has been subjected during drilling are too complex, not only in the tangential direction of the drill bit, but also the feed force and friction in the shaft and in the drilling direction [27]. The resistance measurement is an indirect magnitude and is expressed in amplitude to quantify the torque and feed work that the operator requires when passing through the drilled material. To better study the behavior of the drill machine, Zhao and Ehmann [28] discuss the influence of the geometry of the drill bits for wood drilling. Sharapov et al. [19, 27, 29] studies the behavior of the drill bit and investigated the service life of the drill needle applying the term called feed rate per cutting edge to consider damage to the drill bit. Researchers [27] also quantifies the obtained amplitudes with the feed force and the drilling power, but the further use of the regressed physical values has not been investigated. The most commonly used approach is the mean amplitude of the resistance profile in the area of interest to correlate with the desired properties of the wood as reviewed in [6].

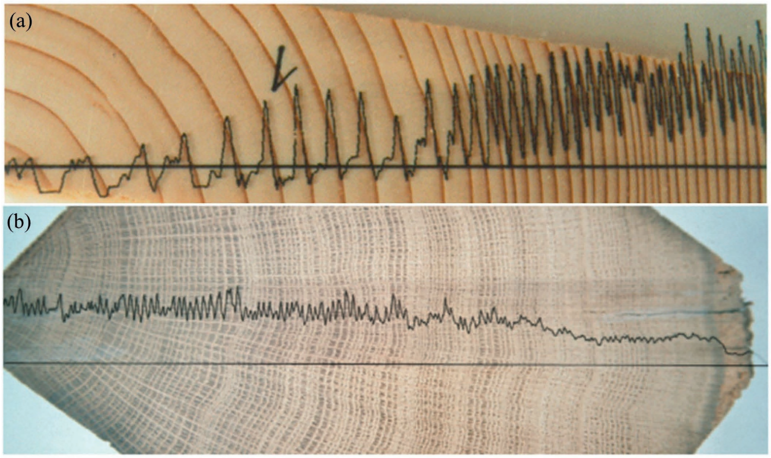

Figure 7.2: Comparison between anatomical features and resistance profile. (a) Conifer tree; (b) ring-porous oak tree. Modified from [4].

To better interpret the results, knowledge about the anatomy of wood is a prerequisite to be able to interpret the results profiles correctly. As shown in Figure 7.2, the resistance profile is compared with the anatomical characteristics of the conifer tree (Figure 7.2 a) and the oak tree (Figure 7.2 b), respectively. As described in [4], the combination of latewood and earlywood in a clear growth ring (Figure 7.2 a) determines the typical shape of the resistance profile. In ring-porous wood, such as oak (Figure 7.2 b), resistance profiles commonly rise in the center of the beams and then drop down again when the needle comes closer to the other side. This drop-down effect can only be distinguished from decay or insect damage in profiles that are linearly correlated to density and provide high resolution. Resistance profile derived from tropical species without distinct tree-rings show similar behavior as many diffuse-porous species from moderate zones and mostly rise up in the centre.

For interpreting resistance micro-drilling measurements, microscopic inspection [4, 7], sonic inspection [9] and X-ray density investigation [2, 8] are used. Typical profiles reflect wood anatomical structures, and the accurate interpretation of the profile obtained must be confirmed from other information. For example, the early decay stage is relatively difficult to identify only from the resistance profile, since the drop-down effect on resistance variations was not significant compared to variations in early wood and late wood [4]. In other words, resistance drilling only delivers reliable results, if applied at the appropriate point and interpreted with respect to the anatomical features of the wood.

In this chapter, the approach of resistance micro-drilling measurement is applied for the inspection of self-growing connections. Drilling resistance comparisons are performed at different drilling locations, i.e., the stem region, the low-level fusion region, and the high-level fusion region within a connection fused by *Ficus benjamina*. The interpretation of the drilling resistance profile is further studied with microscopic investigation of the anatomical features and density measurement from X-ray. Based on understanding, this approach is further extended to inspecting the self-growing connection fused by *Tilia cordata* in the TU Delft Hortus Botanicus (see Figure 6.1). It aims at better understanding the internal features from a semi-/nondestructive method for the future monitoring application of living tree structures.

7.2 Materials and methods

7.2.1 Self-growing connections by *Ficus*

Following the studies in previous chapters, this chapter studied the self-growing connections fused by weeping fig (*Ficus benjamina*) as a reference and analogy for further studies on other tree species, as well as in different conditions. The advantage of employing connections from *Ficus* is the availability and feasibility of rigorous lab tests. The definition of coordinates and geometric information follows the principles stated in Figure 3.4 in Chapter 3.

Seven connections were selected from the same growing pot (as in Figure 3.3 a). As shown in Figure 7.3, the geometric parameters were measured and listed in Table 7.1. The difference in fusion was calculated from the difference between the fusion width and the sum of the two diameters. The degree of fusion was then expressed as the percentage of the difference in fusion with respect to the average (avg.) diameter of a connection. The equation can be referred to as Equation 5.3. Within the sample size studied, the diameter of the connection ranged from 12 to 26.3 mm. Furthermore, the degree of fusion ranged from 7.9% to 33.5%.

7.2.2 Drilling plan on *Ficus* connections

The drilling device used is the IML-RESI PD 400 tool (IML System GmbH, Wiesloch, Germany); and its equipped needle is 3 mm in diameter at a tip and 1.5 mm in diameter at its shaft. Resistance amplitudes were recorded every 0.1 mm during drilling. The drilling feed rate was set as 25 cm/min and the rotational speed was 1500 rpm for *Ficus* self-growing connections. The determination of this speed option was mainly based on experience, since this option was able to provide a clear profile for drilling on fig connections. When drilling activity was performed, the equipment and sample were fixed to a stable table to achieve the desired and stable drilling measurements.

Table 7.1: Geometric information of studied self-growing connections from *Ficus benjamina*

Connection	Diameter		Avg. diameter	Angle	Fusion width	Fusion degree
	D_1, mm	D_2, mm	mm	degree	mm	%
Connection 1	16.5	14.0	15.3	28.5	29.3	7.9
Connection 2	28.0	24.5	26.3	45.5	47.7	18.3
Connection 3	25.2	21.5	23.4	42.1	39.2	32.1
Connection 4	21.5	14.0	17.8	64.0	30.5	28.2
Connection 5	22.6	14.5	18.6	74.5	34.1	16.2
Connection 6	12.6	11.3	12.0	56.1	22.1	15.1
Connection 7	14.0	13.6	13.8	68.0	22.7	33.3

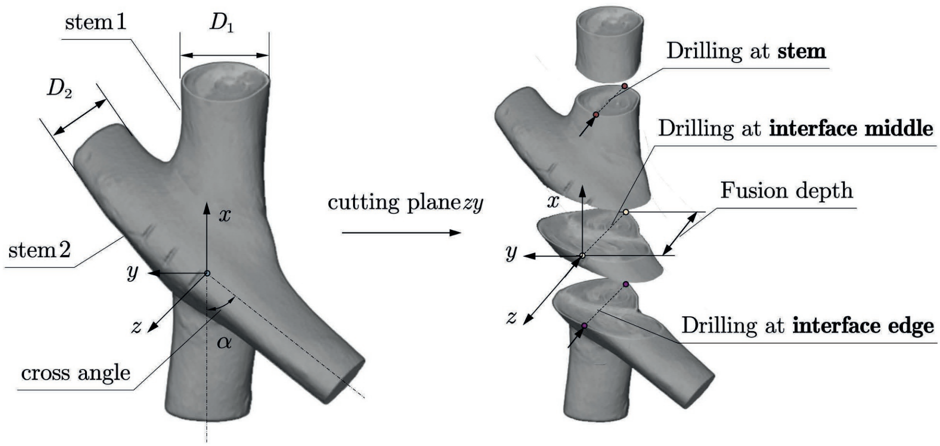

Figure 7.3: Illustration of a self-growing connection and its drilling locations.

Drilling locations in the self-growing connection distributed in two regions in a connection: stem and interconnected regions, as in the example shown in Figure 7.3. The drilling directions were aligned with the direction of the axis *z*.

In the stem region, the drilling lines in the stems were located in the area away from the interconnected region (approximately 2 cm), and the drilling needle passes through the stem pit if possible. Three drilling lines on each stem were preferable. When the size of the connection was too small to achieve (e.g., one the diameter size of connection 1 is 14 mm, which is too small to obtain stable results), at least one drilling was performed at each of the stems. This information was used as a reference to compare the resistance difference between the stem and the intersected area.

In the intersected region, the drilling location selected was at the edges and middle locations (interface edge and interface middle in Figure 7.3) within the intersected area. The drilling line passed through two stems at the interface. These two locations were used to compare the resistance difference due to the level of fusion of a self-growing connection. The features of the resistance profile will be further explained on the basis of the characteristics of the cross section at different fusion levels.

Table 7.2: Drilling plans on *Ficus* self-growing connections

Connection	Stem1	Stem2	Interface edge	Interface middle
Connection 1	X	X	X	X
Connection 2	X	X	X	X
Connection 3	X	X	X	X
Connection 4	-	-	-	X
Connection 5	-	-	-	X
Connection 6	-	-	-	X
Connection 7	-	-	-	X

The drilling plan performed on each connection was presented in Table 7.2. The drilled position was marked as 'X'. Connections 1 to 3 were drilled both in the stems and in two locations in the interfacial region. Others were drilled only at the middle location of the fusion region. The drilling results were analyzed by removing the first 2 mm and last 2 mm drilling depth to remove the influence of the bark. In the rest profile, the mean value and standard deviation were calculated for both the drilling and the feed amplitudes.

7.2.3 Microscopic inspection on *Ficus* connections

Microscopic studies were performed after debarking the connections. Then they were sliced in the cutting plane *zy* as shown in Figure 7.3. Since microscopic observation was performed after drilling activity, to obtain a better visual identification, the cross sections below or above the drilled material were investigated under the optical microscope (Keyence VHX7000, Germany). The preparation process followed the method described in Section 4.2.2 and 4.2.3.

7.2.4 X-ray inspection on *Ficus* connections

X-ray inspection was performed using the CT device (Siemens Somatom Volume Zoom CT scanner). As studied in Chapter 3, Section 3.2.2, this obtained slice was constructed using pictures represented by gray values. Each scanned slice has a resolution of 0.3 × 0.3 mm^2. The gray value was studied to linearly correlate with the density of the material studied. Therefore, in this work, the results obtained were first calibrated using Equation 5.1. Then, at the drilling locations, the density profile was plotted to compare with the resistance profile. To better illustrate the density variations, the obtained gray value results were further segmented into four regions to signify the varied density regions within a cross section. The chosen thresholds were 800, 1000, 1100 and 1300 kg/m^3. The determination of thresholds was based on the concentration of gray values in the histogram. Image analysis was performed by ImageJ.

7.2.5 Estimation of the *Tilia* self-growing connection

From studies on self-growing connections by weeping figs, the expected results may provide an understanding of the relationship between the variations of resistance and internal properties (density variation and location of defects). It means that when the resistance variation is known, it can be used to correlate and estimate the possible physical properties and microscopic features. Therefore, drilling activities were performed on living trees and living self-growing connections fused by limes (*Tilia cordata*) to infer their internal features. The challenge of this estimation was that the living tree and connections cannot be carried out by destructive experiments, such as anatomical studies. Thus, drilling testing acts as a non-destructive monitoring technique in this situation. The drill speed was set at 2500 rpm; and the feed speed was 150 cm/min. The picture of the operating drilling activity is shown in Figure 7.4.

7

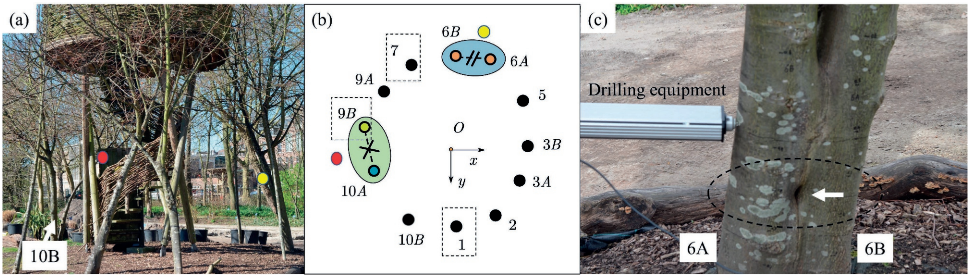

Figure 7.4: Picture of drilling operating on the parallel self-growing connection. (a) Photo of the distribution of single and interconnected trees around the *Living Tree Pavilion*; (b) horizontal configuration of the distribution of the trees; (c) the studied parallel self-growing connection, where at the height of 0.25 m following the direction of the arrow, it has an area not fully merged.

As shown in Figure 7.4 b, three single trees (trees 1, 7, and 9B) were picked in the rectangles that surround the pavilion. They were drilled at a height of 1 m. The diameters measured at the drilled location were 75, 78 and 134 mm, respectively. The purpose of this activity was to understand the typical drilling profile of living lime trees to help interpret the results when they fused into a connection.

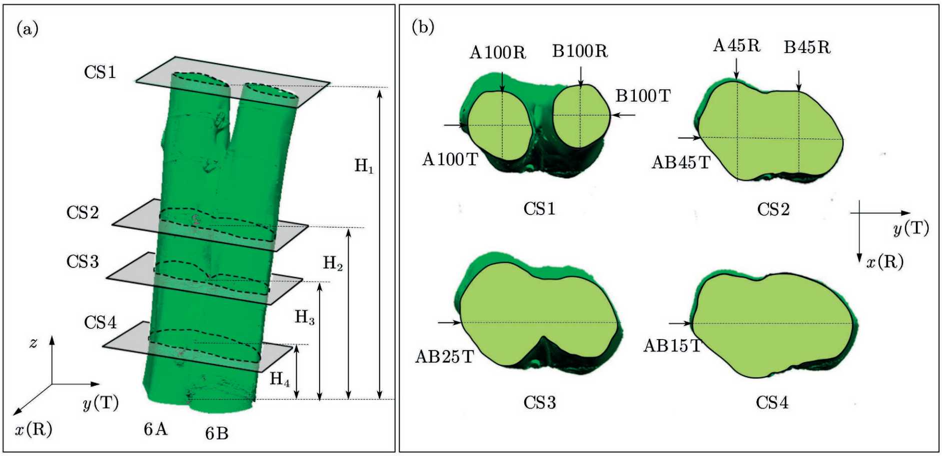

Figure 7.5: Illustration of the drilling plan on parallel interconnected *Tilia* trees 6A and 6B. As seen in this figure, (a) gives the scanned shape of the parallel connection, in which four cross sections (shortened in CS1 to CS4) are chosen to drill. Heights of each cross section from H_1 to H_4 are 0.15, 0.25, 0.45 and 1 m respectively. At each cross section, the drilling locations are presented in (b). The drill label gives the information of the direction and location of the path, for example, A100T means tree 6A is drilled at height of 1 m in the tangential direction or aligning with axis y.

Regarding the drilling plan for the connection, the parallel connection was selected. The drilling locations are illustrated in Figure 7.5. The parallel self-growing connection was fused by trees 6A and 6B, as shown in Figures 7.4 b and c. First, the drilling cross sections were selected at heights of 1 m (H_1), 0.45 m (H_2), 0.25 m (H_3), and 0.15 m (H_4) in Figure 7.5 a. At a height of 1 m, the two trees 6A and 6B were drilled in two directions, namely radial (A100R, B100R) and tangential (A100T, B100T) directions. At a height of 0.45 m, it is located in the fused region and the drilling paths were made in the radial direction for two trees (A45R and B45R). However, in the tangential direction, only one path was made at this height passing trees 6A and 6B (AB45T). It should be noted that at a height of 0.25 m, it is the location indicated by the white arrow in Figure 7.4 c. At this height, only a tangential path (AB25T) was taken passing trees 6A and 6B. The AB15T tangential drilling path was made at a height of 0.15 m passing two trees.

7.2.6 Investigation structure

The structure of investigations in both the *Ficus* connections and the *Tilia* connections is organized in Figure 7.6. Regarding the *Ficus* connections, the methods utilized include CT scanning, microscopy, and drilling. The connection was first scanned and then drilled at the marked location. Subsequently, it was cut for microscopy. The results obtained from the three steps include the resistance profile, anatomical observations, and density profile. The obtained results were further compared and analyzed on the basis of the relation at the studied locations. For example, in Figure 7.6, it gave the result in the middle intersected region as an example, the red rectangle marked the area of interest. The compared aspects include anatomical characteristics, resistance trends, and density variance. With understanding of the *Ficus* connection, the anatomical feature of the *Tilia* connection was further inferred based on the resistance profile.

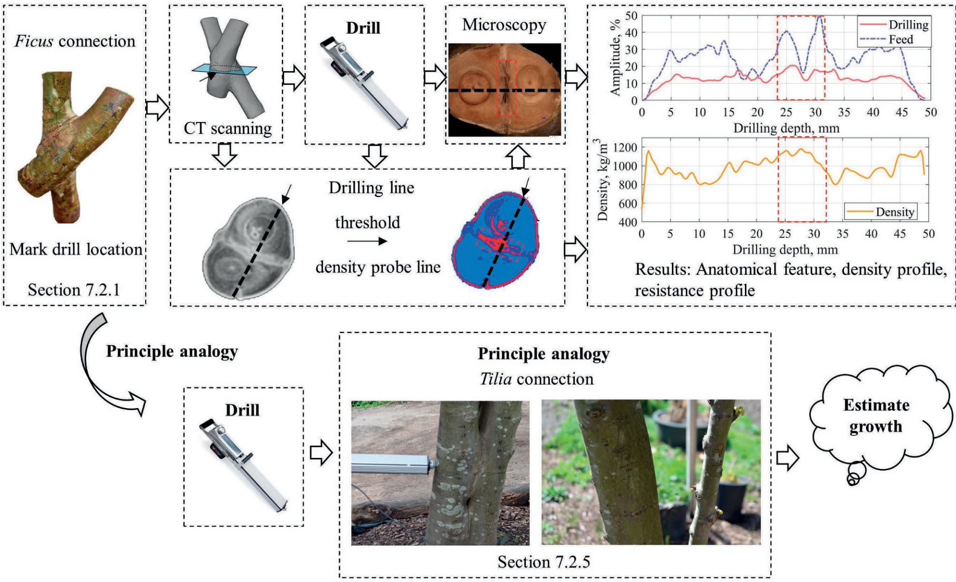

Figure 7.6: Investigation structure. *Ficus* connection is used as a reference species to understand the relation between growth features and resistance patterns. This understanding is implemented to understand the growth of *Tilia* connection from its resistance patterns.

7.3 Results and analyses

The results are presented in two sections according to the studied materials, namely *Ficus* connections and *Tilia* connections. First, the interpretation of the internal characteristics of the self-growing connections fused by *Ficus* is based on the results of the resistance profile, anatomical characteristics, and density variation profiles in different cross sections in the stem and fused region. The second part of the results shows the estimation of the internal characteristics of the *Tilia* connections from the resistance information.

7.3.1 Investigation on *Ficus* connections

Connection 1

The results of the *Ficus* connections are represented by the results of connections 1 and 2 at drilled locations distributed in the stem and intersected regions. The rest of the analysis can be referred to the Appendix D.

Connection 1 has the feature of a low fusion level (7%) and its fusion condition does not show much difference in edge and middle. In the stem region, as shown in Figure 7.7, a comparison is presented between density variations and resistance profile. The drilling line that passes through the location is marked in the dashed line in this figure.

Figure 7.7 a indicates the location on the stem from which it is drilled. Figure 7.7 c is the density map after being segmented by different density ranges (1000, 1100, and 1300 kg/m^3). Figure 7.7 d shows the comparison between the resistance profile of the drilling and the density variations. From the density variation, as indicated by the drilling path, it has first experienced a relatively high density region, then reached the pith and dropped, and it has been following a small rise again. Overall, it shows a symmetric pattern. Between 2 to 15 mm distances, the mean density of wood is analyzed as 1078.5 kg/m^3 with a coefficient of covariance (CoV) of 4%. According to the resistance profile, the drilling amplitude has an average of 10.1% and a CoV of 23%. The feed amplitude has an average of 15.5% and a CoV of 16.8%.

The anatomical characteristics of the cross sections in the stem and interfacial regions where the drilling needle has passed are shown in Figure 7.8 a. Regarding anatomical features, as studied in Chapter 4, *Ficus benjamina* is a tropical hardwood species without distinct growth rings. Instead, the growth increment is composed of bundles of fibers and parenchyma rings alternating with each other. Therefore, the drilling profile may not distinguish ups and downs, which indicates the locations of the growth rings.

In the interconnected area, as can be seen in Figures 7.8 b and c, the discontinuous gap between two stems is obvious. This area is identified primarily as consisting of bark tissues and less lignified cells. In comparison, the stem part in the interconnected section is similar to the normal stem. The resistance profile, together with the density variation, is shown in Figure 7.9. Figure 7.9 a shows the location where the cross section is drilled. This cross section is then taken from CT scanning and shown in Figure 7.9 b. This cross section is further segmented according to the defined thresholds and is shown in Figure 7.9 c.

From the density map (Figure 7.9 c and d), the intersected region, namely within the 13 to 17 mm distance, has a relatively high density compared to the stem region. This agrees with the finding in Chapter 3, Figure 3.6. However, the drilling profile shows a valley and drop-down effect in this region. This can be explained by the fact that the needle passes the gap (Figure 7.8 c) between two stems and there is less torque and feed needed to break the passing material that is considered soft tissues.

In this case, the pattern of the resistance profile is characterized by a drop-down valley when passing through the interface. Further quantified amplitude and its corresponding density within the same distance are shown in Table 7.3.

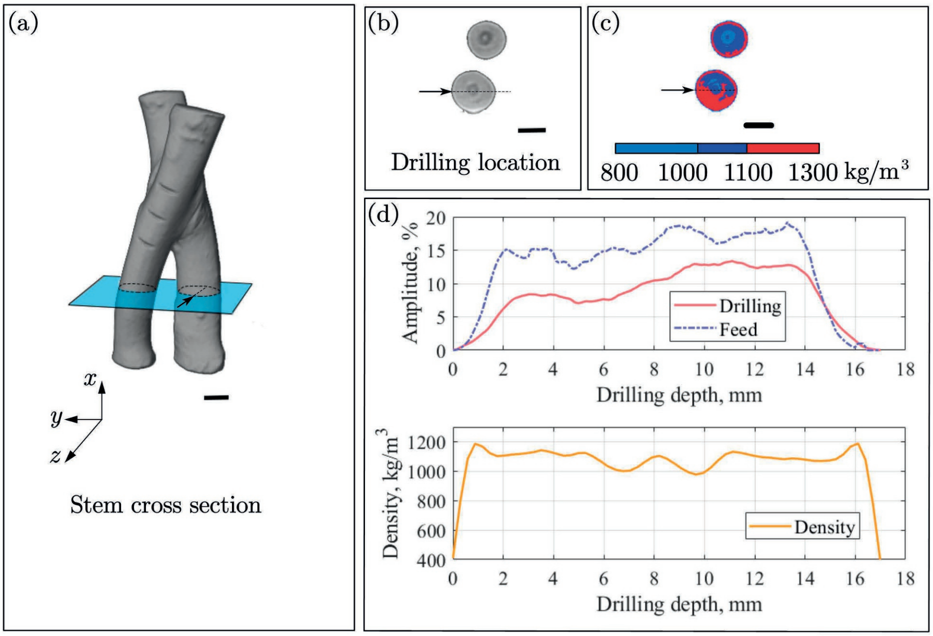

Figure 7.7: Connection 1 drilled in stem region in stem1: 3D and cross-sectional appearance, drilling location, density map, and comparison between drilling resistance and density variations along the drilling path. (a) Location of the drilled line in the connection; (b) drilling location corresponding to the X-ray scanning results; (c) density map based on gray values in (b); (d) comparison between resistance profile (top) and density profile (bottom) in the drilling location. Scale bar = 10 mm.

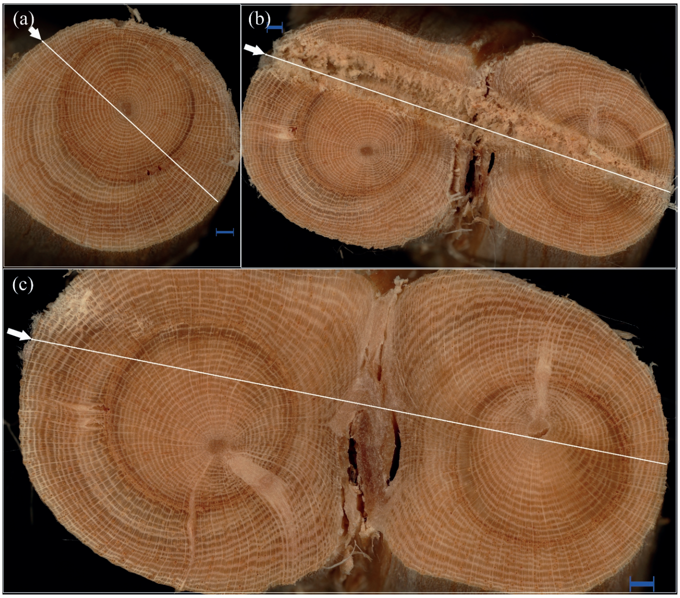

Figure 7.8: Anatomical features of connection 1 in (a) stem region, (b) and (c) interconnected region. Cross section (b) shows the material damaged from drilling, where cross section (c) is the section below the drilled path. White lines and arrows indicate the path and direction of the drilling needle. Scale bar = 1 mm.

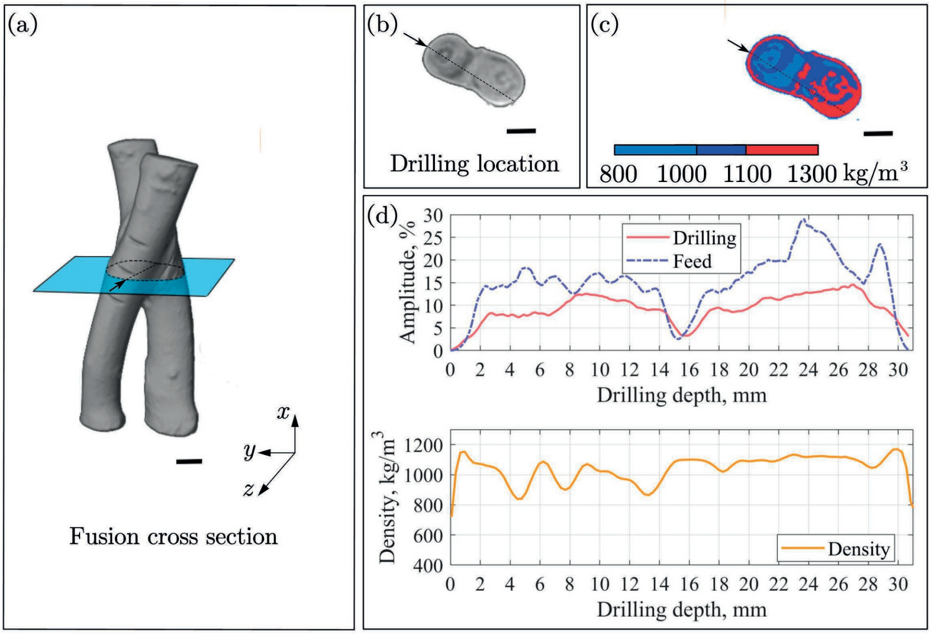

Figure 7.9: Connection 1 drilled in the interface middle region: 3D and cross-sectional appearance, drilling location, density map, and comparison between drilling resistance and density variations along drilling path. (a) Location of the drilled line in the connection; (b) drilling location corresponding to the X-ray scanning results; (c) density map based on gray values in (b); (d) comparison between resistance profile (top) and density profile (bottom) in the drilling location. Scale bar = 10 mm.

Connection 2

The results of connection 2 are also presented in the stem and intersected regions at each drilled location. Figures 7.10 and 7.11 show the results in the stem region. Figure 7.12 shows the results in the intersected region drilled at the edge. Figure 7.13 shows the results drilled in the middle of the intersected area.

In the stem region in Figures 7.10 drilled in stem1 and 7.11 drilled in stem2, similar to the case in connection 1, the drilling profile does not show abrupt ups and downs when the drilled stem is not decayed. The CoV of the feed resistance in stem1 is 17.4%; and 21.1% in stem2. However, the actual density varied less, with a CoV of 8.8% and 11.6% in stem1 and stem2, respectively. The anatomy of the stem is shown in Figure 7.14 a.

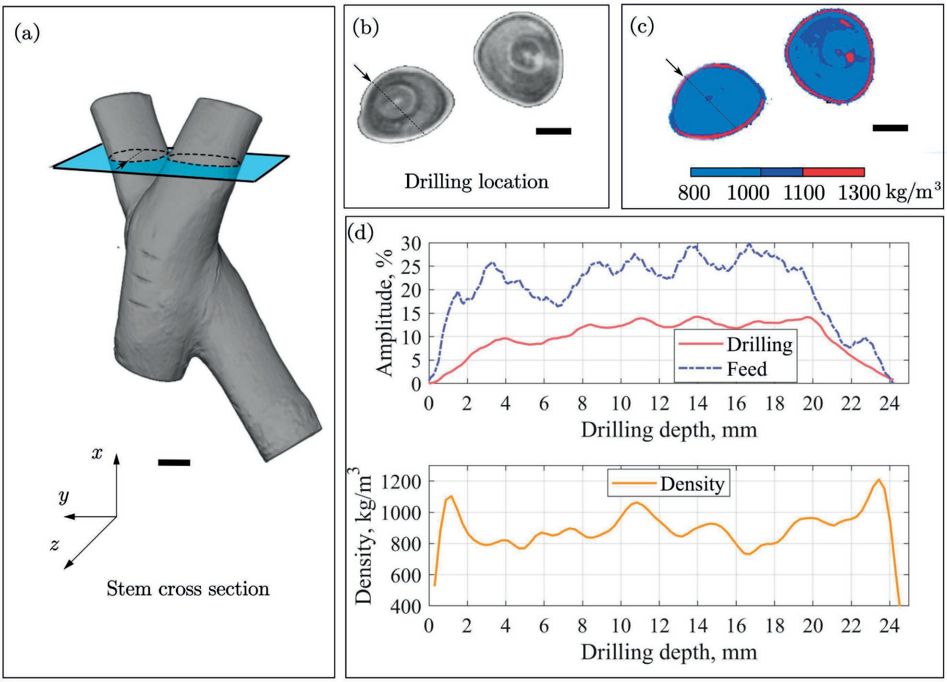

Figure 7.10: Connection 2 drilled in stem region (stem1): 3D and cross-sectional appearance, drilling location, density map, and comparison between drilling resistance and density variations along the drilling path. (a) Location of the drilled line in the connection; (b) the drilling location corresponding to the X-ray scanning results; (c) density map based on gray values in (b); (d) comparison between resistance profile (top) and density profile (bottom) in the drilling location. Scale bar = 10 mm.

7

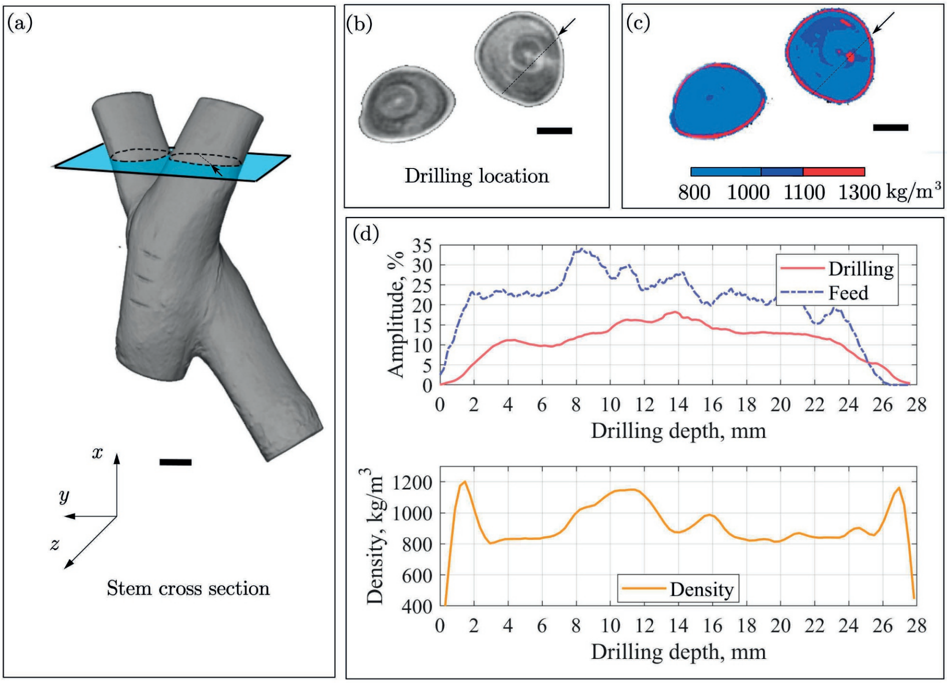

Figure 7.11: Connection 2 drilled in stem region (stem2): 3D and cross-sectional appearance, drilling location, density map, and comparison between drilling resistance and density variations along the drilling path. (a) Location of the drilled line in the connection; (b) the drilling location corresponding to the X-ray scanning results; (c) density map based on gray values in (b); (d) comparison between resistance profile (top) and density profile (bottom) in the drilling location. Scale bar = 10 mm.

In the intersected region, the density variations and resistance profile show complex patterns compared to the stem region. In Figure 7.12 a, this cross section is located at the edge of the intersected region. In this cross section, as shown in Figure 7.12 b, one of the stems has a defect (in dark color) within the material, at the drilling depth of 29 mm and at the density profile of depth of 26 mm in Figure 7.12 d. This characteristic can be observed in the anatomical picture in Figure 7.14 b. The area surrounding the defect shows a relatively higher density. Similarly, the intersected region exhibits a higher density variation. The resistance profile pattern shows a valley region in the gap between two stems at a distance of 20 mm. Furthermore, when the needle hits the defect, the profile drops at a distance of 29 mm.

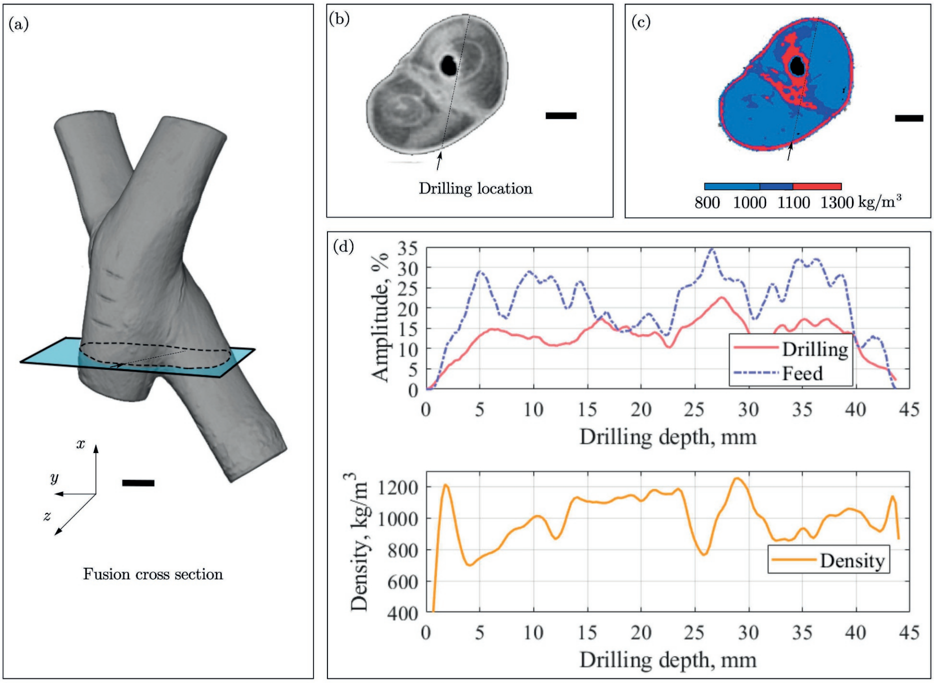

Figure 7.12: Connection 2 drilled in the interface edge region: 3D and cross-sectional appearance, drilling location, density map, and comparison between drilling resistance and density variations along the drilling path. (a) Location of the drilled line in the connection; (b) the drilling location corresponding to the X-ray scanning results; (c) density map based on gray values in (b); (d) comparison between resistance profile (top) and density profile (bottom) in the drilling location. Scale bar = 10 mm.

Figure 7.13 shows the results in the intersected region drilled in the middle location. This can be seen as a typical resistance pattern for drilling in the middle of the fused region. Regarding the density distribution, the profile at the intersected location shows an increase compared to the stem region, which aligns with the conclusion in Chapter 3. According

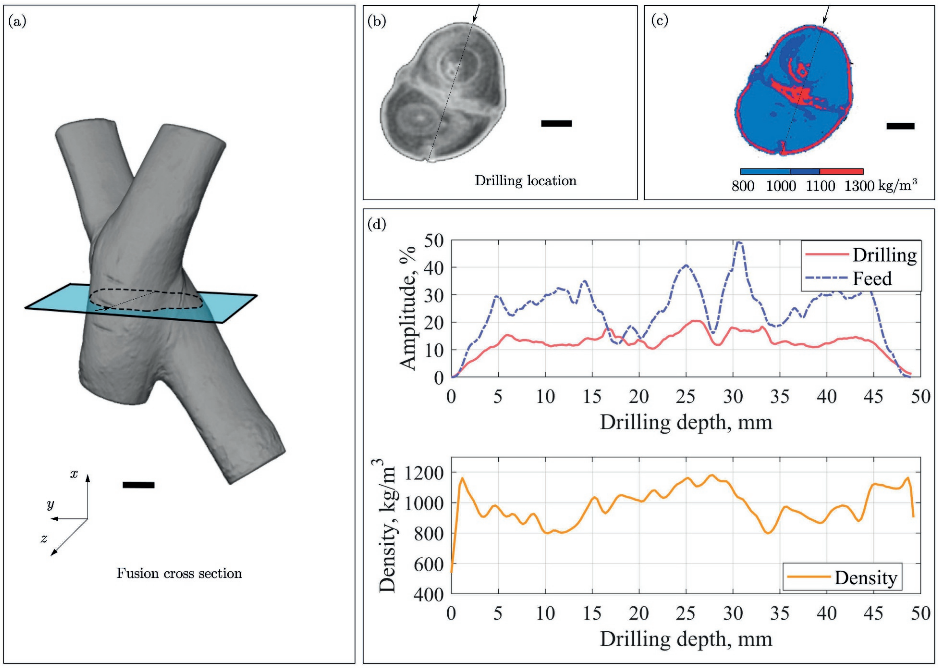

Figure 7.13: Connection 2 drilled in the interface middle region: 3D and cross-sectional appearance, drilling location, density map, and comparison between drilling resistance and density variations along the drilling path. (a) Location of the drilled line in the connection; (b) the drilling location corresponding to the X-ray scanning results; (c) density map based on gray values in (b); (d) comparison between resistance profile (top) and density profile (bottom) in the drilling location. Scale bar = 10 mm.

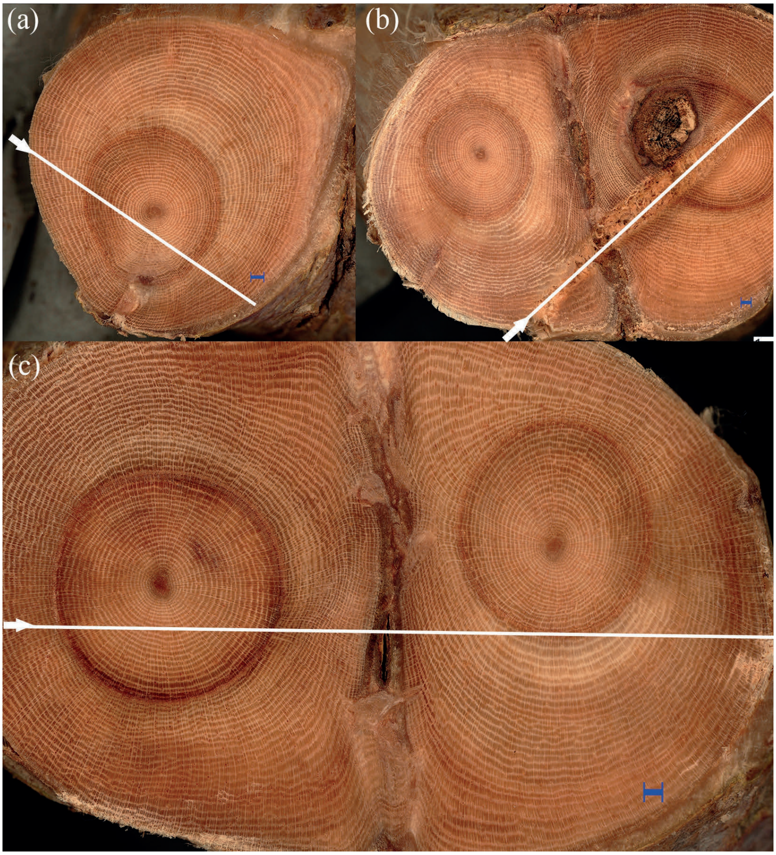

Figure 7.14: Anatomical features of connection 2 at the drilled cross sections. Drilling locations at (a) stem, edge of the intersected region (b) and middle of the interfacial region (c). The white lines indicate the path of the drill, and arrows point the direction of the needle.

to the drilling line, the valley region from a distance of 25 to 30 mm corresponds to the location of the included bark within the interface as in Figure 7.14 c.

The resistance measured from all samples studied is further analyzed and listed in Table 7.3. Several observations are found as follows.

- When comparing the CoV of density and resistance in general, the variation (CoV) in resistance of both drilling and feed is greater than that of density.
- Regarding the relationship between density and resistance, the coefficient of determination (R^2) of the mean drilling amplitude and density is 0.03; and that of the feed amplitude and density is 0.07.
- Regarding the comparison in magnitude of resistance in different regions, no clear statistical pattern can be drawn.

7.3.2 Estimation on the *Tilia* connection

Single tree

Regarding the living lime trees, the drilling results for the three single trees are first presented. This provides basic information as a reference to understand the resistance profile of this tree species. The results performed on single trees are shown in Figure 7.15. Anatomically, the lime tree (*Tilia cordata*) is a diffuse porous hardwood with clear growth rings. From this point on, the resistance profile can be seen showing clear ups and downs, indicating the location of growth rings. However, without accurate anatomy information at the drilled place, the width and location of each ring are still difficult to distinguish.

Regarding the parallel self-growing connection fused by trees 6A and 6B. The drilling plan is shown in Figure 7.5. The first drilling profile of tree 6A at a height of 1 m in both radial and tangential directions is presented in Figure 7.16. The profiles correspond to the indication 'A100R' and 'A100T' in Figure 7.5 b. In general, the overall pattern of the resistance profile has a drop trend close to the midregion. On the contrary, at the distance from where the drilling needle is about to penetrate the stem, the resistance increases again. For example, in the tangential direction of 6A (A100T), in Figure 7.16 a, the distance between 65 and 105 mm, the overall resistance is low, but in the distance from 105 mm to the end of the path, the resistance increases again.

Then the same drilling height and direction is performed on tree 6B, as in Figure 7.17. Figure 7.17 corresponds to the 'B100T' and 'B100R' in Figure 7.5 b. The resistance profiles of tree 6B in the two directions present a pattern similar to that of tree 6A.

The pattern of the resistance profiles on single stems (tree 1, 7, 9B, 6A and 6B in Figures 7.15 to 7.17) does not show obvious differences. For example, there are no regions with very low values that are noticed. The general pattern on the stems presents continuous hills and valleys.

Tilia self-growing connection

In the connected region, three lines are drilled. They are 'AB15T', 'AB25T', and 'AB45T' in Figure 7.5 b. In the 100 to 200 mm region, where two stems meet, the profile pattern exhibits a pattern that first increases, then experiences a valley, and then increases again. It is similar to the pattern in Figure 7.13. This may indicate the location of the internal

Table 7.3: *Ficus* connection drilled in stem and interface regions: Comparison between resistance amplitude and corresponding density

Connection (Conn)	**Drilling location**	**Distance**, mm	**Drilling resistance**, %		**Feed resistance**, %		**Density**, kg/m^3	
			Mean	CoV	Mean	CoV	Mean	CoV
Conn 1	Stem 1	2-15	10.1	23.0	15.5	16.8	1078.5	4.0
	Interface middle	2-10	9.2	21.0	15.1	10.2	987.6	8.0
		10-20	8.5	28.0	12.3	35.0	1021.7	7.2
		20-28	12.4	22.4	10.2	59.6	1107.9	1.6
Conn 2	Stem1	2-22	11.4	19.4	22.6	21.1	880.5	8.8
	Stem 2	2-24	12.8	20.6	23.8	17.4	916.5	11.6
	Interface edge	2-15	11.9	19.4	23.1	20.3	920.5	14.6
		15-25	14.3	12.0	18.1	21.0	1118.3	5.7
		25-41	15.8	21.1	25.4	23.5	985.6	12.6
	Interface middle	2-23	12.5	17.6	23.4	27.2	943.1	8.9
		23-33	16.7	14.2	33.3	25.4	1057	10.9
		33-47	11.3	33.3	22.1	42.5	949.9	9.5
Conn 3	Stem1	2-23	11.8	22.6	21.6	28.3	965.3	14.2
	Stem 2	2-20	12.3	22.1	19.8	17.4	928.2	10.8
	Interface edge	2-16	12.6	15.2	29	12.2	963.5	11.2
		16-26	11.9	18.8	18.2	34.3	973.7	7.0
		26-28	11.8	22.6	9.2	38.2	999.9	3.3
	Interface middle	2-13	13.2	15.4	24.6	15.3	909.4	4.9
		13-23	12.8	22.1	17.4	35.7	982.3	9.1
		23-36	15.3	16.0	32.4	22.7	968.9	9.7
Conn 4	Interface middle	2-13	10.9	22.7	17.1	11.8	930.5	8.3
		13-23	13.2	15.6	21.2	17.9	969	8.9
		23-25	13.0	5.0	23.3	6.9	955.5	2.0
Conn 5	Interface middle	2-12	13.6	20.4	21.8	19.4	1081.9	6.8
		12-22	17.4	15.5	22.2	27.9	1070.3	9.7
		22-32	15.7	17.9	24.1	31.8	928.8	8.3
Conn 6	Interface middle	2-9	13.6	27.2	28.3	33.1	1058.9	9.8
		9-15	14.3	10.8	19.4	13.2	1074.1	11.8
		15-21	13.9	10.3	29.4	20.1	1007.5	5.8
Conn 7	Interface middle	2-8	8.6	17.8	16.9	12.1	936.8	10.1
		8-14	10.4	20.8	12.9	31.6	1146.0	3.0
		14-21	12.9	11.2	22	12.4	1091.7	8.2

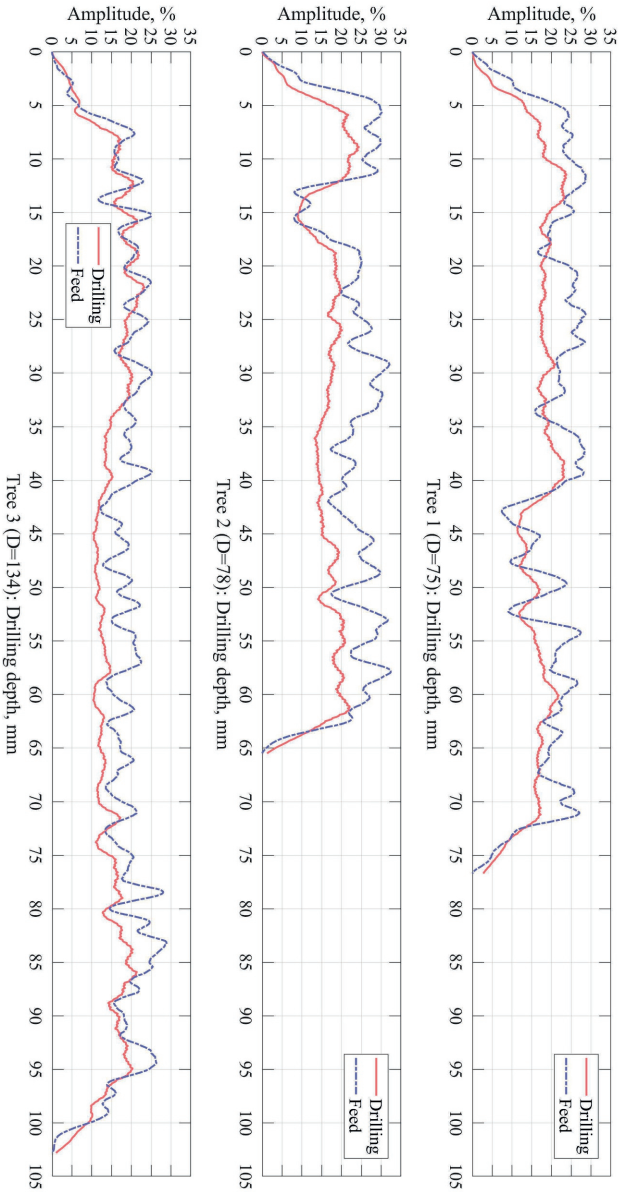

Figure 7.15: Resistance profiles of single *Tilia* trees. Top: tree 1 with a diameter at 1 m of 75 mm; middle: tree 7 with a diameter at 1 m of 78 mm; bottom: tree 9B with a diameter at 1 m of 134 mm.

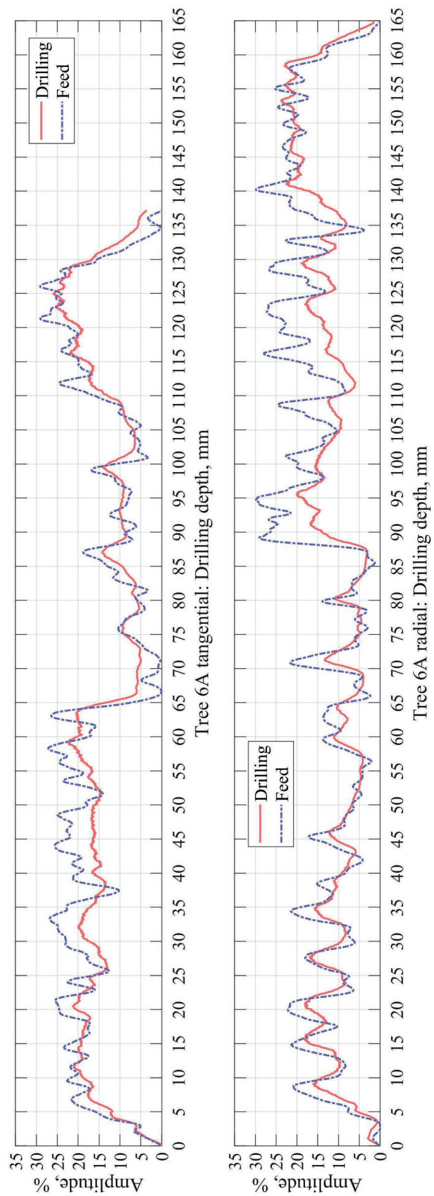

Figure 7.16: Resistance profiles of tree 6A at the height of 1 m in tangential direction (top) and radial direction (bottom). The drilling line corresponds to the drilling path of A100R and A100T in Figure 7.5.

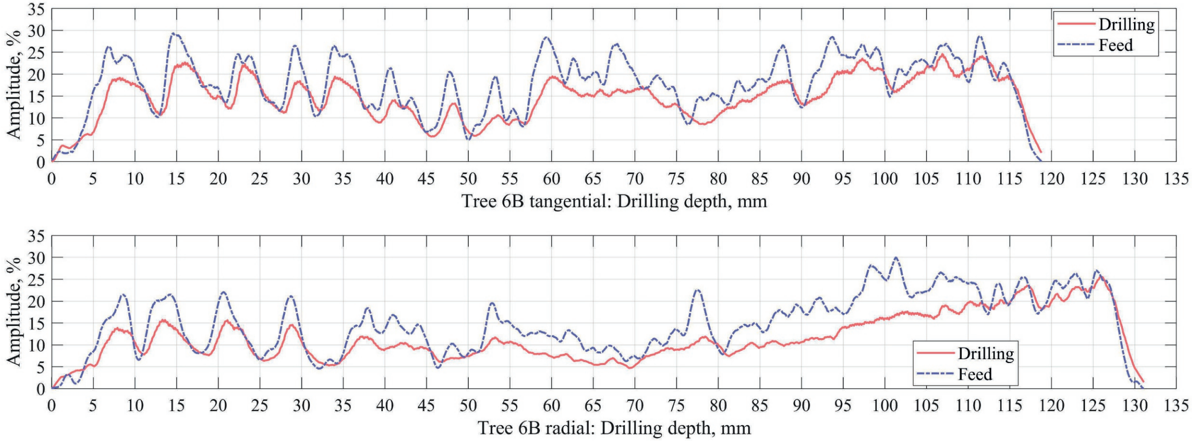

Figure 7.17: Resistance profiles of tree 6B at the height of 1 m in tangential direction (top) and radial direction (bottom). The drilling line corresponds to the drilling path of B100R and B100T in Figure 7.5.

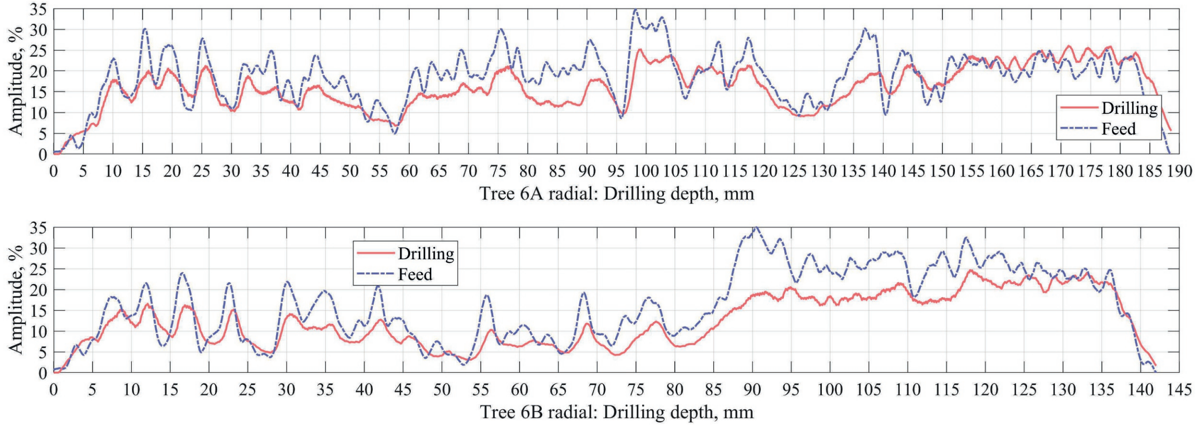

Figure 7.18: Resistance profiles of tree 6A (top) and 6B (bottom) at the height of 0.45 m in radial direction. The drilling line corresponds to the drilling path of A45R and B45R in Figure 7.5.

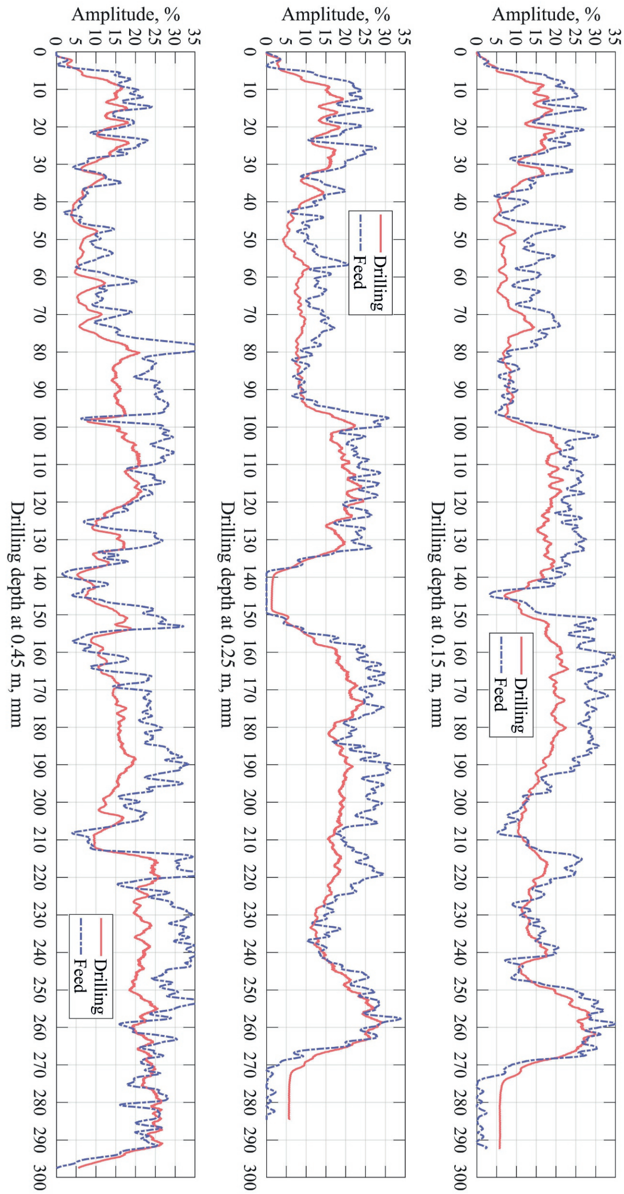

Figure 7.19: Drilling resistance in the parallel connection. Top: at a height of 0.15 m; middle: at a height of 0.25 m; bottom: at a height of 0.45 m.

discontinuity (i.e., included bark tissue). This drop-down effect is similar to the characteristic observed in the intersected region in the *Ficus* connection. At a height of 0.25 m, as can be seen in Figure 7.4, there is a gap between. This is reflected in the drilling profile as a region without resistance. In general, without an informative anatomical study, the information that can be inferred from the drilling is the location of the discontinuity inside the interface and the location of a large defect area.

7.4 Discussion

7.4.1 Relation between resistance and density

According to the results in Table 7.3, no statistical relationships are found between resistance and density. Reasons may arise from two aspects. One is the number of samples studied, which does not provide sufficient density variation to distinguish the correlation. Second, it is due to the resolution of the resistance measurement and its influencing factors. The variation in resistance values is twice that of the variation in density. The scattered resistance obtained can also be explained by other parameters, such as moisture content and fiber deviations. Thus, in this case, to obtain a clear statistical relationship between resistance and density, factors that influence fiber deviations and wear behavior must be controlled.

Although less quantitative findings can be applied to the internal inspection of the self-growing connection, the qualitative features of the results can be utilized. When the drill bit passes through the interconnected area, the resistance profile shows a decrease. This corresponds to the microscopic feature in this region where the tissues are not fused. This observation of drop-down can be utilized to locate the position of the internal discontinuity.

7.4.2 Limitations of resistance measurements

One of the concerns about the use of resistance drilling tools in trees is the accuracy of the measured resistance. The drilling process, from needle rotation to shaft progress and data logger, as elaborated in Section 7.1, is complex and influenced by many factors. In principle, resistance drilling in wood is a wood cutting process. When the needle moves in the drilling material while rotating, the torque moment involves tangential cutting force components acting on the main cutting edges and cutting forces acting on the side surfaces of the drilling part, while the feeding force involves a normal cutting force component acting on the main cutting edges in the direction of penetration of the drill bit [21]. Resistance recording is an indirect measure of power consumption, and the exact history of the force and torque applied to the testing material is not measured. Depending on the machine and needle type, there is a more or less disturbing source of systematic errors in the profiles, caused by friction to the needle shaft during drilling. Friction is an important parameter that affects the precision of the measurements [13, 20, 29]. There is little quantitative knowledge of how the friction of the drill bit will affect the sensitivity of the resistance profile in terms of the prediction of the wood properties. In this work, the influence of shaft friction was not corrected.

Parameters related to the drill needle have a significant influence on measured results. The feed and rotation rate of the drill bit in this work is established on the basis of experience. The extent to which rate choice influences the precision of the results is not clearly explained in the literature, as most of this approach is used for qualitative interpretation [4].

The topology and service life of the drill bit is another factor that influences the result. As stated in [27, 29, 30], cutting edge blunting affects the precision of wood density evaluation. The degree of blunting of the bit depends on the experimental conditions. Furthermore, in the operation of the drilling device, it also stated that the drilling measurement is still accurate up to a maximum of approximately 380 times. In this case, the service life of this drilling bit is influenced by the accuracy of the results obtained. Although the condition of the tests in this work is guaranteed to be accurate, the blunting of the wear and the influence on the measurement are not quantified.

The local properties of the wood in the position of the tip of the needle are the main factor that influences the resistance to mechanical penetration. These properties involve the density of the local material, the moisture content, the orientation, and organization of the tissues, as well as the local defects (e.g., decay). Consequently, as a result of variations in different properties, the shape of the resistance profile exhibits a rather complex pattern when passing through a highly heterogeneous material. The interface of a self-growing connection is a typical example with features of a varied density distribution, deviated fiber directions, and multiple tissue compositions. Thus, it is difficult to provide clear information about the shape of the resistance profile when the features are coupled.

7.5 Concluding remarks

This chapter attempts to investigate the utilization of the micro-drilling technique in inspection of the internal features of a self-growing connection. The main findings of this chapter can be listed as follows.

1. Regarding the self-growing connections fused by *Ficus benjamina*, within the samples studied, no significant statistical relationships are found between resistance and density. However, the qualitative features of the pattern in the resistance profile can be used to locate the tissues of the included bark.

2. When the drilling needle passes through the intersected region, a drop-down effect is identified. To be specific, the resistance profile in the range of the intersected region, the magnitudes of resistances first increase, then drop down, and then follow an increase again shaping into a valley. The valley region in the resistance profile corresponds to the location of the bark included in the microscopic investigations.

3. Regarding the living self-growing connection fused by *Tilia cordata*, without information from anatomical studies, the location of internal discontinuities can be inferred from the resistance profile. Further conclusions need to be validated on the basis of the study of the anatomical structures.

Although the accuracy of the information from resistance drilling is limited, the approach of micro-doing can still be used as a way to get some information about the internal features of a connection. However, to obtain a good interpretation, experience with the drilling plan and knowledge of the properties of the local material are required.

References

[1] C. Mattheck, K. Bethge, and W. Albrecht. How to read the results of resistograph M? *The International Journal of Urban Forestry*, 21:331–346, 1997.

[2] F. Rinn, F. H. Schweingruber, and E. Schär. Resistograph and X-ray density charts of wood comparative evaluation of drill resistance profiles and X-ray density charts of different wood species. *Holzforschung*, 50:303–311, 1996.

[3] X. Wang, B. K. Brashaw, R. J. Ross, and L. Wang. Rapid assessment of wood density of standing trees with nondestructive methods - a review. In *International Conference on Biobase Material Science and Engineering*, pages 262–267, 2012.

[4] F. Rinn. Basics of micro-resistance drilling for timber inspection. *Holztechnologie*, 53 (3):24–29, 2012.

[5] S. Imposa, G. Mele, M. Corrao, G. Coco, and G. Battaglia. Characterization of decay in the wooden roof of the S. Agata church of Ragusa Ibla (Southeastern Sicily) by means of sonic tomography and resistograph penetration tests. *International Journal of Architectural Herigtage*, 8:213–223, 2013.

[6] T. P. Nowak, J. Jasieńko, and K. Hamrol-Bielecka. In situ assessment of structural timber using the resistance drilling method – evaluation of usefulness. *Construction and Building Materials*, 102:403–415, 2016.

[7] W. F. Gard and J. W. G Van de Kuilen. Micro-drilling resistance measurements of dense hardwoods for hydraulic structures. In *WCTE-World Conference on Timber Engineering*, 2018.

[8] G. Ravenshorst, W. Gard, J. W. G Van De Kuilen, O. Beketova-Hummel, and G. Pagella. An integral approach for the assessment of timber pile foundations. In *WCTE-World Conference on Timber Engineering*, 2021.

[9] S. Y. Wang, C. M. Chiu, and C. J. Lin. Application of the drilling resistance method for annual ring characteristics: Evaluation of Taiwania (*Taiwania cryptomerioides*) trees grown with different thinning and pruning treatments. *Journal of Wood Science*, 49:116–124, 2003.

[10] F. Isik and B. Li. Rapid assessment of wood density of live trees using the Resistograph for selection in tree improvement programs. *Canadian Journal of Forest Research*, 33: 2426–2435, 2011.

[11] G. Szewczyk, R. Wąsik, K. Leszczyński, and R. Podlaski. Age estimation of different tree species using a special kind of an electrically recording resistance drill. *Urban Forestry and Urban Greening*, 34:249–253, 2018.

[12] X. Wang and R. B. Allison. Decay detection in red oak trees using a combination of visual inspection, acoustic testing, and resistance microdrilling. *Arboriculture and Urban Forestry*, 34:1–4, 2008.

[13] T. Biechele. Drilling resistance measurement and the effect of shaft friction-using feed force information for improving decay identification on hard tropical wood silviculture of Teak (*Tectona grandis*). In *19th International Nondestructive Testing and Evaluation of Wood Symposium*, 2015.

[14] C. L. Goh, R. A. Rahim, M. H. F. Rahiman, M. T. M. Talib, and Z. C. Tee. Sensing wood decay in standing trees: A review. *Sensors and Actuators A: Physical*, 269:276–282, 2018.

[15] E. Sharapov, C. Brischke, H. Militz, and E. Smirnova. Effects of white rot and brown rot decay on the drilling resistance measurements in wood. *Holzforschung*, 72:905–913, 2018.

[16] S. Gao, X. Wang, M. C. Wiemann, B. K. Brashaw, R. J. Ross, and L. Wang. A critical analysis of methods for rapid and nondestructive determination of wood density in standing trees. *Annals of Forest Science*, 74:1–13, 2017.

[17] J. Oliveira, X. Wang, and G. B. Vidaurre. Assessing specific gravity of young Eucalyptus plantation trees using a resistance drilling technique. *Holzforschung*, 71:137–145, 2017.

[18] D. F. Llana, G. Íñiguez González, J. Montón, and F. Arriaga. In-situ density estimation by four nondestructive techniques on Norway spruce from built-in wood structures. *Holzforschung*, 72:871–879, 2018.

[19] E. Sharapov, C. Brischke, H. Militz, and E. Smirnova. Prediction of modulus of elasticity in static bending and density of wood at different moisture contents and feed rates by drilling resistance measurements. *European Journal of Wood and Wood Products*, 77: 833–842, 2019.

[20] V. Gendvilas, G. M. Downes, M. Neyland, M. Hunt, A. Jacobs, and J. O'Reilly-Wapstra. Friction correction when predicting wood basic density using drilling resistance. *Holzforschung*, 75:508–516, 2021.

[21] E. Sharapov, C. Brischke, H. Militz, and E. Smirnova. Combined effect of wood moisture content, drill bit rotational speed and feed rate on drilling resistance measurements in Norway spruce (*Picea abies* (L.) Karst.). *Wood Material Science and Engineering*, 15: 198–204, 2018.

[22] C. Ceraldi, V. Mormone, and E. R. Ermolli. Resistographic inspection of ancient timber structures for the evaluation of mechanical characteristics. *Materials and structures*, 34:59–64, 2001.

[23] A. O. Feio, L. Paulo, and J. S. Machado. Parellel to the grain behavior and ndt correlations for chestnut wood (*Castanea sativa* Mill). In *CEC-EST*, pages 294–303, 2005.

[24] L. Acuña, L. A. Basterra, M. Casado, G. López, G. Ramón-Cueto, E. Relea, C. Martínez, and A. González. Application of resistograph to obtain the density and to differentiate wood species. *Materiales de Construcción*, 61(303):451–464, 2011.

[25] M. Kloiber, M. Drdácký, J. Tippner, and J. Hrivnák. Conventional compressive strength parallel to the grain and mechanical resistance of wood against pin penetration and microdrilling established by in-situ semidestructive devices. *Materials and Structures/-Materiaux et Constructions*, 48:3217–3229, 2015.

[26] D. M. Johnstone, P. L. Ades, G. M. Moore, and I. W. Smith. Predicting wood decay in eucalypts using an expert system and the IML-Resistograph drill. *Arboriculture and Urban Forestry*, 33(2):76, 2007.

[27] E. Sharapov, X. Wang, E. Smirnova, and J. P. Wacker. Wear behavior of drill bits in wood drilling resistance measurements. *Wood and Fiber Science*, 50:1–13, 2018.

[28] H. Zhao and K. F. Ehmann. Topology of spade drills for wood drilling operations, Part 1: Spade drill point geometry definition. *Journal of Manufacturing Science and Engineering*, 127:298–309, 2005.

[29] E. Sharapov, X. Wang, and E. Smirnova. Drill bit friction and its effect on resistance drilling measurements in logs. In *Proceedings of the 20th International Nondestructive Testing and Evaluation of Wood Symposium*, pages 12–15, 2017.

[30] H. Zhao and K. F. Ehmann. Mechanistic model for spade drills for wood drilling operations, Part 2: Analysis of spade bit geometry and performance. *Journal of Manufacturing Science and Engineering*, 125:236–244, 2003.

8

Conclusion and outlook

8.1 Demonstration example

Integration of greenery into buildings has opened possibilities for the implementation of vertical forests, but concerns about technological uncertainties have limited their widespread application. To address this, an approach to reduce the risks associated with vertical tree growth is the use of artificial stabilization methods. However, in this dissertation, a more natural and innovative approach is proposed, involving the use of self-growing connections as a means to stabilize trees. An example is presented in Figure 8.1, where two single trees are joined by a self-growing connection. In this way, the trees can support and stabilize each other. These interconnected trees can act as a basic structural element and can be extended into a structural pattern depending on the local environments. This structure can also be integrated with buildings in various forms in spatial distribution.

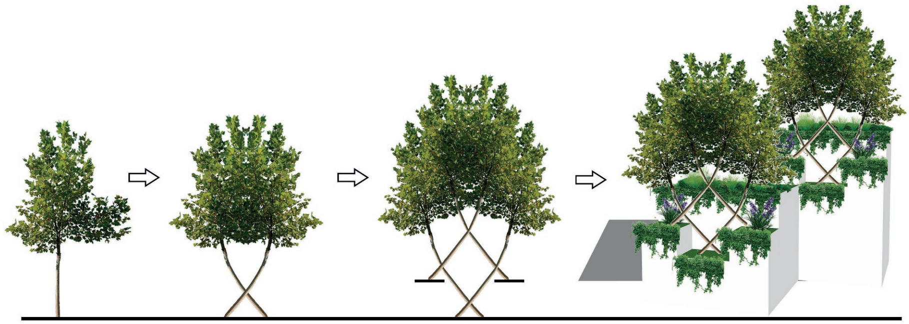

Figure 8.1: Illustration and development of urban integrated living tree structures, from a single standing tree to vertical living structures.

8.2 Conclusions

In this doctoral dissertation, the main research question is:

‘*What are the biomechanical properties of self-growing connections and interconnected tree systems?*’

Research aims to analyze the connection and tree system from three perspectives: studies of self-growing connections, examinations of interconnected tree systems, and the development of the growth monitoring technique. According to each perspective, this dissertation attempts to analyze the biological and mechanical properties of self-growing connections and interconnected tree systems. Each aspect is described below.

- On the connection level, a microscopic and macroscopic characterization of self-growing connections is established.
- On the connection level, the mechanical performance (tensile out-of-plane behavior) and the effects of fusion are measured and studied.

- On the interconnected system level, the mechanical behavior under different scenarios (in the connected plane and out-of-the-plane cases) and growth effects are examined.
- Regarding the technique for inspecting growth features of self-growing connections, the method of micro-drilling resistance is evaluated.

For each of these aspects, the detailed conclusions of this work are described in Sections 8.2.1, 8.2.2, 8.2.3, and 8.2.5.

To answer the main research question in short, the relations between various levels under the main research question can be summarized in Figure 8.2. The design of the self-growing structure is based on the basic element of individual trees connected by self-growing connections to form a system of parallel or cross interconnected trees. The growth of the self-growing structure can be monitored by the micro-drilling technique with minimal damage.

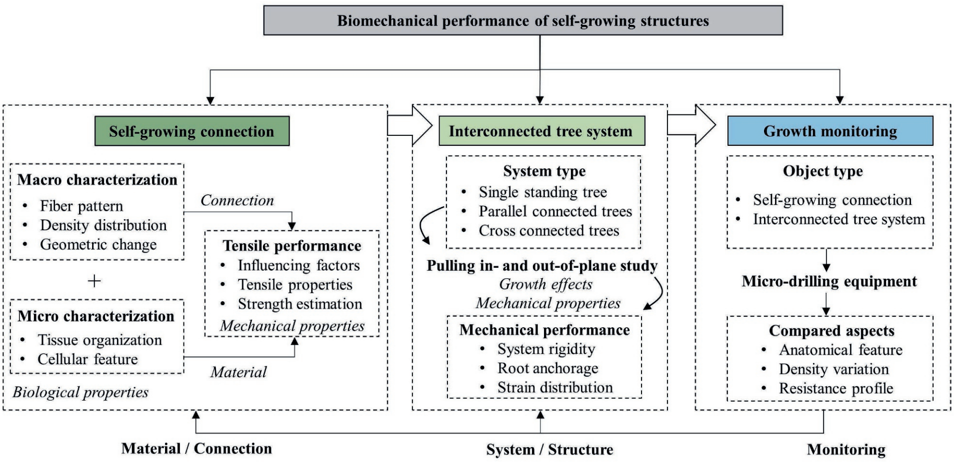

Figure 8.2: Relations between studied aspects to the research question.

Characterization of a self-growing connection at both macro- and micro-scales identifies the fundamental biological or growth features of the self-growing connection. Among these features, the characteristics of the merged fibers (their volume, distribution, and structure) determine the level of fusion of a self-growing connection. The mechanical properties of a connection can be further predicted by these growth features. In particular, the tensile strength can be better predicted by the diameter and interface curvature of a connection. These findings can provide guidance for the structural design of self-growing connections.

Knowledge at the connection level further contributes to the design of the interconnected tree system. This system can have various design forms (i.e., variations in cross-angles and locations of self-growing connections). Each form has different mechanical characteristics and is influenced by growth over time (e.g., increased geometry). The cross self-growing connection offers improved in-plane bracing support, while the parallel self-growing connection ensures a stronger root anchorage to the interconnected trees. Studies at this level can provide information to guide the application of the interconnected tree system according to its use purposes.

After the self-growing structure can be applied to real-life scenarios, micro-drilling at the middle location of the self-growing connection can offer information of the fusion condition. When the drilling needle passes the internal bark area within a self-growing connection, the drop-down effect is obvious to notice on the resistance profile from micro-drilling equipment. In this way, long-term monitoring of growth or deterioration can be achieved with minimal damage to the structure.

8.2.1 Characterization of *Ficus* self-growing connections

The ability of trees to fuse and form connections in response to mechanical stimuli is a natural phenomenon. The characterization is performed at different scales, from the cellular scale, to the measurement on the cross sections, and to the quantification of the entire connection.

A connection can be divided into the stem region and the interfacial region. The interfacial region is outlined by a spatial curve merged by the bark of two stems, shaped like a ‘saddle’. From a macroscopic perspective (in Chapter 3), the density, geometry, and structure of the connections are examined. The main findings on this scale are listed below.

- Density distribution. Within the same cross-section of a self-growing connection, in comparison with the stem region, the intersected area exhibits a higher density.
- Geometric variation. Along the same cutting view direction of a self-growing connection, in the intersected region, the measured area is larger than in the stem region. This indicates that the fused area has more material allocated.
- Fiber pattern. The fiber structures of a self-growing connection are characterized by three main fiber bundles: merged fibers, deviated fibers, and original fibers. The merged fiber bundles are produced by both stems, which connect the stems together. They play the most important role in structural integrity and loading capacity. Merging fibers are mainly found in the large cross-angle, whereas the deviated fibers flow around the small cross-angle at the interface.

Furthermore, the microscopic features (in Chapter 4) of the self-growing connections are further analyzed to support the observations identified on the macroscopic scale. The tissue organization in the stem region and the fused region of the connections are compared and characterized. These features can be described in the following aspects.

- Merged fiber tissues. The interface at the periphery of the fused region consists primarily of bark tissues, whereas bundles of merged fibers with deviated directions are found in the outer layer of the connection. On the contrary, the inner part of the connection contains fewer continuous merged fibers, mainly organized by parenchyma cells.

- Internal defects. In the internal region of the connected area, most of the tissues identified are barks and soft tissues. These defects are sensitive to changes in moisture and easy to crack.
- Reaction wood. The microscopic analysis reveals the presence of crystals and tension wood with G-layers in the fused region.

These characteristics can be illustrated by a unified description, which is fusion quality. Better fusion is characterized by fewer internal defects and more portions of continuous merged fibers. A practical approach to measuring and estimating the fusion quality is to compare the fusion depth between two stems measured at the middle location of the fused region. This inference is based on the interpretation of the correlation between the distribution of the merged fibers and the geometric information.

8.2.2 Biomechanical properties of *Ficus* self-growing connections

After establishing the characterization of self-growing connections, the following parameters are identified for the analysis, namely density, moisture content, cone ratio, cross-angle, average diameter, diameter ratio, fusion degree, interface curvature and interfacial area. Tensile testing perpendicular to the interface is conducted to investigate mechanical properties, including stiffness, strength, and load-carrying capacity, which are related to the described parameters of the connections. In addition, an artificial neural network prediction model is used to assess the tensile strength of the connections. The key conclusions derived from this research are as follows.

- The fusion condition of self-growing connections can be estimated in a non-destructive manner using the proposed parameters: fusion degree and interface curvature.
- The use of four-point loading is recommended as a customized setup, allowing for effective measurement of mechanical characteristics (tensile out-of-plane behavior) for connections of varying sizes.
- The force-deformation curves of the tensile tests show a gradual cracking region as of 80% of the maximum load. The propagation of cracks is mainly affected by the shape of the interface and the portion of the merged fibers. When the fusion degree is less than 15%, the failure occurs at the interface of a connection, but when the fusion degree is greater than 15%, the failure plane crosses the stems to form a ‘Y’ shape. This failure process is mainly controlled by the combination of rolling shear and the tensile perpendicular strength of the wood material.
- Tensile strength shows a moderate correlation with both diameter and interface curvature.

8.2.3 Biomechanical performance of *Tilia* interconnected tree systems

After examining biomechanical properties on the scale of a connection, this research focuses further on the investigation of the biomechanical characteristics of interconnected tree systems, including cross interconnected trees, parallel interconnected trees, and single standing trees. The study also examines the effects of biomass growth on the mechanical behavior of the system, specifically the loading capacity, the deformation of the stems and roots, and the rigidity of the system. Pulling tests are conducted under various loading scenarios, categorized as in-plane and out-of-plane loading with respect to the connected tree plane. Finite element models are employed to complement the experimental measurements and provide additional insights into the reactions of the system. During a two-year growth period, the influence of growth on mechanical properties is analyzed and compared. The key findings and conclusions of this study are as follows.

- In most of the cases studied, the growth of trees induces a reduction in deformation, rotation, and local elongations; additionally, the stiffness of the entire system increases.
- Regarding the cross-interconnected trees, they show a significant bracing effect in the plane, which is reflected by fewer deformations and less stress responses compared to out-of-plane loading. However, the loading capacity of the system depends on the supporting trees.
- For parallel connected trees, the connected lower region increases the basal stiffness but presents a certain asymmetric behavior.

8.2.4 Micro-drilling monitoring technique

The following section of the research explores the utilization of the micro-drilling technique for inspecting the internal features of self-growing connections. The approach is initially applied to a self-growing connection fused by *Ficus benjamina* (weeping fig), where resistance magnitude and profile pattern are interpreted based on anatomical features (fiber structures and locations of defects) and density variations. Subsequently, the technique is applied to a living self-growing connection fused by *Tilia cordata* (small-leaved lime) to infer internal features. The conclusions are listed below.

- For self-growing connections fused by *Ficus benjamina*, no significant statistical relationships between resistance and density are observed due to the limited data intervals for density. However, qualitative analysis of resistance profile patterns can help identify internal discontinuities (i.e., bark tissues).
- In the intersected region of the self-growing connection, a drop-down effect is identified in the resistance profile when the drilling needle passes the fused interface. This effect corresponds to the findings in microscopic investigations on the location of the included bark.
- In the case of the self-growing connection fused by *Tilia cordata*, the resistance profile can provide information about the structure features, i.e., location of internal bark tissues and growth rings. However, further conclusions require validation through anatomical studies.
- Although the accuracy of the information obtained by resistance drilling is limited, micro-drilling can still serve as a valuable tool for gaining insights into the internal

features of a connection. Successful interpretation of results is based on experience in drilling location and knowledge of the properties of the local material.

8.2.5 Main outcomes for practice

This doctoral dissertation has advanced our understanding of the biomechanical performance of self-growing connections and interconnected tree systems. The findings have implications for the design, evaluation, and application of these innovative structures in other relevant fields. The starting point of this study is in the field of vertical greening, providing a nature-based solution to stabilize trees and form natural tree structures. However, the application of self-growing connections and cross-tree systems can be extended to other fields. For example, the following aspects can illustrate the applied value of this research.

- **Windbreak trees**. In agriculture, tree grafting technology to form a stable connected structure can be used to build agricultural windbreaks to improve the stability of the forest belt, slow the speed of the wind, and reduce the impact of wind damage on farmland.
- **Protective structures of the embankment**. In civil engineering, this technique can be used to build structures with protective functions, increase the stability of vegetation, and improve soil retention. It can utilize the environmental and structural functions of connected living trees.
- **Landscape engineering**. In landscape engineering, the use of tree grafting to form a unique connected structure can create a more artistic and natural landscape design, attracting more people's attention. Meanwhile, it also increases people's concern for nature, thus promoting harmony between man and nature.
- **Bioinspired design or biomimicry**. The optimization of the self-growing connection in nature can provide inspiration for research on structures, such as composite structures. Engineers can learn from the natural growth patterns of self-growing connections to construct more stable and efficient structures.
- **Development in bioeconomy**. The living tree structure utilizes trees, providing a pathway for sustainable resource utilization in the bioeconomy. By using natural trees and biological materials, dependence on finite resources can be reduced, promoting environmental protection and economic development.

8

8.3 Recommendations for future research

This research is a multidisciplinary topic that covers a wide range of relevant fields, from landscape design to plant science. From the current research findings, the topics to which this research can be extended are listed below.

1. **The biological mechanism of the fusion process of self-growing connections.**

In this work, Chapter 3 only reviews the mechanism of the fusion process of a self-growing connection in terms of adaptive growth. Research can be further carried out on the studies of physiological and biochemical changes in this process. The reasons why fusion is activated and how fusion is controlled and developed can be explored by understanding the role of signaling molecules, hormones, and genetic factors in tree species.

Advanced imaging techniques such as microscopy and tomography can be employed to visualize and analyze the fusion process. Understanding the underlying mechanisms can provide information for the quantification of shape change over the course of time. On the basis of this information, the structural properties of a self-growing connection can be better managed and predicted.

2. The possibility, technique, and mechanism of fused self-growing connections with other tree species.

In this work, two tree species, *Ficus benjamina* (weeping fig) and *Tilia cordata* (small-leaved lime), are examined. However, to utilize the concept in a broader picture, compatibility investigation between different tree species for fusion should be performed for wider application. The technique for fusion of a connection in this work is by compressing and tying two stems together under natural conditions. Having a better controlled and effective technique to create a self-growing connection is worthy of investigation. Factors that influence the quality of the fusion can be examined, such as age, physiological condition, and genetic relationship. To improve the quality of fusion, the exploration of techniques, such as grafting methods and hormonal treatments, can be evaluated. With different fusion techniques, the connections' mechanical properties (e.g., interfacial strength), growth features (e.g., fiber structures) and durability can be further investigated.

3. Mechanical performance of self-growing connections under shear loading.

In this research, out-of-plane tensile tests are performed on self-growing connections in Chapter 5. The interfacial region shows a complex stress distribution. The failure strength of the interface is a combination of the limits of the tensile perpendicular (stress $\sigma_{t,90}$, strength $f_{t,90}$) and shear strength (stress σ_v, strength f_v). Failure criteria can be expressed as below.

$$\left(\frac{\sigma_{t,90}}{f_{t,90}}\right)^2 + \left(\frac{\sigma_v}{f_v}\right)^2 \leq 1 \tag{8.1}$$

However, it is not clear which stress component plays the governing role, as well as the crack propagation mechanism. In this case, as supporting evidence, it is valuable to examine the behavior of self-growing connections when subjected to shear loading along the interface.

Under this research direction, the objectives include investigating the stress and strain distribution around the connection interface, analyzing the influence of material composition, fiber orientation, and geometric characteristics on the failure of self-growing connections. Experimental setups must be customized according to the irregular shape of a connection. Numerical models are urged to develop as a tool to improve the understanding of the failure mechanism.

4. Stability assessment of single trees and interconnected trees growing vertically.

This dissertation has explored the failure mechanism of single and interconnected trees by performing pulling tests in Chapter 6. Factors that influence the stability of a tree are identified, including tree size, wood strength and stiffness, as well as root anchorage. The load capacity until failure is estimated on the basis of the extrapolated results from pulling tests. With this understanding, when trees are planted in the vertical space with limited soil volume as in a vertical forest, how a single tree or an interconnected tree performs can be assessed. Subsequently, the risk of a tree losing stability can be studied.

5. Optimization of structure patterns with self-growing connections.

In this investigation, a connected tree system with only one connection is studied. For future investigations, it can aim to investigate different design patterns, such as braided or interwoven structures with multiple connections, and to evaluate their mechanical performance in terms of load-bearing capacity and rigidity. Additionally, this research topic can also explore the integration of other artificial materials or reinforcements within self-growing connections to further enhance their mechanical properties. Computational modeling and optimization algorithms will be used to identify the most efficient and effective design patterns for self-growing connections. Ultimately, optimizing the design pattern of structures with self-growing connections will contribute to the development of more resilient, adaptive, and efficient architectural and engineering solutions.

6. Dynamic performance of self-growing connections and interconnected systems.

This dissertation is limited to studying the static loading behavior of connections and systems. However, in reality, a tree is constantly experiencing dynamic wind loads. It is important to have a deeper understanding of mechanical behavior and performance in dynamic environments, such as wind loads or vibrations, for example, caused by animals.

To predict the dynamic response and stability of self-growing connections and interconnected systems, researchers can develop mathematical models that capture the complex dynamics of these systems. These models will incorporate factors such as material properties, geometrical characteristics, and growth patterns to accurately simulate the behavior of self-growing connections under dynamic loading. Validation of these models through experimental tests will enhance their reliability and applicability.

Another interesting aspect of exploration is the potential of self-growing connections to adapt to changing dynamic loads and self-repair in response to damage. Investigating the growth patterns and mechanisms that enable self-healing will lead to the development of innovative design approaches that incorporate self-healing capabilities into self-growing connections and interconnected systems.

7. Growth simulation and mechanical prediction of living tree structures.

Future research on self-growing connections could focus on model development for their biological growth and prediction of mechanical properties. It could focus on developing computational tools, integrating growth simulations with mechanical models, validating simulation results with experimental data, and optimizing simulation parameters. These tools will consider factors such as cell division, elongation, and differentiation to model the complex biological processes that drive tree growth. By combining growth simulations with mechanical models, researchers can predict how growth processes influence the structural behavior of living tree structures. This integration will enable the prediction of important mechanical properties, such as stiffness, strength, and deformation characteristics. Exploring advanced simulation techniques such as computational fluid dynamics is another direction for future research.

8. Nature-inspired design based on self-growing connections.

This research topic concerns studying the principles and mechanisms of design found in self-growing connections and using them to optimize artificial structures. The aim is to explore how these concepts can be applied to architectural and engineering designs to improve sustainable design.

Some of the natural growth characteristics identified in this work are induced by natural self-adaptation and optimization. These growth principles can be migrated and applied to engineering structures. For example, the fiber structure of self-growing connections can be used to design the fiber distribution of a composite structure for maximum efficiency in load transfer.

9. Risk management and robust design optimization for living tree structures.

This aspect involves assessing the potential risks and hazards associated with the construction of living structures and implementing strategies to mitigate them. The establishment of a living tree structure is a lifelong process that includes the initial formation of connections, the gradual maturation of connections, and the eventual decay of materials. Throughout its service life, the changing reliability due to potential risks and uncertainties is worth investigating and monitoring.

This includes identifying growth-related issues, uncertain environmental conditions, fire risks, and other external threats. Robust design optimization techniques help to account for uncertainties in growth patterns, environmental conditions, and other factors, ensuring the stability and performance of living tree structures in various scenarios. Additionally, guidelines and standards are developed for the construction and maintenance of living tree structures to ensure their long-term safety and functionality. By implementing these measures, the risks associated with living tree structures can be effectively managed, and their sustainable integration into the built environment can be achieved.

This research is expected to motivate further studies and contribute to the formation of natural, sustainable and resilient solutions in engineering, urban planning, and ecological design.

A

Chapter 3: Macroscopic Characterization

This section is supplementary material to Chapter 3, Sections 3.3.1 and 3.3.2.

A

A.1 Density variations

Density variations in the braided tree structures (Tree_B and Tree_S) are presented. Figure A.1 gives the density variations in Tree B. The reconstructed tree structure is presented in Figure A.1 a, where two cross sections are selected, namely Tr_B_lc1 and Tr_B_lc2. The gray value is further calibrated in Figure A.1 b; and based on the threshold set, the selected cross sections are presented in Figures A.1 c and d.

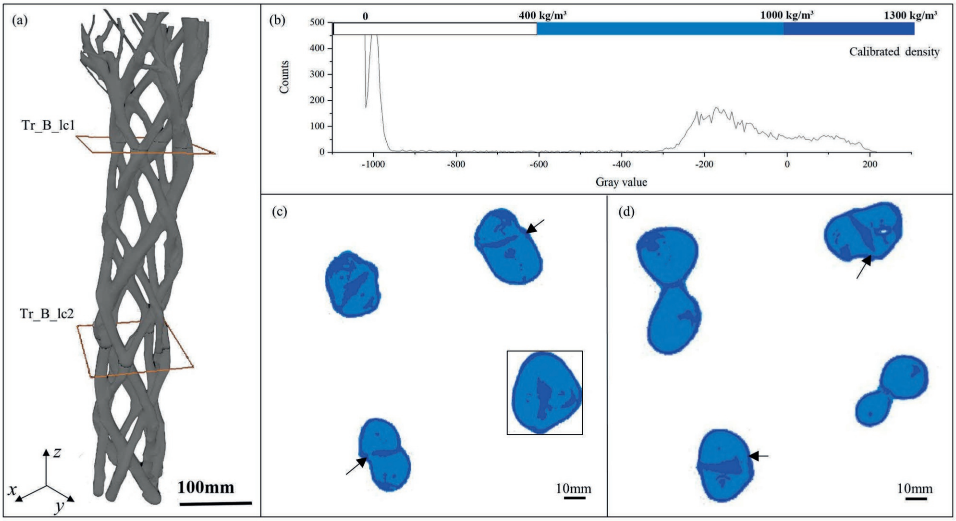

Figure A.1: Reconstructed Tree_B density distribution within two locations (Tr_B_lc1 and Tr_B_lc2). (a) Inspected locations in the scanned tree; (b) histogram of gray value distributions within local rectangular area in (c); (c) density map at top viewing location (Tr_B_lc1) in (a); (d) density map at bottom viewing location (Tr_B_lc2) in (a).

Figure A.2 gives the density variations in Tree_S. The reconstructed tree structure is presented in Figure A.2 a, where two cross sections are selected, namely Tr_S_lc1 and Tr_S_lc2. The gray value is further calibrated in Figure A.2 b; and based on the threshold set, the selected cross sections are presented in Figures A.2 c and d. The interpretation in Figures A.1 and A.2 can be referred to the description in Section 3.3.1.

Figure A.1 c and Figure A.2 c are further taken to perform the analysis based on the line probe. The results are presented in Figures A.3 and A.4, respectively.

A

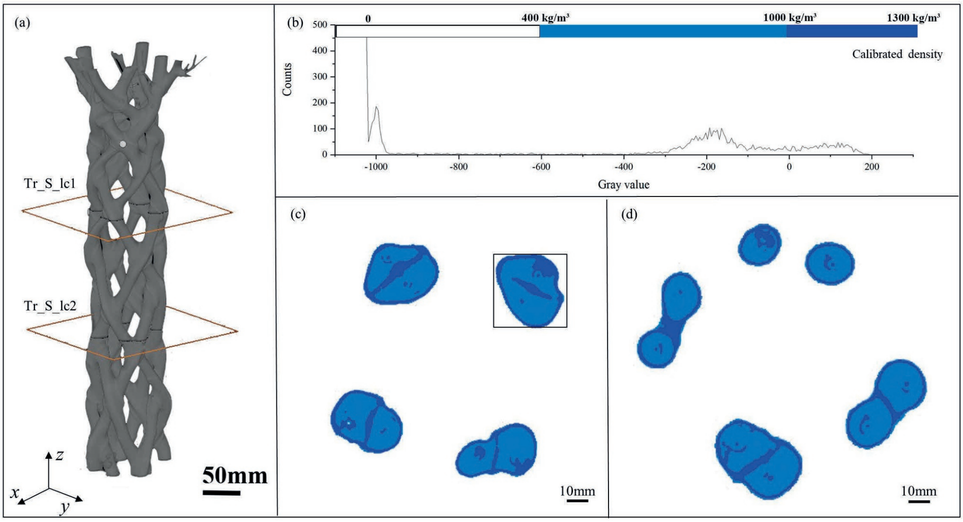

Figure A.2: Reconstructed Tree_S density distribution within two locations (Tr_S_lc1 and Tr_S_lc2). (a) Inspected locations in the scanned tree; (b) histogram of gray value distributions within local rectangular area in (c); (c) density map at top viewing location (Tr_S_lc1) in (a); (d) density map at bottom viewing location (Tr_S_lc2) in (a).

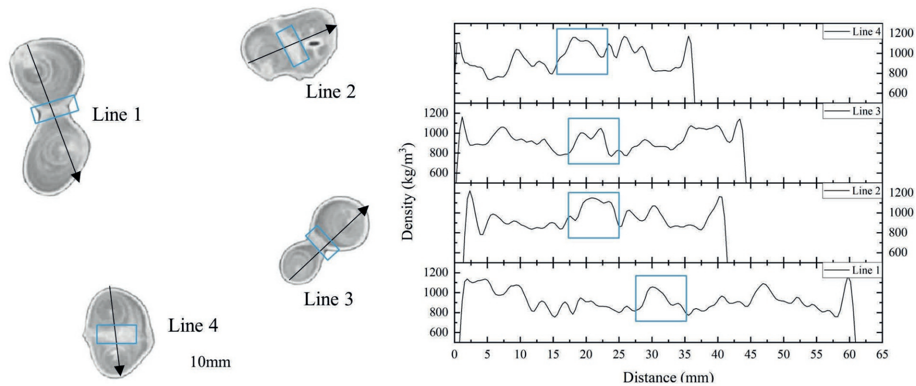

Figure A.3: Density line profiles within cross-section in figure A.1 d. (a) Locations of probe lines in the selected cross-section; (b) density variations along the probe lines.

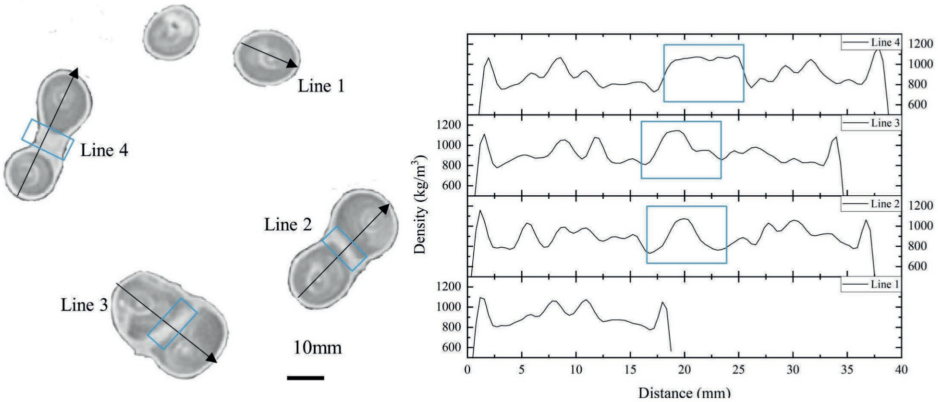

Figure A.4: Density line profiles within cross-section in figure A.2 d. (a) Locations of probe lines in the selected cross-section; (b) density variations along the probe lines.

A.2 Geometric changes

This section is supplementary material to Section 3.3.2. Figures A.5 and A.6 present the results of Tree_B and Tree_S. It shows the diameter variations along the stem in the braided tree structure.

To better understand the geometric changes within a self-growing connection, Figures A.7, A.8, A.9, A.10, and A.11 give the measured results from other stems in Tree B and Tree S, respectively.

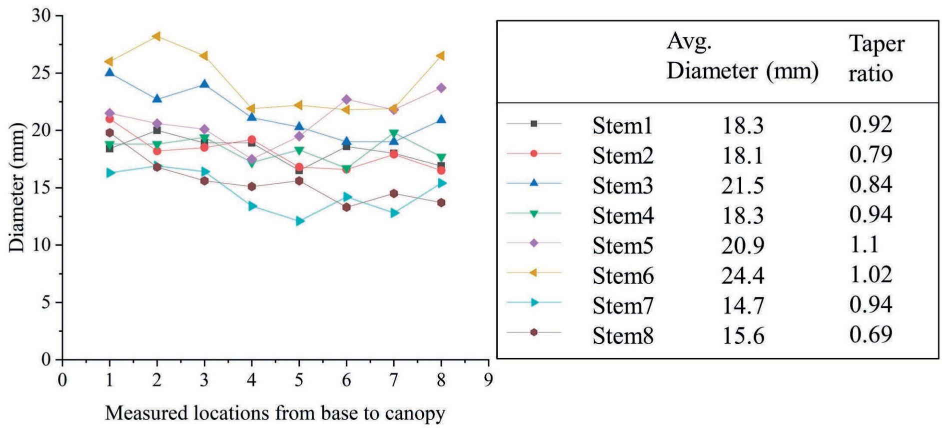

Figure A.5: Diameters and taper ratios of Tree_B. Left: Diameter variations at 1 to 7 intervals from roots to canopy; right: average stem sizes and calculated taper ratio.

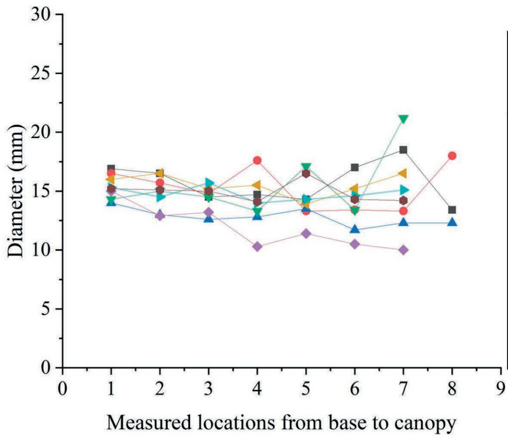

	Avg. Diameter (mm)	Taper ratio
Stem1	15.7	0.79
Stem2	15.3	1.09
Stem3	12.8	0.88
Stem4	15.5	1.48
Stem5	11.9	0.67
Stem6	15.5	1.03
Stem7	14.8	0.99
Stem8	14.9	0.93

Figure A.6: Diameters and taper ratios of Tree_S. Left: Diameter variations at 1 to 7 intervals from roots to canopy; right: average stem sizes and calculated taper ratio.

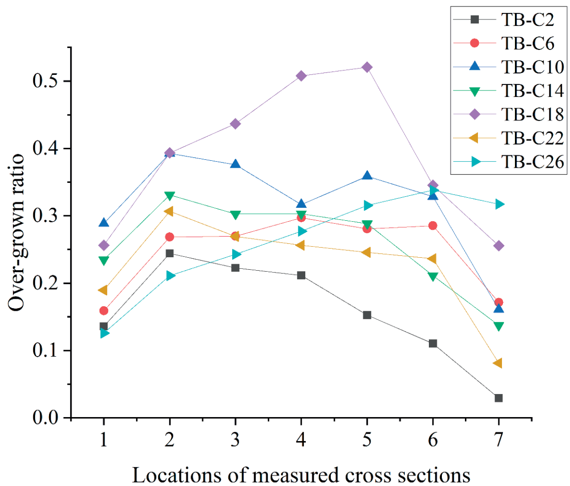

Figure A.7: Along stem2 of Tree_B, area variations in fused and stem region, measured locations following Figure 3.6, where the naming rules of 'TB_C' stands for connections from Tree_B.

A

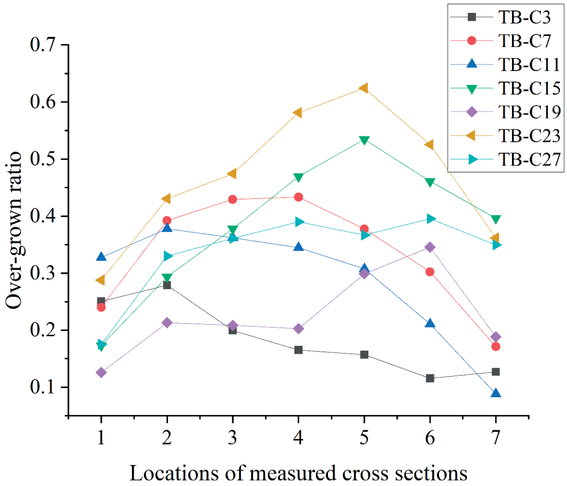

Figure A.8: Along stem3 of Tree_B, area variations in fused and stem region, measured locations following Figure 3.6, where the naming rules of 'TB_C' stands for connections from Tree_B.

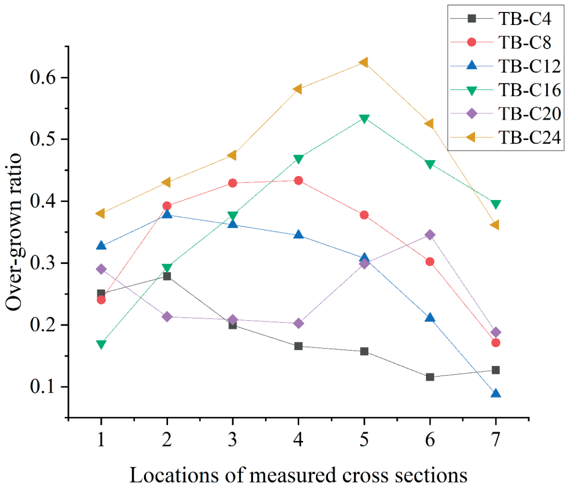

Figure A.9: Along stem4 of Tree_B, area variations in fused and stem region, measured locations following Figure 3.6, where the naming rules of 'TB_C' stands for connections from Tree_B.

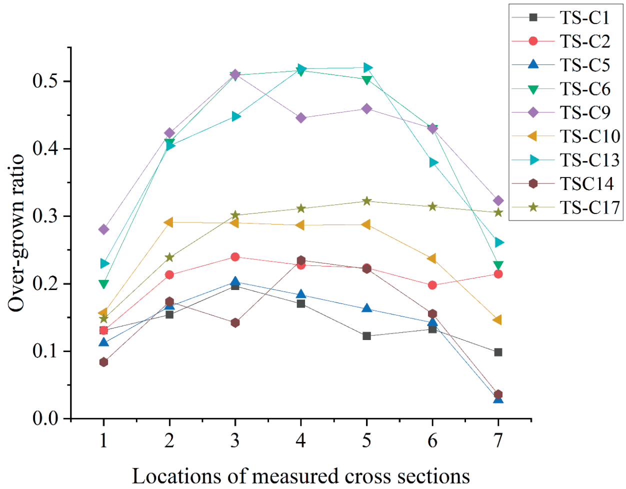

Figure A.10: Along stem1 and stem2 of Tree_S, area variations in fused and stem region, measured locations following Figure 3.6, where the naming rules of 'TS_C' stands for connections from Tree_S.

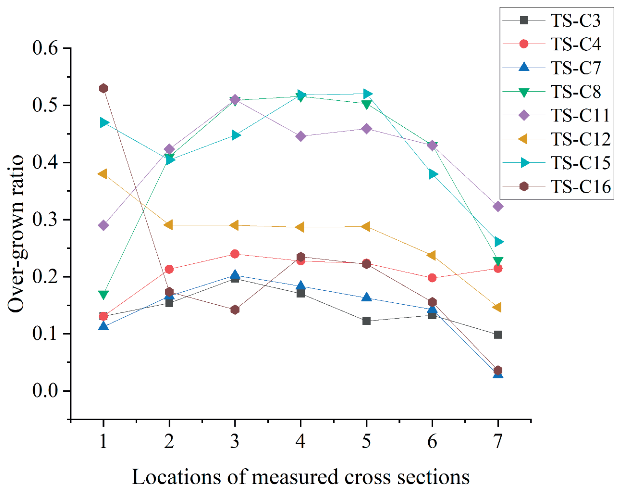

Figure A.11: Along stem3 and stem4 of Tree_S, area variations in fused and stem region, measured locations following Figure 3.6, where the naming rules of 'TS_C' stands for connections from Tree_S.

B

Chapter 4: Microscopic Characterization

This section is supplementary material to Chapter 4, Sections 4.3.1 and 4.3.2.

B

B.1 Clipping cross sections

Rays have different appearances in three normally used sections (i.e., transverse, tangential, and radial). It is mainly due to the pattern of the organization of ray cells. On the basis of the information from the rays organization, it can help to further identify the direction of fibers. Therefore, Figure B.1 shows the appearance of the cross section when the angle between the cutting plane and the horizontal surface is less than 90°. In contrast, Figure B.2 shows the cross section when the cutting angle is greater than 90°.

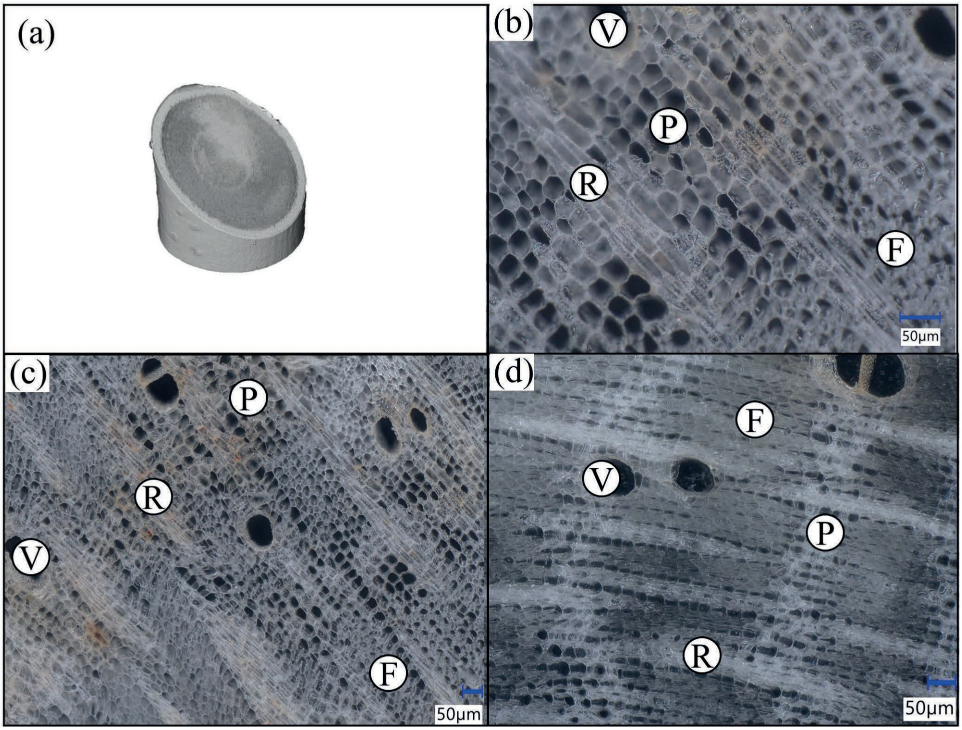

Figure B.1: Clipping plane of the stem region. Tissue types: Fibers (F), parenchyma cells (P), rays (R), and vessel (V).

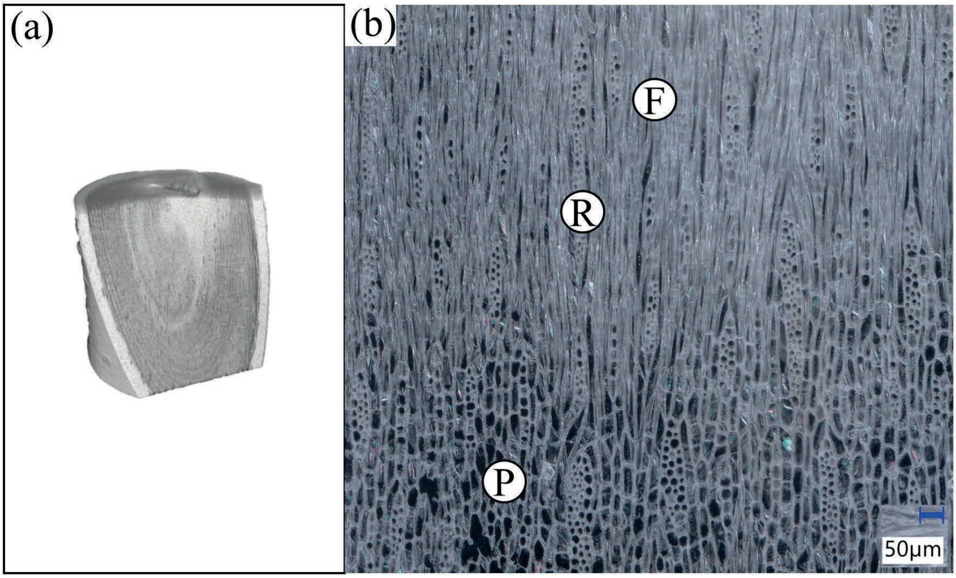

Figure B.2: Clipping plane of the stem region. Tissue types: Fibers (F), parenchyma cells (P), rays (R), and vessel (V).

B.2 Cross sections in the fused region

In the main content of Chapter 4, only an interpretation of the edge and middle location in the fused region is provided. As shown in Figure 4.4, the other locations present in Figures B.4, B.5, B.6, and B.7.

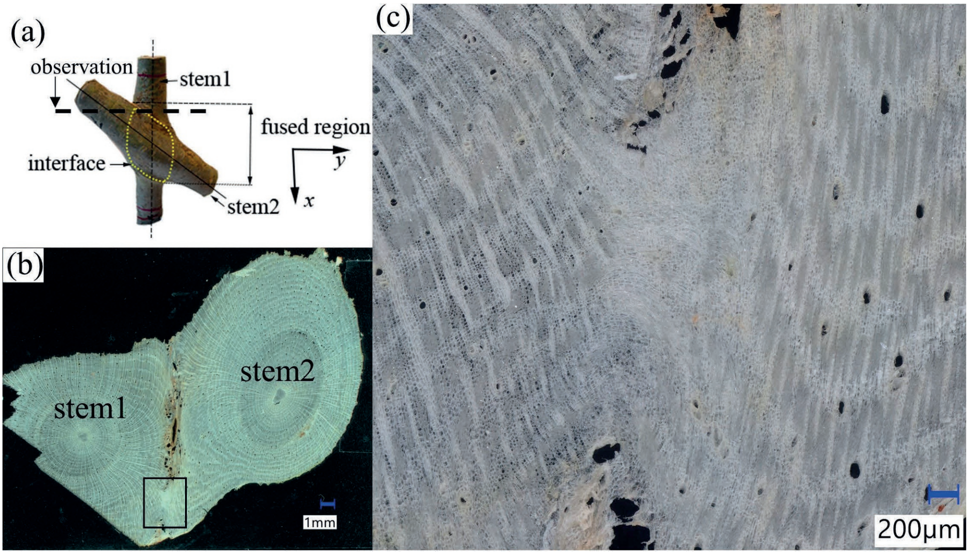

Figure B.3: Tissue organization at the edge location of the fused region in x direction. (a) The inspection location (x_lc2) in a connection; (b) cross-sectional appearance of the inspected section, where the rectangular area is magnified for further examination in (c).

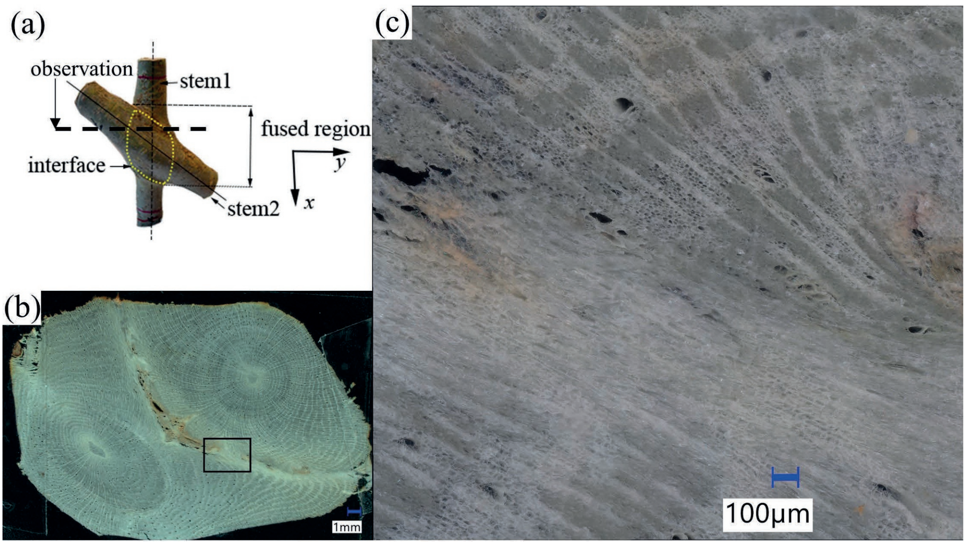

Figure B.4: Tissue organization at the edge location of the fused region in x direction. (a) The inspection location (x_lc3) in a connection; (b) cross-sectional appearance of the inspected section, where the rectangular area is magnified for further examination in (c).

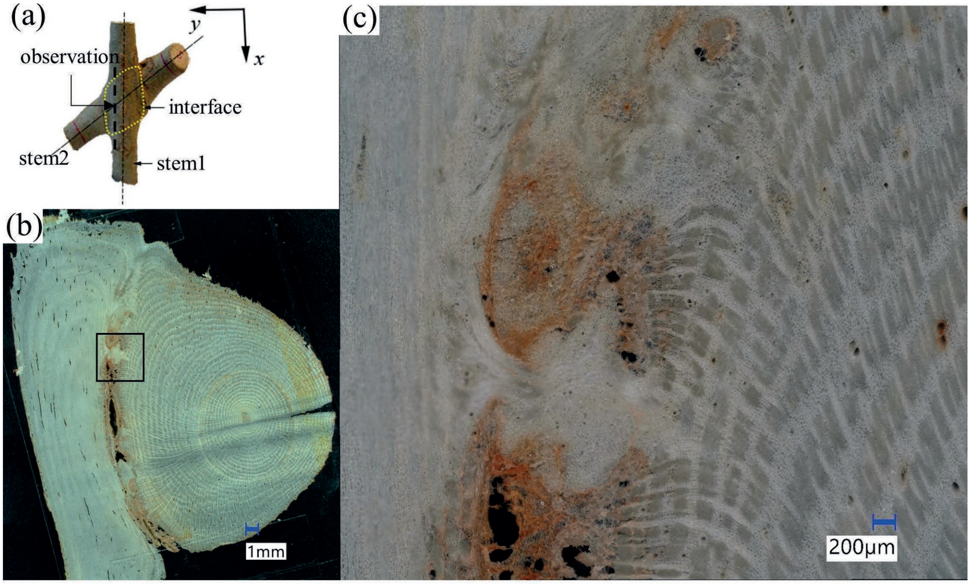

Figure B.5: Tissue organization at the edge location of the fused region in y direction. (a) The inspection location (y_lc2) in a connection; (b) cross-sectional appearance of the inspected section, where the rectangular area is magnified for further examination in (c).

B

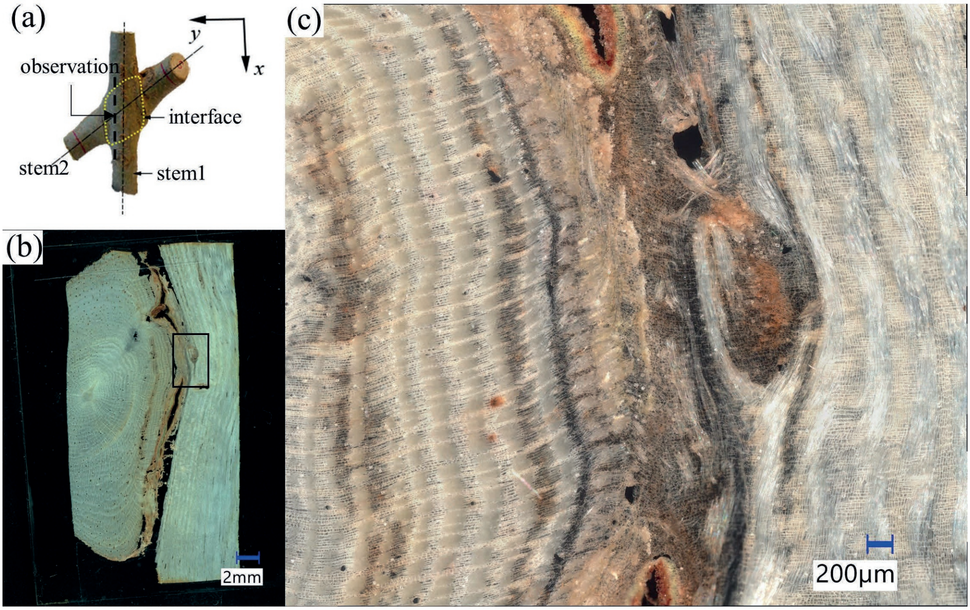

Figure B.6: Tissue organization at the edge location of the fused region in y direction. (a) The inspection location (y_lc3) in a connection; (b) Cross-sectional appearance of the inspected section, where the rectangular area is magnified for further examination in (c).

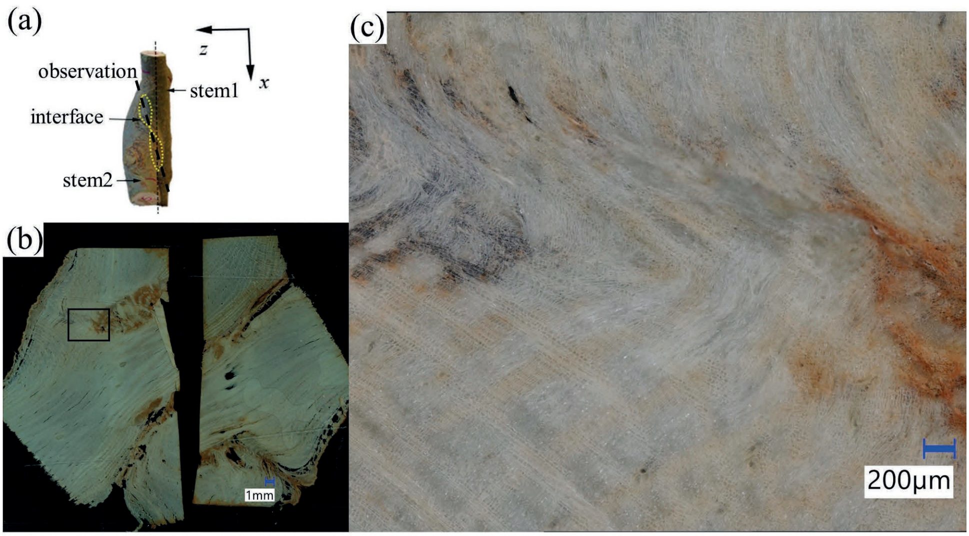

Figure B.7: Tissue organization at the middle location of the fused region in z direction. (a) The inspection location (z_lc2) in a connection; (b) cross-sectional appearance of the inspected section, where the rectangular area is magnified for further examination in (c).

C

Chapter 5: Biomechanical properties of self-growing connections

This section is supplementary material to Chapter 5, Sections 5.2.2 and 5.3.2.

C.1 Spatial location of self-growing connections

In Chapter 5, five braided tree structures are investigated. The spatial location of self-growing connections within a braided tree structure is represented by Tree C in the main content. In addition to that, Tree D (Figure C.1), Tree H (Figure C.2), Tree K (Figure C.3), and Tree I (Figure C.4) are presented in this section.

(a)

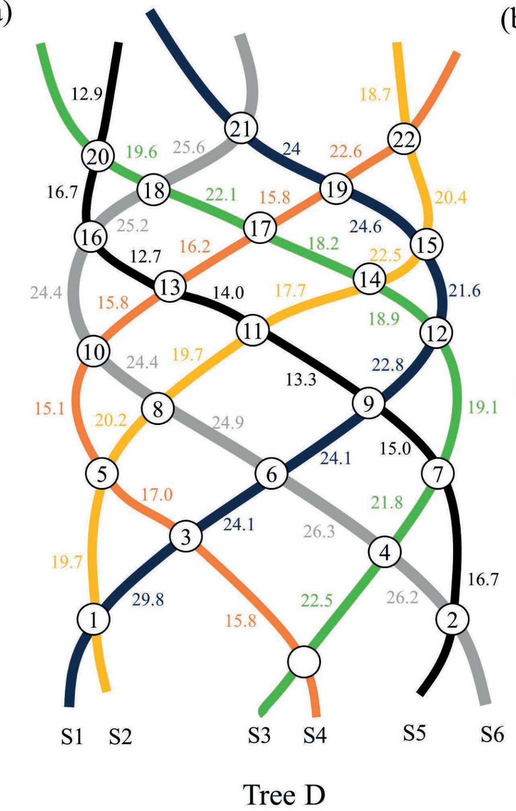

(b)

Stem (S) ID	Avg. Diameter (mm)	CoV (%)	Taper ratio
S1	24.4	10.6	0.81
S2	19.8	7.5	0.95
S3	20.3	8.7	0.87
S4	16.9	15.3	1.43
S5	14.5	11.8	0.77
S6	25.3	3.1	0.98

(c)

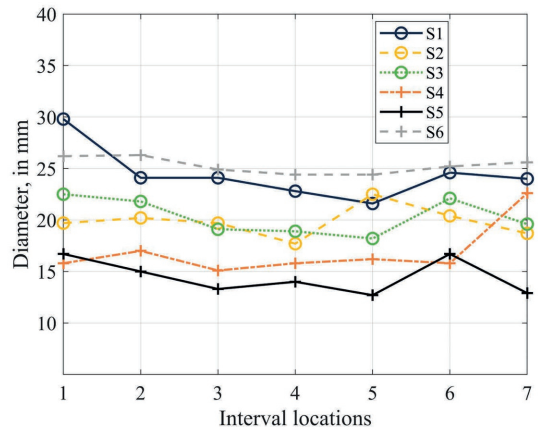

Figure C.1: Geometric information on the braided tree structure Tree D. (a) Schematic illustration of the braided tree structure Tree D; (b) diameter variations in Tree D; (c) diameter variations along stems.

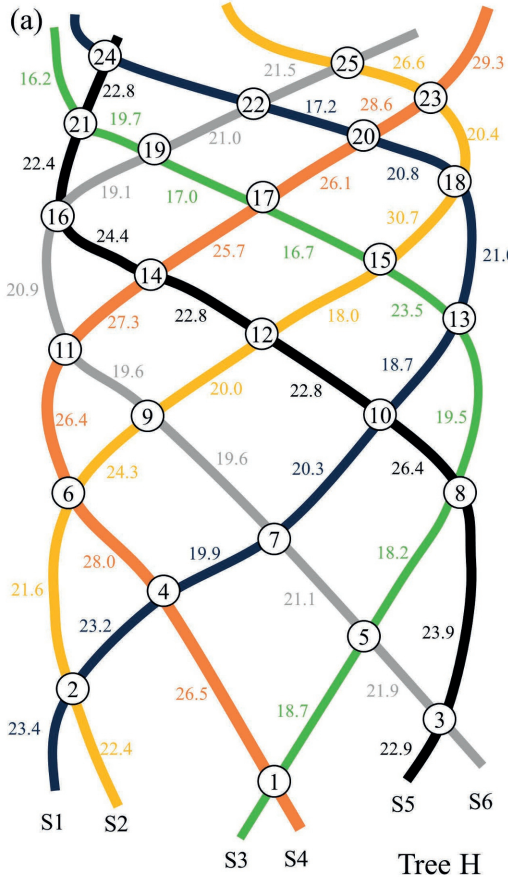

(b)

Stem (S) ID	Avg. Diameter (mm)	CoV (%)	Taper ratio
S1	20.6	10.2	0.74
S2	23.0	17.8	1.12
S3	18.7	12.5	0.87
S4	27.2	4.7	1.11
S5	23.4	4.4	1.00
S6	20.6	4.9	0.98

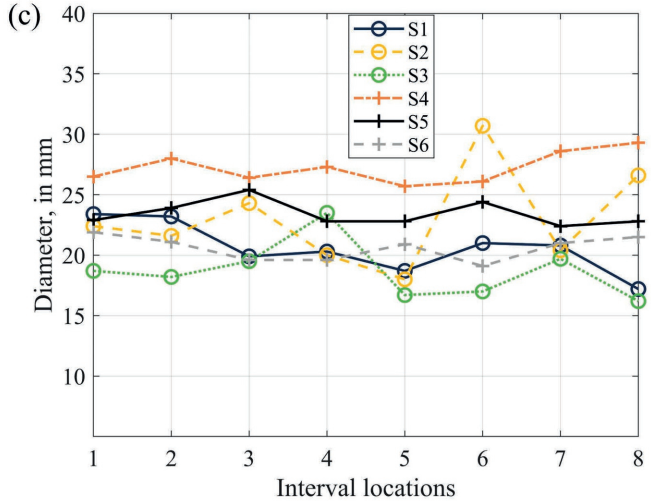

Figure C.2: Geometric information on the braided tree structure Tree H. (a) Schematic illustration of the braided tree structure Tree H; (b) diameter variations in Tree H; (c) diameter variations along stems.

(a)

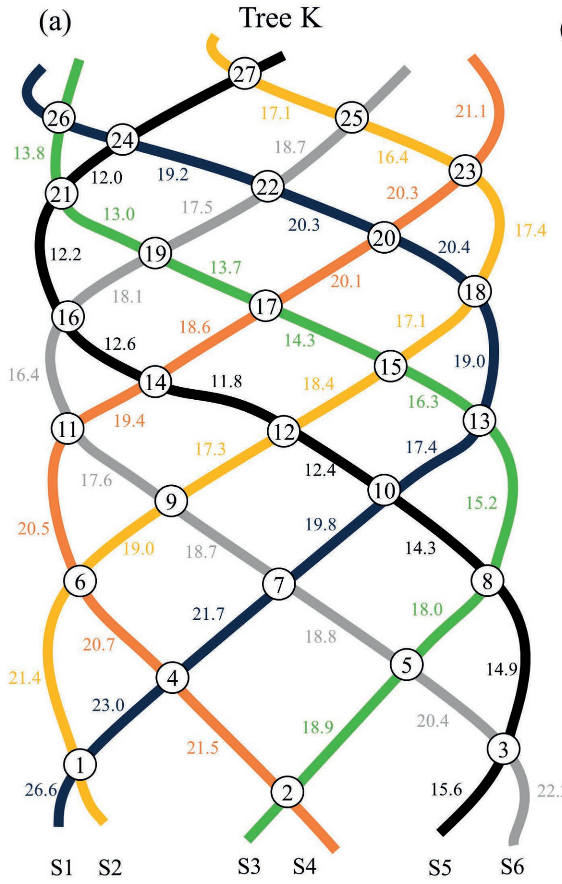

(b)

Stem (S) ID	Avg. Diameter (mm)	CoV (%)	Taper ratio
S1	21.0	13.3	0.76
S2	18.0	8.8	0.80
S3	15.4	13.9	0.73
S4	20.3	4.6	0.98
S5	13.2	11.2	0.77
S6	18.7	9.8	0.79

(c)

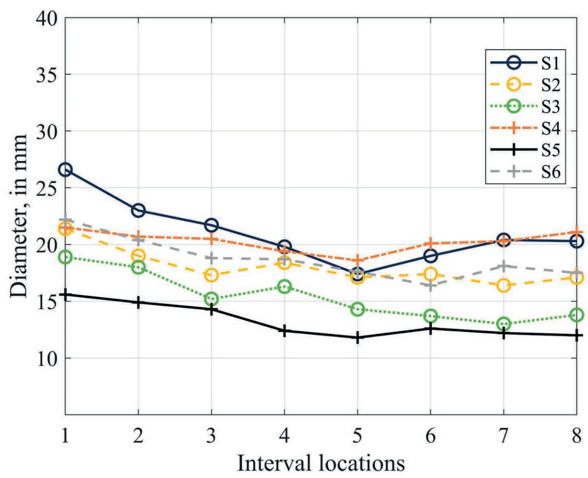

Figure C.3: Geometric information on the braided tree structure Tree K. (a) Schematic illustration of the braided tree structure Tree K; (b) diameter variations in Tree K; (c) diameter variations along stems.

(a)

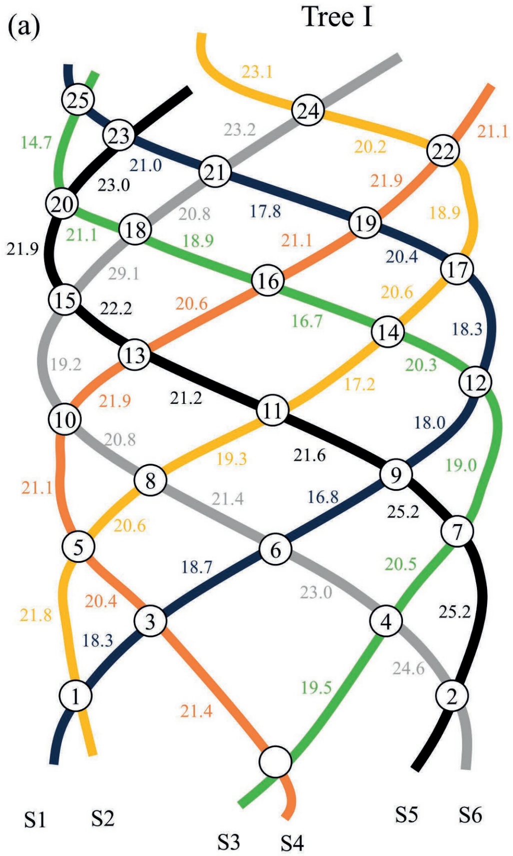

(b)

Stem (S) ID	Avg. Diameter (mm)	CoV (%)	Taper ratio
S1	18.3	6.0	0.97
S2	20.5	12.1	0.76
S3	21.2	7.5	1.10
S4	19.4	2.8	1.02
S5	22.7	5.9	0.91
S6	22.6	14.6	0.85

(c)

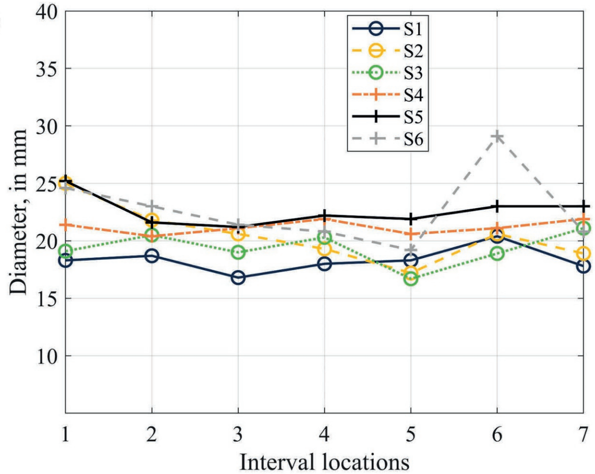

Figure C.4: Geometric information on the braided tree structure Tree I. (a) Schematic illustration of the braided tree structure Tree I; (b) diameter variations in Tree I; (c) diameter variations along stems.

C

C.2 Mechanical performance of self-growing connections

In the main content, only the results of the connection **I**11 are thoroughly explained. In addition to connection **I**11, results from connection D5 and K11 are presented in Figure C.5, C.6. C.7, and C.8.

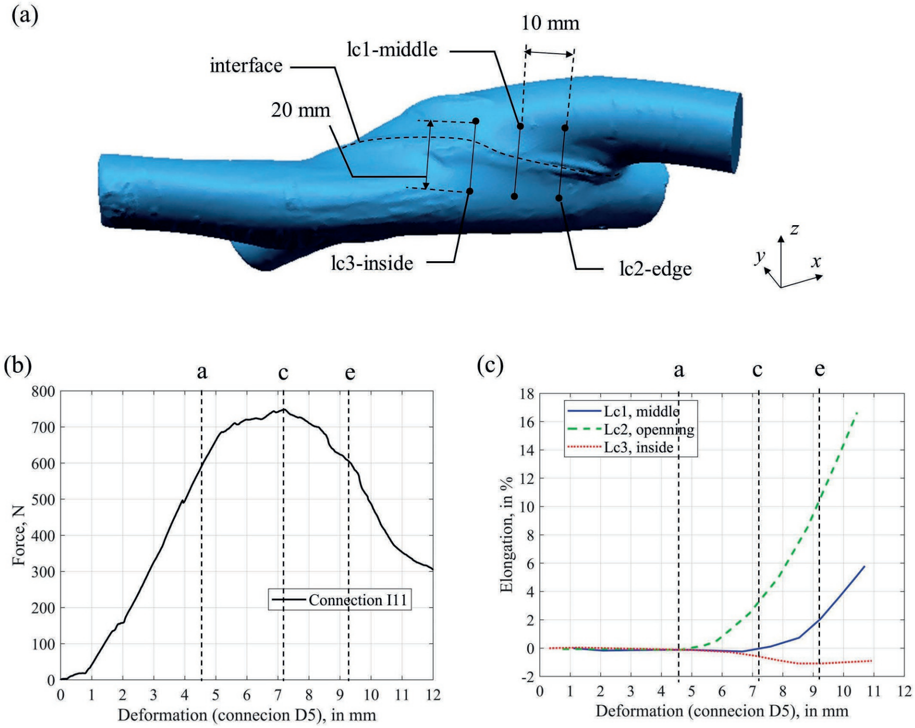

Figure C.5: Force-deformation responses of connection **D**5. (a) Locations to measure the elongation of the interface; (b) overall deformation of connection **D**5; (c) interface elongation of connection **D**5.

C

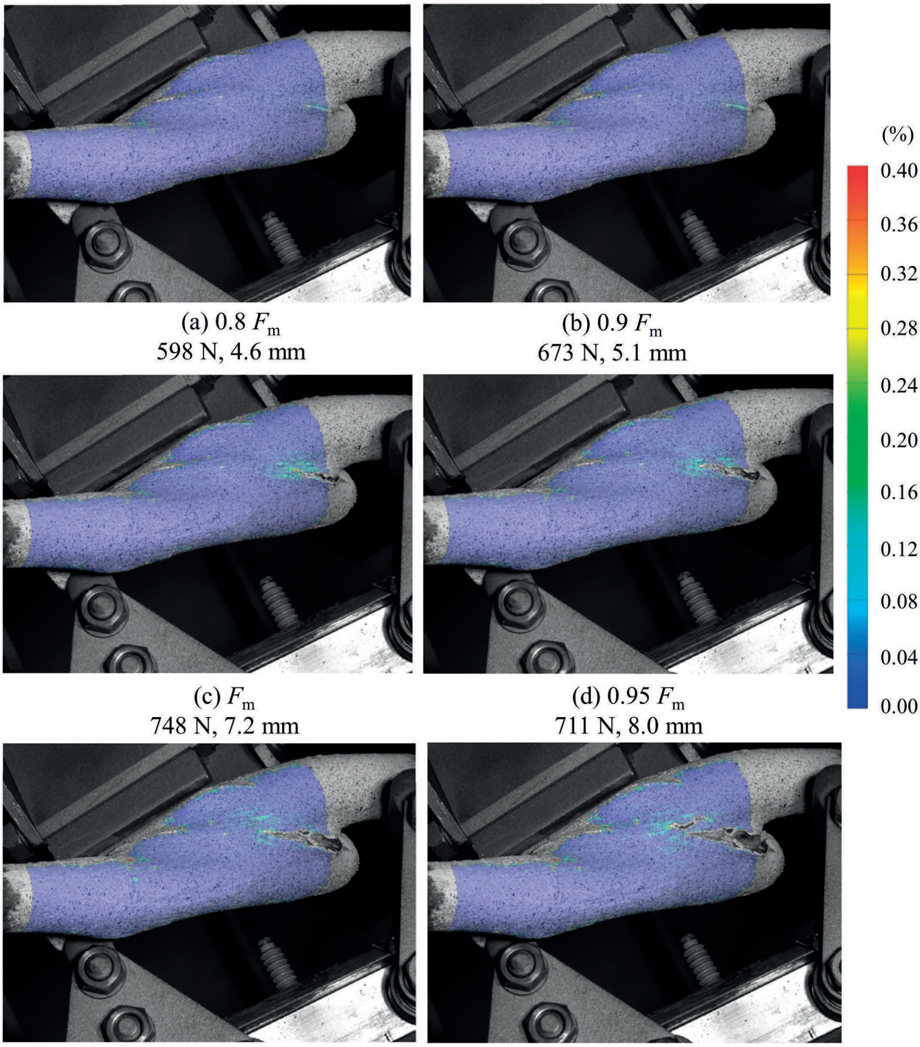

(a) 0.8 F_m
598 N, 4.6 mm

(b) 0.9 F_m
673 N, 5.1 mm

(c) F_m
748 N, 7.2 mm

(d) 0.95 F_m
711 N, 8.0 mm

(e) 0.8 F_m
598 N, 9.4 mm

(f) 0.5 F_m
374 N, 10.7 mm

Figure C.6: Development of surface strain in connection **D**5.

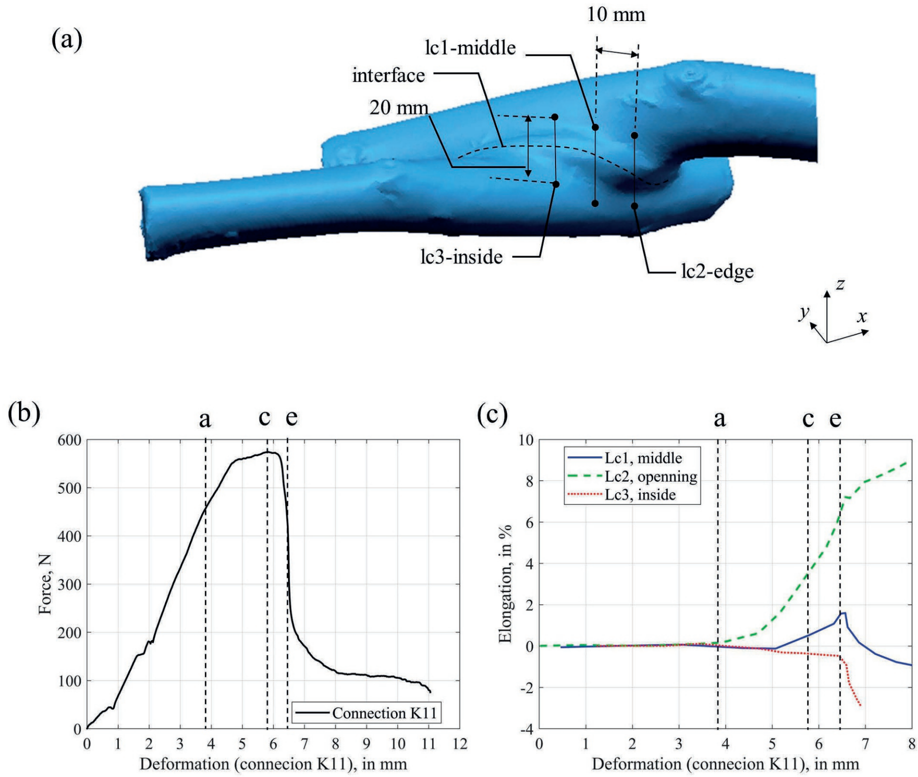

Figure C.7: Force-deformation responses of connection **K**11. (a) Locations to measure the elongation of the interface; (b) overall deformation of connection **K**11; (c) interface elongation of connection **K**11.

C

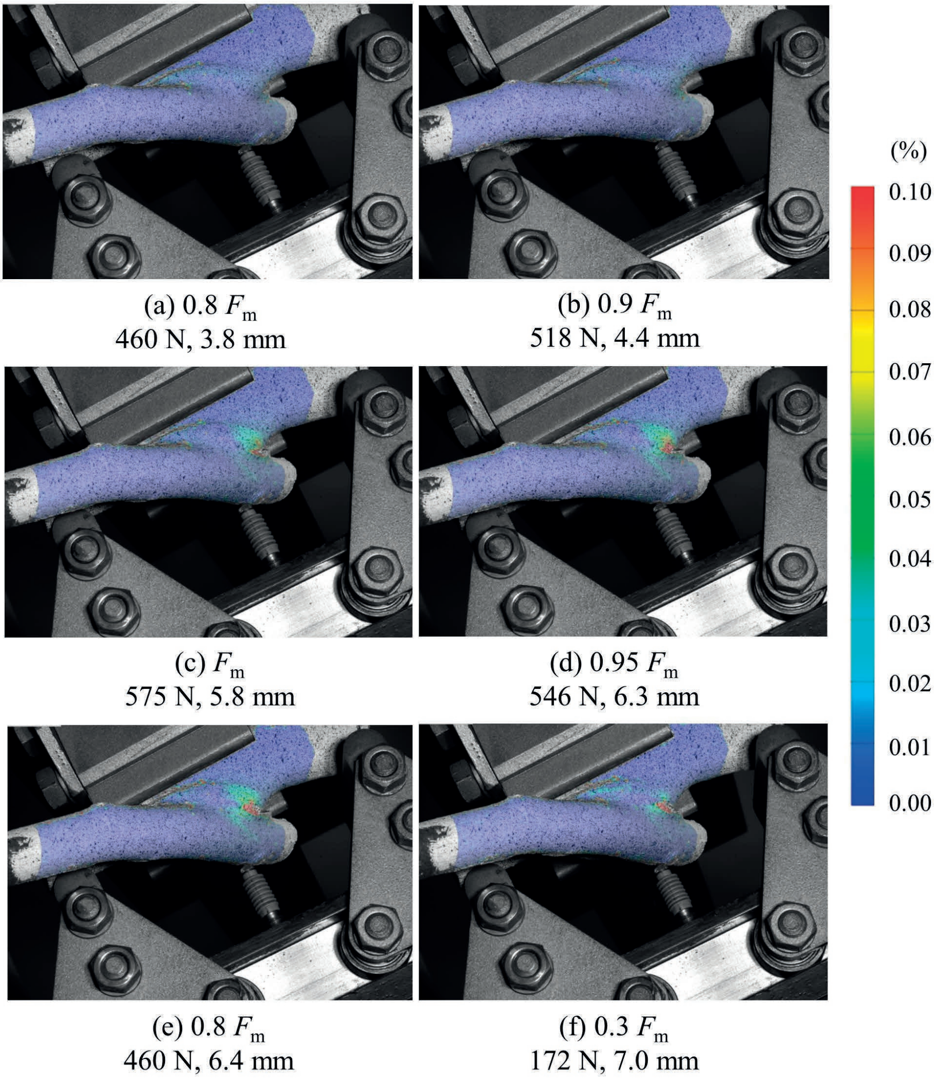

(a) 0.8 F_m
460 N, 3.8 mm

(b) 0.9 F_m
518 N, 4.4 mm

(c) F_m
575 N, 5.8 mm

(d) 0.95 F_m
546 N, 6.3 mm

(e) 0.8 F_m
460 N, 6.4 mm

(f) 0.3 F_m
172 N, 7.0 mm

Figure C.8: Development of surface strain in connection **K**11.

D

Chapter 7: Micro drilling inspection

This section is supplementary material to Chapter 7, Sections 7.3.1.

D.1 DRILLING RESISTANCE PROFILE

In this section, the results in connections 3 to 7 of fused *Ficus benjamina* are presented.

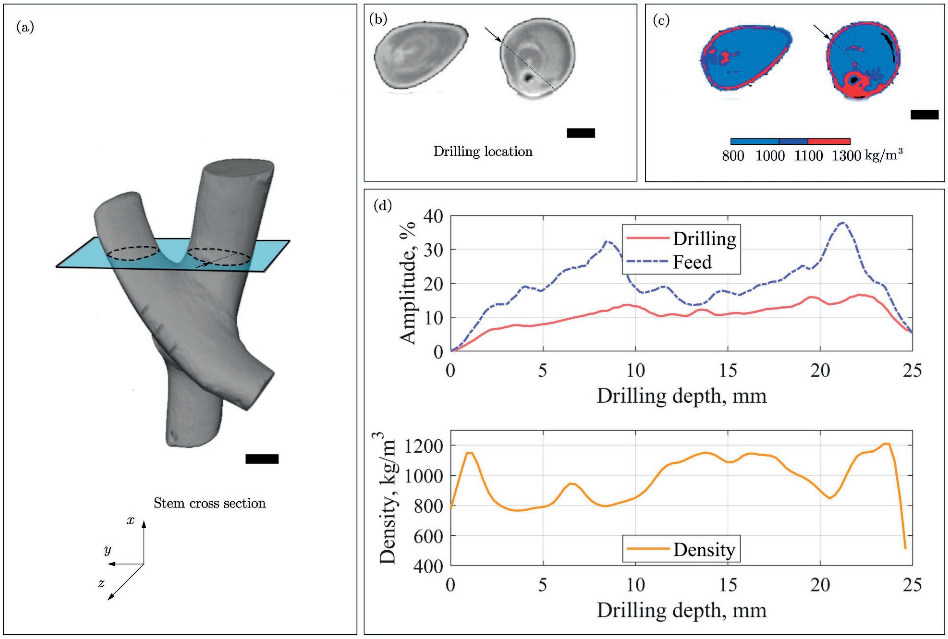

Figure D.1: Connection 3 drilled in stem region (stem1): Density and resistance profiles comparison. (a) Location of the drilled line in the connection; (b) drilling location corresponding to the X-Ray scanning results; (c) density map based on gray values in (b); (d) comparison between resistance profile (top) and density profile (bottom) in the drilling location. Scale bar = 10 mm.

D

D

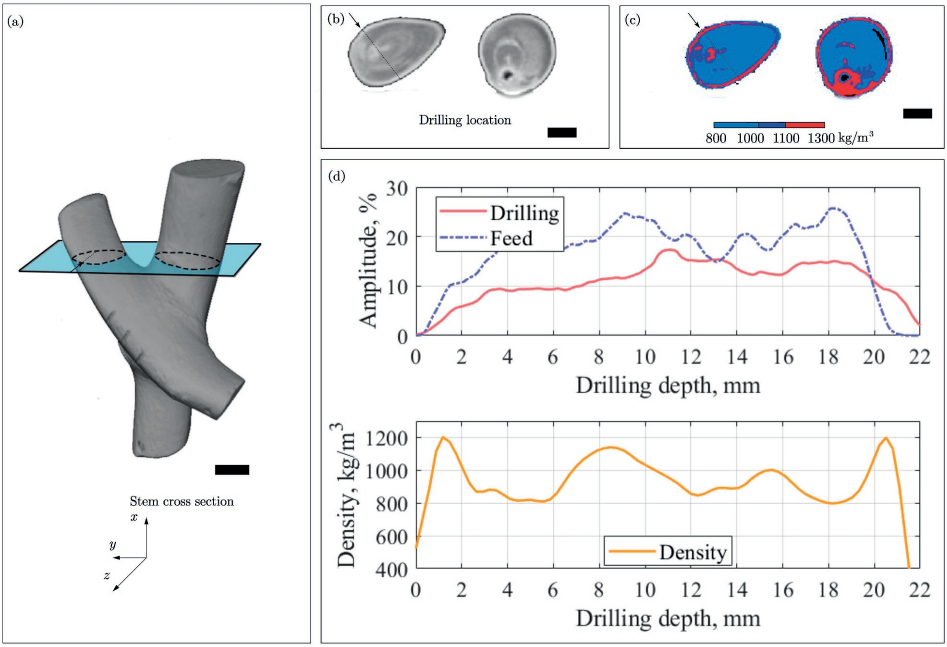

Figure D.2: Connection 3 drilled in stem region (stem2): Density and resistance profiles comparison. (a) Location of the drilled line in the connection; (b) drilling location corresponding to the X-Ray scanning results; (c) density map based on gray values in (b); (d) comparison between resistance profile (top) and density profile (bottom) in the drilling location. Scale bar = 10 mm.

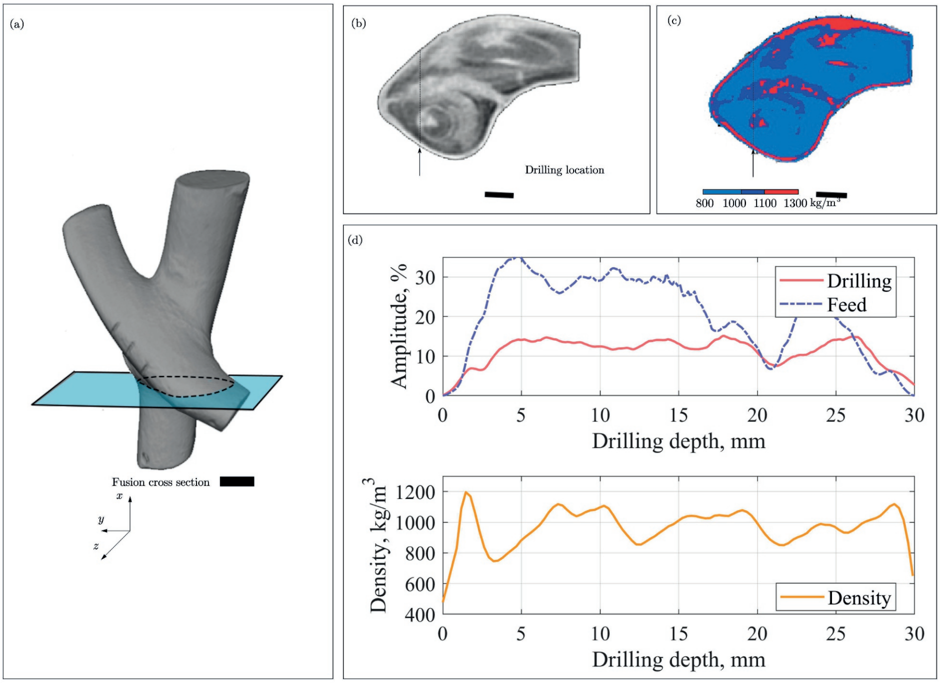

Figure D.3: Connection 3 drilled in the edge of intersected region: Density and resistance profiles comparison. (a) Location of the drilled line in the connection; (b) drilling location corresponding to the X-Ray scanning results; (c) density map based on gray values in (b); (d) comparison between resistance profile (top) and density profile (bottom) in the drilling location. Scale bar = 10 mm.

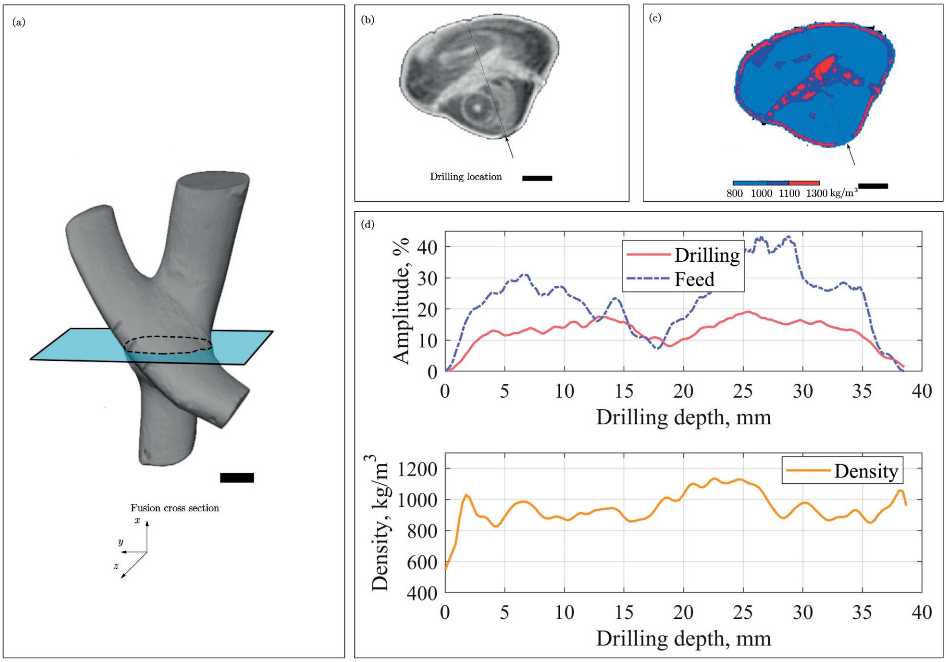

Figure D.4: Connection 3 drilled in the middle of the intersected region: Density and resistance profiles comparison. (a) Location of the drilled line in the connection; (b) drilling location corresponding to the X-Ray scanning results; (c) density map based on gray values in (b); (d) comparison between resistance profile (top) and density profile (bottom) in the drilling location. Scale bar = 10 mm.

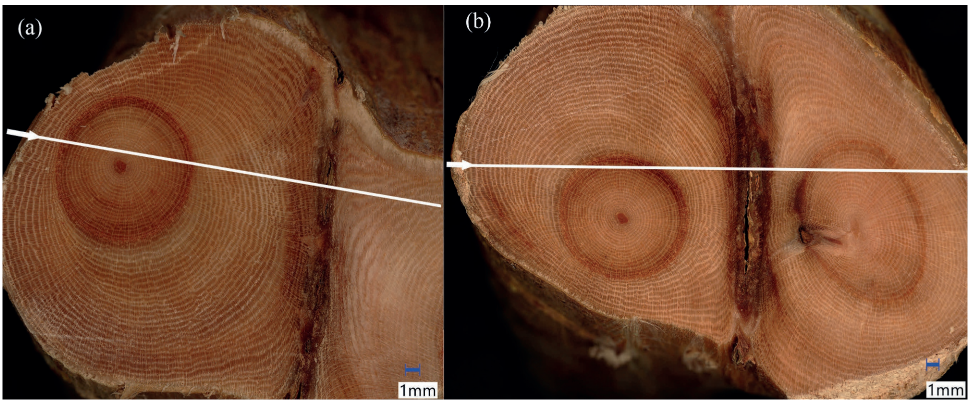

Figure D.5: Anatomy of connection 3. (a) corresponds to the location in Figure D.3; (b) corresponds to the location in Figure D.4.

D

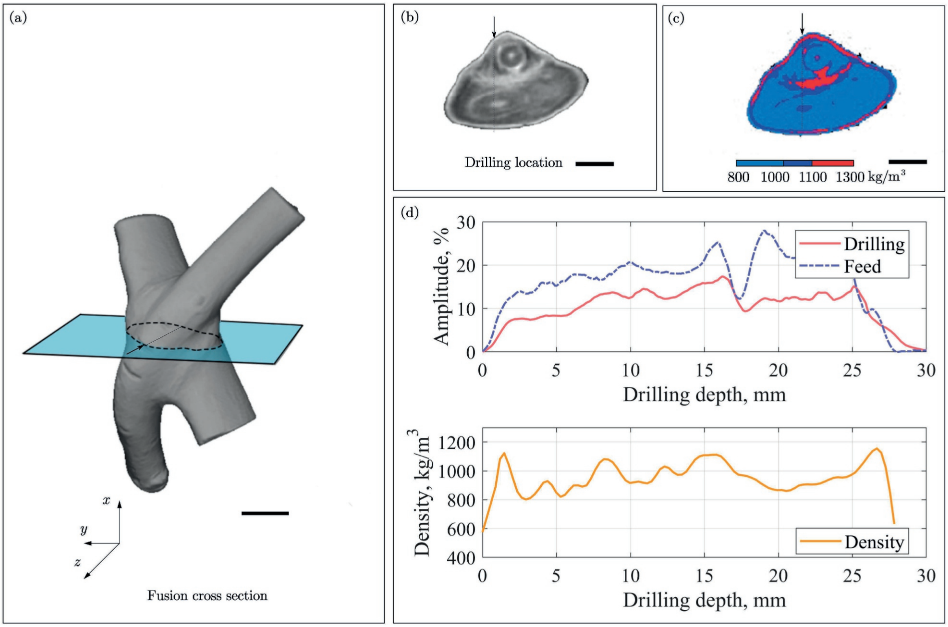

Figure D.6: Connection 4 drilled in the middle of the intersected region: Density and resistance profiles comparison. (a) Location of the drilled line in the connection; (b) drilling location corresponding to the X-Ray scanning results; (c) density map based on gray values in (b); (d) comparison between resistance profile (top) and density profile (bottom) in the drilling location. Scale bar = 10 mm.

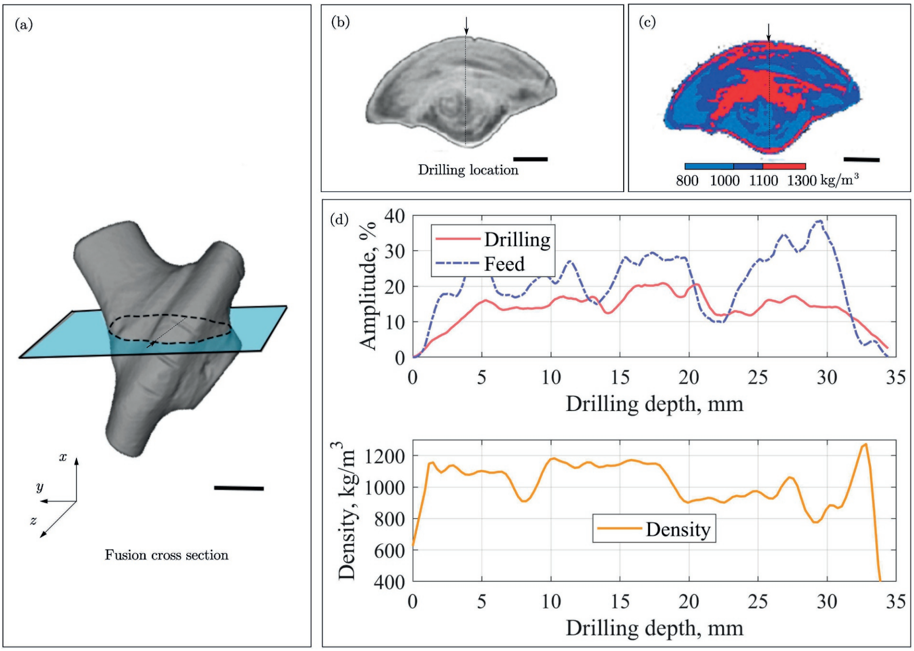

Figure D.7: Connection 5 drilled in the middle of the intersected region: Density and resistance profiles comparison. (a) Location of the drilled line in the connection; (b) drilling location corresponding to the X-Ray scanning results; (c) density map based on gray values in (b); (d) comparison between resistance profile (top) and density profile (bottom) in the drilling location. Scale bar = 10 mm.

D

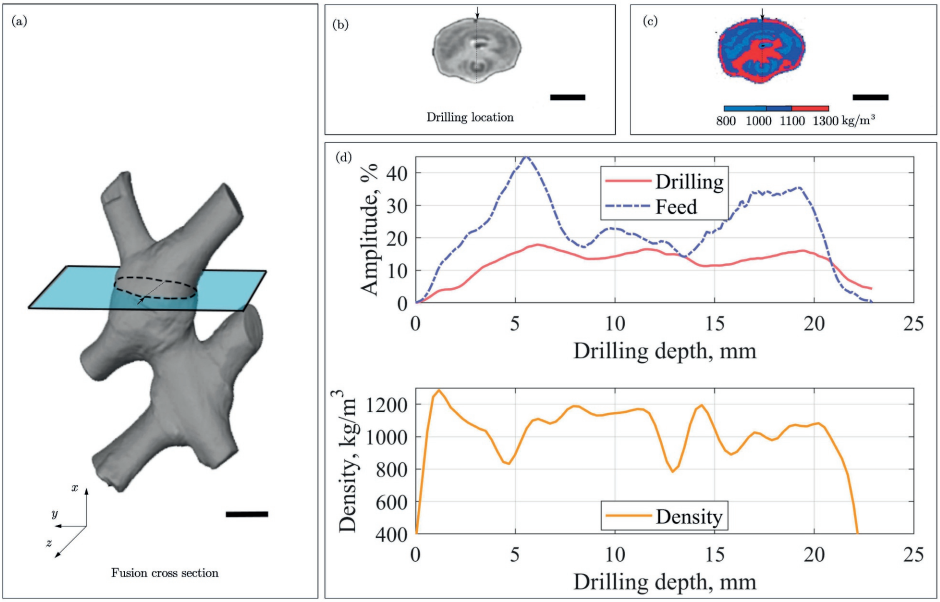

Figure D.8: Connection 6 drilled in the middle of the intersected region: Density and resistance profiles comparison. (a) Location of the drilled line in the connection; (b) drilling location corresponding to the X-Ray scanning results; (c) density map based on gray values in (b); (d) comparison between resistance profile (top) and density profile (bottom) in the drilling location. Scale bar = 10 mm.

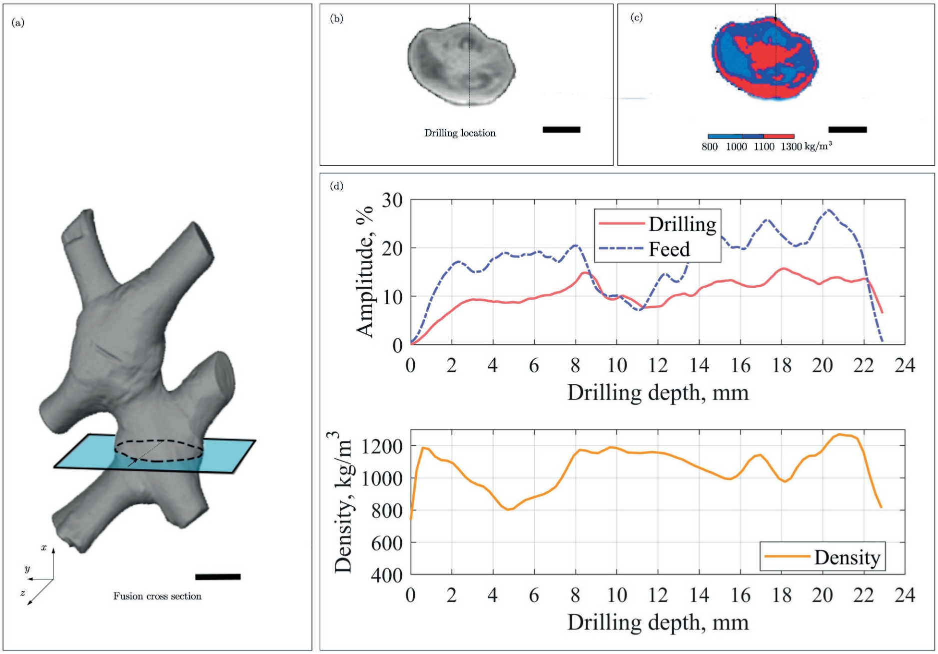

Figure D.9: Connection 7 drilled in the middle of the intersected region: Density and resistance profiles comparison. (a) Location of the drilled line in the connection; (b) drilling location corresponding to the X-Ray scanning results; (c) density map based on gray values in (b); (d) comparison between resistance profile (top) and density profile (bottom) in the drilling location. Scale bar = 10 mm.

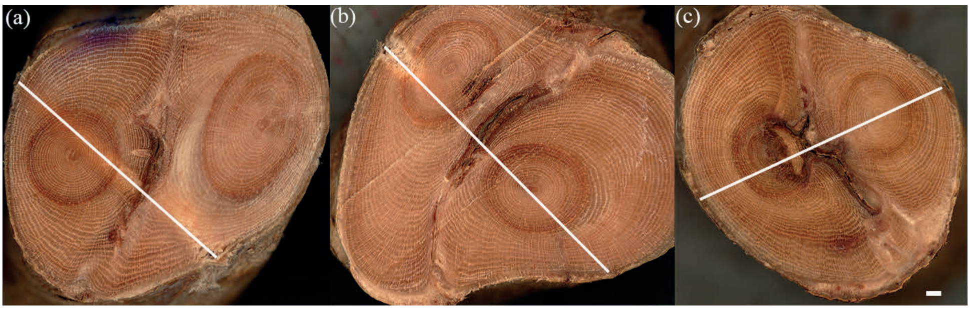

Figure D.10: Anatomy of the middle location of connections. (a) Connection 4; (b) Connection 5; (c) Connection 6. Scale bar = 1 mm.

Acknowledgments

From the beginning of my master's research on wood structures, I developed a deep love for trees, which motivated me to pursue this Ph.D. degree. When my promotor, Jan-Willem, first introduced me to the concept of living tree structures, I believed that I had found the 'dream topic' that combined my engineering background and my personal passion. Little did I know that this dream topic would often appear as a nightmare dressed as a daydream. It turns out that working with nature is not always engineering friendly.

However, as I reflect on the transformation of this initially daunting journey into one filled with growth and achievements, I could not have made this doctoral journey without the support and encouragement of my family, supervisors, colleagues, and friends.

First of all, my parents deserve my deepest gratitude. Their unconditional love, tolerance, patience, and understanding sustained me through the long hours, setbacks, and sacrifices that come with pursuing a doctorate.

Subsequently, I would like to thank my supervisors. Jan-Willem van de Kuilen, thank you for giving me the opportunity to explore the fascinating, yet strange, world of living structures. I want to thank you for your encouragement, constructive criticism, and the freedom to explore and experiment with new ideas. I want to express my sincere appreciation to my second promotor, Nathalie de Vries. You have continuously supported me by providing me with access to a wide range of resources and opportunities to talk with talented architects and landscape designers. Your generosity and patience are vital.

Special thanks to Wolfgang Gard, my daily supervisor. You taught me to grow like a tree at the beginning of my Ph.D. program. In the years to come, the resilience and growth mindset learned from trees will undoubtedly enrich my life. Wolfgang, you are more than just a supervisor and also a friend and mentor. Our academic discussions and our chats on political and philosophical matters have left a lasting impression. Our road trip adventures and the Christmas dinner are beautiful memories for me in the Netherlands. Thank you for your constant guidance and support. I hope you are enjoying your retirement.

My thanks to the committee members Henk Jonkers, Alexia Stokes, Errki Verkasalo, and James Byng for the consideration given to this dissertation and the time taken to examine it. I appreciate your feedback and am honored to have you been present in the final steps in achieving this milestone.

Two special friends that I want to thank are my tree Thomas Ficus and my feline friend Wyvern. Thomas, the first braided tree structure I discovered, has been beside my desk for four years. My Dutch family, Wyvern, has become a family to me and we have relied on each other in the Netherlands.

During my experiments, I have been fortunate to receive valuable support from a group of individuals. I owe my gratitude to those who have played an important role in shaping this journey. I express my thanks to Rene Hoonhout and Harold Bosman from the Green Team of TU Delft. Rene, your help in exploring trees on campus and taking me to tree nurseries has been instrumental in my research. It was through Harold that I came to meet

Thomas, the tree that is important to my research. Your willingness to provide support is greatly appreciated.

In the laboratory, I am grateful to Ellen Meijvogel-de Koning and Wim Verwaal for their assistance with the CT scans. Peter de Vries and Giorgos Stamoulis provided me with a lot of advice and guidance on the design of my mechanical experiments. Giorgos, thank you for your assistance; my tests would not go well without you. Ruben Kunz, John Hermsen, Louis den Breejen, and Fred Schilperoort are thanked for their help with my projects and the free Dutch lessons that enriched the work in the lab. Special thanks to Marco Poot, who provided generous help during my tests in the pavement lab.

The TU Delft Hortus Botanicus is both my playground and my testing field during my research. I express my gratitude to the director, James Byng, and the former director, Bob Ursem, for their constant support of my project. Eveline Oranje, I want to express my gratitude for offering me the opportunity to present my work in the garden. The staff of the TU Delft Hortus Botanicus, Ernst, Sabine, and Ignacio, your assistance during my experiments was valuable. Dennis de Goederen, your assistance during the pulling tests in the garden was crucial to my research. I want to express my appreciation for the insights you shared that enriched my understanding of trees.

My office roommates Abhijith Kamath and Rui Yan, you are the people I see the most every day in my Ph.D. A special mention is reserved for Abhi, a fellow pioneer and friend in the world of plants. I am fortunate to have you by my side, sharing both the ups and downs. Rui, your work ethic and personality have given me a lot of strength. I am grateful to you and Yuxuan Feng for helping me in my life. I extend my thanks to Hagar EI Bamby for introducing me to Islamic culture and providing insight into Dutch and Egyptian societies. I also want to acknowledge Linda Buecking, Vittoria Laghi, and Sigurour Egilsson for making the office experience truly enjoyable.

My research has been shaped by effective communication and collaboration with my colleagues. I want to thank Geert Ravenshorst for your insightful comments on my topic. Yasmine Mosleh, I appreciate your assistance in the later stages of my dissertation. I also express my thanks to Marko Pavlovic for sharing access to DIC and scanner equipment. I thank my colleagues in the group of Biobased Structures and Materials (BSM), Michele Mirra, Giorgio Pagella, Valentin Perruchoud, Maria Felicita for their help, pleasant coffee breaks, and dinners. In addition to being a member of BSM, I had the opportunity to have fun with two other groups of Steel and Composite Structures and Pavement Engineering. Thank Roland Abspoel for your beautiful picture of the vertical forest. Gratitude to Haohui Xin, Weijian Wu, Lu Cheng, Pei He, Weikang Feng, Zhanchong Shi, Fei Yang, Da Xiang, Xiaoling Liu, and Tao Yang for the pleasant dinners and delightful moments shared with you. I would like to extend my appreciation to Ruxin Jing, Yangming Gao, Peng Lin, Chen Wang, Lu Zhou, Shisong Ren, Dongyu Niu, and Lili Ma for their kind invitations to celebrate holidays together. I also thank Li Wang for his sincere advice, constant encouragement, and interest in my doctoral topic. My other friends from the Department of Engineering Structures, Fengqiao Zhang, Yubao Zhou, Yitao Huang, Cheng Chang, Yi Zheng, Yunlong Guo, Chunyan He, Pan Zhang and Yaxi Peng, are thanked for the positive and joyful atmosphere you have brought.

I want to extend my appreciation to the master students, Tessa Lievestro and Zhinan Wu. I am thankful for your willingness to collaborate on this unconventional topic. Tessa, your dedication to pulling experiments is appreciated and Zhinan, your contributions to the digital design with living structures have been valuable.

During the challenging period of COVID-19, my neighbors have supported me greatly. Thanks to Chao Ma, Jun Xu, Jingwei Dong, Yuqian Tu, Xin Liu and Yucheng Liao, Fanxiang Xu, Min Zhang, Dengxiao Lang and Shuo Zhang. In addition, the friends I have made in Delft have made my life feel more dynamic; my thanks go to Zhi Wan, Wen Zhou, Langzi Chang, Ze Chang, Xuehui Zhang, Jingyu Li, Xuhui Liang, and Xiuzhe Wang. My fellow cat lovers, Yue Shang, Yuxuan Feng, and Jiafang Chen thank you for sharing the experience.

Throughout the dissertation writing process, most of my time was spent in the library, where I was gradually becoming part of a fantastic study group. It began with Xin Ren, Kailan Wu, and Robert Baumgartner; and this extended to the group 'TUD lib rolling king'. I would like to express my gratitude to the group members, Pan Fang, Yunzhong Zhou, Zhaochong Cai, Yitao Huang, and Yuexin Huang. This study group has been a source of support during the most challenging stage of my dissertation. We shared food, gossip, and grievances while working toward common goals; and your emotional support was very important.

I would like to extend my gratitude to my old and beloved friends, Pengjuan Sha, Ke Lu, Tianran Yao, Meng Zhao, Zixiao Wang, Yu Zhang and Yan Wang. Although we are in different countries and cities, your constant support and friendship have been a great source of strength for me. Despite the distances between us, the depth of understanding and connection that we shared is beyond miles.

My final gratitude is reserved for my husband, Zhiqiang Wan, whose presence in my life has been a blessing. Your support has been the safety net for my journey. I have seen in you a great journey of personal growth, optimism, insatiable curiosity, and love of life. Your influence not only has brought happiness to my life, but has also improved my growth as a scientist. You are my self-growing connection.

Each of you has made a mark on my academic and personal growth. I am deeply grateful for your genuine support and kindness.

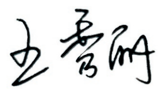

Xiuli Wang
Delft, November 2023

Curriculum Vitæ

Xiuli Wang

05-02-1993	Born in Shandong, China.

Education background

2011-2015	Bachelor of Technology, Civil Engineering Chang'an University Xi'an, China
2015-2018	Master of Science, Structural Engineering Tongji University Shanghai, China
2018-2023	Ph.D. student, Faculty of Civil Engineering and Geosciences Dept. of Engineering Structures, TU Delft the Netherlands
E-mail	stefwangxiuli@hotmail.com

List of Publications

In progress:

1. **X.Wang**, W. F. Gard, Y. Mosleh and J. W. G. Van de Kuilen. Morphological analysis of inosculated connections in weeping figs: Insights on density, geometry, fiber structure, and composition variations. *New Phytologist*, 2024, in preparation.

2. **X.Wang**, W. F. Gard, and J. W. G. Van de Kuilen. Investigations on the tensile out-of-plane properties and performance of self-growing connections in weeping figs. *Biosystem Engineering*, 2024, in preparation.

3. **X.Wang**, W. F. Gard, and J. W. G. Van de Kuilen. Load response analysis and growth effects in interconnected tree systems of *Tilia cordata. Urban Forestry and Greenery*, 2024, in preparation.

Published:

1. **X. Wang**. Anatomical features of self-growing connections in weeping figs (*Ficus benjamina* L.). *EURO2021(Ecological design of the Urban and Rural Environnment)*, conference report, 2021.

2. **X. Wang**, W. Gard, H. Borska, B. Ursem, and J.W.G. Van de Kuilen. Vertical greenery systems: from plants to trees with self-growing interconnections. *European Journal of Wood and Wood Products*, 78:1031–1043, 2020.

3. **X. Wang**, W. Gard, and J.W.G. Van de Kuilen. Vertical forest engineering: Applications of vertical forests with self-growing connections in high-rise buildings. *ISCHP (International Scientific Conference on Hardwood) Proceedings*, 184-197, 2019.

TU Delft Delft University of Technology

9 789463 845618